

Transverse beams stability studies at the Large Hadron Collider

THÈSE N° 6321 (2015)

PRÉSENTÉE LE 30 JANVIER 2015

À LA FACULTÉ DES SCIENCES DE BASE
LABORATOIRE DE PHYSIQUE DES ACCÉLÉRATEURS DE PARTICULES
PROGRAMME DOCTORAL EN PHYSIQUE

ÉCOLE POLYTECHNIQUE FÉDÉRALE DE LAUSANNE

POUR L'OBTENTION DU GRADE DE DOCTEUR ÈS SCIENCES

PAR

Xavier BUFFAT

acceptée sur proposition du jury:

Prof. G. Meylan, président du jury
Prof. L. Rivkin, Dr T. Pieloni, directeurs de thèse
Dr W. Fischer, rapporteur
Dr M. Meddahi, rapporteuse
Prof. M. Q. Tran, rapporteur



ÉCOLE POLYTECHNIQUE
FÉDÉRALE DE LAUSANNE

Suisse
2014

Whatever you do will be insignificant,
but it is very important that you do it.
— Mahatma Gandhi

Acknowledgements

I would like to acknowledge the many people who contributed to the work presented in this thesis and, most importantly, made my stay at CERN a great pleasure. In particular, I'd like to thank my supervisor, Tatiana Pieloni, for the time she spent into teaching me many aspects of accelerators physics, especially related to studies of beam-beam effects and for following my work closely, providing guidance, as well as constructive criticism. Her enthusiasm with new ideas, new studies really was motivating.

I also would like to mention the particular scientific contribution of three people. I will start with Werner Herr, who puts a great deal of importance in transmitting his knowledge to younger generations. In particular, his experience in design, study and operation with several colliders, i.e. with all colliders ever built at CERN, is a valuable gift that he shared through an unreasonable amount of morning coffees. It was much appreciated and the studies presented in this thesis greatly profited from these discussions.

As my office mate and as one of the impedance expert for the LHC, Nicolas Mounet was put to great contribution by my incessant requests and questions linked to beam dynamic in the presence of beam coupling impedance and in particular to Landau damping. Nicolas' thirst for novel theoretical developments is not to be underestimated, which drove extremely interesting discussions that are at the heart of several developments described in this thesis. When at CERN, Simon White was never far from our office when such discussion would happen. In particular, he revived the studies of the combined effect of beam-beam interactions and the beam coupling impedance using a linear model and started the studies with a multi-particle tracking codes. This fruitful collaboration lead to several results discussed in this thesis.

Along with Tatiana, Werner, Nicolas and Simon, I would like to thank my close colleagues and friends with which we shared many lunches and coffees. Through several debates in an open and relaxed atmosphere, they managed to turn the pressure, the stress and the controversies around daily operation of the LHC and its injectors, as well as during machine development studies, into valuable, usually humorous, times. While fairly non-serious looking in several occasion, this attitude provides great opportunities for both personal and scientific development. As I strongly believe that it is somewhat dangerous to focus all ones efforts in one or the other direction, I consider this type of environment to be very valuable. Consequently, I'm very grateful to Tatiana, Werner, Nicolas, Simon, Benoit Salvant, Rogelio Tómas, Giovanni Rumolo, Kevin Li, Giovanni Iadarolla, Hannes Bartosik, Adrian Öftiger, Rama Calaga, Elias

Chapter 0. Acknowledgements

Métral and Javier Barraco. I do consider that I come out of this experience at CERN grown up on a personal and professional level and I owe a lot to them.

The CERN organisation deserves acknowledgement for financing this study and providing resources including, of course, beam time for experimental studies. Also, I would like to mention the effort of Tatiana, as well as Elias and Gianluigi Arduini to support and promote our work, giving strength to our proposals for operational changes and experimental tests. Collaborations with the operation team of the LHC, as well as the different instrumentation teams, was extremely fruitful, not only for the data acquisition and analysis during daily operation, but also during the design, implementation and realisation of experimental studies. Among many people, I'm thinking in particular to Jorg Wenninger, Stefano Redaelli, Giulia Papotti, Rossano Giachino, Mike Lamont, George Trad, Wolfgang Hofle and Daniel Valuch.

I am very grateful to Lenny Rivkin, first for introducing me to the field of accelerator physics with rather exciting lectures on the matter. Secondly, Lenny gave me the opportunity to work at CERN in the frame of laboratory work during my Master studies at EPFL, later for the Master thesis and then for this PhD study. He was constantly supportive for my work, in particular, he financed precious computing time on EPFL's High Performance Computing machines. Lenny also provided financing for a trip to Brookhaven National Laboratory, in order to perform experimental studies at the Relativistic Heavy Ion Collider, as well as to the International Particle Accelerator Conference 2014 in Dresden, two enjoyable and enriching trips. The opportunity to work as a teaching assistant for MAD-X exercises was also very much appreciated.

I would also like to acknowledge Brookhaven National Laboratory, in particular Wolfram Fischer and Simon, for inviting me for two weeks, in order to collaborate on experimental studies on their collider. Despite the lack of convincing outcome from our experiments due to misfortune with beam instrumentation, this trip was very enriching from a personal and from a scientific point of view. Indeed, through the design and realisation of an experiment on another machine, in a different environment, I add the chance to acquire valuable experience and learn from interesting people.

The help of EPFL's High Performance Computing team was very much appreciated. In particular, the availability of the resources is simply amazing, as well as the availability of the people to provide advices and help. The lectures given by Vittoria Rezzonico on parallel computing were particularly useful and had a significant impact on the developmental of the parallelised codes and, thus, allowed me to use more efficiently the resources.

I would like to thank the members of the jury for the time they spent on reading on commenting this thesis.

Most importantly, I would like to thank my family, especially my parents, for their uncon-

ditional love and support, a driving force for anything I do. As well as all my friends, for all the fun we have, I am thinking in particular to the *Abri Cool* team, the *VBC Pailly* and the *Jeunesse the Pailly*. Above all, I thank my beloved one, Aurélie, for she provides me sunshine on cloudy days.

Résumé

Un faisceau de particules chargées circulant à une vitesse proche de celle de la lumière produit un fort champ de sillage électromagnétique qui, par l'intermédiaire des éléments environnants, affecte les particules du faisceau. Le système couplé de particules chargées et de champs de sillage peut devenir instable, et par conséquent détériorer la qualité du faisceau. Ce type d'effet joue un rôle important dans la plupart des anneaux de stockage existants, puisqu'ils limitent souvent la performance maximale. Dans un collisionneur de particule, la présence d'un deuxième faisceau change significativement la dynamique, car les interactions électromagnétiques des faisceaux l'un sur l'autre sont généralement fortes et peuvent aussi limiter la performance. Cette thèse traite de la stabilité des deux faisceaux dans un collisionneur, avec une attention particulière pour le Grand Collisionneur de Hadron du CERN (Large Hadron Collider). Par rapport aux autres machines, le Grand Collisionneur de Hadron a la particularité d'avoir beaucoup de paquets de particules par faisceau, chacun d'eux subissant plusieurs interactions faisceau-faisceau à distance et frontales. Les modèles décrivant la stabilité des faisceaux existants ne sont pas utilisables dans de telles configurations et doivent donc être étendus.

Les interactions faisceau-faisceau sont très non-linéaires, en conséquence, les particules du faisceau oscillent à des fréquences légèrement différentes, ce qui provoque l'amortissement des mouvements cohérents par effet Landau. Un intégrateur numérique a été développé pour estimer cet effet sur des modes d'oscillation potentiellement instables. Comme les propriétés de la machine et des faisceaux changent durant le cycle opérationnel, les effets faisceau-faisceau et, par conséquent, les effets Landau varient de façon significative. Il est démontré que la stabilité des faisceaux est critique durant certaines phases opérationnelles. Des observations d'instabilités durant ces phases, ainsi que durant des expériences dédiées, appuient le modèle dans la majorité des cas. Plusieurs cas restent toutefois inexplicables dans le cadre de ce modèle. Un mécanisme est proposé pour expliquer ces différences. Il est montré que la distribution des particules dans le faisceau peut être affectée par la présence de bruit externe. Comme l'effet Landau dépend fortement de la distribution des particules, il est démontré qu'une déformation non-mesurable de la distribution peut sévèrement détériorer la force de l'amortissement Landau. Des simulations multi-particules sont utilisées pour démontrer l'importance de cet effet dans des configurations réalistes.

Les effets non-linéaires liés aux interactions faisceau-faisceau ont un effet bénéfique sur la stabilité cohérente des faisceaux, pourtant le système couplé comprenant les deux faisceaux peut être moins stable que les deux systèmes découplés. Un modèle linéaire existant

décrivant la stabilité de faisceaux composés d'un unique paquet collisionnant en un seul point est étendu de façon à pouvoir décrire les faisceaux du Grand Collisionneur de Hadron, c'est à dire incluant multiples paquets et multiples points d'interaction. Il est démontré que dans certaines conditions, l'action résonante des forces faisceau-faisceau et des champs de sillage peut conduire à de fortes instabilités. Une expérience a été réalisée, montrant des résultats en accord avec le modèle. Des techniques possible de mitigation sont étudiées. Il est montré qu'un feedback résistif, tel qu'implémenté dans le Grand Collisionneur de Hadron, est efficace contre ce type d'instabilité. Ce modèle ne tient pas compte des effets non-linéaires des forces faisceau-faisceau et, par conséquent, l'amortissement par effet Landau. Cet effet est étudié en comparant les résultats obtenus avec des simulations multi-particules qui tiennent compte des effets cohérents et incohérents des forces faisceau-faisceau.

Une solution opérationnelle ayant pour but de diminuer les contraintes dues aux instabilités cohérentes, profitant de l'effet stabilisant des collisions faisceau-faisceau frontales, est analysées à la lumière des modèles développés et est testée expérimentalement.

Mots-clés : Accélérateur de particules, Collisionneur, Champ de sillage électromagnétique, Interaction faisceau-faisceau, Effect collectif, Stabilité du faisceau, Amortissement de Landau, diagramme de stabilité, simulation multi-particules

Summary

A charged particle beam travelling at a speed close to that of light produces large electromagnetic wake fields which, through interactions with its surroundings, act back on the particles in the beam. This coupled system of charged particles and electromagnetic fields may become unstable, resulting in a deterioration of the beam quality. Such effects play a major role in most existing storage rings, as they usually limit the maximum performance achievable. In a collider, the presence of a second beam significantly changes the dynamics, as the electromagnetic interactions of the two beams on each other is usually very strong and may also limit the collider performance. This thesis treats the coherent stability of the two beams in a circular collider, including the effects of the electromagnetic wake fields and of the beam-beam interactions, with particular emphasis on CERN's Large Hadron Collider. Unlike colliders, this machine features a large number of bunches per beam each experiencing multiple long-range and head-on beam-beam interactions. Existing models describing the beams stability are not valid in such configurations and therefore need to be extended.

The beam-beam interactions are very nonlinear, as a result, different particles in the beams oscillate with slightly different frequencies, generating Landau damping of coherent motion. A numerical integrator is developed in order to estimate the effect of Landau damping on potentially unstable coherent modes of oscillation. As the characteristics of the machine and the beams vary along the operational cycle of the Large Hadron Collider, the beam-beam forces and consequently the effect of Landau damping may vary significantly. It is shown that some configurations are particularly critical. Measurements of coherent instabilities during these operational phases, as well as in dedicated experiments in similar conditions, are presented and compared to the model. While most observations are in agreement with the model, some observed instabilities remain unexplained. A mechanism is proposed as an explanation for these instabilities. It is shown that the distribution of particles in the beam can be distorted in the presence of external noise. As the Landau damping effect strongly relies on the distribution of particles in the beams, it is shown that non-measurable variations of the distribution functions can lead to significant deterioration of the Landau damping strength. Multi-particle tracking simulations are used to demonstrate this effect in realistic conditions.

While the nonlinearity of the beam-beam interactions have a positive effect on the coherent stability of the beams, the coupled system including the two beams may be less stable than the two individual beams considered separately. An existing linear model for the beams

Chapter 0. Summary

stability introduced earlier to describe single bunches encountering a single beam-beam interaction is extended to describe the beams in the Large Hadron Collider, i.e. involving multiple bunches and multiple beam-beam interactions. It is shown that under certain circumstances, a resonant action of the beam-beam forces and the electromagnetic wake fields may lead to strong instabilities. An experiment was performed to test these effects in the Large Hadron Collider, showing a good agreement with the models. Mitigation techniques against these instabilities are investigated, it is shown that a transverse resistive feedback can suppress such instabilities. This model does not include nonlinear effects, and consequently Landau damping effects. In order to address this effect, we compare the predictions of the linear model to those of a multi-particle tracking code, featuring both the coherent and the incoherent aspects.

An operational solution to relax the limitations due to coherent instabilities, taking advantage of the stabilising effect of the head-on beam-beam interactions, is discussed based on the models developed and tested experimentally.

Keywords : Particle accelerator, Collider, Electromagnetic wake field, Beam-beam interaction, Collective effect, Beam stability, Landau damping, Stability diagram, multi-particle tracking simulation

Contents

Acknowledgements	v
Résumé	ix
Summary	xi
List of figures	xvii
List of tables	xxvii
List of symbols	xxix
List of acronyms	xxxiii
Glossary	xxxv
1 Introduction	1
2 Beam Dynamics	3
2.1 Single particle dynamic	3
2.1.1 Beam-beam interactions	8
2.2 Collective effects	9
2.2.1 Beam coupling impedance	9
2.2.2 Coherent Beam-beam effects	11
2.2.3 The circulant matrix model	12
2.2.4 (Non-)normal mode analysis	16
2.2.5 Landau damping	20
2.2.6 Multi-particle tracking simulation	22
2.3 Singular value decomposition	22
2.4 Luminosity	23
3 The Large Hadron Collider	25
3.1 Physics case	25
3.2 Configuration	25
3.2.1 Standard operational cycle	34
3.3 Instrumentation	35

Contents

3.3.1	Transverse feedback	35
3.4	Impedance model	35
4	Landau damping of head-tail modes	37
4.1	Numerical method	37
4.2	Applications to the LHC operational cycle	38
4.2.1	Betatron squeeze	38
4.2.2	Bringing the beams into collision	43
4.2.3	Luminosity production	47
4.2.4	Levelling with a transverse offset	51
4.3	Non-Gaussian distribution functions	51
4.3.1	Distortion due to resonant diffusion	52
4.3.2	Broadband excitation	53
4.4	Conclusion	59
5	Coherent Dynamic	63
5.1	Coherent motion without impedance	63
5.1.1	Observations	63
5.2	Coherent motion with impedance	67
5.2.1	Simulations	67
5.2.2	Non-normal behaviour	85
5.2.3	Observations	89
5.3	Conclusion	99
6	Applications for the operation of the LHC	101
6.1	Instabilities at the end of the squeeze	102
6.1.1	First part of 2012	102
6.1.2	Second part of 2012	104
6.2	Squeezing with colliding beams	105
6.2.1	Orbit stability at the IP	107
6.2.2	Controls aspects	112
6.2.3	Additional requirements for commissioning	114
6.3	Chromaticity control	114
6.4	Conclusion	115
7	Conclusion	117
A	COMBI	121
A.1	Implementation of the first level of parallelisation	121
A.1.1	Performance	122
A.2	A second level of parallelisation	124
A.2.1	Hybrid approach : COMBHY	124
A.2.2	MPI and shared memory : COMBISH	124
A.2.3	Performance	125

A.2.4	Conclusion	129
A.3	Implementation of the actions	130
A.3.1	Beam-beam	130
A.3.2	Lattice transfer	131
A.3.3	External noise	131
A.3.4	Beam coupling impedance	131
A.3.5	Transverse damper	132
B	PySSD	135
B.1	The module	135
B.2	Interface with MAD-X	136
B.3	Demo code	138
C	BimBim	139
C.1	Beams	140
C.2	Basis	140
C.3	System	140
C.4	Actions	141
C.4.1	Transport	141
C.4.2	Beam beam	142
C.4.3	Impedance	144
C.4.4	Damper	145
C.5	Demo code	147
D	The online beam-beam footprint viewer	149
D.1	Implementation	149
D.1.1	Automatic acquisition of machine and beam parameters	150
D.1.2	Bunch selection	150
D.1.3	Maintenance	151
D.2	Usage	151
D.2.1	Working point optimisation	151
D.2.2	Stability consideration	153
D.3	How to	153
D.3.1	Basics	153
D.3.2	Advanced	154
	Bibliography	165

List of Figures

2.1	Curvilinear coordinate system. We shall work in the paraxial approximation, thus for convenience, the conjugate variables are given by $(x, x' = p_x/p_0)$, $(y, y' = p_y/p_0)$ and (s, δ) , where p_0 is the canonical momentum. p_x, p_y are the transverse projections and δ is the relative deviation to the design momentum.	3
2.2	Phase space ellipse.	6
2.3	Beam-beam kick experienced by the single particles as a function of their position with respect to the closed orbit, in different configurations where the two beams collide HO, with a small transverse offset or LR. Particles oscillating with different amplitudes, i.e. with different actions, span different part of the force turn after turn (black arrows). The horizontal and vertical tunes of particles oscillating with different transverse actions, (J_x, J_y) , are reported on a tune digram for the different types of collisions.	9
2.4	Illustration of the discretisation of the longitudinal phase space in the CMM.	13
2.5	Longitudinal pattern of the first 6 azimuthal head-tail modes, derived from eigenvectors of the unperturbed one turn matrix M_0 (Eq. 2.46).	15
2.6	Evolution of the norm of $v(n)$, for a non-normal matrix M (Eq. 2.54), with $K_2 = 0$ and a normal matrix $K_2 = K_1$. The dashed line shows the linearly growing contribution shown in Eq. 2.55.	18
2.7	Eigenvalues of $M + E$, with $K_1 = 10K_2$ (Eq. 2.54) and E random matrices with $\ E\ = \epsilon$ (dots). All eigenvalues are within the pseudospectrum of M for the different values of ϵ (lines).	19
2.8	Representation of the pseudospectrum of M with $K_1 = 10K_2$ (Eq. 2.54), obtained by colour coding the complex plane according to the ϵ given by Eq. 2.57.	20
2.9	Kreiss constant for M as a function of the ratio between the coupling coefficient (Eq. 2.54).	21
3.1	Configuration of the IPs in the LHC and nominal filling scheme [30].	26
3.2	CERN accelerator complex. Protons are accelerated as follows : LINAC2 (50 MeV) \rightarrow BOOSTER (1.4 GeV) \rightarrow PS (25 GeV) \rightarrow SPS (450 GeV) \rightarrow LHC (7 TeV) [31].	26
3.3	The LHC nominal optics in the CMS interaction region, around IP5 [30].	28

List of Figures

3.4	Normalised separation around CMS interaction point (IP5) with 2012 machine and beam parameters. The dots are located every 3.75 m in the common beam pipe around the IP, representing the potential location for the LR interactions with 25 ns spaced beams.	29
3.5	Schematic representation of two trains of bunches colliding with a crossing angle, experiencing HO and LR beam-beam interactions.	30
3.6	Number of LR interactions for each bunch of the nominal filling scheme in the two high luminosity experiments, with a zoom on the first 360 bunches.	31
3.7	Number of LR interactions for each bunch of the nominal filling scheme, in the two lower luminosity experiments.	32
3.8	Standard LHC operation cycle (Example : Fill 2718), starting with multiple injections from the SPS followed by the energy ramp and the betatron squeeze before bringing the beams into collision (Adjust) in order to start the production of luminosity (Physics).	34
3.9	Absolute value of the transverse dipolar and quadrupolar wake functions from the 2012 LHC impedance model of Beam 1 ring [19, 52].	36
4.1	Observation of an instability during luminosity production with 1380 bunches per beam. The beam oscillation amplitude in the horizontal plane of beam 1 (blue) shows a coherent excitation which is correlated with a significant intensity drop of a single bunch, as shown by the measured bunch by bunch intensities (red).	39
4.2	Comparison of the analytical and numerical derivation of a stability diagram with the LHC octupoles powered with -500 A for a 4 TeV beam with a normalised emittance of $2 \mu\text{m}$	39
4.3	Stability diagrams from octupoles powered with opposite polarities for a 4 TeV beam with a normalised emittance of $2 \mu\text{m}$	40
4.4	Normalised BB separation at the location of the LR interactions in interaction region 5 while the beams are colliding HO at the IP (red). The upper plots shows the comparison with the same configuration where the orbit was modified, resulting in a separation of 1.3 mm in the separation plane at the IP or of 0.4 mm in the crossing angle plane. The combined effect of the separation in both planes, corresponding to the configuration at the end of the squeeze, is shown on the bottom plot.	41
4.5	Stability diagrams for both polarities of the octupoles for different LR contributions, corresponding to the configuration before the squeeze (black), after the squeeze, considering a nominal bunch, i.e. largest LR contribution (red) and a PACMAN bunch with least LR contribution (blue).	42

4.6	Comparison of the stability diagrams of the most critical bunch at the end of the squeeze with either polarity of the octupoles. With 2012 parameters (Fig. 4.5) (left), the stability diagrams are very similar for negative real tune shifts. With nominal LHC parameters (right), the stability diagram obtained with the negative polarity of the octupoles is significantly more critical.	43
4.7	Evolution of the nominal bunch's stability diagram as the normalised separation between the beams is reduced by varying the crossing angle. All other parameters are those of the nominal LHC configuration with negative (left) and positive (right) polarity of the octupoles. The normalised separation in the nominal LHC configuration is 12σ	44
4.8	Example of tune footprint of a bunch colliding at IP1 with different separations in the horizontal plane using machine and beam parameters of the 2012 run of the LHC.	44
4.9	Evolution of the stability diagram as a function of the normalised separation between the beams at the IPs 1 and 5 for the negative (left) and positive (right) polarity of the octupoles. The upper and bottom plots corresponds to the 2012 and nominal configurations.	46
4.10	Stability diagrams and growth rates as a function of the separation at IP1, in two configurations. In the first, the separation is in the horizontal plane, in the second on the diagonal, i.e. the separation is equal in the vertical and horizontal plane. The machine and beam parameters are those of 2012, without octupoles.	48
4.11	Evolution of the separation between the beams in both planes at the IPs 1 and 5 during the process that brings the beams into collision, as implemented in the LHC in the first part of the 2012 proton run (top). This can be compared to the histogram of the time at which the instabilities were observed during this process in the first part of 2012 (middle) and the corresponding stability diagram of a nominal bunch during the procedure (bottom).	49
4.12	Comparison of footprints (left) and corresponding stability diagrams generated by octupoles powered with 500 A, LR in the interaction regions 1 and 5 or HO at the IPs 1 and 5 (Nominal config.).	50
4.13	Separation between the beams at the IP during luminosity levelling at IP8, derived from measured luminosity at the IPs 1, 5 and 8 (top), as well as the intensity of the 49 bunches colliding only at IP8, the other 1331 bunches follow a standard quasi-exponential decay (bottom). This measurement took place during the first part of the 2012 proton run of the LHC (Fill 2644).	52
4.14	Kernel density estimation [65] of the separation between the beams at the moment of the instability. 30 occurrences are considered with an uncertainty of 24% on the measured separation, accounting for bunch to bunch variations of the emittance (10%) as well as for the error on the β^* at the IPs 1, 5 and 8 [66].	53

List of Figures

4.15	Distortion of the particle distribution due to quasi-harmonic noise obtained with multi-particle tracking simulation. The effect on the stability diagram is evaluated by numerical integration using the simulated distribution as input.	54
4.16	Analysis of the strength of the octupoles needed to stabilise the beams in the configuration of the broadband excitation study case, i.e. a single bunch with 2012 parameters and transverse feedback gain corresponding to a damping time of 100 turns.	55
4.17	Time evolution of the most unstable modes, obtained from multi-particle tracking with COMBI, for a single bunch with 2012 parameters, a chromaticity of 10 units and a transverse feedback gain corresponding to 100 turns damping time. The octupoles are powered with 300 A, more than the 120 A required for short term stability. The beam experiences a broadband excitation of amplitude $2 \cdot 10^{-3} \sigma_{x'}$.	56
4.18	Deviation from the initial Gaussian distribution in the middle and towards the end of the latency (Fig. 4.17) in action space and the corresponding projection in real space.	57
4.19	Spacial singular vectors associated to the 3 largest singular values during the latency (Fig. 4.17).	59
4.20	Dependency of the latency, for a single bunch with 2012 machine and beam parameters, on the noise amplitude, for different octupole strength with a chromaticity of 2 units (top) and 10 units (bottom). We recall that in these configurations 260 A and 120 A are required for the short term stability of the beam (Fig. 4.16a).	60
5.1	Spectrogram in the vertical plane of beam 1, measured by the BBQ, during an experiment aiming at probing high BB parameters.	64
5.2	The SVD of turn by turn data of both measurement and simulation gives two singular vectors corresponding to the addition (blue) and subtraction (red) of the data of both beams. The spectrum associated to the time singular vectors are plotted. The two column corresponds to the time defined in Fig. 5.1, i.e. for which the beams are colliding at one or two IPs. The upper plots show measurement from the BBQ and the lower plots results from self-consistent tracking with COMBI using measured intensities and emittances as input.	65
5.3	Spectrogram in the vertical plane of beam 1, from measured BBQ data, during luminosity production. The blurred line at ~ 0.321 is the machine tune Q_v , the sharp lines at ~ 0.307 and ~ 0.298 are noise lines and the blurred line starting ~ 0.305 and moving towards the machine tune is consistent with $Q_v - \xi$, ξ being the BB parameter of the most common bunch, which decays during the fill with the beam brightness.	66
5.4	Unstable π -mode observed during a dedicated experiment aiming at probing large HO BB parameter at injection energy with one high brightness bunch per beam colliding it the IPs 1 and 5.	67

5.5	Evolution of the coherent frequencies for two bunches colliding at one single IP, as a function of the normalised separation between the beams at the IP for a chromaticity of zero (top) and 10 units (bottom). The plots show the comparison between simulations with COMBI (spectrogram) and BIMBIM (crosses).	68
5.6	Evolution of the coherent frequencies as a function of the normalised separation between the beams, obtained with COMBI (spectrogram) and BIMBIM (crosses). There are four bunches per beam, colliding at 4 IPs with identical separation with a chromaticity of zero unit (top) and 10 units (bottom).	69
5.7	Imaginary tune shift of the most unstable mode for a single bunch with typical 2012 LHC parameters as a function of the chromaticity, without transverse feedback (red) and for two different transverse feedback gains corresponding to a damping time of 1000 turns (blue) and 100 turns (green). The solid lines, crosses and dots represents results of BIMBIM, COMBI and HEADTAIL respectively.	71
5.8	Simulation of the TMCI threshold, i.e. zero chromaticity and no transverse feedback, with the different codes for identical machine and beam parameters. The real part of the coherent tunes normalised to the synchrotron tune, Q_s , (top) as well as the imaginary part (bottom) are in agreement and the instability threshold is found for an intensity slightly above $3 \cdot 10^{11}$ p per bunch in all codes.	72
5.9	Imaginary tune shift of the most unstable mode for a train of bunches of different size obtained with different codes. The machine and beam parameters are those of the LHC 2012 run with a chromaticity of zero unit and without transverse feedback.	73
5.10	Comparison of the simulation of the time evolution of the most unstable modes obtained with BIMBIM and COMBI for a single beam composed of a train of 16 bunches with typical 2012 LHC parameters.	74
5.11	Coherent modes as a function of the BB parameter for two bunches colliding at a single IP with $\beta^*/\sigma_s \approx 90$ and a chromaticity of zero unit. The effect of the beam coupling impedance was set to be constant over the whole scan, based on the typical 2012 LHC machine and beam parameters.	75
5.12	Spectrogram in the horizontal (top) and vertical (bottom) planes for two bunches colliding at a single IP with $\beta^*/\sigma_s \approx 90$ and a chromaticity of zero unit, while varying the normalised separation between the beams in the horizontal plane at the IP. They were obtained with with BEAMBEAM3D using LHC 2012 machine and beam parameters as input.	76
5.13	Real (bottom) and imaginary (top) part of the coherent tunes of the modes obtained with the CMM for two trains of 8 bunches colliding in one interaction region with a chromaticity of 0 unit and no transverse feedback. The PACMAN effects are enhanced by allowing collisions only on one side of the IP.	77

List of Figures

5.14 Imaginary part of the most unstable mode (colours) for two bunches colliding at a single IP computed by the CMM as a function of the BB parameters for different transverse feedback gains (top) and chromaticities (bottom). The ratio β^*/σ_s is equal to 100, the other machine and beam parameters are those of the LHC in 2012. 78

5.15 Imaginary part of the coherent tune of the most unstable mode obtained with BIMBIM (lines) and tracking with COMBI (dots) for two trains of 16 bunches with LHC 2012 parameters colliding in one interaction region as a function of the normalised separation between the beams at the location of the LR encounters for different chromaticities (top) and transverse feedback gains (bottom). 79

5.16 Imaginary part of the coherent tune of the most unstable mode obtained with the CMM for two trains of 16 bunches colliding in one interaction region, for different chromaticities and transverse feedback gains, expressed as the corresponding damping time. The machine and beam parameters are those of the LHC in 2012, with separations at the location of LR encounters of 20σ (above) and 13σ (below). 80

5.17 Imaginary part of the coherent tune of the most unstable mode obtained with the CMM for two trains of 16 bunches colliding in one interaction region, for different chromaticities and transverse feedback gains, expressed as the corresponding damping time. The machine and beam parameters are those of the LHC in 2012, except for the effect of the beam coupling impedance which is doubled. The separations between the beams at the location of the LR encounters is 20σ (above) and 10σ (below). 81

5.18 Imaginary part of the tune of the most unstable mode obtained with the CMM for two trains of 16 bunches colliding in two interaction regions with alternating crossing angle planes, for different chromaticity and transverse feedback gain at separations of 20σ (above) and 10σ (below). 82

5.19 Maximum imaginary tune shift obtained with the CMM in a configuration with a single bunch per beam colliding in a single IP and different chromaticities. The BB parameter is varied, while the effect of the beam coupling impedance is kept constant, based on LHC 2012 machine and beam parameters. 85

5.20 Imaginary tune shift of the most unstable mode from tracking simulations with COMBI of two trains composed of 16, 32 and 64 bunches colliding in one interaction region as a function of the normalised separation between the beams at the location of the LR encounters. The two plots show a comparison between two configurations with typical 2012 LHC machine and beam parameters with a chromaticity of zero unit and transverse feedback gain corresponding to 100 turns damping time (left) and a chromaticity of 10 units and without transverse feedback (right). 86

5.21 Pseudospectrum of the one turn matrix obtained with BMBIM corresponding to a single bunch with 2012 LHC machine and beam parameters and different transverse feedback gains. The effect of the impedance is enhanced by a factor two and the chromaticity is -8 units. Vertical lines mark the unperturbed tune (solid) and the first upper and lower synchrotron sidebands (dashed). 87

5.22 Pseudospectrum of the one turn matrix obtained with BMBIM for single train composed of different numbers of bunches with 2012 LHC machine and beam parameters. The effect of the impedance is enhanced by a factor two, the chromaticity is -8 units and the transverse feedback gain corresponds to a damping time of 250 turns. Vertical lines mark the unperturbed tune (solid) and the first upper and lower synchrotron sidebands (dashed). 88

5.23 Kreiss constant of the one turn matrix obtained with BMBIM for single train composed of different numbers of bunches and different transverse feedback gains. The machine and beam parameters are those of the LHC in 2012, except for the effect of the impedance which is enhanced by a factor two and the chromaticity which is -8 units. 89

5.24 Time and spacial singular vector from the SVD of tracking data with COMBI for a train composed of different numbers of bunches. 2012 LHC parameters were used as input, with a chromaticity of -8 units and a transverse feedback gain corresponding to a damping time of 250 turns. 90

5.25 Comparison of the behaviour of the amplitude of the time singular vector obtained with COMBI for the configuration with 64 bunches already shown in Fig. 5.24a (black) and for the same configuration with a slightly higher transverse feedback gain (blue). 91

5.26 Spectrogram measured by the BBQ in the vertical plane of Beam 1 during an experiment with two bunches per beam (Tab. 5.1a) colliding with a varying transverse offset in IP1. The normalised separation between the beams at the IP (black) is deduced from the measured luminosity reduction factor (Eq. 2.70). 92

5.27 Beam oscillation amplitude measured with the BBQ in the vertical plane of both beams during an experiment with two bunches per beam (Tab. 5.1a) colliding with a normalised separation between the beams of 6σ (above) and 1.4σ (below) at IP1. The darkened area shows when the transverse feedback was active. 93

5.28 Sketch of the simplified collision schedule used to model the bunches colliding HO at IP8 only. In the configuration with a single bunch per beam (solid), the two bunches collide with each other at IP8 only. In the asymmetric configuration (solid and stripped), the single bunch of Beam 1 (solid blue) collides with the second bunch of Beam 2 (stripped red) at the IPs 1 and 5, whereas the first bunch of Beam 2 (solid red) still collides only at IP8 with the single bunch of Beam 1. 94

List of Figures

5.29	Spectrum, obtained with BIMBIM, of the simplified model of bunches colliding only at IP8 in the two configurations sketched in Fig. 5.28 for different normalised separations between the beams at IP8. The effect of the beam coupling impedance is based on the machine and beam parameters of the LHC in 2012.	95
5.30	Maximum imaginary tune shift simulated with COMBI in the two configurations sketched in Fig. 5.28 for different normalised separation between the beams at IP8. The effect of the beam coupling impedance is based on the machine and beam parameters of the LHC in 2012.	96
5.31	Beam oscillation amplitude measured by the BBQ during an instability during luminosity production (Fill 2646). The beams were colliding HO in the IPs 1 and 5. Based on the relative difference in the measured luminosity at the IPs 1, 5 and 8, one finds the luminosity reduction factor and the corresponding normalised separation between the beams at IP8 (Eq. 2.70) of $1.5 \pm 0.4 \sigma$	97
5.32	Beam oscillation amplitude measured by the BBQ during an instability while bringing the beams at all IPs, according to the process described in Fig. 4.11 (Fill 2668). As the peak luminosity was not achieved due to the premature extraction of the beam, the separation between the beams at the IPs could not be evaluated based on the measured luminosity reduction factor.	98
5.33	Relative intensity loss measured by the FBCT during the last 20 seconds before the beams were extracted from the machine due to a coherent instability (Fig. 5.32).	99
6.1	Comparison of the beams brightness at injection and at the beginning of luminosity production, for different fills during the 2012 proton run. Courtesy H. Bartosik [79]	101
6.2	Chromaticity measurements from the BBQ at the end of the squeeze for each fill for luminosity production of the LHC 2012 proton run. The vertical dashed line mark fill number 2924, when several operational parameters were changed, including the chromaticity.	102
6.3	Intensity at the end of the squeeze for all fills during the 2012 proton run. The intensity is marked with a blue cross for fills without observations of coherent instabilities, a red dot if an instability was observed at the end of the squeeze and a yellow dot if an instability was observed while bringing the beams into collision (Sec. 5.2.3). The vertical dashed line mark fill number 2924.	103
6.4	Luminosity lifetime measurement before and after the change of configuration. Courtesy M. Lamont [81].	104
6.5	Spectrogram measured by the BBQ in the vertical plane of beam 1 at the end of the squeeze, during fill 3253. The horizontal black lines mark the end of the squeeze (solid), as well as the start and end of the process that brings the beams into collision (dashed).	106
6.6	Luminosity during first attempt of β^* levelling	108

6.7	Measured and expected (cf Eq. 2.68) specific luminosity reduction due to β^* .	108
6.8	Transverse separation at the IP deduced from the measured luminosity reduction factor during the first three executions of the squeeze with colliding beams, chronologically from top to bottom. The first two were executed with a single bunch per beam, the last with a train of 36 bunches spaced by 50 ns.	109
6.9	Beam separation at the interaction point interpolated from adjacent BPMs.	110
6.10	Correction of the orbit at the IP from luminosity optimisation during the 2012 run. Courtesy J. Wenninger.	111
6.11	Two examples of squeeze sequence for β^* luminosity levelling with low flexibility.	113
A.1	Three steps of the execution of the COMBI code with three bunches per beam. The blue disks represent bunches of the beam rotating clockwise and in red the bunches of the beam rotating counter-clockwise. The black lines linking the two beams shows the position of potential BB interactions. A BB interaction occurs only if the bunch finds a partner in the other beam.	122
A.2	Comparison of the performance of the parallelised version of COMBI with an estimation of the equivalent serialized code.	123
A.3	Execution time of COMBI as a function of the number of macro particle per bunch, for different number of bunches per beam.	123
A.4	Execution time of COMBHY as a function of the number of threads per process in the high waste configuration.	126
A.5	Best performance achieved by the hybrid version with both gcc and Intel compilers.	126
A.6	Least square fit of Amdahl's law on COMBHY's performance measurement in the high waste configuration.	127
A.7	Performance with and without management of the processes priority at runtime. The performance with a single thread is given as a reference. (Tested on a 16 core HP ProLiant BL460c Gen8 blade with 2 Intel(R) Xeon(R) CPU E5-2690 @ 2.70GHz with hyper-threading on.)	127
A.8	Minimum execution time on a single Aries node.	128
B.1	Description of the PYSSD module.	135
B.2	Footprint (right) and corresponding stability diagram (left) obtained with LHC 2012 parameters at the end of the squeeze, including LR interactions in interaction regions 1 and 5 with a full separation of 4σ at the IP and the octupoles powered with -500 A.	136
C.1	Classes	139
C.2	Illustration of the longitudinal displacement of the collision point, s_{CP} , with respect to the IP for two bunches colliding HO with a crossing angle.	143
D.1	Example of the result of an automatic scan during a fill for physics.	151

List of Figures

D.2 Two illustrations of a FMA for the HL-LHC project. On the left, the tunes of particles oscillating with different transverse amplitudes in the tune diagram, colour coded according to their diffusion rates obtained from single particle tracking simulations. Solid lines corresponding to different resonance conditions are shown for comparison. On the right, the same data in action space. Courtesy A. Valishev (FNAL, Batavia, USA). 152

D.3 Luminosity lifetime at start and end of luminosity production (namely during stable beam (SB)) during the 2012 proton run of the LHC. Courtesy A.L. Macpherson [116]. 153

D.4 Start the application from the control room, select the beam and then start online mode. 154

D.5 Control side panels 156

List of Tables

3.1	LHC machine and beam parameters in collision for different configuration. .	27
3.2	Number of bunches with a different number of HO collision scheme, for different filling scheme, nominal and three of the filling schemes used in 2012. The corresponding technical names are [37, 38]: FS1 : 50ns_1374_-1368_0_1262_144bpi12inj FS2 : 50ns_1380b_1380_0_1274_144bpi12inj FS3 : 50ns_1380b_1331_0_1320_144bpi12inj	33
3.3	Configuration of the interaction regions during the 2012 physics run with protons.	33
5.1	Measured quantities during the experiment dedicated to the observation of mode coupling instabilities of colliding beams.	92
6.1	Average fill to fill difference of the orbit correction required to optimize the luminosity at the IPs 1 and 5 in μm	110
A.1	Definition of the actions available in COMBI version 2.0. (H. stands for Horizontal, V. for Vertical and L. for Longitudinal.). The separations, amplitude and boundaries are given in beam σ in the respective plane. The frequencies are in tune units.	134

List of symbols

x, y	Horizontal and vertical coordinates
p_x, p_y	Horizontal and vertical momentum
x', y'	Horizontal and vertical angles with respect to the beam's direction of travel
J_x, J_y	Horizontal and vertical action variables
Φ_x, Φ_y	Horizontal and vertical angle variables
s	Longitudinal coordinate
δ	Relative momentum deviation
p_0	Design momentum
$\vec{x} = \begin{pmatrix} x \\ y \\ s \end{pmatrix}$	3D spacial coordinates
$\underline{x} = \begin{pmatrix} x \\ x' \\ y \\ y' \\ s \\ \delta \end{pmatrix}$	6D phase space coordinates
\bar{x}	Generalized coordinates at a Poinaré section
c	Speed of light
ρ	Bending radius
k_1	Quadrupole strength
$\beta(s), \alpha(s), \gamma(s)$	Optical Twiss functions
β^*	Value of the β function at the interaction point
Φ	Total phase advance
α_c	Momentum compaction factor
$\alpha_{c,2}$	Second order momentum compaction factor
Q_β	Betatron tune
Q_x, Q_y	Horizontal and vertical betatron tunes
Q'_x, Q'_y	Horizontal and vertical chromaticities
Q''_x, Q''_y	Horizontal and vertical second order chromaticities
$a_x, a_{x,y}, a_y$	Transverse amplitude detuning coefficients

List of Tables

ϵ_x, ϵ_y	Horizontal and vertical physical emittances
ϵ_n	Normalised emittance
σ	R.m.s. transverse beam size
σ_x, σ_y	R.m.s. horizontal and vertical beam sizes
σ_s	R.m.s. bunch length
σ'_x, σ'_y	R.m.s. horizontal and vertical angular spread
σ_δ	R.m.s. momentum spread
γ_r	Lorentz factor
ω_s	Harmonic frequency
ω_{RF}	Frequency of the radio-frequency cavity
h	Harmonic number
f_{rev}	Revolution frequency
r_0	Classical proton radius
N	Number of particle
r	Transverse distance to the close orbit
d	Transverse separation between the beams
s_s, s_t	Longitudinal positions of the source and target particles
$\vec{w}_{\text{dip},x}, \vec{w}_{\text{dip},y}, \vec{w}_{\text{dip},s}$	Horizontal, vertical and longitudinal dipolar wake functions
$\vec{w}_{\text{quad},x}, \vec{w}_{\text{quad},y}, \vec{w}_{\text{quad},s}$	Horizontal, vertical and longitudinal quadrupolar wake functions
$\vec{W}_{\text{dip},x}, \vec{W}_{\text{dip},y}, \vec{W}_{\text{dip},s}$	Horizontal, vertical and longitudinal total dipolar wake functions
$\vec{W}_{\text{quad},x}, \vec{W}_{\text{quad},y}, \vec{W}_{\text{quad},s}$	Horizontal, vertical and longitudinal total quadrupolar wake functions
$\Psi(x, y)$	Transverse particle distribution
B_0	Unperturbed linear betatron transfer matrix
C_w	Beam coupling impedance matrix
C_{BB}	Beam-beam coupling matrix
Q_{coh}	Coherent tune
Q_σ, Q_π	Coherent tune of the beam-beam σ - and π -modes
Y	Yokoya factor
ξ	Beam-beam parameter
N_s, N_r	Number of slices and rings in the circulant matrix model
N_{dof}	Number of transverse degrees of freedom
N_c	Number of cells in the circulant matrix model
w_i	Cell weight in the circulant matrix model
\mathbb{I}_n	Identity matrix of size n
$\sigma(A, \epsilon)$	Pseudospectrum of the matrix A
$K(A)$	Kreiss constant of the matrix A
n_A	Azimuthal head-tail mode number
\mathcal{L}	Total luminosity
\mathcal{L}_b	Luminosity per bunch crossing

σ_e	Event cross section
R_e	Event rate
$N_{b,IP}$	Number of bunch crossing at the interaction point
θ	Full crossing angle between the beams
S_{drift}	Normalised separation between the beams in the drift space around the interaction point
G_{FB}, τ_{FB}	Transverse feedback gain and corresponding damping time
G_x, G_y	Horizontal and vertical transverse feedback gains
I_{oct}	Current in the focusing octupole magnets.
N_{slot}	Number of slots per ring
N_b	Number of bunches per beam
S_u	Speed-up
N_{CPU}	Number of CPU
α_{np}	Fraction of non-parallelisable code
s_{CP}	Longitudinal position of the collision point

List of acronyms

AC	Action Code. 128–130
ALICE	A Large Ion Collider Experiment. 25, 30, 33
API	Application Programming Interface. 147
ATLAS	A Toroidal LHC Apparatus. 25, 33
BB	Beam-Beam. 8–12, 16, 22, 27, 34, 37, 38, 45, 47, 50, 59, 61, 62, 64, 65, 68–71, 74–76, 81, 82, 89, 95, 97, 100, 113, 119, 120, 123, 128, 137, 140, 141, 147, 149, 150, 152
BBQ	Base Band Tune. 35, 38, 47, 51, 58, 61, 62, 64, 95, 96, 112
BPM	Beam Position Monitor. 108, 110, 112, 130
BSRT	Beam Synchrotron Radiation Telescope. 35
CMM	Circulant Matrix Model. 12, 16, 17, 20, 54, 65, 68–70, 74, 76, 81–83, 85, 86, 103, 137, 141
CMS	Compact Muon Solenoid. 25, 33
CPU	Central Processing Unit. 120, 122, 124, 126, 128
FBCT	Fast Beam Current Transformer. 35, 148
FCC	Future Circular Collider. 2
FFT	Fast Fourier Transform. 68, 134, 153
FMA	Frequency Map Analysis. 149
GUI	Graphical User Interface. 147
HFMM	Hybrid Fast Multipole Method. 128
HL-LHC	High Luminosity LHC. 2, 117
HO	Head-On. 8, 11, 12, 27, 29, 34, 43, 45, 47, 50, 51, 60, 62, 64, 71, 74, 82, 87, 92, 94–96, 103–105, 110, 112, 113, 115, 128, 141, 142, 148, 151, 153
IP	Interaction Point. 8, 11, 12, 23–25, 27, 29, 30, 33, 34, 38, 40, 43, 45–47, 50, 51, 61, 69, 71, 74, 81, 87, 92, 94–96, 98, 104, 105, 108, 110, 112, 115, 117, 120, 123, 128, 137, 141, 148
ISR	Intersecting Storage Rings. 47

List of acronyms

LHC	Large Hadron Collider. 1, 2, 25, 27, 29, 34–38, 40, 42, 45, 47, 51, 53, 54, 58, 59, 61, 71, 74, 81, 82, 92, 97–100, 102–104, 112, 113, 115–117, 128–130, 137, 138, 147, 148, 150, 151
LHCb	LHC beauty experiment. 25, 30, 33
LR	Long-Range. 8, 11, 27, 29, 34, 38, 40, 42, 43, 45–47, 51, 59, 62, 71, 74–76, 82, 101, 112, 128, 141, 148
MPI	Message Passing Interface. 119, 120, 122, 126, 127
RF	Radio Frequency. 7, 129, 130
SPS	Super Proton Synchotron. 99
SVD	Singular Value Decomposition. 18, 22, 54, 61, 62, 112
TMCI	Transverse Mode Coupling Instability. 21, 68, 69

Glossary

abort gap	Large longitudinal gap in the beam free of particles. 25, 29
adjust	Operational phase during which the orbit at the interaction points is adjusted such as to bring the beams into collision. 34
betatron	Relative to the motion of the particles in the directions transverse to the beam's direction of travel. 5, 17, 38, 59, 113, 139
bunch	Set of particles oscillating around the same longitudinal fixed point. 7, 10–12, 14–17, 19, 20, 23–25, 27, 29, 30, 35, 36, 38, 42, 43, 45, 50, 51, 58, 61, 62, 65, 68, 69, 71, 74, 75, 81–87, 92, 94–97, 103, 105, 112, 113, 116, 117, 119, 120, 122, 123, 126, 128–131, 138–143
filling scheme	Scheme specifying which slots are occupied, or not, by a bunch. 27, 29, 38, 92, 94, 137, 138
footprint	(Or tune footprint) Graphical representation of the transverse amplitude detuning by reporting the tunes in the two transverse planes against each other for different particles on a mesh in action space. 8, 43, 47, 134, 147–153
head-tail	Relative to the standard basis describing longitudinal coherent modes of oscillation. 68–71, 76, 84, 86, 89, 97, 116, 130
hourglass effect	Longitudinal variation of the beam size around the interaction point due to the optical focusing. 23, 24, 128, 141
interaction region	Straight section around an interaction point. 27, 29, 62, 71, 75, 81, 82, 112
PACMAN	Bunch with a reduced number of long-range beam-beam interactions with respect to the nominal bunch. 29, 30, 38, 42, 74, 81, 112, 147
slot	Longitudinal fixed point available to host a bunch. 27, 29, 30, 119, 131, 138

Glossary

squeeze	Operational phase during which the optics of the machine is modified, such as to reduce the beam size at the interaction points. 33, 34, 38, 40, 42, 43, 46, 47, 59, 74, 87, 100–105, 108, 110, 112, 113
Super-PACMAN	Bunch with a reduced number of head-on beam-beam interactions with respect to the nominal bunch. 29, 113
synchro-betatron	Relative to the motion of the particles in both transverse and longitudinal directions. 14, 65, 69, 128, 139
synchrotron	(Noun) Circular particle accelerator with a fixed closed orbit. (Adjective) Relative to the longitudinal motion of the particles, i.e. in the beam's direction of travel. 4, 5, 7, 14, 27, 70, 71, 129, 139
train	(Or bunch train) Set of consecutive slots occupied by a bunch. 27, 29, 68, 74, 75, 81–86, 105, 116, 117, 138

1 Introduction

The performance of a collider is essentially characterised by the centre of mass energy of the collisions between two particles as well as the luminosity, a quantity that is proportional to the rate of events that can be observed in the detectors. Achieving a high rate is critical to allow for the observation of rare events, e.g. channels involving the Higgs boson, with a sufficiently large statistics. The energy in a circular collider is constrained by the radius of the machine together with the achievable strength of the magnets used to bend the trajectories of the particles on a closed orbit. On the other hand, the luminosity strongly depends on the quality of the two counter rotating beams, in particular the number of particles per unit of phase space volume, i.e. the beam brightness. The preservation of the beams' quality from their production to the collisions is therefore critical. In particular the degradation of their brightness due to perturbations of the particle distribution driven by the electromagnetic wake fields created by the particles of the beams has to be avoided.

The stability of the coherent modes of oscillation of a single beam has been studied extensively, leading to well established theories and methods to describe the limitations for realistic machine and beam configurations. Still, observations of coherent instabilities during different phases of the cycle of the Large Hadron Collider (LHC) at CERN could not be explained within the existing models. As the instabilities caused a significant deterioration of the machine performance during the 2012 run and might strongly affect the future runs at higher energies, the models need to be extended in order to understand the driving mechanisms and find appropriate mitigation techniques.

The observations suggested that the presence of the second beam and, in particular, the electromagnetic interactions between the beams, play an important role in the dynamics of the coherent instabilities. Not only are the normal modes of oscillation affected by the coupling forces between the two beams but the nonlinearity of the beam-beam interactions strongly impacts the frequency spread of the particles in the beam, leading to significant modifications of the strength of the Landau damping effect. In this thesis, these effects are quantified in order both to understand the observations of coherent instabilities in the LHC and study possible mitigation techniques.

The understanding of the limitations due to coherent instabilities in the LHC casts light on

Chapter 1. Introduction

the challenges to be addressed in the design of future colliders. Increasing requirements in terms of beam brightness not only for the LHC but also for its upgrade, the High Luminosity LHC (HL-LHC), rely on efficient beam stabilisation techniques and therefore on an accurate modelling of the different forces affecting the stability of the beams, as well as the interplay between them. Furthermore, the optimisation of the detection efficiency in the different experiments operating simultaneously requires a tight control of the luminosity in each of them. The different manipulations of the beams needed to achieve the required flexibility often lead to complex configurations of the multiple beam-beam interactions for which the beam stability should be assessed at every stage of the procedure. The Future Circular Collider (FCC), a 100 km long hadron collider currently under study at CERN, features many similarities with the LHC. Most importantly the expected strong effects of the electromagnetic wake fields as well as the complex configuration of multiple beam-beam interactions could lead to instability mechanisms similar to those observed in the LHC.

After an introduction to the dynamics of charged particle beams in a circular collider in Chap. 2, and a description of the relevant specificities of the LHC in Chap. 3, the focus will be on two main aspects of the coherent stability of the beams. First, the effect of the interactions between the two beams on the frequency spread of the individual particles in each beam and, most importantly, their effect on Landau damping of coherent instabilities is discussed in Chap. 4. Secondly, the description of the normal modes of oscillation of the two coupled beams is addressed in Chap. 5. Finally, Chap. 6 is devoted to the applications of the models developed for the operation of the LHC. In particular, an operational method to push further the limitations due to coherent instabilities is suggested and experimental tests are reported.

2 Beam Dynamics

2.1 Single particle dynamic

In order to later describe the behaviour of a charged particle beam in a collider, let us first have a look at a single particle in a storage ring. The behaviour of a single particle with 6D coordinates \underline{x} through a magnetic element can be described as a nonlinear map m ,

$$\underline{x} = m(\underline{x}_0). \quad (2.1)$$

A circular machine made of n elements is therefore fully described by a series of maps m_1, m_2, \dots, m_n and the coordinates of a particle after a full turn are given by

$$\underline{x} = m_n \circ \dots \circ m_2 \circ m_1(\underline{x}_0) = M(\underline{x}_0) \quad (2.2)$$

where M is the so-called one turn map. The one turn map provides important information on the behaviour of the particles. In particular, there should exist a stable fixed point such

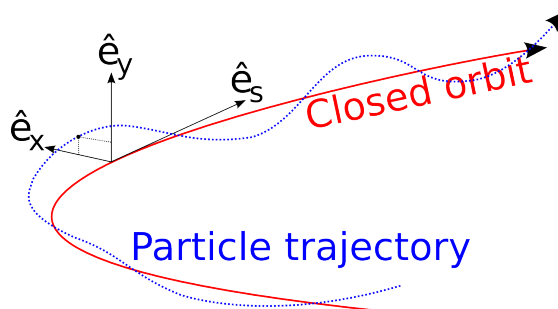


Figure 2.1 – Curvilinear coordinate system. We shall work in the paraxial approximation, thus for convenience, the conjugate variables are given by $(x, x' = p_x/p_0)$, $(y, y' = p_y/p_0)$ and (s, δ) , where p_0 is the canonical momentum. p_x, p_y are the transverse projections and δ is the relative deviation to the design momentum.

that

$$\underline{x}_0 = M(\underline{x}_0), \quad (2.3)$$

the trajectory of a particle with \underline{x}_0 defines the closed orbit. The motion of the particles is then naturally described in a curvilinear system following the closed orbit, as described in Fig. 2.1.

According to classical Hamiltonian mechanics [1], the evolution of a dynamical variable $f(\underline{x})$, in a element described by the time independent Hamiltonian $H(\underline{x})$ is described by

$$\frac{df}{dt} = -[H, f] + \frac{\partial f}{\partial t} \quad (2.4)$$

with $[,]$ the Poisson brackets [1]. Considering f not explicitly dependent on time, and naively solving for f , we find the following equation :

$$f(\underline{x}(t)) = e^{-(t-t_0):H}: f(\underline{x}(t_0)) \quad (2.5)$$

with the Lie operator $:H: f = [H, f]$. A rigorous proof of the validity of this approach can be found in [2]. Considering ultra relativistic particles, in the paraxial approximation, this equation can be rewritten such as to show the behaviour of f over a distance L_0 :

$$f(\underline{x}(s+l)) = e^{-\frac{L_0}{c}:H}: f(\underline{x}(s)) \quad (2.6)$$

with c the speed of light. This gives an expression of the map describing the element from its Hamiltonian :

$$m = e^{-\frac{l}{c}:H}: \quad (2.7)$$

According to Eq. 2.2, one can rewrite the one turn map :

$$M = e^{-\frac{L_1}{c}:H_{m_1}} \circ e^{-\frac{L_2}{c}:H_{m_2}} \circ \dots \circ e^{-\frac{L_n}{c}:H_{m_n}} = e^{-\frac{L}{c}:H_{\text{eff}}}, \quad (2.8)$$

introducing the effective Hamiltonian H_{eff} . Its derivation may be quite involved in realistic configurations, and often necessitates the use of a computer program. Nevertheless, the effective Hamiltonian immediately yields several relevant physical quantities. Indeed, let us start simple. To first order, a synchrotron is made of dipole and quadrupole magnets, in order to respectively define the closed orbit and provide stability around the fixed point. For simplicity, let us consider a single independent degree of freedom, we have the following

Hamiltonians :

$$H_{\text{drift}} = \frac{p_x^2}{2} \quad (2.9)$$

$$H_{\text{dip.}} = \frac{p_x^2}{2} + \frac{x^2}{2\rho^2} \quad (2.10)$$

$$H_{\text{quad}} = \frac{p_x^2}{2} + \frac{k_1}{2} x^2 \quad (2.11)$$

where ρ is the bending radius of the dipole and k_1 the strength of the quadrupole. In large machines, the bending radius is large, and the focusing effect of the dipole can be neglected. The synchrotron is therefore described by a sequence of drift spaces and quadrupoles, both described by linear transfer maps, i.e. matrices. For an element of length l , a little arithmetic yields :

$$m_{\text{drift}} = \begin{pmatrix} 1 & l \\ 0 & 1 \end{pmatrix} \quad (2.12)$$

$$m_{\text{quadrupole}} = \begin{pmatrix} \cos(\sqrt{k_1}l) & \frac{1}{\sqrt{k_1}} \sin(\sqrt{k_1}l) \\ -\sqrt{k_1} \sin(\sqrt{k_1}l) & \cos(\sqrt{k_1}l) \end{pmatrix}. \quad (2.13)$$

For any sequence of drifts and quadrupoles, the transfer matrix between two points in the ring can be parametrized using optics functions $\alpha(s)$ and $\beta(s)$ as defined by Courant and Snyder [3] :

$$M_{\text{sequ}} = \begin{pmatrix} \sqrt{\frac{\beta_0}{\beta}} (\cos(\phi) + \alpha_0 \sin(\phi)) & \sqrt{\beta \beta_0} \sin(\phi) \\ \frac{-(1 + \alpha_0 \alpha) \sin(\phi) + (\alpha - \alpha_0) \sin(\phi)}{\sqrt{\beta \beta_0}} & \sqrt{\frac{\beta}{\beta_0}} (\cos(\phi) - \alpha \sin(\phi)) \end{pmatrix} \quad (2.14)$$

where ϕ is the positive eigenvalue of the transfer matrix, often referred to as phase advance. Thus, the one turn map of the synchrotron can be written :

$$M_{\text{turn}} = \begin{pmatrix} \cos(\Phi) + \alpha \sin(\Phi) & \beta \sin(\Phi) \\ \frac{-(1 + \alpha^2) \sin(\Phi)}{\beta} & \cos(2\pi Q) - \alpha \sin(\Phi) \end{pmatrix} \quad (2.15)$$

where we have introduced Φ the phase advance over a full turn. Usually, one defines the betatron tune as $Q_\beta = \Phi/2\pi$. In order to picture the physical meaning of these quantities, let us observe a Poincaré section. All possible trajectories of a particle off resonance, i.e. with an irrational tune, describe an ellipse parametrized by the optical functions (Fig. 2.2). The equation of the ellipse is

$$J = \frac{1}{2} \left(\frac{1 + \alpha^2}{\beta} x^2 + 2\alpha x x' + \beta x'^2 \right) \quad (2.16)$$

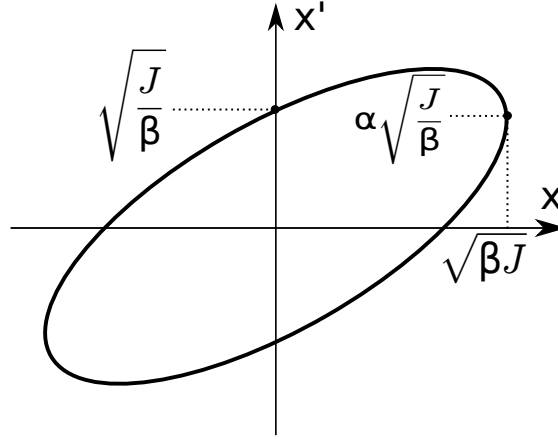


Figure 2.2 – Phase space ellipse.

with J being a constant of motion. Thus, we can write the oscillation amplitude of the particle at a location s :

$$\Delta x = \sqrt{\beta(s)J}. \quad (2.17)$$

Also, the one-turn matrix may be rewritten in its Jordan normal form, which in this case is a unitary rotation of angle Φ , by the transformation :

$$M_{\text{turn}} = AR(\Phi)A^{-1} \quad (2.18)$$

with

$$A = \begin{pmatrix} \frac{1}{\sqrt{\beta(s)}} & 0 \\ -\frac{\alpha(s)}{\beta(s)} & \frac{1}{\beta(s)} \end{pmatrix} \text{ and } R(\Phi) = \begin{pmatrix} \cos(\Phi) & \sin(\Phi) \\ -\sin(\Phi) & \cos(\Phi) \end{pmatrix}. \quad (2.19)$$

This transformation immediately yields action angle variables, (J, Φ) and thus the effective Hamiltonian [4]:

$$H_{\text{eff}} = J\Phi. \quad (2.20)$$

Introducing a fixed energy deviation, i.e. neglecting longitudinal focusing, the kinematic term of the Hamiltonian becomes

$$\frac{p^2}{2(1+\delta)} \quad (2.21)$$

which yields the following effective Hamiltonian :

$$H_{\text{eff}} = J\Phi + \frac{1}{2}\alpha_c \delta^2 + Q'J\delta \quad (2.22)$$

where we have introduced the first order chromaticity Q' , corresponding to the variation of the tune due to energy deviation, and the momentum compaction factor α_c , which parametrizes the change of the total length of the closed orbit : $\Delta L = \alpha_c \delta$. The extension to two uncoupled transverse degrees of freedom is straight forward :

$$H_{\text{eff}} = J_x \Phi_x + J_y \Phi_y + Q'_x J_x \delta + Q'_y J_y \delta + \frac{1}{2} \alpha_c \delta^2. \quad (2.23)$$

Introducing higher-order magnetic fields forces us to use maps instead of matrices, nevertheless, one may apply the same procedure to write the effective Hamiltonian in a normal form such as to reveal the important physical quantity. Most generally, one may write a forth-order expansion of the effective Hamiltonian [4] :

$$\begin{aligned} H_{\text{eff}} = & J_x \Phi_x + J_y \Phi_y + \frac{1}{2} \alpha_c \delta^2 \\ & + Q'_x J_x \delta + Q'_y J_y \delta + \alpha_{c,1} \delta^3 \\ & + a_x J_x^2 + a_{xy} J_x J_y + a_y J_y^2 + Q''_x J_x \delta^2 + Q''_y J_y \delta^2 + \alpha_{c,2} \delta^4 \end{aligned} \quad (2.24)$$

where we have introduced few well-known optical parameters : higher order momentum compaction factors $\alpha_{c,1}$ and $\alpha_{c,2}$, second order chromaticities Q''_x and Q''_y , as well as the linear detuning parameters a_x , a_{xy} , and a_y , describing the variation of the tune with the transverse actions, in other words with the oscillation amplitudes.

When considering a full beam, we have a distribution of particles in action space $\Psi(J_x, J_y)$. An exponential distribution in action space corresponds to a Gaussian distribution in real space :

$$\Psi(J_x, J_y) = e^{-\epsilon_x J_x - \epsilon_y J_y} \quad (2.25)$$

where we have introduced the beam normalised transverse emittances ϵ_x and ϵ_y , which relate to the physical beam size by $\sigma(s) = \sqrt{\frac{\beta(s)\epsilon}{\gamma_r}}$, with the relativistic factor γ_r .

In the longitudinal plane, particles are kept in a potential well around the fixed point by an oscillating electric field provided by a Radio Frequency (RF) cavity [5]. In modern hadron synchrotrons, the oscillation in the longitudinal plane is orders of magnitude slower and is usually weakly coupled to the dynamics in transverse planes, for these reasons the dynamics are usually described separately. In our case we will not take into account nonlinear effects from the RF fields, and therefore the movement in the longitudinal direction is simply described by an harmonic oscillation with frequency ω_s . The frequency of the RF field is a multiple of the revolution frequency and we have $\omega_{\text{RF}} = h \frac{2\pi}{T_{\text{rev}}}$, with h the harmonic number. As opposed to the transverse plane, we have h equivalent fixed point in the longitudinal plane. A subset of particles of the beam oscillating around the same longitudinal fixed point is referred to as a bunch. The different bunches composing the beam are separated by a finite spacing, which may span several fixed points.

2.1.1 Beam-beam interactions

In colliders, the two beams exert a force on each other at the Interaction Points (IPs), known as the Beam-Beam (BB) force. By integration of Poisson's equation, using a Gaussian distribution of particles, with r.m.s. transverse beam size $\sigma = \sigma_x = \sigma_y$, one obtains the kick felt by a test particle at a position (x, y) with respect to the other beam's centroid [6]:

$$\Delta x' = -\frac{2r_0 N}{\gamma_r} \frac{x}{r^2} \left(1 - e^{-\frac{r^2}{2\sigma^2}} \right) \quad (2.26)$$

where we have introduced N , the number of charges in the beam, r_0 the classical radius and $r = \sqrt{x^2 + y^2}$. The quadrupolar component of the force is strong and changes significantly the optical properties of the beam. It is convenient to characterize the strength of the BB force by the tune shift that it provokes for particles with vanishing actions :

$$\Delta Q_{HO} = \frac{Nr_0}{4\pi\epsilon}. \quad (2.27)$$

The BB force is usually very strong and can therefore not be treated perturbatively, as usually done when considering multipolar magnets. Nevertheless, the derivation of an effective Hamiltonian, and consequently of the amplitude detuning, is possible using Lie transforms [4]. In complex configurations, involving multiple BB interactions, this method is not necessarily the most efficient. Especially if the amplitude detuning is the main interest, we will rather use single particle tracking simulations. Knowing the transfer map of each element, we can compute the coordinates of a particle element by element. As the amplitude detuning is a smooth function of the actions, one may reconstruct it by tracking particles with different actions for several turns, and extract the oscillation frequency by a Fourier transformation. The result of such a simulation is usually represented in a tune footprint showing the tune in both transverse planes for each particle, as shown in Fig. 2.3b. One may interpret these footprints looking at the BB force in Fig. 2.3a. For a particle oscillating with a small amplitude (upper arrow), the force can be linearised locally, the tune shift is directly related to the slope of the force. Particles oscillating with a larger (lower arrow) amplitude span, over several turns, the nonlinear part of the force. In the case where the two beams collide Head-On (HO) at the IP, we have a large tune shift for particles at small amplitude, and for very large amplitudes, the averaged force vanishes. These effects are visible on the tune footprint, as the tune of particles with small oscillation amplitude are shifted away from the unperturbed tune, whereas particles with larger oscillation amplitudes move closer to the unperturbed tune. The behaviour is very different in configurations where the beams are separated spatially at the IP, i.e. for Long-Range (LR) interactions. In this case, the tune shift for small amplitude particles is much smaller and has a different sign with respect to HO tune shift (Fig. 2.3). Indeed, for large separations d between the beams, i.e. $e^{-\frac{d^2}{2\sigma^2}} \ll 1$,

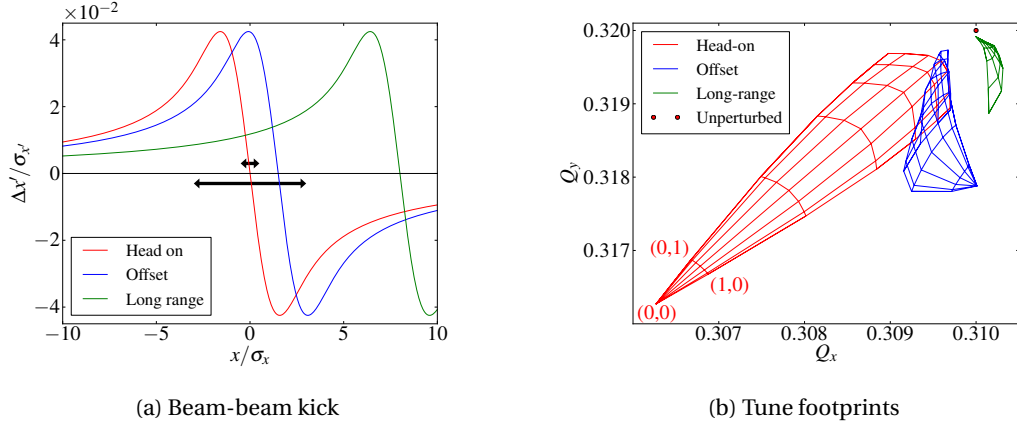


Figure 2.3 – Beam-beam kick experienced by the single particles as a function of their position with respect to the closed orbit, in different configurations where the two beams collide HO, with a small transverse offset or LR. Particles oscillating with different amplitudes, i.e. with different actions, span different part of the force turn after turn (black arrows). The horizontal and vertical tunes of particles oscillating with different transverse actions, (J_x, J_y) , are reported on a tune digram for the different types of collisions.

the tune shift for particles with a small action is given by :

$$\Delta Q_{LR} = -\frac{N r_0 \beta}{2\pi \gamma d^2}. \quad (2.28)$$

In between these two extreme cases, i.e. when the beams are colliding with a small transverse offset, the behaviour can be quite complex. We note that the tune shift vanishes at $d \sim 1.6 \sigma$, i.e. at the maximum of the BB force.

2.2 Collective effects

In the previous section, we have described the trajectory of a single particle in a the electromagnetic field provided by external elements. When considering intense beams, the fields generated by the beam itself strongly perturb the dynamics. In this case, the dynamics of the beam as a whole has to be considered, which is often referred to as the coherent dynamics of the beam.

2.2.1 Beam coupling impedance

The electromagnetic wake fields generated by each charged particle affect the other particles in the beam via an interaction with its surroundings, i.e. magnetic elements, cavities,

beam pipe or other instrumentations. The resulting forces are known as the beam coupling impedance [7]. In order to describe the effect of these forces, let us consider a test particle, with transverse and longitudinal coordinates (\vec{x}_t, s_t) , experiencing the field of a source particle at (\vec{x}_s, s_s) , both travelling over a short distance $d s$, such that the relative coordinates of both particles remain constant when travelling over that distance. The beam oscillation amplitudes are assumed to be much smaller with respect to the typical size of its surroundings, therefore we may express the angular kick due to the beam coupling impedance as a Taylor expansion up to first order:

$$\begin{aligned} d x' &= \vec{w}_{\text{dip},x}(s_s, s_t) \vec{x}_s + \vec{w}_{\text{quad},x}(s_s, s_t) \vec{x}_t \\ d y' &= \vec{w}_{\text{dip},y}(s_s, s_t) \vec{x}_s + \vec{w}_{\text{quad},y}(s_s, s_t) \vec{x}_t \\ d \delta &= \vec{w}_{\text{dip},s}(s_s, s_t) \vec{x}_s + \vec{w}_{\text{quad},s}(s_s, s_t) \vec{x}_t \end{aligned} \quad (2.29)$$

where $w_{\text{dip}}(s_s, s_t)$ and $w_{\text{quad}}(s_s, s_t)$ are the dipolar and quadrupolar wake functions in the different degrees of freedom. Within the ultra relativistic approximation, the wake depends only on the distance between the two particles $\Delta s = s_t - s_s$. Also, it is interesting to note that the forces felt by a particle over a turn due to the beam coupling impedance are usually small compared to the ones of other magnetic elements, therefore, we may treat their effect as a perturbation and assume that the optical functions are not affected. Thus, we express the wake functions in the normalised phase space all along the ring, using the transformation given by Eq. 2.18 and integrate their contributions over a full turn such as to obtain the total wake functions. Thus, we can express the total change of momentum in all degrees of freedom :

$$\Delta x' = \vec{W}_{\text{dip},x}(\Delta s) \vec{x}_s + \vec{W}_{\text{quad},x}(\Delta s) \vec{x}_t \quad (2.30)$$

$$\Delta y' = \vec{W}_{\text{dip},y}(\Delta s) \vec{x}_s + \vec{W}_{\text{quad},y}(\Delta s) \vec{x}_t \quad (2.31)$$

$$\Delta \delta = \vec{W}_{\text{dip},s}(\Delta s) \vec{x}_s + \vec{W}_{\text{quad},s}(\Delta s) \vec{x}_t.$$

A more rigorous treatment may be found in [8]. As the element surrounding the beams are much larger than the beam oscillation amplitude, the nonlinear part of the wake can be neglected. However, the direct interactions between particles within a bunch, known as direct space charge effects are very nonlinear. Nevertheless, as discussed in [9], this effect is negligible in high energy machines.

In order to assess the effect of the beam coupling impedance on the beam dynamic, one has to extend the description of a single particle to the whole beam. There exists various models, each having their one advantages and disadvantages [8, 10–12]. Here, we shall focus on a model convenient to describe both the beam coupling impedance and coherent BB effects.

2.2.2 Coherent Beam-beam effects

As the two beams are strongly coupled through the BB force, they may oscillate in a coherent manner, with frequencies different from the unperturbed frequencies of each beam. A description of such a system, based on Vlasov equation, can be found e.g. in [13]. While fully self-consistent and exact, this formalism becomes very heavy when considering complex configurations, with multiple bunches and multiple BB interactions arbitrarily distributed along the ring. To treat such cases, we will describe a simplified linear model and later extend the results with numerical simulations.

The net force on the bunch as a whole, or coherent force, is obtained by integration of the single particle force $\Delta x'$ over the beam distribution $\Psi(x, y)$.

$$\Delta x'_{\text{coh}}(x, y) = \int_{-\infty}^{\infty} \Delta x'(X, Y) \Psi(X - x, Y - y) dX dY. \quad (2.32)$$

Using a round Gaussian distribution and Eq. 2.26, we have [14]:

$$\Delta x'_{\text{coh}}(x, y) = -\frac{2r_0 N}{\gamma_r} \frac{x}{r^2} \left(1 - e^{-\frac{r^2}{4\sigma^2}} \right), \quad r = \sqrt{x^2 + y^2}. \quad (2.33)$$

For the particular case of HO interaction, we find that the coherent kick is half the single particle kick, whereas for large separation, i.e LR interactions, the difference between coherent and incoherent vanishes.

In order to get the frequency of the coherent modes, we first start with two identical bunches, a single IP and one transverse degree of freedom. We define B_0 , the one turn matrix describing the transverse motion of a single particle (Eq. 2.15), with a tune Q_β and $\alpha = 0$. For now, let us assume that the bunch as a whole is fully described by its centre of mass, in other words, the bunches are rigid. The one turn matrix describing the motion of the bunch is equivalent to the single particle one. For two identical bunches, the motion is described by the following 4x4 matrix :

$$B_{2b} = \begin{pmatrix} B_0 & 0 \\ 0 & B_0 \end{pmatrix}. \quad (2.34)$$

We introduce the coupling between the two bunches due to BB :

$$C_{\text{BB}} = \begin{pmatrix} 1 & 0 & 0 & 0 \\ -\frac{\partial \Delta x'_{\text{coh}}}{\partial x}(x_0, y_0) & 1 & \frac{\partial \Delta x'_{\text{coh}}}{\partial x}(x_0, y_0) & 0 \\ 0 & 0 & 1 & 0 \\ \frac{\partial \Delta x'_{\text{coh}}}{\partial x}(x_0, y_0) & 0 & -\frac{\partial \Delta x'_{\text{coh}}}{\partial x}(x_0, y_0) & 1 \end{pmatrix} \quad (2.35)$$

where we have linearised the coherent BB kick around the closed orbit (x_0, y_0) . Neglecting

the variation in the vertical plane (App. C), we have :

$$\Delta x'_{\text{coh}}(x, y) \approx \Delta x'_{\text{coh}}(x_0, y_0) + \frac{\partial \Delta x'_{\text{coh}}}{\partial x}(x_0, y_0) \Delta x. \quad (2.36)$$

The constant term results in a modification of the closed orbit that can be taken into account beforehand [6, 15]. For a round Gaussian beam (Eq. 2.33), we have :

$$\frac{\partial \Delta x'_{\text{coh}}}{\partial x}(x, y) = -\frac{2N r_0}{\gamma_r} \left[\left(\frac{1}{r^2} - \frac{x^2}{r^4} \right) \left(1 - e^{-\frac{-r^2}{4\sigma^2}} \right) + \frac{x^2}{2r^2\sigma^2} e^{-\frac{-r^2}{4\sigma^2}} \right]. \quad (2.37)$$

The one turn map including BB effects becomes :

$$M = B_{2b} \circ C_{\text{BB}}. \quad (2.38)$$

We express the coherent tunes Q_{coh} as a function of the eigenvalues λ , such that :

$$\lambda = e^{-2\pi i Q_{\text{coh}}}. \quad (2.39)$$

The normal mode analysis of M reveals two frequencies each corresponding to two de-generated modes. The two modes of oscillation corresponds to either in-phase oscillation of the two bunches (σ -mode), or out-of-phase oscillation (π -mode) : $Q_\sigma = Q_\beta$ and $Q_\pi = Q_\beta + \beta^* \frac{\partial \Delta x'_{\text{coh}}}{\partial x}(x_0, y_0) / (2\pi)$, where β^* correspond to the value of the β function at the IP. In the particular case of HO collision, we get $Q_\pi = Q_\beta + \xi$. As the BB force was linearised, it is expected to have a difference with respect to the exact solution. This difference is characterized by the Yokoya factor : $Q_\pi = Q_\beta + Y \xi$. For round Gaussian beams we have $Y \approx 1.21$ [16]. In more complex configurations, the linear model can easily be extended to multiple bunches and multiple interactions (App. C). Such a model is very useful to derive the coherent tunes in a complex configuration, nevertheless, the difference with respect to exact solution remains. In order to obtain a more accurate estimate of the coherent spectrum, we will need numerical simulations, which will be discussed in Sec. 2.2.6.

2.2.3 The circulant matrix model

The forces due to the beam coupling impedance are linear, therefore a matrix formalism similar to the rigid bunch model used to describe coherent BB interactions seems appropriate to obtain the coherent spectrum in the presence of both effects. Nevertheless, the longitudinal distribution has an impact on the forces due to the wake, therefore we have to relax the rigid bunch approximation in the longitudinal plane. To that purpose, the Circulant Matrix Model (CMM) [17] is based on the decomposition of the longitudinal phase space distribution $\Psi_l(R)$, with $R = \sqrt{(s/\sigma_s)^2 + (\delta/\sigma_\delta)^2}$, σ_s and σ_δ being the r.m.s. bunch length and momentum deviation. As is illustrated in Fig. 2.4, we have N_r rings and N_s slices, each cell (s, r) is described by its longitudinal position, momentum deviation and weight given by :

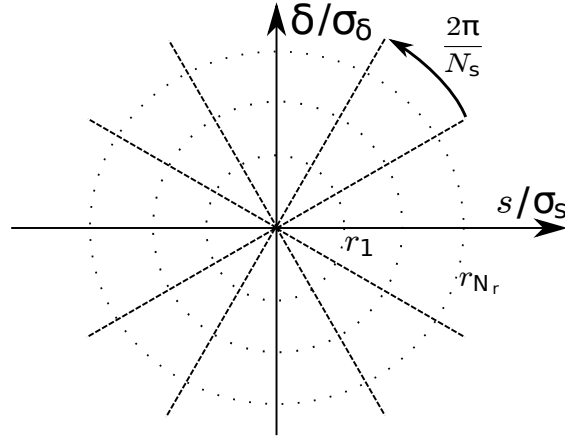


Figure 2.4 – Illustration of the discretisation of the longitudinal phase space in the CMM.

$$\begin{aligned}
 s_{(s,r)} &= \int_{2\pi \frac{s}{N_s}}^{2\pi \frac{s+1}{N_s}} d\theta \int_{r_r}^{r_{r+1}} R dR \Psi_l(R) s(R, \theta) \\
 \delta_{(s,r)} &= \int_{2\pi \frac{s}{N_s}}^{2\pi \frac{s+1}{N_s}} d\theta \int_{r_r}^{r_{r+1}} R dR \Psi_l(R) \delta(R, \theta) \\
 w_{(s,r)} &= \frac{2\pi}{N_s} \int_{r_r}^{r_{r+1}} R dR \Psi_l(R)
 \end{aligned} \tag{2.40}$$

where the radius of the rings, r_r , may be chosen arbitrarily, as well as the longitudinal distribution. Considering a Gaussian distribution, we choose the r_i 's, such that all weights are equal, $w_{(s,r)} = 1/(N_r N_s)$, using :

$$e^{-r_{i+1}} - e^{-r_i} = \frac{1}{N_r}. \tag{2.41}$$

Each element of the discretised distribution is described by its transverse phase space coordinates. Then the transverse motion of each cell is given by $B_0(\delta)$, the linear transfer matrix, where the tune is adjusted due to chromatic effects. Then the transverse transfer matrix for the whole distribution is a matrix of size $N_c = N_{\text{dof}} \cdot N_r \cdot N_s$, where N_{dof} is the number

of transverse degrees of freedom :

$$B_\beta = \begin{pmatrix} w_1 B_0(\delta_0) & & & \\ & w_2 B_0(\delta_1) & & \\ & & \ddots & \\ & & & w_{N_c} B_0(\delta_{N_c}) \end{pmatrix}. \quad (2.42)$$

In this model, the synchrotron motion is assumed to be unperturbed, in other words, we neglect the longitudinal component of the impedance. Therefore, the synchrotron motion corresponds to a rotation of the slices within each ring. Recalling the synchrotron tune, Q_s , the longitudinal one turn matrix is given by the circulant matrix :

$$S_r = P_{N_s}^{N_s Q_s} \quad (2.43)$$

where P_{N_s} is a permutation matrix :

$$P_{N_s} = \begin{pmatrix} 0 & 1 & & \\ & 0 & 1 & \\ & & \ddots & \ddots \\ 1 & & & 0 & 1 \end{pmatrix}. \quad (2.44)$$

The synchrotron motion is therefore described by :

$$S_0 = \mathbb{I}_{N_r} \otimes S_r. \quad (2.45)$$

Finally, we can write the unperturbed synchro-betatron one turn matrix for a single bunch :

$$M_0 = S_0 \otimes B_0. \quad (2.46)$$

Based on Eq. 2.31, we can define a coupling matrix $C_{w,\text{single}}$, describing the forces between each element of the distribution due to the beam coupling impedance. Considering a single transverse degree of freedom, we have :

$$(C_{w,\text{single}})_{ij} = \begin{cases} \begin{pmatrix} 1 & 0 \\ \sum_k W_{\text{quad}}(s_i - s_k) & 1 \end{pmatrix}, & \text{if } i = j \\ \begin{pmatrix} 0 & 0 \\ W_{\text{dip}}(s_i - s_j) & 0 \end{pmatrix}, & \text{if } i \neq j \end{cases}. \quad (2.47)$$

The one turn map becomes :

$$M_{1b} = M_0 \circ C_{w,\text{single}}. \quad (2.48)$$

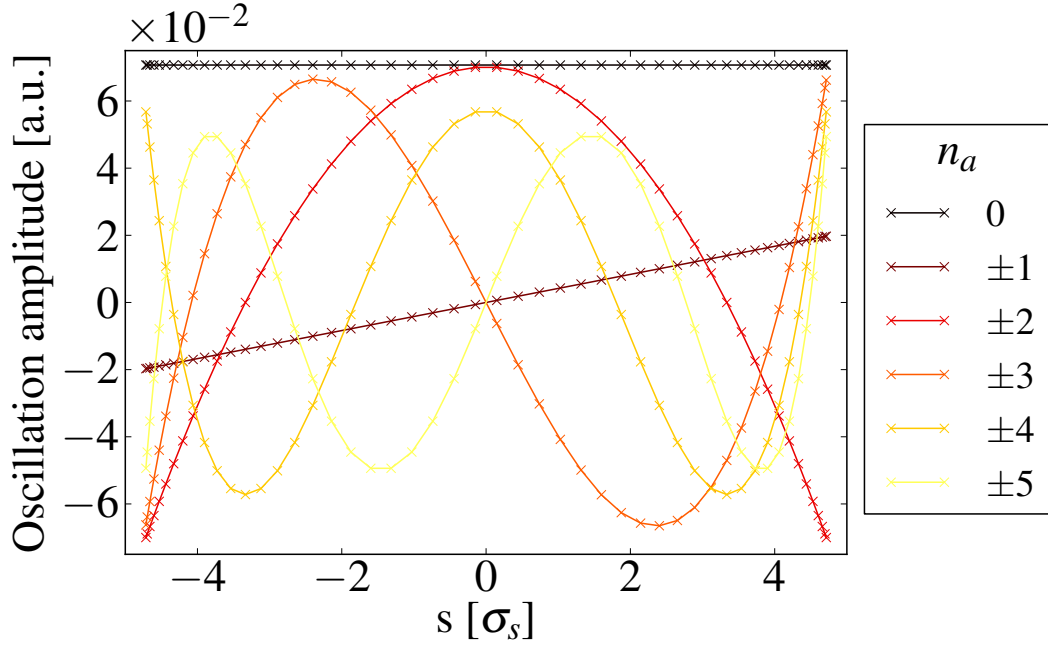


Figure 2.5 – Longitudinal pattern of the first 6 azimuthal head-tail modes, derived from eigenvectors of the unperturbed one turn matrix M_0 (Eq. 2.46).

For N_b identical bunches, we have :

$$M_{N_b} = \mathbb{I}_{N_b} \otimes M_{1b} \circ C_{w,mult} \quad (2.49)$$

where we have introduced the coupling matrix between the different bunches $C_{w,mult}$, which may be computed similarly to the single bunch coupling matrix, based on the wake functions and the distance between the bunches (App. C).

We have constructed the one turn matrix describing the transverse evolution of the longitudinal distribution, the stability of the system may be analysed using normal mode analysis (Sec. 2.2.4).

The head-tail mode basis

It is convenient to define a basis for the unperturbed longitudinal modes, given by the spectrum of unperturbed one turn matrix M_0 . For simplicity, let us assume that N_s is odd, we have :

$$\mathbf{Q}_0 = \left\{ Q_{\text{coh}} = \pm(Q_\beta + n_a Q_s) : n_a \in \mathbb{Z}, |n_a| < \frac{N_s - 1}{2} \right\}, \quad (2.50)$$

each eigenvalue being degenerated N_r times. The longitudinal profile of the modes is shown in Fig. 2.5, derived from the corresponding eigenvectors of M_0 . We observe the usual standing

wave patterns with a number of nodes equal to n_a , the so-called azimuthal mode number. The degenerated modes with identical azimuthal mode number are usually referred to as radial modes.

Beam-beam interactions

As mentioned earlier, the main advantage of this decomposition is that BB effects may be easily introduced. Indeed, as shown in the previous section, coherent BB effects may be described with a coupling matrix C_{BB} (Eq. 2.35). This matrix was derived by averaging the BB kick over the transverse distribution, which is identical for each element of the discretised longitudinal distribution. We may introduce the coupling between all elements of the distributions of two colliding bunches through a similar coupling matrix. Moreover, as the elements of the longitudinal distribution have a fixed position in the longitudinal direction, one may introduce the variation of the BB force in the longitudinal direction, e.g. due to a crossing angle or to the variation of the optical properties along the interaction [18]. An algorithm to build the matrix in complex configurations of BB interactions is described in App. C.

The CMM is a powerful tool to assess the stability of the beams, nevertheless, some significant approximations were used. First, the wake field is usually longer than the length of the accelerator, this contribution cannot be considered in the one turn map formalism. However, in many cases of interest, especially for large machines, the so-called multi-turn effect of the wake is negligible with respect to the single turn [19]. Secondly, the nonlinear effects of both longitudinal and transverse degrees of freedom have been neglected, thus neglecting Landau damping effects [20], which will be discussed in Sec. 2.2.5.

2.2.4 (Non-)normal mode analysis

Normal mode analysis is a standard approach to determine the stability of a system described by an operator. We will focus our interest on linear operators of finite dimensions, i.e. operators which may be described by a matrix M . From its eigenvectors and eigenvalues, we can rewrite M as a function of D , a diagonal matrix with the eigenvalues on the diagonal, and W a change of basis matrix :

$$M = W^{-1}DW. \quad (2.51)$$

The long term behaviour is described by the large power of M :

$$M^n = W^{-1}D^nW \quad (2.52)$$

where D^n is still a diagonal matrix with the n th power of the eigenvalues on its diagonal. We can write explicitly the behaviour of a system with initial condition $v(n=0) = \sum_i a_i V_i$, where V_i is an eigenvector with corresponding eigenvalue λ_i , after n iterations :

$$v(n) = \sum_j a_j \lambda_j^n V_j = \sum_j a_j e^{-in2\pi Q_j} V_j \quad (2.53)$$

with $Q_i = i \log(\lambda_i)/(2\pi)$. The system is called unstable if the imaginary part of one of the Q_i is strictly positive, as any initial condition with a non-zero component of this mode will grow exponentially. On the other hand, modes with a negative imaginary tune are naturally damped.

The normal mode analysis does not properly describe the behaviour of non-normal operators, i.e. operators for which a complete basis of eigenvectors does not exist. An effect of non-normality has been observed in linear accelerators resulting in so-called beam breakup and multi-bunch beam breakup instabilities [8]. Neglecting the multi-turn effect of the beam coupling impedance, the system we describe very much resembles a linear accelerator. While introducing multi-turn effects may remove the non-normality of the matrix, the short term behaviour of the system may be very different than the one predicted by normal mode analysis, especially in cases where the multi-turn wake is negligible when compared to the short range wake. In order to illustrate this effect, let us consider a simple model, using the CMM with a single slice and a single ring, in other words, the longitudinal distribution is rigid. We consider two bunches following each other within a distance much smaller than the ring circumference, the one turn matrix is of the type :

$$M = \begin{pmatrix} B_0 & K_2 \\ K_1 & B_0 \end{pmatrix} \quad (2.54)$$

where B_0 is the betatron one turn matrix, and K_1 and K_2 , describes the forces that the bunches exert on each other through the beam coupling impedance. As the distance between the first bunch and the second is much smaller than from the second to the first, K_1 and K_2 may be very different, let us consider the extreme case $K_2 = 0$. The spectrum of M is the identical to the one of B_0 , but degenerated twice. As a consequence, the normal mode analysis yields that the system is stable. Yet, let us observe the behaviour of the vector $v(0) = (x_0, x_0)$, where x_0 is an eigenvector of B_0 , with eigenvalue λ_0 , we obtain :

$$v(n) = \begin{pmatrix} B_0 & 0 \\ K_1 & B_0 \end{pmatrix}^n \begin{pmatrix} x_0 \\ x_0 \end{pmatrix} = \lambda_0^n \begin{pmatrix} x_0 \\ x_0 \end{pmatrix} + \lambda_0^{n-1} \begin{pmatrix} 0 \\ (n-1)K_1 \cdot x_0 \end{pmatrix} \quad (2.55)$$

where the first term of the right hand side corresponds to the normal behaviour of each bunch, while the second term corresponds to an oscillation with a linearly growing amplitude, as shown by the blue curve in Fig. 2.6. The behaviour is typical of a beam breakup instability. Let us re-introduce $K_2 = K_1$ in the one turn matrix, which describes two bunches travelling

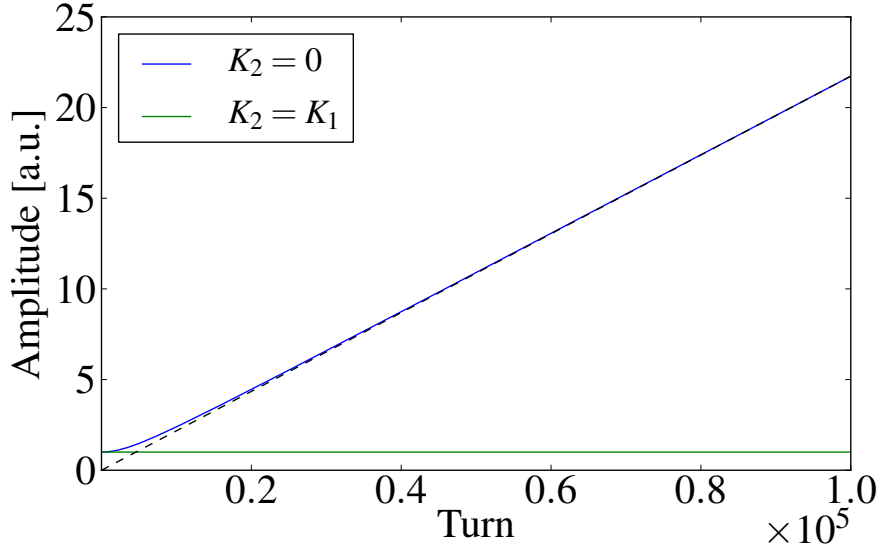


Figure 2.6 – Evolution of the norm of $v(n)$, for a non-normal matrix M (Eq. 2.54), with $K_2 = 0$ and a normal matrix $K_2 = K_1$. The dashed line shows the linearly growing contribution shown in Eq. 2.55.

with opposite azimuth and M becomes normal. Actually, the matrix M remains normal for K_2 strictly non-zero, yet, the non-normal behaviour of the system will be dominating on a short time scale when $K_1 \gg K_2$. In order to characterize such behaviour in more complex systems, several mathematical tools have been introduced to go beyond the normal mode analysis, among which the pseudospectrum appeared as a convenient tool.

Pseudospectrum

While the spectrum of an operator gives the resonant frequencies of the system, it provides no information on the width of the resonances, the pseudospectrum provides such an information. Mathematically, it is defined as follows [21]. Let A be a complex matrix and I the identity matrix of the same size, then the pseudospectrum is given by:

$$\sigma(A, \epsilon) = \left\{ \|(z \cdot I - A)^{-1}\| > \frac{1}{\epsilon} \mid z \in \mathbb{C} \right\} \quad (2.56)$$

with $\epsilon \in \mathbb{R}^+$. The pseudospectrum is conveniently computed using the following feature of the Singular Value Decomposition (SVD) [21]:

$$\|(z \cdot I - A)^{-1}\| = \frac{1}{s_{\min}(z \cdot I - A)} \quad (2.57)$$

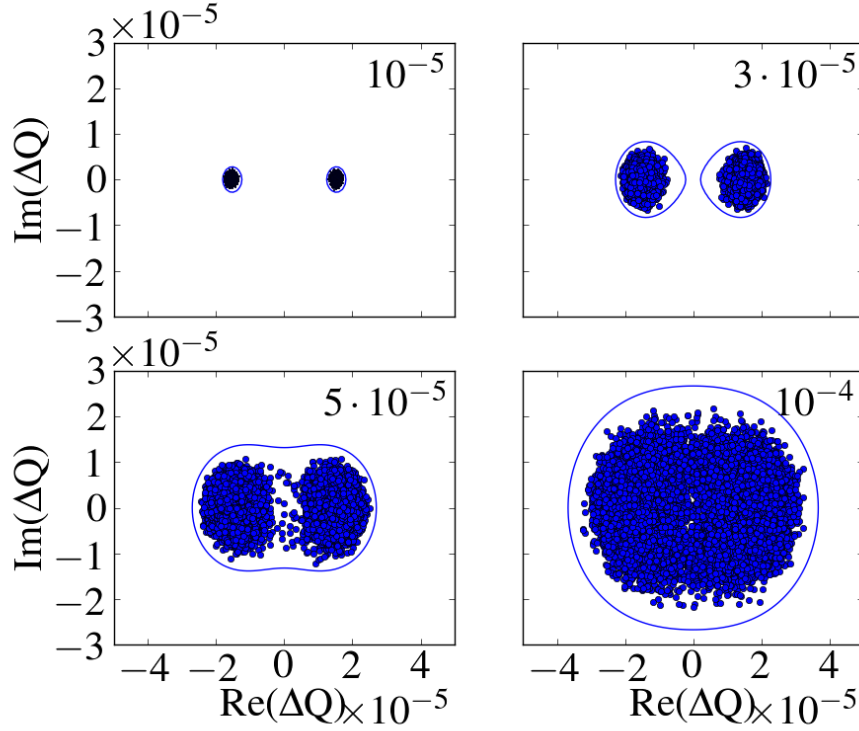


Figure 2.7 – Eigenvalues of $M + E$, with $K_1 = 10K_2$ (Eq. 2.54) and E random matrices with $\|E\| = \epsilon$ (dots). All eigenvalues are within the pseudospectrum of M for the different values of ϵ (lines).

where $s_{min}(\cdot)$ corresponds to the smallest singular value. A physical interpretation of the pseudospectrum is illustrated in Fig. 2.7, where we observe that $\sigma(\epsilon)$ gives the spectrum of the system, perturbed by a random matrix of order ϵ , in other words it is a measure of the sensibility of the system to a perturbation. We represent the pseudospectrum for different ϵ in a contour plot, as in Fig. 2.8, showing the same case. We observe that, while the eigenvalues all have zero or negative imaginary parts, the pseudospectrum extends towards the positive imaginary parts, which intuitively indicates that the system is sensitive to perturbations. Yet, quantifying the stability is more delicate than for normal systems, as it now strongly depends on the perturbation, as already indicated by the simplified two-bunch model (Eq. 2.55). In order to quantify this effect, we use the so-called Kreiss matrix theorem, which gives bounds for the maximum values which may be achieved by the powers of a matrix A of size N [21]:

$$K(A) \leq \sup_{k \geq 0} \|A^k\| \leq e \cdot N \cdot K(A) \quad (2.58)$$

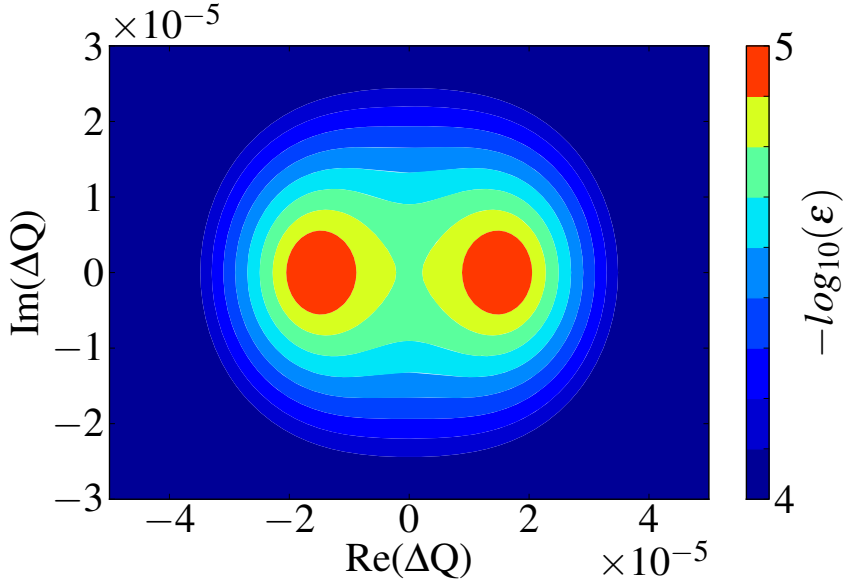


Figure 2.8 – Representation of the pseudospectrum of M with $K_1 = 10K_2$ (Eq. 2.54), obtained by colour coding the complex plane according to the ϵ given by Eq. 2.57.

where we have introduced the Kreiss constant of A , $K(A)$, which may be computed based on the pseudospectrum [21]:

$$K(A) = \sup_{|z|>1} \{ (|z|-1) \cdot \|(z \cdot I - A)^{-1}\| \}. \quad (2.59)$$

For a stable system, the Kreiss constant is lower or equal to 1, but diverges when there are unstable eigenvalues. It is therefore an interesting parameter to characterize systems at the limit of stability, in the normal mode analysis sense, for which transient amplification of a perturbation might be expected. The amplification factor being greater or equal to the Kreiss constant. Looking back at the two-bunch model, we observe in Fig. 2.9 that, indeed, the Kreiss constant grows with the ratio K_1/K_2 . The transient amplification of a perturbation may be large, potentially leading to significant emittance growth or beam losses, similarly to a normal instability.

2.2.5 Landau damping

The main effect of nonlinearities is to generate amplitude detuning, i.e. the particles in the beam will oscillate at different frequencies depending on their action J_x and J_y . In the CMM, by linearising the forces we have implicitly assumed that particles oscillate with identical frequencies. While the coherent tune obtained with the linearised model may have a positive imaginary part, it is possible for this mode to be stable in the presence of a frequency spread [20]. Following [22], we relate the coherent tune derived within the

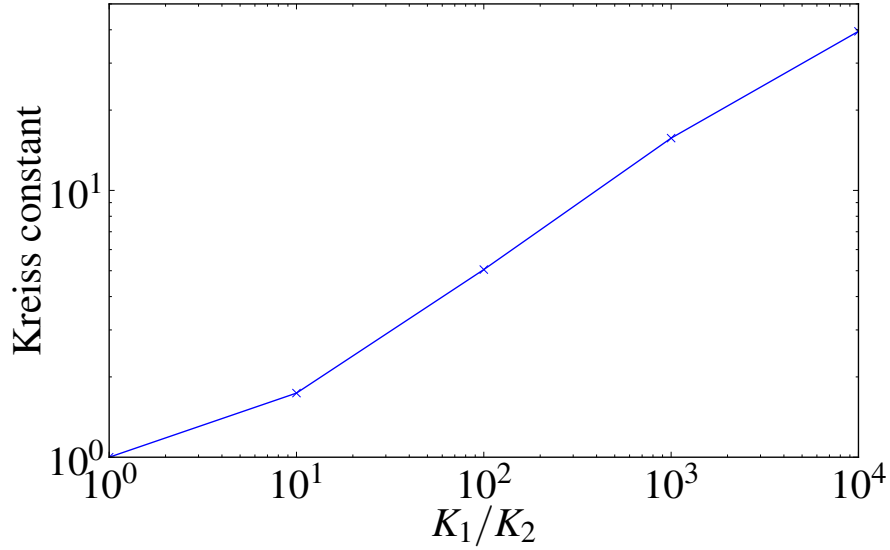


Figure 2.9 – Kreiss constant for M as a function of the ratio between the coupling coefficient (Eq. 2.54).

linearised model q to the the actual coherent tune shift with respect to the unperturbed tunes ΔQ_x , i.e. including the amplitude detuning, with the following dispersion relation :

$$-\frac{1}{\Delta Q_x} = \int \frac{\frac{d\Psi(J_x, J_y)}{dJ_x} J_x dJ_x dJ_y}{q - Q_x(J_x, J_y)} \quad (2.60)$$

with $Q_x(J_x, J_y)$ the amplitude detuning and $\Psi(J_x, J_y)$ the beam distribution function. This relation is often represented in a so-called stability diagram, which represents the area in the complex plane of coherent tunes which yields a stable coherent motion in the presence of detuning, i.e. $Im(q) < 0$. The boundary of stability is defined as :

$$SD(\Psi, Q) = \left\{ - \left(\int \frac{\frac{d\Psi(J_x, J_y)}{dJ_x} J_x dJ_x dJ_y}{q - Q_x(J_x, J_y)} \right)^{-1} : q \in \mathbb{R} \right\}. \quad (2.61)$$

In cases where $q - Q(J) \neq 0 \forall J$, then the integral is purely real and the boundary is simply the real axis. However, when there exist singularities the dispersion integral contains an imaginary part, which may be positive or negative. Following Landau [20], we choose the positive value, therefore the boundary moves to the positive side of the imaginary plane. Several approximations are used to derive this dispersion relation. First, while this relation does include Landau damping from the tune spread in both planes, it does not include coupling between the planes [23]. Secondly, it is assumed that the different modes are well separated, which is not a valid approximation for high intensity beams where coupling modes

may lead to strong instabilities, such as the Transverse Mode Coupling Instability (TMCI) [24]. Thirdly, the derivation is based on perturbation theory, assuming small oscillation amplitude. In order to go beyond these approximation, we will resort to computer simulations.

2.2.6 Multi-particle tracking simulation

As we have seen, an analytical derivation of the coherent behaviour necessitates severe approximations, the validity of which is questionable in many real cases. In order to check the validity of our assumptions and go beyond when necessary, we shall use multi-particle tracking simulations. The beam is modelled by a set of macro-particles, which motion through each element of the machine is describe by a map. Each map may be nonlinear and may depend on the global properties of the beam. Such a simulation describes the single particle dynamic as well as the coherent dynamic in a consistent manner. The presence of a second beam and the resulting BB interaction may also be modelled in a fully self-consistent manner. However, this approach requires significant computing power and is usually used as a complement to theoretical models. A full description of the code COMBI can be found in App. A.

2.3 Singular value decomposition

The SVD is a convenient tool to extract the modes of oscillation out of experimental or tracking data. Following [25], we define the SVD of a rectangular $n \times t$ matrix M as :

$$M = USV^* \quad (2.62)$$

with U and V two orthogonal unitary matrices of size $n \times n$ and $t \times t$. V^* denotes the conjugate transpose of V and S is a diagonal matrix of size $n \times t$. The values on the diagonal of S , s_i , are strictly positive real numbers called the singular values of M .

We note \bar{x}_j a discrete vector of size n representing the measured or simulated beam parameters at a Poincaré section during turn t_j , e.g. the moments of the beam distribution. For a sample of $t > n$ turns, we build the raw data matrix as :

$$M = (\bar{x}_1 \dots \bar{x}_j \dots \bar{x}_t). \quad (2.63)$$

Expanding and identifying the terms of the SVD, we can write [26]:

$$\bar{x}_j = \sum_{i=1}^n s_i \bar{U}_i V_{i,j}^*. \quad (2.64)$$

The behaviour of \bar{x}_j has been decomposed over a basis of modes represented by unitary vectors of size n composing the columns of the matrix U , so-called spacial singular vector \bar{U}_i . The relative strength of the modes in the sample is weighted by the corresponding singular

values s_j . The temporal evolution of each mode, i.e. the variation with j , has been singled out in unitary vectors of size t composing the lines of V^* , so-called time singular vectors $\{V_{i,j}^* \mid 0 < j \leq t\}$.

2.4 Luminosity

The aim of a collider is to provide high energy collisions at a high rate within a particle detector. The rate R_e of an event with cross section σ_e is given by the luminosity of the machine \mathcal{L} :

$$R_e = \mathcal{L} \sigma_e. \quad (2.65)$$

To compute the luminosity, let us consider a particle beam. The distribution of particles in a single bunch, centred around a fixed point is given by $\rho(\vec{x}, s_0)$. Where s_0 is the longitudinal position of the fixed point, with respect to a single IP. For each bunch crossing, the luminosity is given by the following integral [27] :

$$\mathcal{L}_b = K N_1 N_2 f_{\text{rev}} \int_{-\infty}^{\infty} \int \int \int \rho_1(\vec{x}, s_0) \rho_2(\vec{x}, -s_0) dx dy ds ds_0 \quad (2.66)$$

where ρ_1 and ρ_2 are the distributions of the two counter rotating bunches, N_1, N_2 the bunch populations, f_{rev} is the revolution frequency, and the kinematic factor

$$K = \sqrt{(\vec{v}_1 - \vec{v}_2)^2 - \frac{(\vec{v}_1 \times \vec{v}_2)^2}{c^2}} \quad (2.67)$$

with \vec{v}_1 and \vec{v}_2 the bunches velocities and c the speed of light. Assuming that their orbits are identical and the beam sizes are constant over the interaction and using Gaussian distributions in all degrees of freedom, with σ_x and σ_y the rms transverse beam sizes and σ_s the rms bunch length, we have :

$$\mathcal{L}_{b,0} = \frac{N_1 N_2 f_{\text{rev}}}{4\pi \sigma_x \sigma_y}. \quad (2.68)$$

The luminosity can be lower than this maximal value. For example, in some machines, the orbit of the two beams are not identical, they rather collide with a crossing angle θ , for instance in the horizontal plane, reducing the luminosity as :

$$\mathcal{L}_{b,\text{Xing}} = \frac{c \cos^2(\frac{\theta}{2})}{\sqrt{1 + (\frac{\sigma_s}{\sigma_x} \tan(\frac{\theta}{2}))^2}} \mathcal{L}_{b,0}. \quad (2.69)$$

Chapter 2. Beam Dynamics

With a constant separation d between the beams :

$$\mathcal{L}_{b,\text{offset}} = e^{-\frac{d^2}{4\sigma^2}} \mathcal{L}_{b,\text{Xing}}. \quad (2.70)$$

The assumption of the constant beam size over the bunch length is also not valid in machines with small β^* , the value of the β function at the IP, compared to the bunch length (hourglass effect) [28]. There exists no analytical formula for the reduction factor in the simultaneous presence of hourglass effect, crossing angle and transverse offset, the overlap integral has to be evaluated numerically.

The total luminosity of a machine depends of the number of bunch crossings per unit time at the different IPs. With $N_{b,\text{IP}}$ bunches colliding at a set of IPs, we have :

$$\mathcal{L} = f_{\text{rev}} \sum_{\text{IP}} N_{b,\text{IP}} \cdot \mathcal{L}_{b,\text{IP}}. \quad (2.71)$$

In principle, the number of events has to be maximized in order to observe rare events with a significant statistics. Nevertheless, the luminosity is constrained in many aspects to fit the requirements of the detectors. Depending on the design of the detector and the physics under study, high collision rates may lead to undesirable effects possibly degrading the detection efficiency [29]. A large flexibility on the control of the luminosity is important in order to deliver optimal conditions to the detectors.

3 The Large Hadron Collider

3.1 Physics case

The LHC aims at colliding high energy particles at a high rate [30]. The properties of particles emerging from the collision are measured and analysed by particle detectors placed around the IPs. Because of the probabilistic nature of quantum physics and of the low cross section of the processes under study, a large data set is required. The physics program of the LHC covers standard model physics, including the Higgs boson, CP symmetry breaking, in particular in B mesons, as well as strong force physics. Physics beyond the standard model is also explored. The requirements for the collider to cover such a large spectrum are challenging, to that purpose the LHC is designed to accommodate four main experiments each having specificities. A Toroidal LHC AparatuS (ATLAS) and the Compact Muon Solenoid (CMS) are two high luminosity experiments specifically designed to detect rare events and in particular Higgs boson signatures. The LHC beauty experiment (LHCb) aims at studying beauty physics. Being a precision experiment, its demand on luminosity is much lower. While these experiments are mainly designed to study proton-proton collisions, A Large Ion Collider Experiment (ALICE) is designed to observe heavy ion collisions, Pb-Pb or proton-Pb. The luminosity requirements of ALICE during proton runs are even lower than LHCb.

3.2 Configuration

The challenges in terms of beam physics are very different when colliding protons or lead ions. The difference mainly comes from the bunch intensities, which are much lower when operating with ion beams. The wake fields as well as the beam-beam forces are therefore much weaker, we shall therefore focus on proton-proton configurations.

The LHC is installed in a 27 km tunnel, with eight straight sections linked by eight arcs. Each straight section serving a different purpose, as pictured in Fig. 3.1. The beams are composed of a set of bunches, nominally there are 2808 bunches spaced by 25 ns, i.e. ≈ 7.5 m. A so-called abort gap of 3 μ s, is kept free of particles to account for the rise time of the extraction

Chapter 3. The Large Hadron Collider

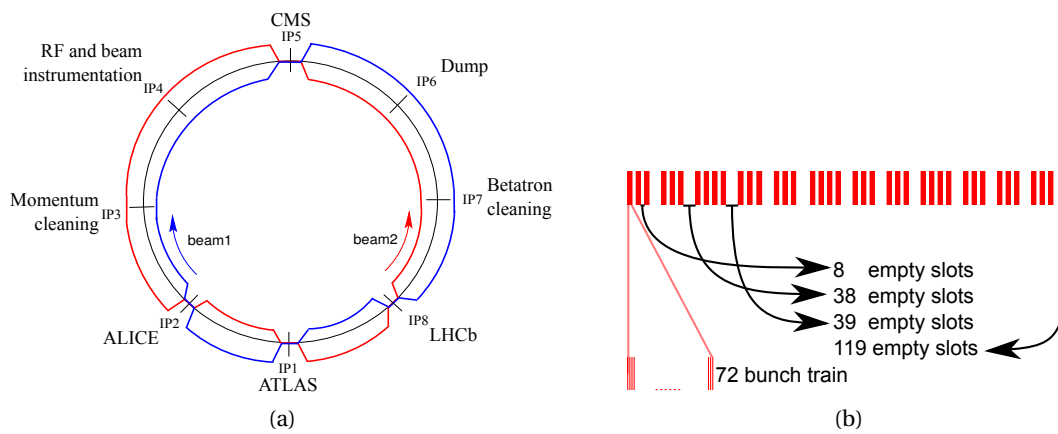


Figure 3.1 – Configuration of the IPs in the LHC and nominal filling scheme [30].

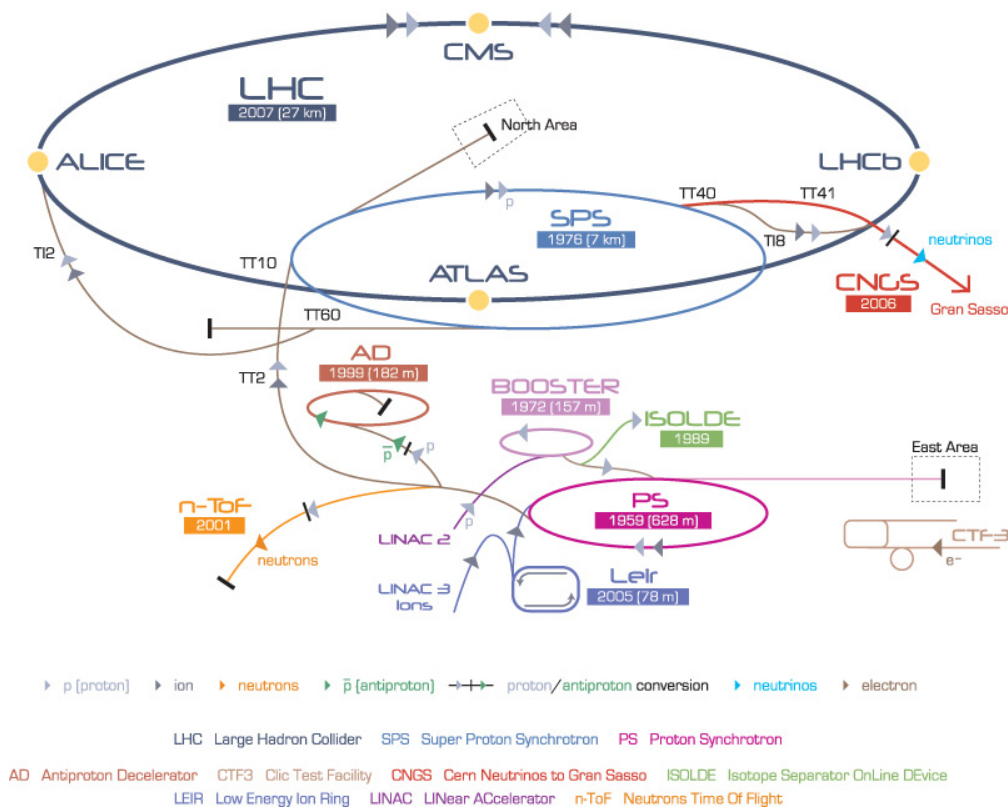


Figure 3.2 – CERN accelerator complex. Protons are accelerated as follows : LINAC2 (50 MeV) → BOOSTER (1.4 GeV) → PS (25 GeV) → SPS (450 GeV) → LHC (7 TeV) [31].

3.2. Configuration

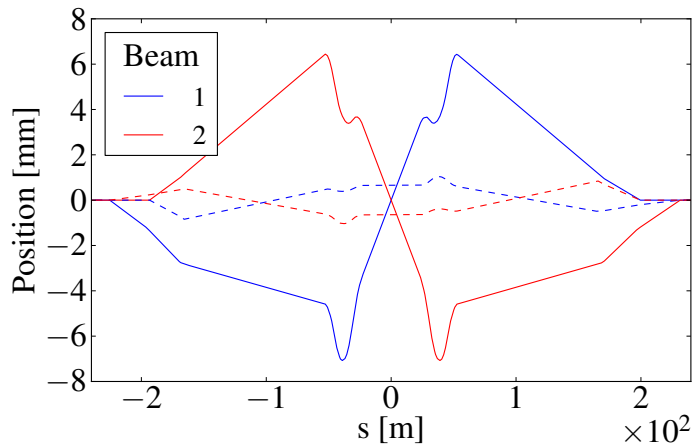
Parameter	Nominal	2012 proton run
Energy [TeV]	7	4
Intensity [10^{11} proton/bunch]	1.15	1.5
Normalised transverse emittance [μm]	3.75	2.5
Number of bunches	2808	1374 (1380)
Bunch spacing [ns]	25	50
Bunch length [ns]	0.26	0.32
Momentum spread [10^{-4}]	1.129	1.6
Horizontal tune		0.31
Vertical tune		0.32
Synchrotron tune [10^{-3}]	1.9	2.3
Momentum compaction		3.225
Revolution frequency [kHz]		11.245

Table 3.1 – LHC machine and beam parameters in collision for different configuration.

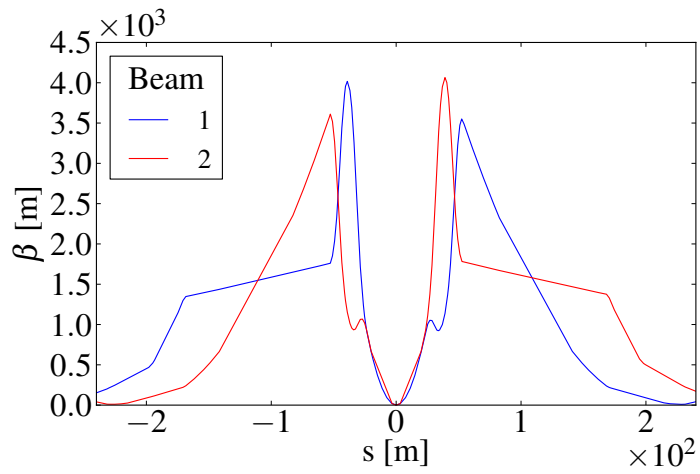
kicker. Indeed, such beams represents 362 MJ, which needs to be extracted safely from the machine, in order to avoid damages to the equipment surrounding the beams, especially the superconducting magnets. Due to constrains from the injection chain, not all available 25 ns slots are filled, to account for injections/extractions from one synchrotron to the next. The injection chain of the LHC is pictured in Fig. 3.2, and the resulting nominal filling scheme in Fig. 3.1b. Bunches having the minimal bunch spacing are produced together in the chain and are therefore referred to as bunch trains. There is a large flexibility concerning the choice of filling scheme, in terms of bunch spacing and train structure. This flexibility results from a lot of experience with different type manipulation of the beams in the injector chain. Being produced differently, the performance of the injectors in terms of beam brightness will be different for different filling schemes. The observation in 2011 of unexpectedly strong electron cloud effects has led to an increase of the bunch spacing used for standard operation to 50 ns [32]. In this configuration, the injectors were able to produce beams with much higher brightness than nominal LHC beams [33]. Usual parameters during the 2012 proton run and nominal parameters are compared in Tab. 3.1. Unless stated otherwise, these parameters are used throughout this thesis.

The beams circulate in different beam pipes in most of the ring, they share a common beam pipe only ≈ 64 m on each side of the IPs. In the nominal case there are 35 BB interactions per interaction region, one of which is HO at the IP, the others being LRs. The separation between the beams is ensured by a crossing angle, as illustrated by Fig. 3.3a. The final focusing is done with a quadrupole triplet, placed anti-symmetrically around the IP, the resulting β function is shown in Fig. 3.3b. As shown in Fig. 3.4, the value of the normalised separation in the drift space around the IP is almost constant. We use this value of the separation to characterize the strength of the LR interactions in a specific configuration :

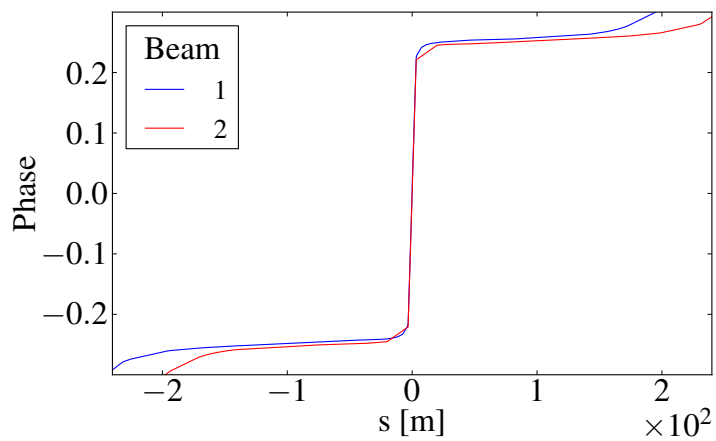
$$S_{\text{drift}} \approx \sqrt{\frac{\beta^* \gamma_r}{\epsilon_n}} \theta \quad (3.1)$$



(a) Orbit with a crossing angle (solid) and parallel separation (dashed)



(b) Horizontal β function



(c) Phase advance with respect to the IP

Figure 3.3 – The LHC nominal optics in the CMS interaction region, around IP5 [30].

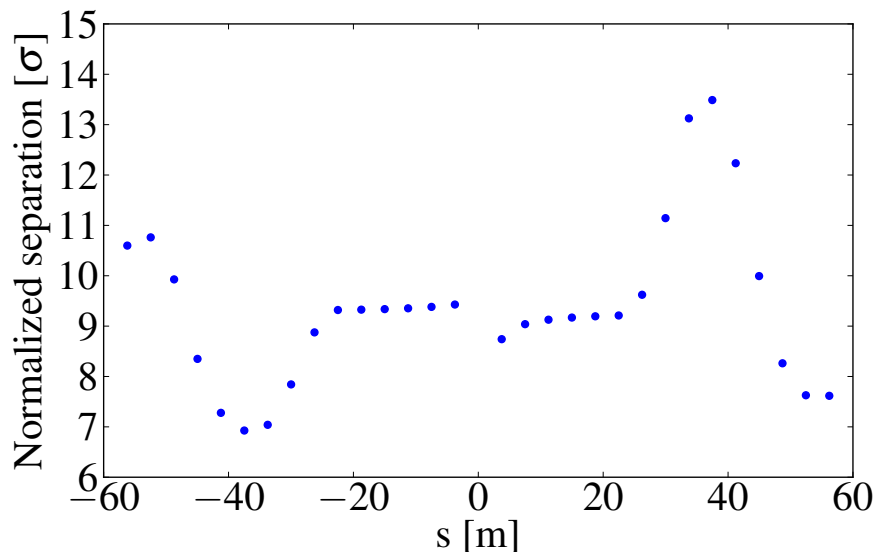


Figure 3.4 – Normalised separation around CMS interaction point (IP5) with 2012 machine and beam parameters. The dots are located every 3.75 m in the common beam pipe around the IP, representing the potential location for the LR interactions with 25 ns spaced beams.

A small value of β^* is desirable to achieve high luminosity. However, the nonlinearities of the LR interactions become important for small separation and eventually compromise the regular motion of the particles. The onset of chaotic motion was found for S_{drift} around 9 to 12 σ , depending on the configuration [34, 35]. Both the β^* and the crossing angle are constrained by this limit and by the physical aperture of the final focusing magnets, where the beam size increases drastically as β^* is reduced. In extreme configurations, considered for future upgrade scenarios, luminosity reduction effects (Sec. 2.4) also become limiting factors.

As illustrated in Fig. 3.5, the bunch train structure of the LHC beams leaves gaps with empty slots, which results in bunches at the head and the tail of the trains experiencing less LR interactions. These bunches are referred to as PACMAN [36]. Figures 3.6 and 3.7 show the number of LR interactions around each IP for the different bunches. The filling scheme of the two beams is identical in the nominal configuration, also the two high luminosity experiments are placed at opposite azimuth, which results in the very regular pattern of Fig. 3.6, where we observe PACMAN bunches at the beginning and end of all the bunch trains. Due to their asymmetric positions, the picture at the IPs 2 and 8 is slightly different. There exist bunches without LR in these interaction regions, due to the abort gap of the other beam. This also results in bunches having different number of HO collision, known as Super-PACMAN bunches (Tab. 3.2).

The effect of LR interactions in the two high luminosity experiment is mitigated by placing them at opposite azimuth and using crossing angles in two different planes, vertical at IP1 and horizontal at IP5. It was shown that this configuration maximizes the dynamic aperture

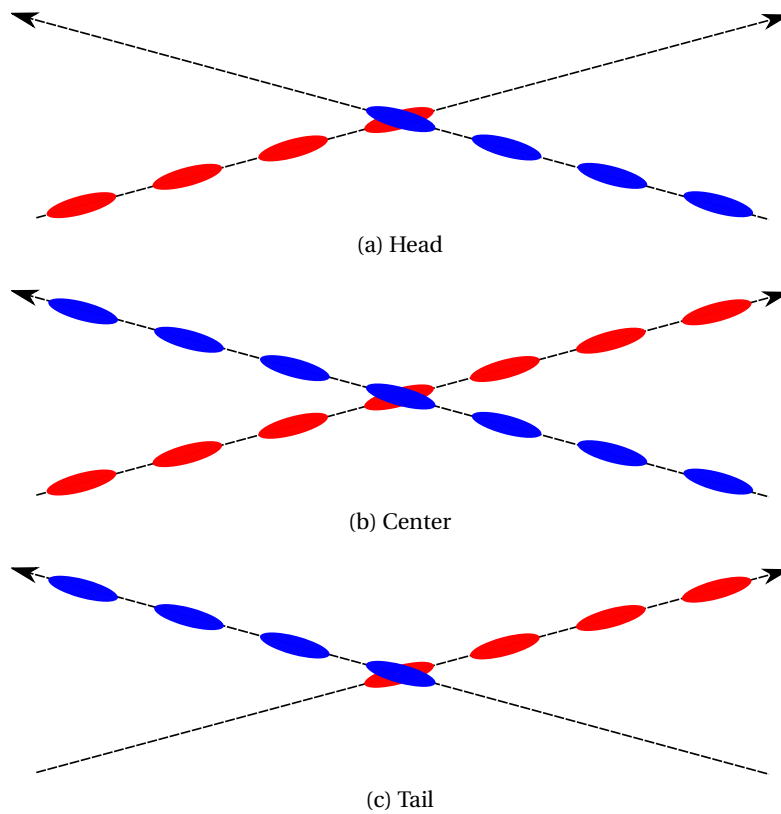
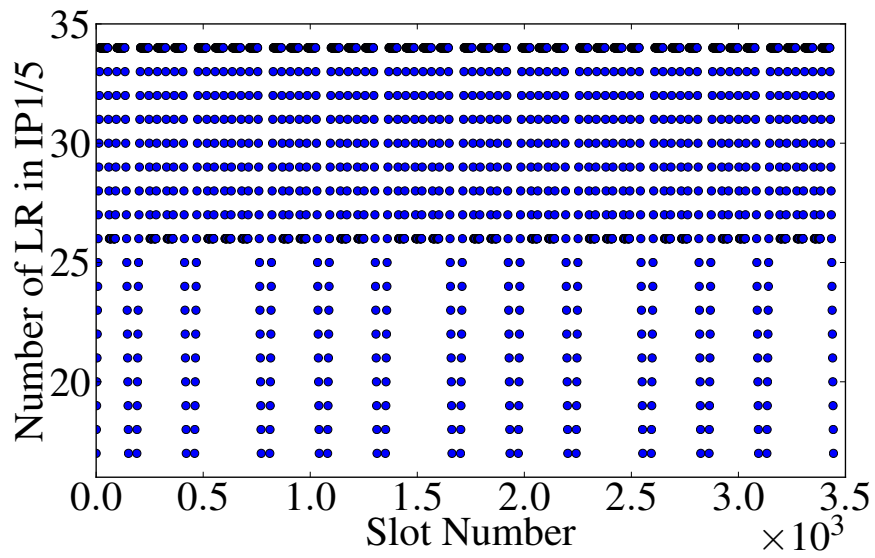


Figure 3.5 – Schematic representation of two trains of bunches colliding with a crossing angle, experiencing HO and LR beam-beam interactions.

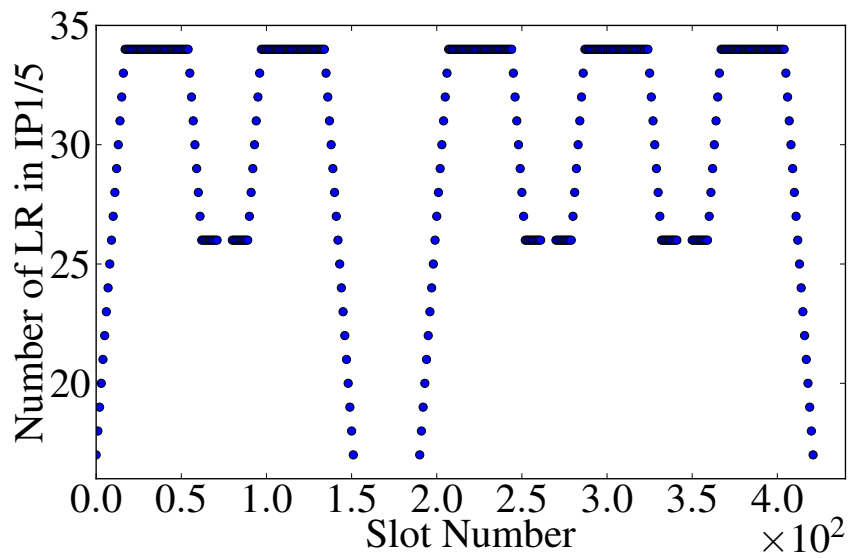
and mitigate several PACMAN effects [35, 36].

In 2012, the target luminosity at IP8, which hosts LHCb, was more than a factor 3 lower than the peak luminosity achieved at IPs 1 and 5 (Tab. 3.3). The reduction of the luminosity is achieved by two means, the β^* was larger and a transverse offset was introduced at the IP. The latter technique allows for an operationally friendly way of compensating the luminosity degradation due to the reduction of the beams brightness by adapting the offset along the production of luminosity. The production of luminosity during a fill of 2012 is illustrated in Fig. 3.8. ALICE, located at IP2, is not shown in the plot, as the luminosity required with proton collisions is a factor 10^{-5} lower than for the high luminosity experiments. The reduction was achieved with a larger β^* and by colliding bunches with almost empty slots of the other beam. No beam was injected in these slots, however the residual beam was sufficient to provide the low luminosity required.

Let us note that both LHCb and ALICE experiments use a spectrometer magnet, which acts on the beam. The angle due to the spectrometer is referred to as internal crossing angle, as opposed to the external crossing angle, ensured by kicker magnets [39]. The configuration

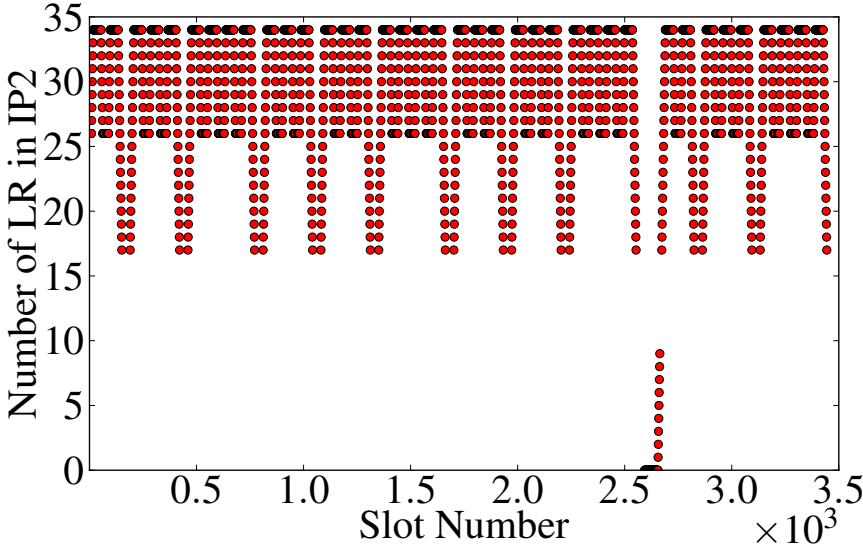


(a)

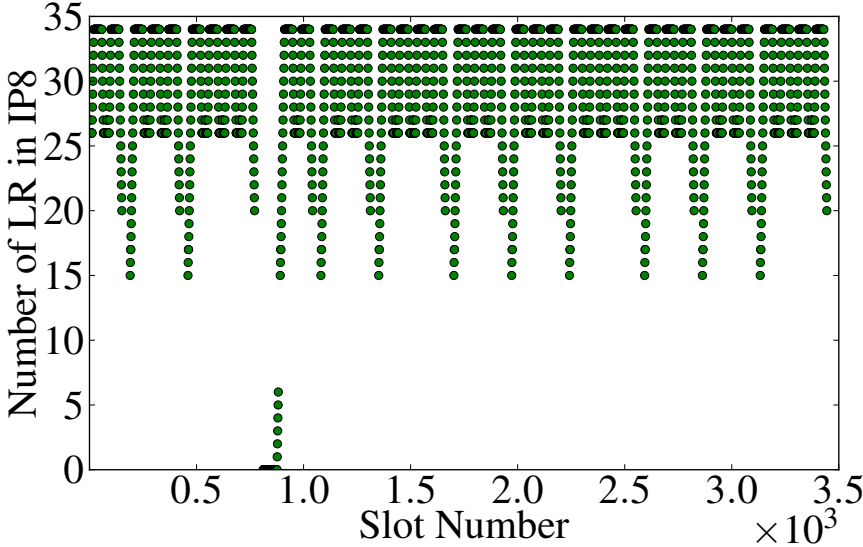


(b) zoom

Figure 3.6 – Number of LR interactions for each bunch of the nominal filling scheme in the two high luminosity experiments, with a zoom on the first 360 bunches.



(a) IP2



(b) IP8

Figure 3.7 – Number of LR interactions for each bunch of the nominal filling scheme, in the two lower luminosity experiments.

IP	Nominal	2012		
		FS1	FS2	FS3
2	0	0	0	0
8	0	6	0	49
1 & 5	3	11	106	60
1, 5 & 8	0	1256	1274	1271
1, 2 & 5	183	0	0	0
1, 2, 5 & 8	2553	0	0	0

Table 3.2 – Number of bunches with a different number of HO collision scheme, for different filling scheme, nominal and three of the filling schemes used in 2012. The corresponding technical names are [37, 38]:

FS1 : 50ns_1374_1368_0_1262_144bpi12inj

FS2 : 50ns_1380b_1380_0_1274_144bpi12inj

FS3 : 50ns_1380b_1331_0_1320_144bpi12inj

Parameter	IP1	IP5	IP2	IP8
	ATLAS	CMS	ALICE	LHCb
β^* before the squeeze [m]	11	11	10	10
β^* after the squeeze [m]	0.6	0.6	3	3
Full external crossing angle (H/V) [μ rad]	290	290	± 290	260(180)
Full internal crossing angle (H/V) [μ rad]	0	0	± 245	± 470
Target luminosity [$10^{34} \text{cm}^{-2} \text{Hz}$]	Peak	Peak	10^{-5}	$4 \cdot 10^{-2}$
Peak luminosity [$10^{34} \text{cm}^{-2} \text{Hz}$]	0.63	0.63	0.14	0.13
Reduction factor	1	1	$\approx 10^{-5}$	≈ 0.3
Luminosity leveling	None	None	bunch-satellite	Transverse offset

Table 3.3 – Configuration of the interaction regions during the 2012 physics run with protons.

of the different IPs is shown in Tab. 3.3. At the IPs 1,2, and 5, the crossing angle and parallel separation bumps are strictly in the horizontal or vertical plane, perpendicular to each other. The configuration of IP8 is slightly different, as it is changed during the fill in a procedure of tilting of the crossing angle. Before the tilting, both the external and internal crossing angles are in the horizontal plane. During the procedure, the external crossing angle is moved to the vertical plane. The internal crossing angle remains in the horizontal plane, as a result the effective crossing angle is in a tilted plane. This procedure was introduced, both to keep the same effective crossing angle at the IP, which is desirable from the experiments point of view, and to ease the operation of the machine when changing the polarity of the spectrometer [40, 41].

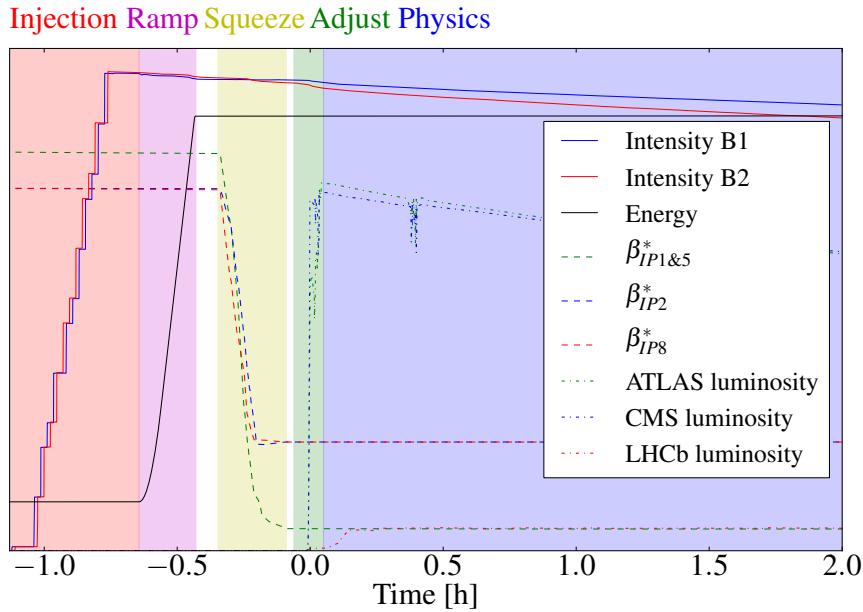


Figure 3.8 – Standard LHC operation cycle (Example : Fill 2718), starting with multiple injections from the SPS followed by the energy ramp and the betatron squeeze before bringing the beams into collision (Adjust) in order to start the production of luminosity (Physics).

3.2.1 Standard operational cycle

The standard operational cycle of the LHC is illustrated in Fig. 3.8. During the first part, the optics is optimized to have an aperture as large as possible for the injection and the energy ramp. As a consequence, the β^* s are large at all IPs. The optics is then modified during the squeeze in order to optimize for luminosity production, i.e. by lowering the β function at the IPs. This operation is done by a successive change of optics, with decreasing β^* s and fixed crossing angle. Thus, the normalised separation at the location of LR interactions is reduced by a factor ~ 10 at the end of the squeeze with respect to before, i.e., BB effects start playing an important role in the dynamic of the beams during the squeeze.

After the squeeze, comes the so-called adjust phase. The parallel separation orbit bumps are collapsed at the IPs 1 and 5, in order to initiate luminosity production. Simultaneously, the IP8 crossing angle tilting procedure is performed. In the two high luminosity experiment, the collision point is optimized empirically to obtain the highest luminosity, which corresponds to perfect HO collision [42]. In the two lower luminosity experiments, the separation between the beams is adjusted such as to obtain the target luminosity.

3.3 Instrumentation

For completeness, let us briefly review the diagnostics used in following studies.

The intensity of each individual bunch is measured simultaneously every second, with a accuracy better than 1% by the Fast Beam Current Transformer (FBCT) [43].

The measurement of single bunch emittances is less obvious. At top energy with multiple bunches, the only device capable of such measurement is the Beam Synchrotron Radiation Telescope (BSRT). The absolute accuracy of the measurement is however difficult to assess, it is mainly used for relative measurement, for which the accuracy is in the order of 10% [44]. As opposed to the FBCT, the emittance measurement is done one bunch at a time, and requires an integration time in the order of a second. Therefore, a measurement of all individual bunches lasts several minutes.

The beam spectrum is measured by a transverse pickups with direct diode detection, also know as the Base Band Tune (BBQ) [45]. The primary aim of this system is to measure the machine tune, which is the result of a mixing of the signals of all bunches in the machine. This device is, in principle, not meant for single bunch measurement, but is capable of detecting the beam spectrum with residual oscillation below the μm level.

All experiments provide on-line luminosity information on each bunch crossing with an accuracy in the order of 10% [46–48].

3.3.1 Transverse feedback

A full description of the implementation of the transverse feedback of the LHC may be found in [49, 50]. The transverse feedback uses two transverse pickups per plane and per beam in order to measure the bunch positions in the transverse planes turn by turn with a resolution of the order of $1 \mu\text{m}$ [51]. This data is used internally and is not recorded systematically. In 2012, it was possible to trigger an acquisition buffer capable of storing 72 turns of turn-by-turn bunch by bunch measurement of the position. The buffer is therefore too small to extract bunch by bunch frequency informations.

For convenience, the the transverse feedback gain, G_{FB} , is often expressed as a function of the corresponding damping time for free oscillations :

$$\tau_{FB} = \frac{2}{G_{FB}} \quad (3.2)$$

3.4 Impedance model

A detailed description of the LHC impedance model can be found in [19]. The model includes the resistive wall impedance of the 44 collimators, the beam screens (86% of the machine) and the vacuum beam pipe (14% of the machine). The cross sections of each of these devices are properly taken into account in the impedance calculations. The LHC impedance largely depends on the settings of the collimators, which are set by machine

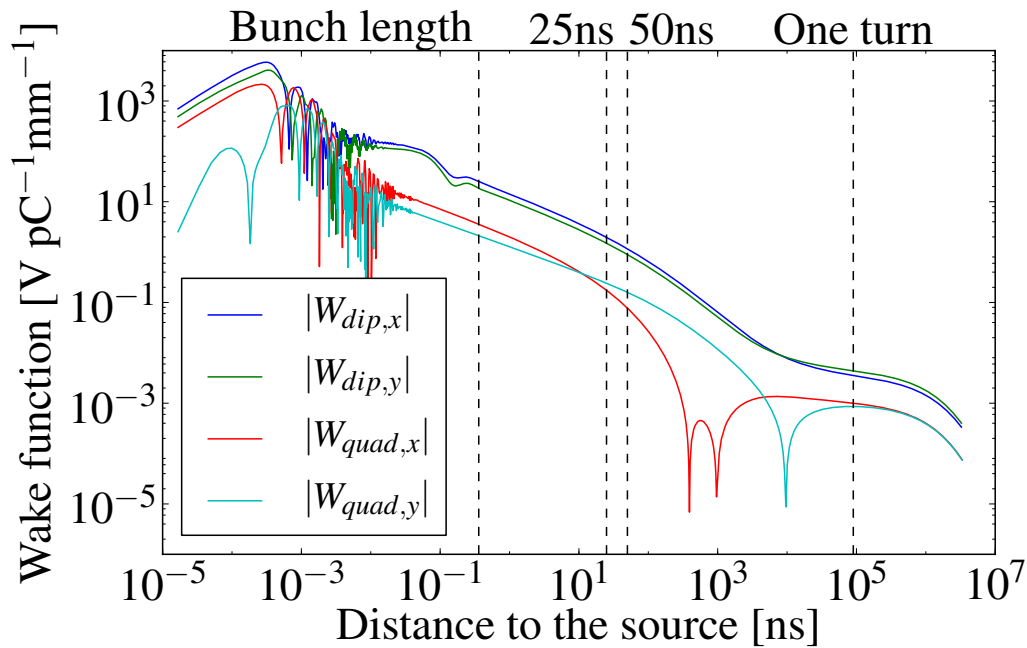


Figure 3.9 – Absolute value of the transverse dipolar and quadrupolar wake functions from the 2012 LHC impedance model of Beam 1 ring [19, 52].

protection considerations [53]. A broadband impedance is also included in order to account for most of the smooth transitions located around the ring. The transverse wake functions resulting from the 2012 model is shown in Fig. 3.9. The wake functions of the other ring, not shown in this figure, are almost equal.

Dedicated measurements were performed in the LHC to validate the impedance model where tune shifts and instability rise times were measured as function of various parameters such as collimator apertures or bunch intensities [54]. Discrepancies of approximately a factor 2-3 were found between the measurements and the model which appears to underestimate the impedance.

4 Landau damping of head-tail modes

Analytical derivations of the stability diagram can be found in simple configurations, e.g. considering linear detuning from octupolar magnets and assuming a Gaussian distribution [22]. In a collider, the amplitude detuning due to BB interactions is usually comparable or larger than the one arising from lattice nonlinearities and therefore has to be taken into account in the computation of the stability diagram. An analytical form of the amplitude detuning can be found for special configurations, usually assuming few interaction points with strong symmetry properties, e.g. in [55]. Facing the complex configuration of multiple BB interactions present in the LHC, a fully numerical approach seems more appropriate. Following the approach developed in [56], we will derive stability diagrams in configurations relevant for the LHC operation, by evaluating the amplitude detuning with single particle tracking simulations and integrate numerically the dispersion integral.

Similarly, considering non-Gaussian distributions rapidly becomes cumbersome [57]. In order to assess discrepancies between models and measurements, we shall investigate the effect of small distortions of the beam distribution function provoked by external excitations, using a numerical integrator that has been developed.

4.1 Numerical method

Whereas difficult to obtain analytically in complex configurations, the detuning is easily obtainable numerically, via particle tracking. The dispersion integral (Eq. 2.60) can then be evaluated by standard numerical techniques. In the relevant cases, the integral has poles, we then solve it numerically by adding a vanishing complex part to the denominator [58] and using trapezoidal integration on an uniform grid [59]. As a result of the finite upper limit in actions the contribution to the stability diagram of the far tails of the distribution is neglected. Considering Gaussian beam profiles, the upper limit was set at 6σ , corresponding to the collimation range in the LHC [53]. Details of the implementation can be found in App. B. As shown in Fig. 4.2, there is a good agreement between the analytical and numerical approach in the case of octupolar detuning (Eq. 4.1) using a Gaussian distribution. In the following, a

Gaussian distribution is always assumed.

In the multi-bunch regime, assuming that all bunches have an identical detuning, the dispersion integral is identical to the single bunch regime. However, in the LHC this assumption is not valid once BB effects are considered. Indeed, the asymmetric layout of the IPs as well as the asymmetric filling scheme lead to a variety of bunches having significantly different detuning, i.e. PACMAN bunches. Theoretical treatment of the beam stability in such a configuration is currently lacking, the possibility to assess these cases using multi-particle tracking simulation is explored in Chap. 5.

Also, the BB interactions do not only introduce bunch dependent detuning, they also change the nature of the coherent modes. The Landau damping of coherent BB modes in the single bunch regime is addressed in [13], the extension to multi-bunch coherent BB mode is, however, not trivial. Studies by the means of multi-particle tracking simulation are also discussed in Chap. 5. Such an approach is well suited to study the LHC in its full complexity. However, it is very demanding in terms of computing resources, which render extended parametric studies difficult. Here, we would like to address a simplified configuration by considering the stability of single bunch modes driven by the beam coupling impedance, yet taking into account detuning from the lattice, as well as BB interactions. Multi-bunch effects from the beam coupling impedance as well as BB coherent modes are neglected. These drastic assumptions are motivated by the observation of single bunch instabilities in the LHC, while operating in the multi-bunch regime. Figure 4.1 shows such an instability at the end of the betatron squeeze during operation of the LHC in 2012. The measurement of the beams oscillation amplitudes provided by the BBQ system indicates a coherent instability on beam 1. The observation of bunch intensities indicates that only one bunch lost its intensity in an abnormal way, with respect to the other bunches, suggesting that this bunch only experienced an instability. This case is not unique since most of the transverse instabilities observed during the operation of the LHC in 2011 and 2012 did not involve the full beam, but rather a single or a small subset of bunches.

4.2 Applications to the LHC operational cycle

4.2.1 Betatron squeeze

The strength of LR interactions mainly depends on the normalised separation between the beams, i.e. the distance between the beams normalised to the beam size, at the location of each interaction (Eq. 3.1). Before the squeeze, the normalised separation in the common area is large, resulting in weak LR interactions. Thus, the amplitude detuning is dominated by the lattice nonlinearities mainly due to octupole magnets meant for that specific purpose [60]. Together with the transverse feedback, they ensure the stability of the beams. They can be powered with up to $I_{\text{oct}} \sim 510$ A, with either polarity, giving rise to a linear amplitude

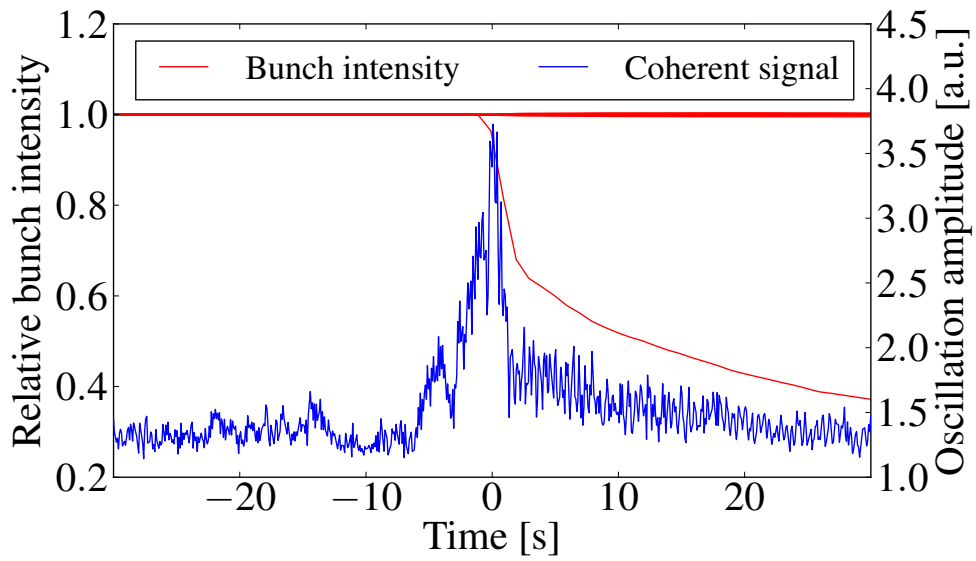


Figure 4.1 – Observation of an instability during luminosity production with 1380 bunches per beam. The beam oscillation amplitude in the horizontal plane of beam 1 (blue) shows a coherent excitation which is correlated with a significant intensity drop of a single bunch, as shown by the measured bunch by bunch intensities (red).

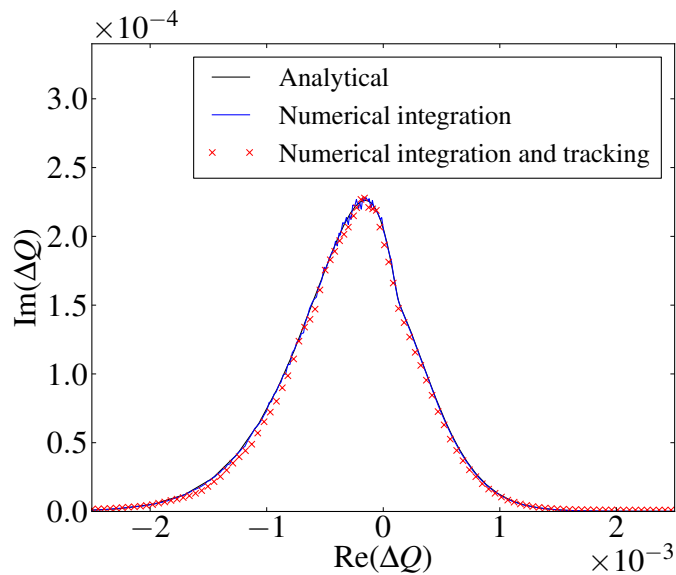


Figure 4.2 – Comparison of the analytical and numerical derivation of a stability diagram with the LHC octupoles powered with -500 A for a 4 TeV beam with a normalised emittance of $2 \mu\text{m}$.

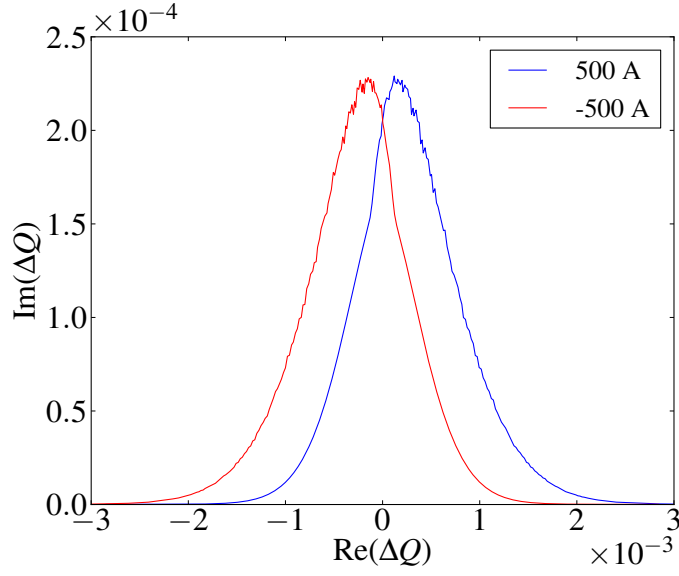


Figure 4.3 – Stability diagrams from octupoles powered with opposite polarities for a 4 TeV beam with a normalised emittance of $2 \mu\text{m}$.

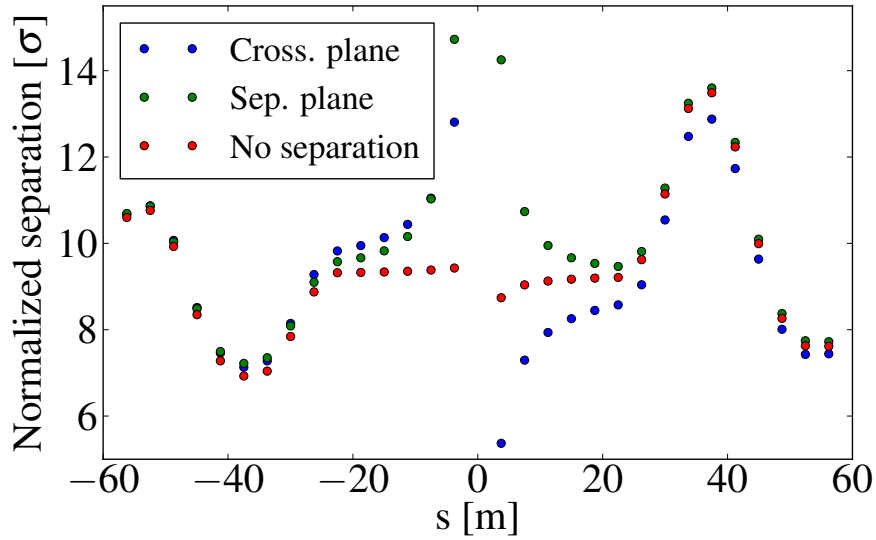
detuning :

$$\begin{cases} \Delta Q_x = a \cdot J_x + b \cdot J_y \\ \Delta Q_y = b \cdot J_x + a \cdot J_y \end{cases} \quad (4.1)$$

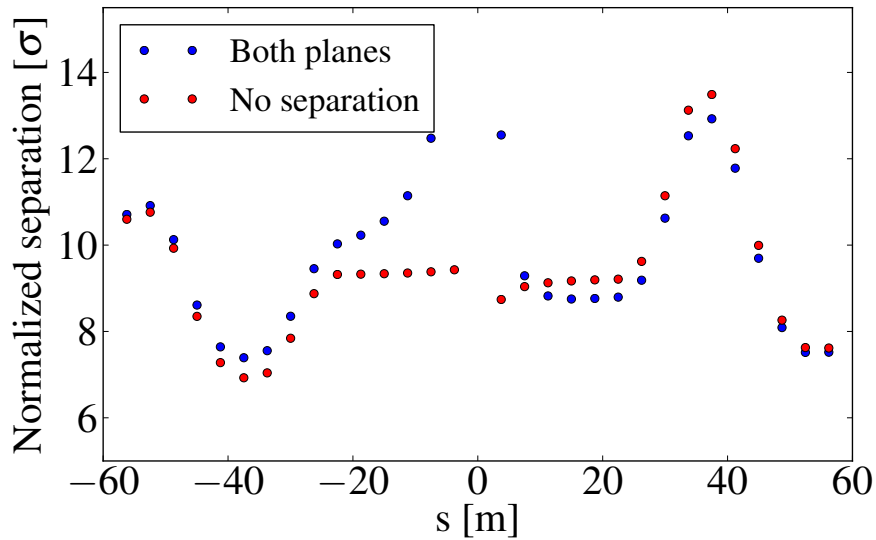
with the detuning coefficient for a beam energy of E_{beam} and a normalised emittance of ϵ :

$$\begin{aligned} a &= 3.28 \cdot \frac{I_{\text{oct}}[\text{A}] \cdot \epsilon[\text{m}]}{E_{\text{beam}}^2[\text{TeV}^2]} \\ b &= -2.32 \cdot \frac{I_{\text{oct}}[\text{A}] \cdot \epsilon[\text{m}]}{E_{\text{beam}}^2[\text{TeV}^2]} \end{aligned} \quad (4.2)$$

The resulting stability diagrams for each polarity are shown in Fig. 4.3. As the expected unstable modes in the LHC have tune shifts with negative real parts [19], the negative polarity is preferable in this configuration [22, 57]. However, going through the squeeze, the effect of the LR interactions starts playing a significant role in the single particle dynamics. As can be seen in Fig. 4.4, at the end of the squeeze, the normalised separation at the location of most of the LR interactions already has the value at which they will remain during luminosity production. The only difference being the parallel separation orbit bump, which affects only the interactions closest to the IP. As discussed in [61], this has a strong impact on the tune



(a) Comparison of the normalised separation between the beams, with a separation either in the crossing plane or in the separation plane.



(b) Comparison of the normalised separation between the beams, with a separation both in the crossing plane and in the separation plane.

Figure 4.4 – Normalised BB separation at the location of the LR interactions in interaction region 5 while the beams are colliding HO at the IP (red). The upper plots shows the comparison with the same configuration where the orbit was modified, resulting in a separation of 1.3 mm in the separation plane at the IP or of 0.4 mm in the crossing angle plane. The combined effect of the separation in both planes, corresponding to the configuration at the end of the squeeze, is shown on the bottom plot.

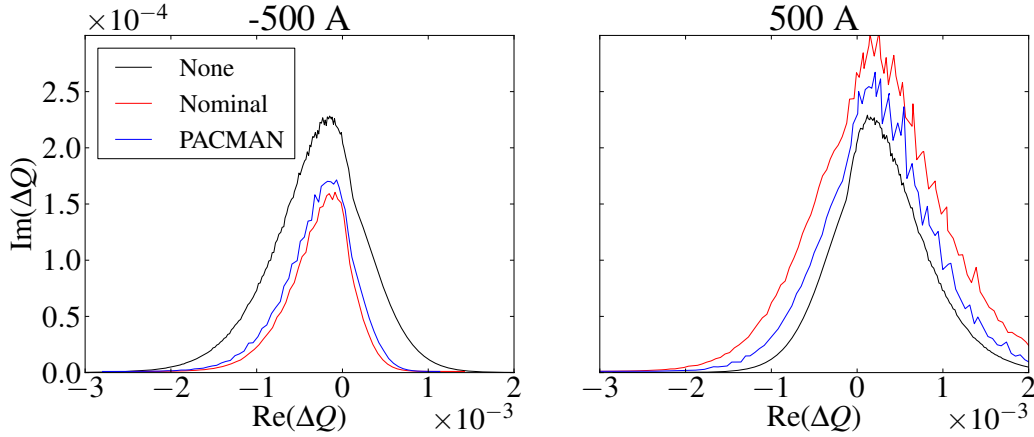


Figure 4.5 – Stability diagrams for both polarities of the octupoles for different LR contributions, corresponding to the configuration before the squeeze (black), after the squeeze, considering a nominal bunch, i.e. largest LR contribution (red) and a PACMAN bunch with least LR contribution (blue).

spread and consequently on the stability diagram. Figure 4.5 shows the modification of the stability diagram during the squeeze for two extreme bunches, one having the maximum number of LRs, referred to as nominal, and one with the least, referred to as PACMAN bunch. With a negative sign of the octupole, the LR contribution is partially compensating the octupoles detuning, resulting in a smaller stability diagram at the end of the squeeze. As a result, nominal bunches have a smaller stability diagram with respect to PACMAN bunches, all bunches being less stable after the squeeze than before. The opposite is true with the positive polarity. Nevertheless, it is important to note that the most unstable bunch is the limitation for the operation of the machine, as the losses generated by a single bunch becoming unstable are capable of triggering the machine protection system of the LHC, and therefore provoke a dump of the beams. Thus, in Fig. 4.6, we compare the smallest stability diagram in both configuration. One observes that, in the negative tune shift part, the stability diagram of PACMAN bunches in the case of $I_{\text{oct}} = 500$ A, is very similar to the nominal one with $I_{\text{oct}} = -500$ A, in the configurations considered. Therefore, one should not expect a significant difference in the stability of the most critical bunches at the end of the squeeze with different polarity of the octupole. This is consistent with observations of instabilities at the end of the squeeze in 2012 with both polarities of the octupole. Nevertheless, there were no dedicated experiment to test this statement and operational data are hardly interpretable, as a single change of polarity was effectuated in standard operation simultaneously to many other critical parameter changes. Observations of instabilities at the end the squeeze in 2012 are discussed further in Sec. 6.1.

The LHC will restart with a larger beam energy of 6.5 to 7 TeV, reducing the effectiveness of the octupoles, while keeping similar LR contributions. The effect of the compensation is therefore more important, with respect to 2012 configuration, resulting in a significantly smaller stability diagram when using the negative polarity of the octupole (Fig. 4.6). As

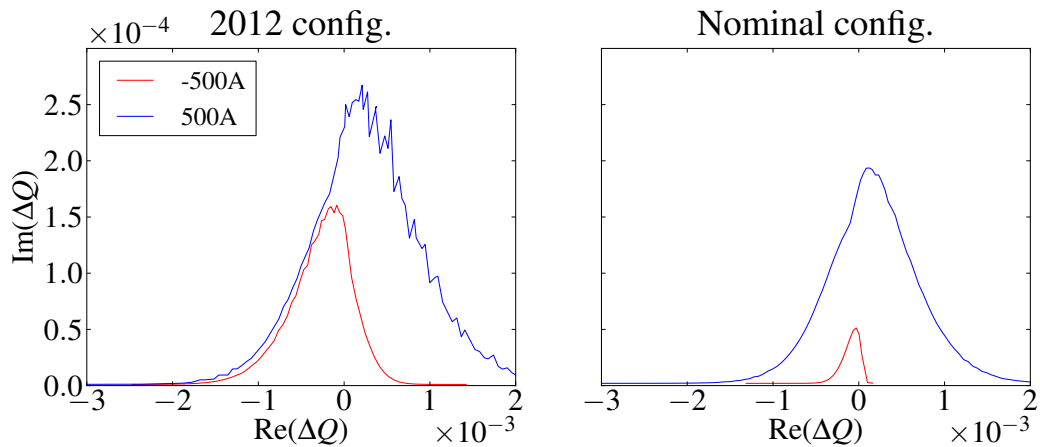


Figure 4.6 – Comparison of the stability diagrams of the most critical bunch at the end of the squeeze with either polarity of the octupoles. With 2012 parameters (Fig. 4.5) (left), the stability diagrams are very similar for negative real tune shifts. With nominal LHC parameters (right), the stability diagram obtained with the negative polarity of the octupoles is significantly more critical.

can be seen in Fig. 4.7, the change from octupole dominated detuning for large normalised separation to a configuration dominated by LR results in a minimum of stability in the case of negative octupole polarity. This minimum appears at different normalised separations depending on the relative effect of the octupoles on the amplitude detuning, which depends on the beam emittance (Eq. 4.2). In configurations with smaller emittances, the effectiveness of the octupole is reduced, while the LR contributions do not change for identical normalised separation. As a result, the minimum of stability will be reached earlier in the squeeze. In such configurations, the positive polarity, while providing a smaller stability diagram before the squeeze, provides a larger stability diagram towards the end of the squeeze and may therefore be preferable (Fig. 4.7).

As will be discussed later, the stability diagram due to HO interactions is significantly larger than the one provided by both LR and octupoles, therefore the considerations above no longer apply if HO collisions are established before the squeeze.

4.2.2 Bringing the beams into collision

Collapsing the separation bump in order to bring the beams into collision at the IP, has two main impacts on the stability diagram. First, as illustrated in Fig. 4.4, the separation at the location of the LR interactions is reduced. As a consequence, their effect on the stability diagram, as described in Sec. 4.2.1, is increased during the process. Secondly, towards the end of the process, the tune shift as well as the amplitude detuning of the colliding bunches change sign as shown by the tune footprint for different normalised separation between the beams at the IP in Fig. 4.8. This last part of the process represents a significant transi-

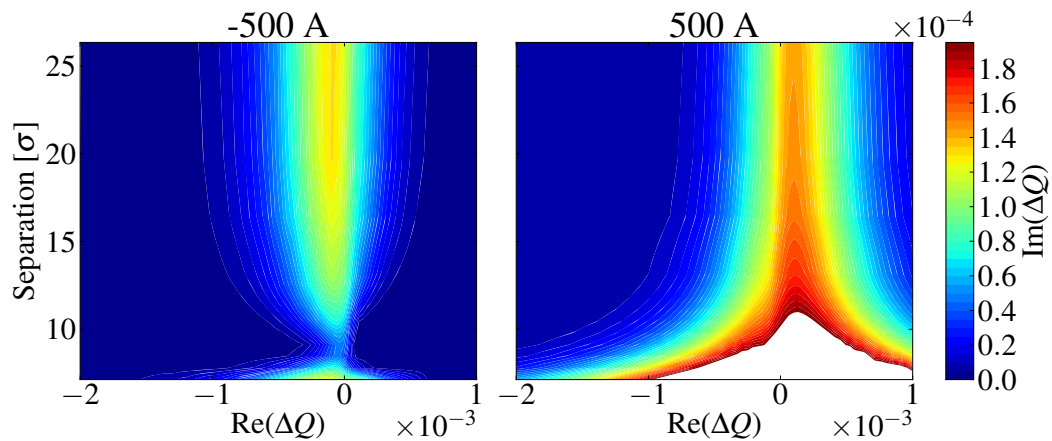


Figure 4.7 – Evolution of the nominal bunch's stability diagram as the normalised separation between the beams is reduced by varying the crossing angle. All other parameters are those of the nominal LHC configuration with negative (left) and positive (right) polarity of the octupoles. The normalised separation in the nominal LHC configuration is 12σ .

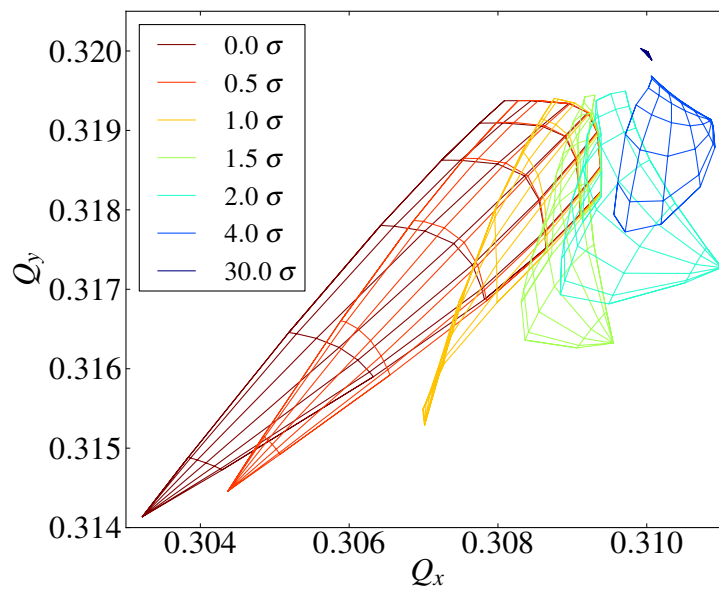


Figure 4.8 – Example of tune footprint of a bunch colliding at IP1 with different separations in the horizontal plane using machine and beam parameters of the 2012 run of the LHC.

tion from a configuration where the single particle dynamics is mainly driven by the lattice nonlinearities and LR interactions, to a regime dominated by the few near HO interactions at the IPs. As shown in Fig. 4.9, the stability diagram is enhanced for separations at the IP in the order of 2 to 4 σ , and then drastically reduced around 1.6 σ , leading to a significant modification of the stability diagram. This minimum of stability depends significantly on the configuration considered and therefore can be different for bunches with different number of LR or HO interactions.

Unlike the interplay between the octupoles and LR interactions, the reduction of the stability diagram for beams colliding with a small transverse offset at the IP is not due to a compensation of the tune spread. It is rather caused by a change of sign of the amplitude detuning, positive when dominated by LR and negative with HO, which leads to a systematic cancellation of nearby poles in the dispersion integral (Eq. 2.60). Even if the minimum of stability exists independently of the polarity of the octupoles, it is clear from Fig. 4.9 that the positive polarity is also favourable in this configuration. Small variations are expected for bunches experiencing different number of LR interactions.

In Fig. 4.9, we considered an ideal process for the collapse of the separation. The separation at the IPs 1 and 5 are collapsed synchronously in the horizontal and vertical plane respectively. In such symmetric configurations, the behaviour of the stability diagram as a function of the separation at the IP is identical in the two transverse planes. Yet, realistic configurations feature an asynchronism of the orbit bumps at the two IPs, as well as a parasitic separation in the plane normal to the separation plane, these effects potentially break the symmetry between the two planes. A symmetric and an asymmetric configuration are compared in Fig. 4.10. In the asymmetric configuration, the minimum of stability in the plane of the separation is similar to the symmetric configuration. While in the other plane, the minimum of stability is much less critical, and slightly asynchronous with respect to the other plane. The dispersion integral that we have used neglects the coupling between the transverse planes. However, when colliding with a small transverse offset, BB interactions introduce strong linear and nonlinear coupling, which may play an important role in the beam stability. We shall illustrate this effect by the means of multi-particle tracking simulations. Coherent BB modes are not considered in the model. Therefore, the BB force is modelled statically, corresponding to the so-called weak-strong model. This multi-particle model features a consistent model of Landau damping with two transverse planes coupled by the beam-beam force. We perform the simulation with the code `BEAMBEAM3D` [62, 63] using a realistic model of the LHC impedance [19]. Figure 4.10 shows a comparison the growth rate of the most unstable mode as a function of the separation in the two configurations. We observe that, in the symmetric configuration, the beams are unstable for small separations, at the minimum of stability, whereas in the case where the symmetry between the planes is broken, the beam is stable for separations below 5 σ . Above this value, the beam is unstable in both configurations, as the tune spread due to the single beam-beam interaction becomes negligible at large separation.

Instabilities were observed when bringing the beams into collision during the first part of

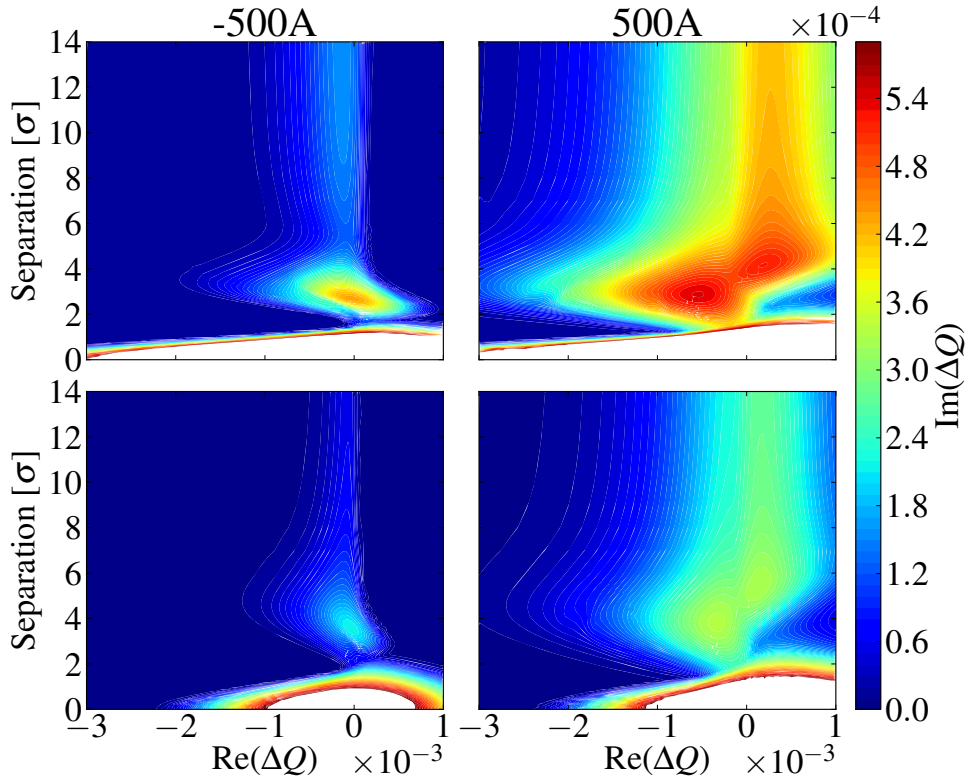


Figure 4.9 – Evolution of the stability diagram as a function of the normalised separation between the beams at the IPs 1 and 5 for the negative (left) and positive (right) polarity of the octupoles. The upper and bottom plots corresponds to the 2012 and nominal configurations.

the year in 2012. The complexity of this process was significantly increased with respect to the previous years, and with respect to the configuration discussed above, as it included a modification of the crossing at IP8 [41]. The length of the overall process was consequently increased. Figure 4.11 shows the separation at the IPs 1 and 5 in both planes during this process, which are to be compared with the histogram of 16 observations of coherent instabilities during this process and to the corresponding stability diagrams. These instabilities were observed with the negative polarity of the octupoles, the effect of LR interactions therefore reduces the stability diagram. Thus, during the first 40 s we observe a reduction of the stability diagram due to the collapse of the separation bumps at the IPs 1 and 5. Except for the two occurrences a few seconds before the end of the process, the instabilities are spread in the intermediate part of the process, during which the stability diagram remains constant. During this period, the separation at the IPs 1 and 5 varies slowly to allow for the crossing angle change at IP8. These instabilities are therefore of the same nature as the ones at the end of the squeeze, i.e. the reduction of the stability diagram is the result of the interplay between the octupoles and the LR interactions. Such an effect is not expected with

the opposite polarity of the octupoles. As for the instabilities observed at the end of the squeeze, the operational data with the positive polarity of the octupoles are hardly comparable, as the chromaticity was significantly different. Also, as this effect being driven by the LR interactions, it is not expected if the beams are brought into collision in a configuration where they are negligible, e.g. before the squeeze.

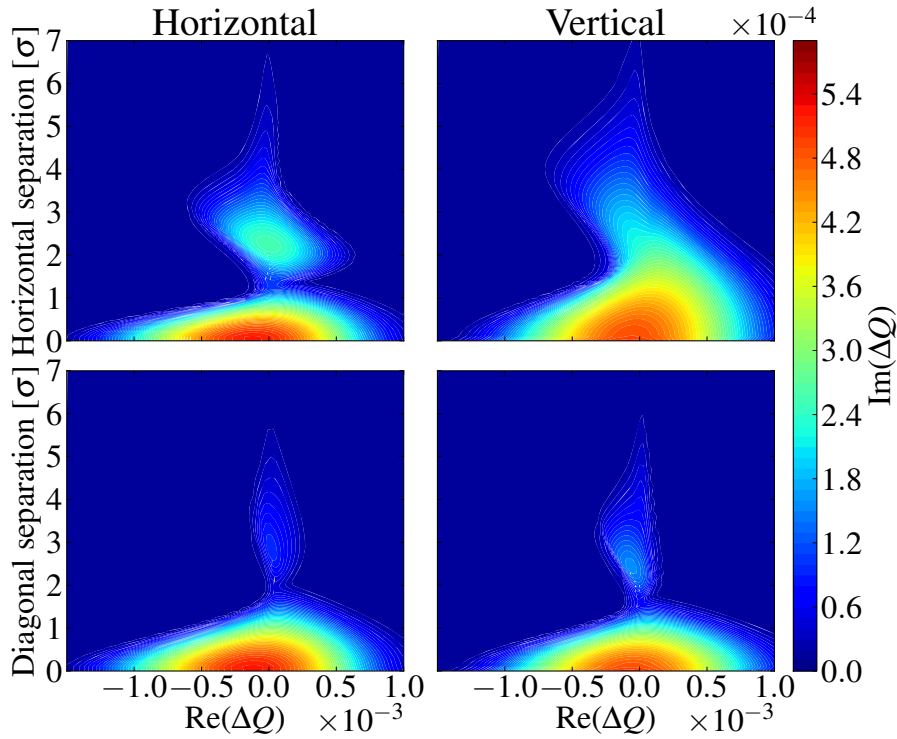
The complication of the process introduced in order to allow for the crossing angle change at IP8 is not strictly necessary. Later in the year the process was reimplemented, separating the collapse of the separation bumps from the change of crossing angle at IP8. This allowed to reduce the duration of the process from 3.6 down to 1.1 minutes. The speed of the process is critical, as a degradation of the beams due to a coherent stability is avoidable by going through critical phases on a shorter time scale. In the LHC, the expected rise times of impedance driven instabilities are typically in the order of a few to several seconds.

For the two instabilities near the end of the process, the separation at the IP can be estimated based on the luminosity measurement. In both cases, the separations at the IPs 1 and 5 are between 1 and 2 σ , corresponding to the minimum of stability described in Fig. 4.9. Nevertheless, as discussed in Sec. 5.2, beams colliding with a small transverse offset may exhibit a strong mode coupling instability, which breaks the assumptions used to derive the dispersion integral (Eq. 2.60). In the configuration considered, the coupling instabilities are expected around a separation of 1.5 σ . The measurement of the beam oscillation amplitude by the BBQ shows activity in both beams simultaneously, suggesting that these instabilities are indeed due to coupling of impedance and BB coherent modes. Nevertheless, the lack of diagnostics capable of measuring the correlation between the two beams prevents to conclude on the exact nature of the instability.

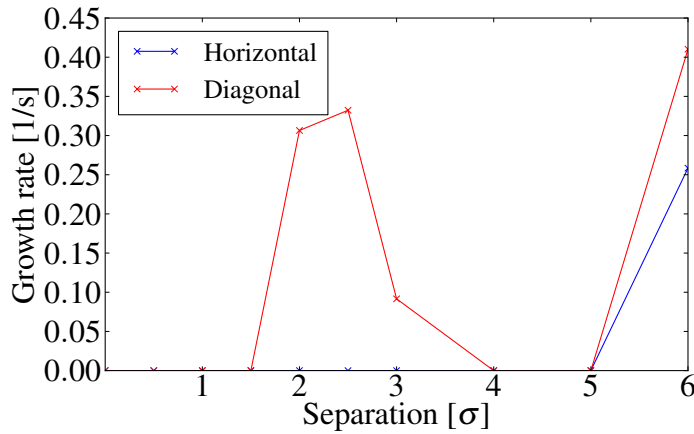
For a significantly different machine, a similar mechanism was invoked to explain beam losses during the same procedure in the Intersecting Storage Rings (ISR) [64].

4.2.3 Luminosity production

While colliding head-on, the BB interactions dominate the nonlinearities experienced by the particles in the core of the beam and consequently provides the dominant contribution to the stability diagram. Figure 4.12 shows a comparison between the tune footprints and resulting stability diagrams generated by octupoles powered with the positive polarity, LR and HO interactions. It is important to note that both the octupoles and LR have a large effect on the particles in the tails of the distribution. Due to the derivative of the distribution function in the nominator of dispersion integral, they yield a smaller stability diagram for a similar detuning. Therefore, the strengths required for the octupoles or LR interactions to obtain a similar stability diagram would lead to an unacceptable reduction of the dynamic aperture [60].



(a) Evolution of the stability diagrams in the horizontal (left) and vertical (right) planes as a function of the normalised separation between the beams at the IP, for a horizontal separation (top) or a diagonal separation (bottom).



(b) Growth rate obtained with weak-strong tracking simulations as a function of the normalised separation between the beams at the IP, for a horizontal or a diagonal separation.

Figure 4.10 – Stability diagrams and growth rates as a function of the separation at IP1, in two configurations. In the first, the separation is in the horizontal plane, in the second on the diagonal, i.e. the separation is equal in the vertical and horizontal plane. The machine and beam parameters are those of 2012, without octupoles.

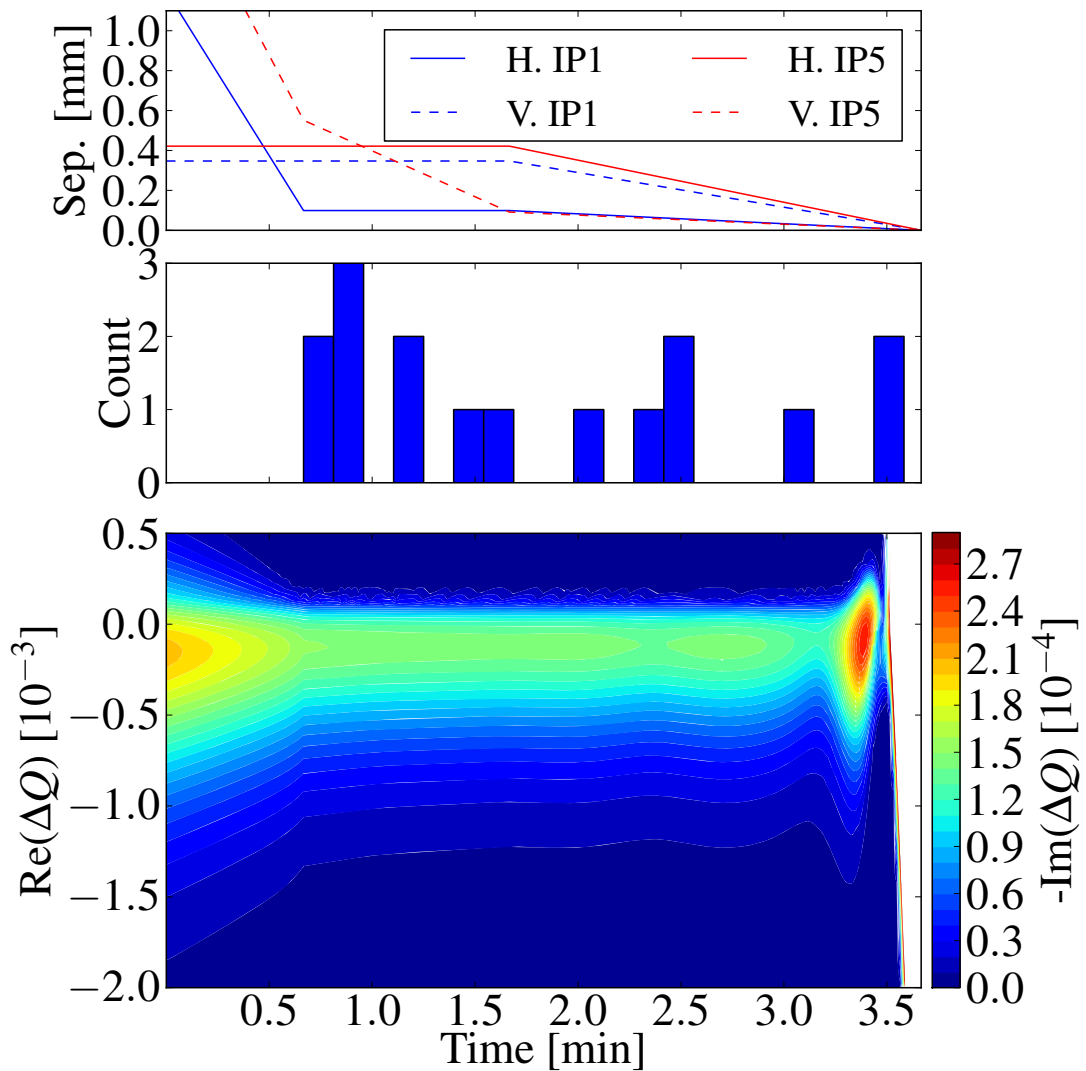


Figure 4.11 – Evolution of the separation between the beams in both planes at the IPs 1 and 5 during the process that brings the beams into collision, as implemented in the LHC in the first part of the 2012 proton run (top). This can be compared to the histogram of the time at which the instabilities were observed during this process in the first part of 2012 (middle) and the corresponding stability diagram of a nominal bunch during the procedure (bottom).

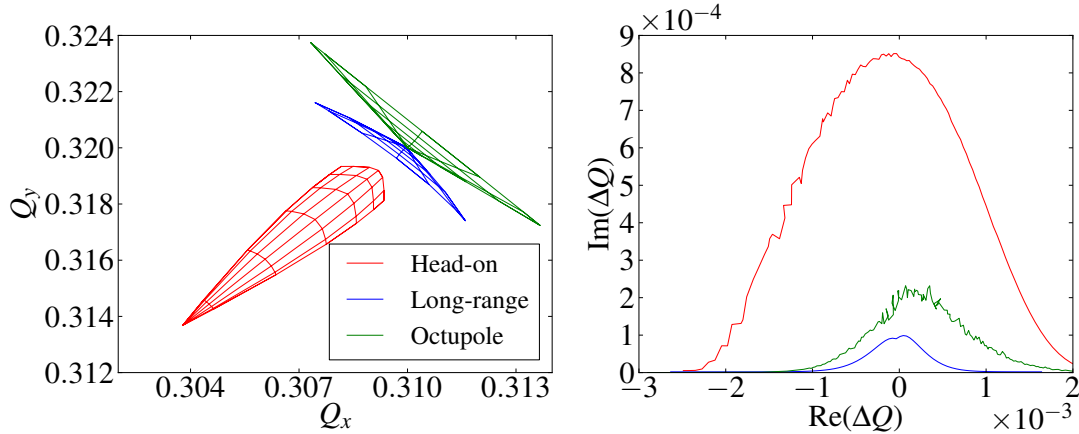


Figure 4.12 – Comparison of footprints (left) and corresponding stability diagrams generated by octupoles powered with 500 A, LR in the interaction regions 1 and 5 or HO at the IPs 1 and 5 (Nominal config.).

The coherent tune shift of most instabilities lies inside the stability diagram provided by HO collisions, therefore stabilisation techniques required before bringing the beams into collision may no longer be required during luminosity production. However, specific requirements of each of the four experiments significantly increase the complexity [29]. The luminosity required at IP2 during proton physics is orders of magnitude lower than in the other experiments, which requires strong luminosity levelling, which leads to vanishing BB forces. IP8 requires weaker luminosity levelling and therefore the HO contribution is not necessarily negligible. During the 2012 run, the luminosity was levelled with a transverse offset at the IP. The beams were therefore colliding HO only in the two high luminosity experiments located at the IPs 1 and 5. As a further complication, the experiments have requested the presence of bunches without HO collision in their detectors, resulting in a series of bunches having no HO collision at all. As already mentioned, the stability of each bunch is crucial, which enforced the use of strong stabilising techniques such as high chromaticity, high transverse feedback gain and high octupole strength, during luminosity production in order to stabilise bunches without HO collisions. While necessary for few bunches, these stabilising techniques are potentially harmful for the intensity lifetime and can cause emittance growth of all bunches. Insuring at least one HO collision for each bunch would allow to relax the needs for stabilisation and therefore allow for luminosity lifetime optimisation.

There exist various ways to achieve this goal, which would fulfil the experiments requests. One of them being the use of luminosity levelling with the β function at IP8. As the tune shift due to HO interaction is nearly independent of the β function at the IP, this technique has the advantage of providing the full HO detuning all along the process of luminosity levelling. Thus, the configuration of bunches may be arranged such that all bunches collide HO at least in one of the three IPs.

4.2.4 Levelling with a transverse offset

During the 2012 run of the LHC, the luminosity was levelled with a transverse offset at IP8. While not harmful for most bunches experiencing HO at the IPs 1 and 5, this technique turned out to be critical for bunches without HO collision in other experiments. The situation of these bunches is similar to the one described in Fig. 4.9. The main difference to the process that brings the beams into collision is the time scale. The separation is varied in small steps and several minutes are spent at each separation, leaving the time for a slow instability to develop. Observations of such instabilities during a fill dedicated to luminosity production are shown in Fig. 4.13. Many bunches undergo an instability at the very beginning of luminosity production, during the adjustment of the orbit at the IPs, while the separation is larger than 3σ . Most bunches lose their intensities in a normal way during five hours of luminosity production but, suddenly lose a significant fraction of their intensity on a time scale of a second, each is accompanied by a coherent signal measured by the BBQ. This device does not, however, measure single bunch oscillations, the measurement of the rise times is therefore not possible.

When comparing the time at which the instabilities occurred with the separation computed from measured luminosities, and combining the data of other similar fills, it appears that the full separation at IP8 at the time of the instabilities were between 0.9 and 1.6σ , consistent with the critical separations discussed previously (Figs. 4.10a and 4.9). It is important to note that the statistics is biased due to the levelling range, which typically started between 2 and 3σ , and, except few exceptions, stopped before 1σ . Nevertheless, the narrowness of the peak suggest that there indeed exists a critical separation around 1.5σ . It is difficult to make quantitative comparison with predications for each individual observation of instability as many critical parameters are not known to a sufficient precision, in particular each bunch emittances. Yet, we may understand the fact that the bunches become unstable at slightly different separation. First, in the configuration of bunches used during these fills, the bunches colliding only at IP8 had each a different number of LR interactions, resulting in slightly different stability diagrams. Secondly, there were bunch to bunch variation of the intensity and emittances in the order of 10%.

4.3 Non-Gaussian distribution functions

In the previous considerations, we have assumed a Gaussian distribution for the beam. Yet, a precise measurement of the beam distribution is difficult to achieve. During standard operation of the LHC, the width of the distribution is measured with an accuracy of the order of 10%, details of the distribution are not known. Dedicated experiments suggest that, while the spacial distribution of the core of the beam seems Gaussian, the tails are likely to be overpopulated [67]. The effect of such a deformation of the distribution was shown to be very important in [57]. Here, we discuss more subtle effects, which, due to the derivative of the distribution function in the nominator of the dispersion integral, lead to a dramatic modification of the stability diagram.

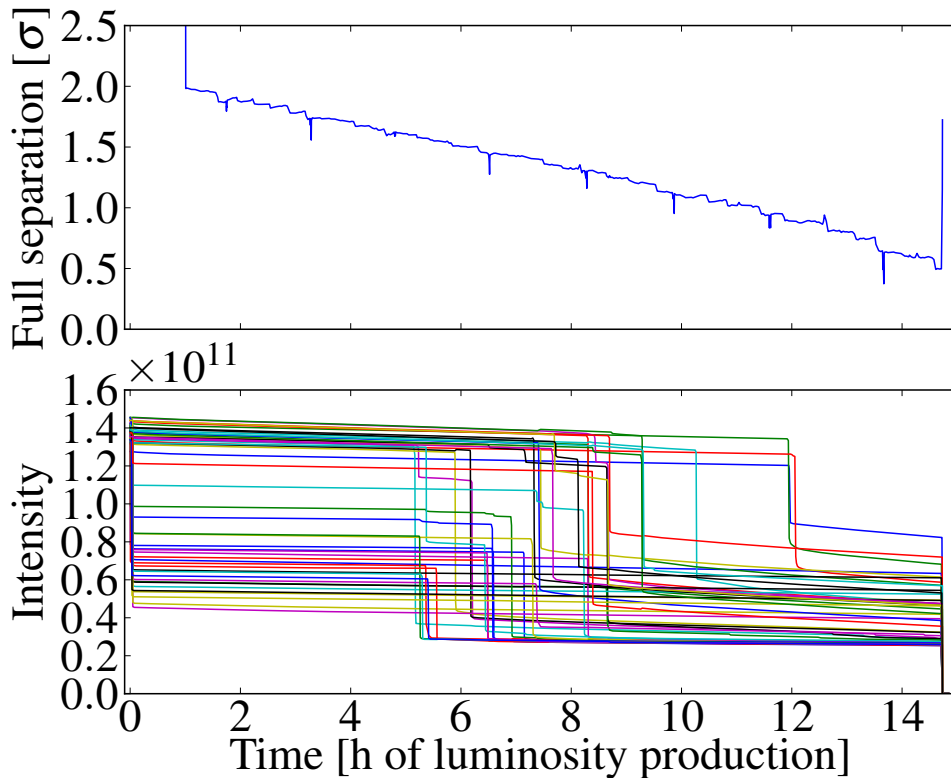


Figure 4.13 – Separation between the beams at the IP during luminosity levelling at IP8, derived from measured luminosity at the IPs 1, 5 and 8 (top), as well as the intensity of the 49 bunches colliding only at IP8, the other 1331 bunches follow a standard quasi-exponential decay (bottom). This measurement took place during the first part of the 2012 proton run of the LHC (Fill 2644).

4.3.1 Distortion due to resonant diffusion

Let us start with a very rough model in order to illustrate the effect under study. Each magnetic element of the machine is subject to variations of their strength in time due to various process, e.g. ground motion or electrical perturbation on the network. Active systems, such as the transverse feedback may also be sources of noise. Let us model all these perturbations by a single source of noise with a defined frequency spectrum. Considering a nonlinear machine, i.e. with finite amplitude detuning, we shall expect that coloured noise will mainly affect resonant particles, therefore creating amplitude dependent diffusion rates. In these condition, the distribution might be affected. The effect of a stochastic perturbation on the distribution function is usually addressed using the Fokker-Planck equation [68]. For later treatment of more complicated systems, we address this problem numerically, using multi-particle tracking simulations with COMBI (App. A). The version of the code used for

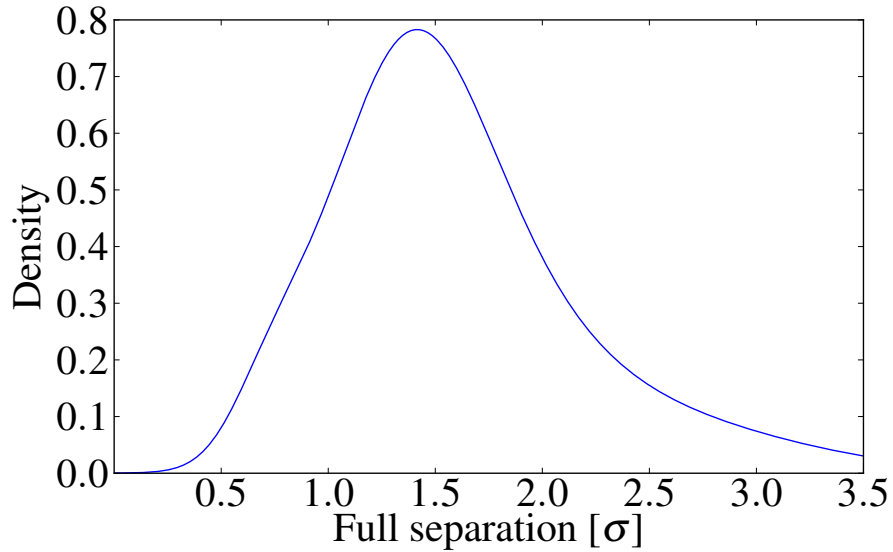


Figure 4.14 – Kernel density estimation [65] of the separation between the beams at the moment of the instability. 30 occurrences are considered with an uncertainty of 24% on the measured separation, accounting for bunch to bunch variations of the emittance (10%) as well as for the error on the β^* at the IPs 1, 5 and 8 [66].

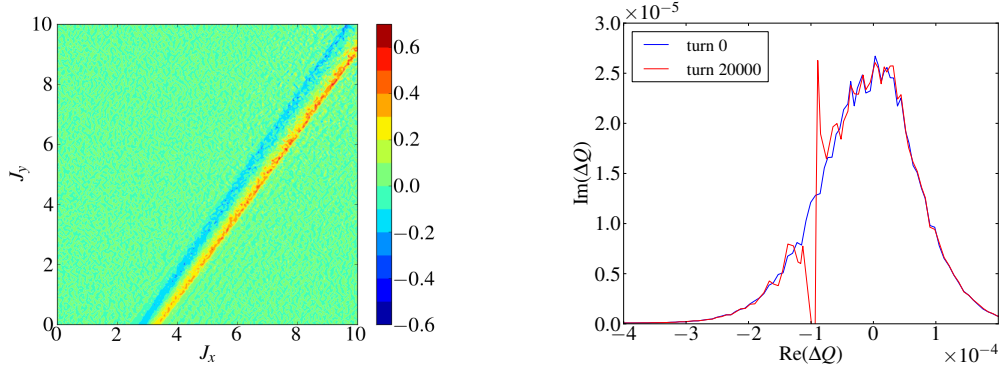
this simulation is a simplified version of the one described in Chap. A, which allows to track uniform macro-particle distributions with weighted charges for a better modelling of the tails of the distribution. Figure 4.15a, shows the relative difference to the initial Gaussian distribution after $2 \cdot 10^4$ turns of simulation of a single beam in the presence of octupole detuning, $a = 1.64 \cdot 10^{-4}$ and $b = -1.16 \cdot 10^{-4}$, and a quasi harmonic excitation of amplitude $10^{-4} \sigma_{x'}$ with the frequency Q_{noise} of the unperturbed tune $+0.05$ and a correlation time of 100 turns.

We observe a depletion of the area around $aJ_x + bJ_y = Q_{\text{noise}}$ and an excess for slightly larger actions, resulting from the enhanced diffusion due to the harmonic perturbation. The effect of this distortion has a large impact on the stability diagram (Fig. 4.15b), as it creates a dip. The distribution in action space is significantly distorted, while the variation of the distribution in physical space is only on the percent level, i.e. well beyond reach with available diagnostics.

Similarly to an external excitation, lattice resonances may also lead to enhanced diffusion for a subset of the phase space and therefore provoke dips in the stability diagram.

4.3.2 Broadband excitation

Let us demonstrate this effect with another simplified model. We consider a single bunch, circulating in the LHC under the influence of the beam coupling impedance, the octupoles,



(a) Relative deviation from the initial distribution in action space

(b) Stability diagram before (blue) and after (red) the distortion of the distribution.

Figure 4.15 – Distortion of the particle distribution due to quasi-harmonic noise obtained with multi-particle tracking simulation. The effect on the stability diagram is evaluated by numerical integration using the simulated distribution as input.

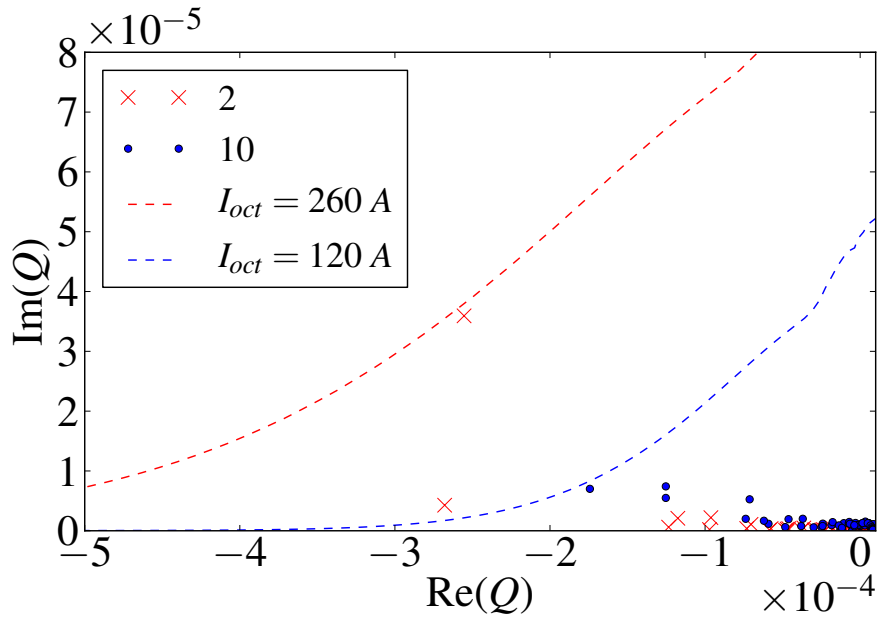
the perfect transverse feedback and an external source of broadband noise. The broadband excitation is modelled as :

$$\Delta x' = \sigma_{x'} R, R \in [-a_n, a_n] \quad (4.3)$$

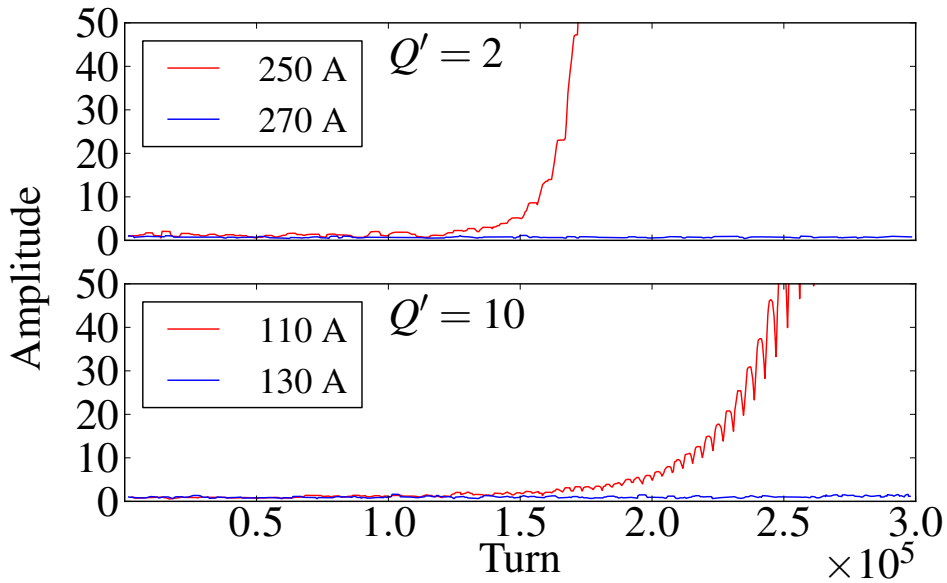
where R is a random variable which changes each turn with a uniform distribution function and a_n is the amplitude of the noise, normalised to $\sigma_{x'}$. The kick is identical for all particles in the bunch. We choose a machine configuration close to operational conditions of the 2012 proton run of the LHC, i.e. large chromaticity (10 units) and larger transverse feedback gain (100 turns). Using the CMM to compute the coherent tunes and comparing them to the stability diagram provided by the octupoles, we obtain Fig. 4.16a. We observe that 120 A are sufficient to stabilise the beams. Doing the same exercise without transverse feedback, we find that 520 A in the octupoles are required to stabilise the beams. The results from the CMM are confirmed by short-term multi-particle tracking with COMBI (Fig. 4.16b).

The tracking code outputs the transverse positions of the longitudinal slices each turn. To interpret this data, we perform a SVD, decomposing the movement in time and spacial singular vectors (Figs. 4.17a and 4.19). Figure 4.17a shows the time evolution of the modes associated with the 3 largest singular values. While they seem stable on the short term, they become unstable after around $1.6 \cdot 10^6$, i.e more than 2 minutes in the LHC. The rise time of the instability is much shorter, $4 \cdot 10^4$ turns according to the fit of the most unstable mode's amplitude, shown in Fig. 4.17b. We clearly observe the presence of two regimes, first a latency at constant amplitude, followed by a strong instability. Later, we shall use the intersection between the linear and the exponential fits to define the latency time.

The reason for the latency is the deformation of the distribution due to the diffusion of

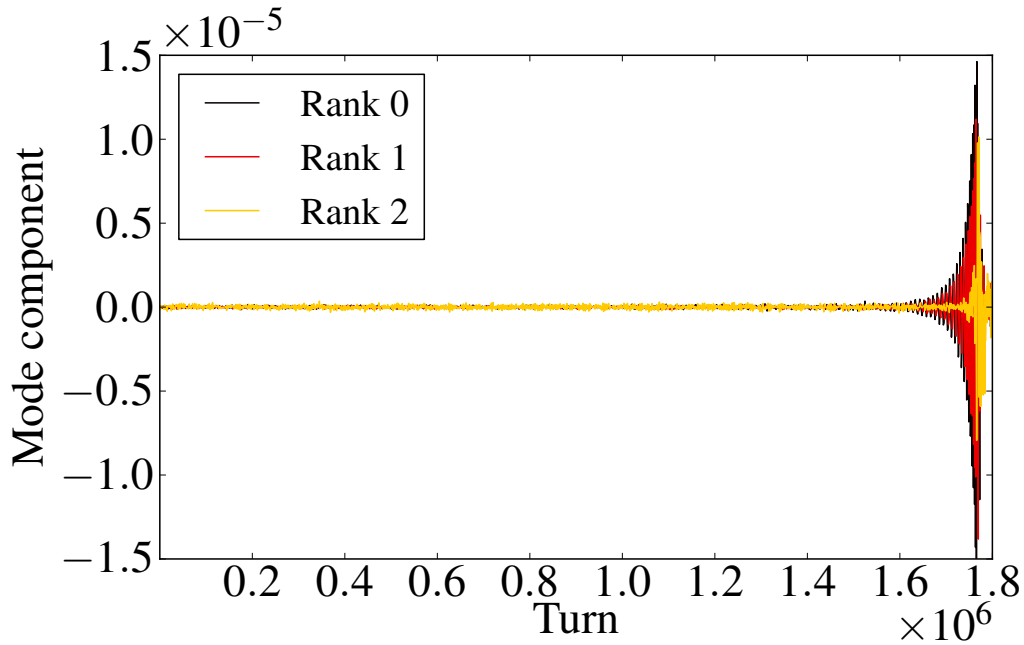


(a) Coherent tunes obtained with the CMM and the stability diagrams corresponding to 260 and 120 A in the octupoles. These are the strength needed to stabilise the beam in the case with a chromaticity of two (red) and 10 (blue) units.

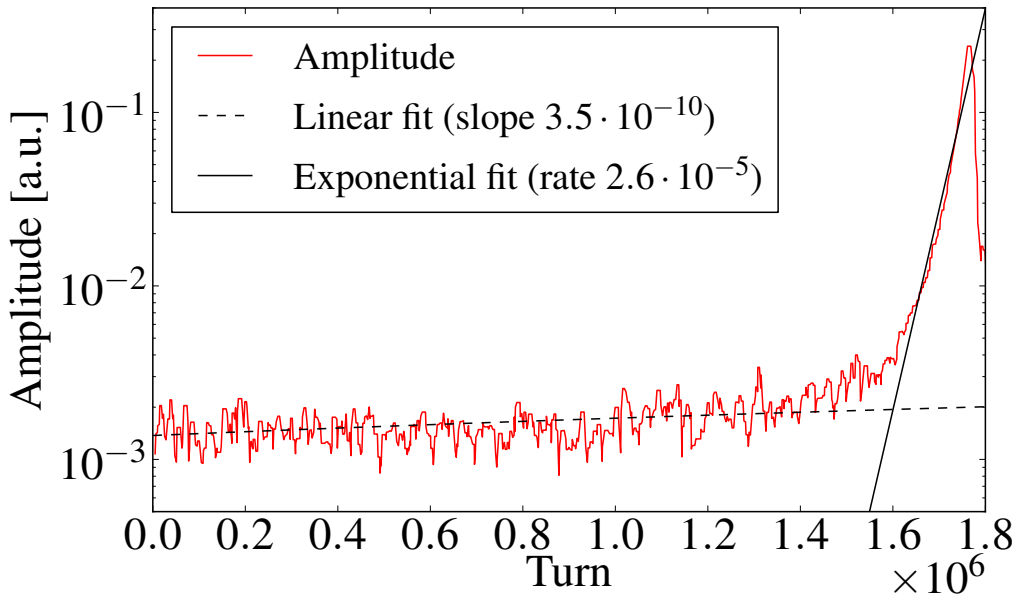


(b) Relative evolution of the amplitude of the time singular vector with the largest singular value obtained from tracking simulation data with COMBI in the case with a chromaticity of two (top) and 10 (bottom) units. The octupole currents are chosen slightly below (red) and slightly above (blue) the stability limit predicted by the linear model in each case (Fig. 4.16a).

Figure 4.16 – Analysis of the strength of the octupoles needed to stabilise the beams in the configuration of the broadband excitation study case, i.e. a single bunch with 2012 parameters and transverse feedback gain corresponding to a damping time of 100 turns.



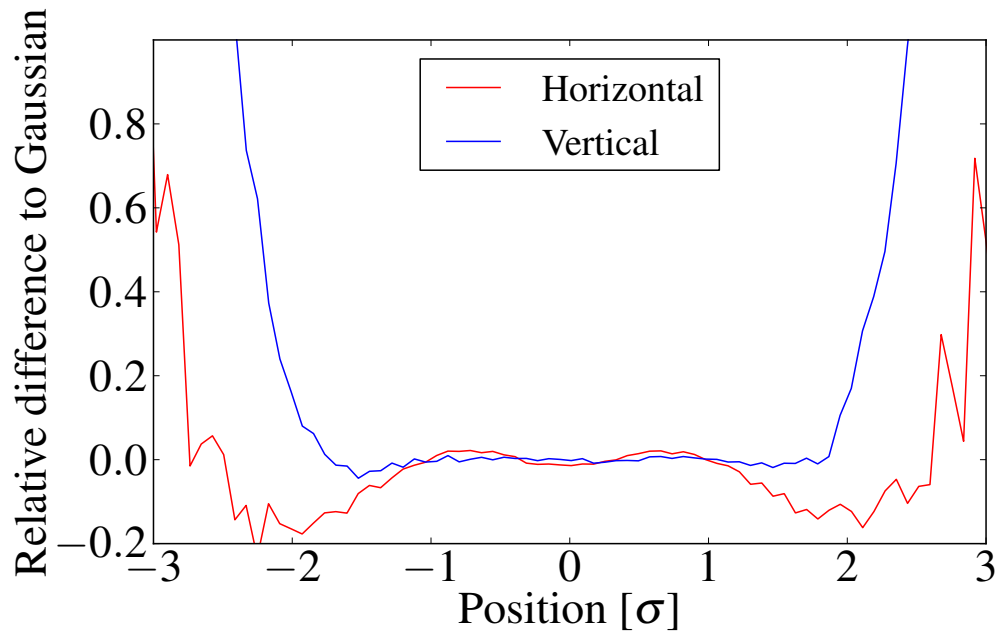
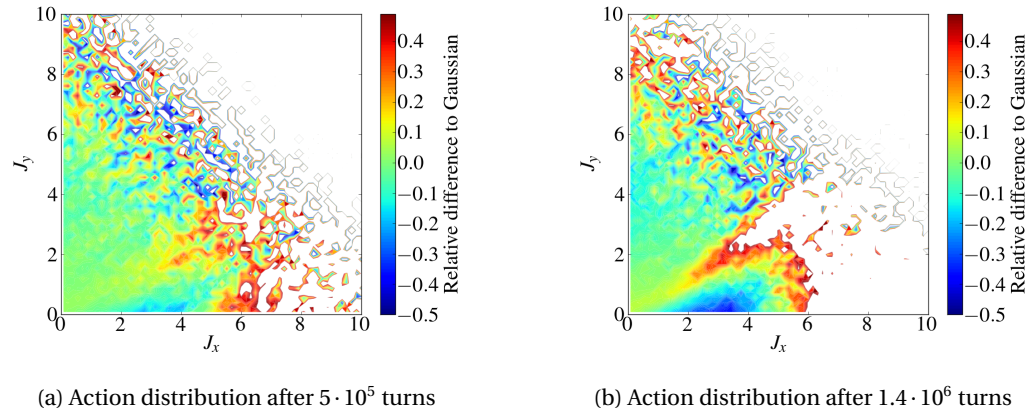
(a) Time singular vector corresponding to the three largest singular values



(b) Amplitude of the mode with largest singular value.

Figure 4.17 – Time evolution of the most unstable modes, obtained from multi-particle tracking with COMBI, for a single bunch with 2012 parameters, a chromaticity of 10 units and a transverse feedback gain corresponding to 100 turns damping time. The octupoles are powered with 300 A, more than the 120 A required for short term stability. The beam experiences a broadband excitation of amplitude $2 \cdot 10^{-3} \sigma_{x'}$.

4.3. Non-Gaussian distribution functions



(c) Real space projections (after $1.4 \cdot 10^6$ turns)

Figure 4.18 – Deviation from the initial Gaussian distribution in the middle and towards the end of the latency (Fig. 4.17) in action space and the corresponding projection in real space.

particles. While the external noise applied is broadband, the response of the beam is peaked around the coherent frequencies. The response of the beam is kept under control by the transverse feedback, yet the beams oscillates with a finite amplitude, which in the presence of amplitude detuning necessarily leads to diffusion, most critical for particles resonating with the coherent modes. Figures 4.18a and 4.18b show the relative difference to the initial Gaussian distribution in action space at different time in the simulation. We observe a progressive depletion of part of the action space. These simulations were performed with the regular version of COMBI, which does not allow for uniform distribution of macro-particles. As a consequence, the number of macro-particles with actions larger than 9 is small, resulting in high noise in the tail of the distribution provided as output. This prevents the numerical derivation of a stability diagram based on that output with a sufficiently low noise, as done in previous section. Yet, the observation of exponentially growing modes after a large latency is a clear indication that one mode, or more, crossed the stability limit.

The distribution in action spaces seems extremely distorted towards the end of the latency. Unfortunately, this quantity is not observable, only the projections in real space are measurable, at least with the available diagnostics. The deviation to a Gaussian distribution in real space are shown in Fig. 4.18c. The deformations of the core are in the percent level, below the accuracy of available diagnostics. The large relative deviations in the tail are difficult to measure. Due to the finite dynamic range, the signal in transverse profile diagnostics is dominated by the strong signal of the core.

The main observable is the beam oscillation amplitude. As shown by the spacial singular vectors, the coherent motion is dominated by modes with significant head-tail components, for which both the transverse feedback and the BBQ are hardly sensitive. We therefore have to compare the measured data with the oscillation amplitude of the bunch centroid position. During the latency, we have an oscillation amplitude of $0.6\sqrt{\beta_{\text{pickup}}}\mu m$, where β_{pickup} is the β function at the position of the pickup in m , which is in the same order of magnitude as the observed residual beam oscillation measured by the BBQ [69]. Further comparison with observations are discussed in Sec. 6.1.

Simulations of the latency are extremely demanding in terms of computing resources. In order to properly model Landau damping and minimise the numerical noise, one needs a significant amount of macro particles, in the following we used $2 \cdot 10^6$ per bunch. Also, the modification of the distribution due to diffusion is a slow process. The simulations are ran for 10^7 turns, i.e. about 15 minutes in the LHC for about a week of simulation time. The following simulations are simplistic and neglect important effect of the lattice or other sources of noise. Quantitative evaluation of the latency are therefore not possible. Nevertheless, we study the relative behaviour of the latency under variations of critical parameters.

For a chromaticity of 2 units, 260 A in the octupoles are required in order to stabilise the beam on a short time scale (Fig. 4.16a). However, as observe in Fig. 4.20, a noise of amplitude $10^{-3}\sigma_{x'}$ is sufficient to destabilise the beam after around 10^6 turns, even with a current of 600 A in the octupoles. Similarly for a chromaticity of 10 units, octupole currents larger than

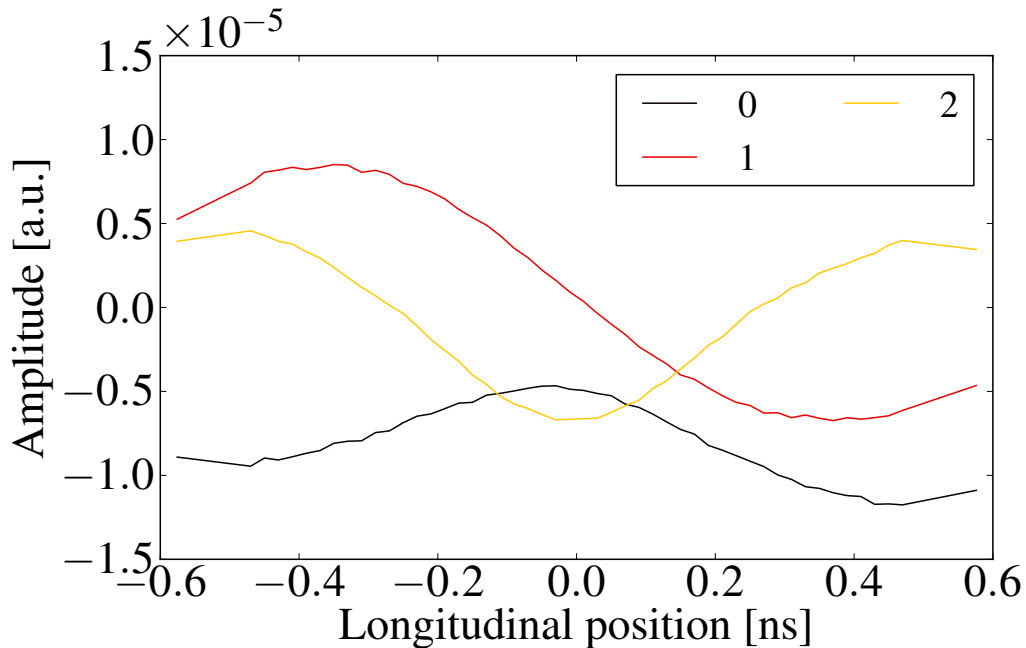


Figure 4.19 – Spatial singular vectors associated to the 3 largest singular values during the latency (Fig. 4.17).

the one required for short term stability, i.e. > 120 A, are not sufficient to stabilise the beam on the long term, in the presence of external noise.

The behaviour of the latency for different octupole current (Fig. 4.20) is in qualitative agreement with a diffusive model. Indeed, in such a model one would expect that the latency increases when the modes deeper inside the stability diagram. This is consistent, as the latency increases with the current in the octupoles in the two configurations. Also, the octupoles powered with the negative polarity provide stronger Landau damping for the impedance driven modes expected in the LHC. As a consequence, the latency is significantly larger for -500 A compared to 500 A.

4.4 Conclusion

A numerical integrator was used to compute the dispersion integral using amplitude detuning evaluated with single particle tracking simulations. This method allows to derive the stability diagram for different operational phases of the LHC, including lattice nonlinearities as well as its full complexity of BB interactions. It was shown that, the stability diagram is significantly affected by the increase of the strength of LR interactions during the betatron squeeze. Depending on the interplay with the lattice nonlinearities, the stability diagram may be reduced leading to instabilities due to a loss of Landau damping towards the end of the squeeze.

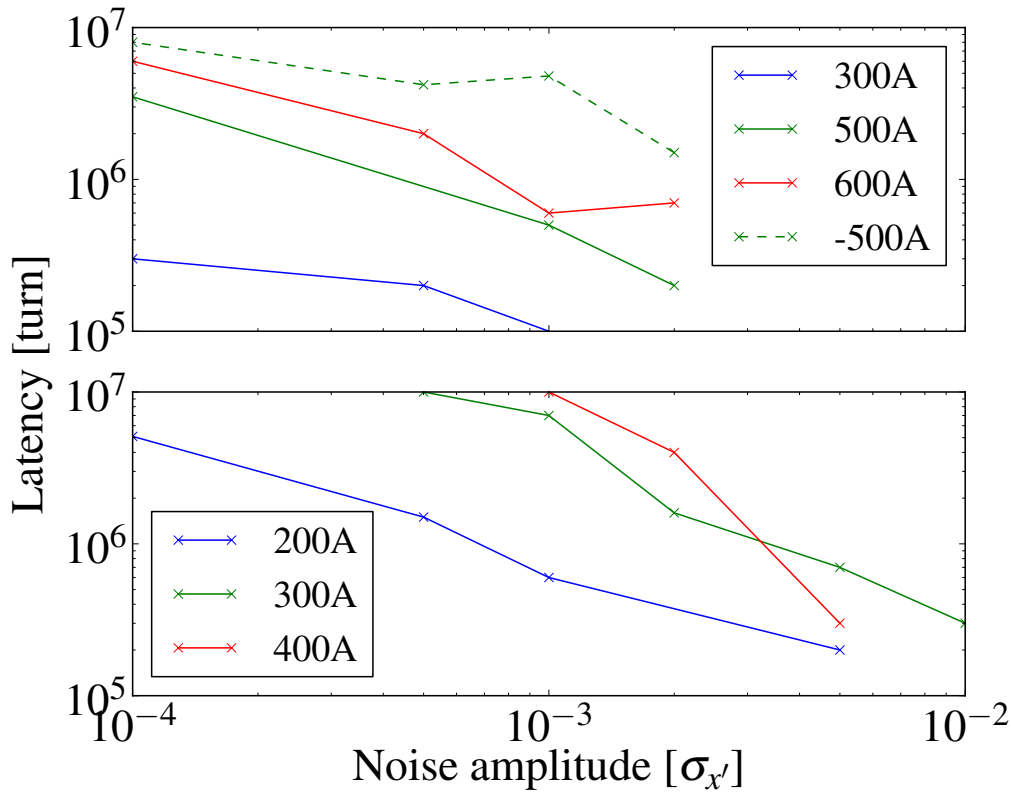


Figure 4.20 – Dependency of the latency, for a single bunch with 2012 machine and beam parameters, on the noise amplitude, for different octupole strength with a chromaticity of 2 units (top) and 10 units (bottom). We recall that in these configurations 260 A and 120 A are required for the short term stability of the beam (Fig. 4.16a).

The stability was shown to be critical with beams colliding with a small transverse offset, in accordance with observations made when bringing the beams into collision and when levelling luminosity with a transverse offset. While avoidable by bringing the beams into collision as fast as possible, this kind of instability is difficult to control when levelling luminosity, which enforce the usage of other stabilising techniques.

Also, it was shown that HO collisions, acting on core particles rather than tails, are very efficient to provide Landau damping.

The stability diagram is very sensitive to the exact beam distribution and therefore may lead to inaccurate predictions in cases where the real beam distribution is not Gaussian. It is shown that loss mechanisms can strongly affect the distribution and therefore the stability diagram. This effect was illustrated by introducing external noise in multi-particle tracking simulations, including the beam coupling impedance. It was shown that the interplay between the two effects can compromise the long term stability of the beam.

5 Coherent Dynamic

In this chapter, we compare models and measurements of coherent modes in the LHC, in the presence of both the BB interactions and the beam coupling impedance.

5.1 Coherent motion without impedance

BB interactions alone do not lead to unstable coherent motion, our main observables in this case are the frequencies of the modes. Also, coherent BB modes are characterized by a correlation between the motion of the two beams, which is a measurable quantity.

5.1.1 Observations

In dedicated experiments

A series of experiments were performed with a single bunch per beam, at injection energy (450 GeV), to probe the maximum BB tune shift achievable in the LHC [70, 71]. In this configuration, the BBQ system is capable to provide the positions of the bunch turn by turn. This allows not only to derive the coherent frequencies, but also to check the correlation between the motion of the two beams. Figure 5.1 shows a spectrogram derived from the BBQ data during one of these experiments. We observe a line at the unperturbed tune $Q_\nu = 0.32$, which is slightly drifting with time. At $t = 0$, the beams are separated and the unperturbed tune is the main frequency component of the beam, other weaker lines are instrumental. Just before $t = 10$ min, the beams are brought into collision at IP1, another frequency component appears slightly below 0.31. Again, just after $t = 35$ min, the beams are brought in collision at IP5, shifting the new frequency component to ≈ 0.303 . A SVD of the BBQ data at two different times, marked by t_1 and t_2 in Fig. 5.1 are shown in Fig. 5.2 and compared to multi-particle tracking simulations using measured beam parameters as input. Not only the frequencies of the modes observed match the self-consistent simulations, but also the oscillations of the two beams are clearly correlated, in the expected in/out of phase manner. A similar

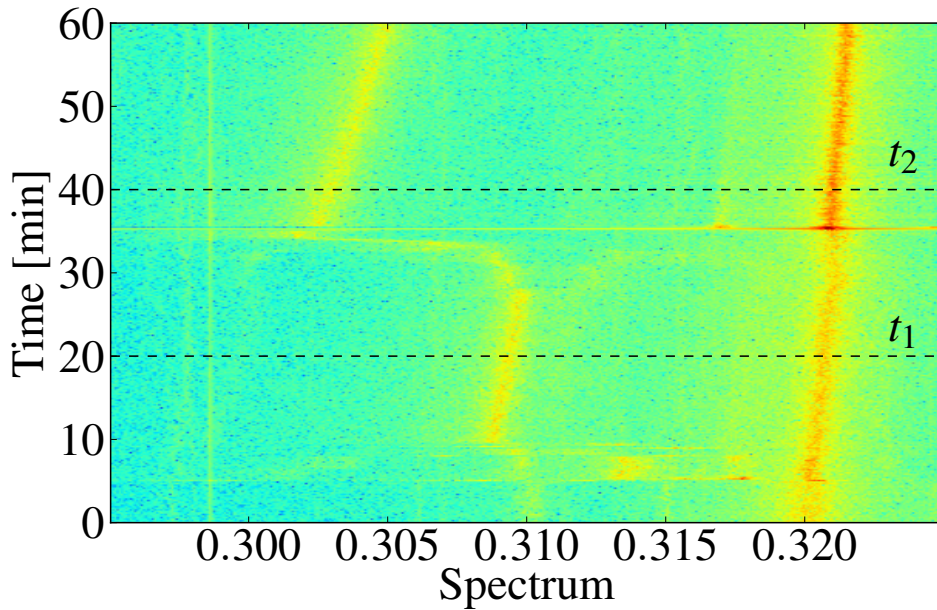


Figure 5.1 – Spectrogram in the vertical plane of beam 1, measured by the BBQ, during an experiment aiming at probing high BB parameters.

behaviour was observed in all experiments performed in similar conditions.

Another set of experiments with high brightness beams, aiming at providing the highest luminosity per bunch crossing, were performed with a few bunches at 4 TeV [72, 73]. The BBQ is not capable to provide turn by turn measurements of the position of each bunch, it is not possible to perform the SVD analysis as previously with this data. The pickups used by the transverse feedback can provide such data. Yet, the acquisition buffer limits the number of consecutive turns measurable and the sensitivity of these pickups is lower than the BBQ's. Also, the transverse feedback was, as opposed to previous experiments, kept on, reducing the coherent signals from the beams. For these reasons, no coherent BB modes were measured in these experiments.

During luminosity production

The configuration during luminosity production is very complex, all 1374 bunches are coupled together via, either HO or LR interactions in the four interaction regions. Consequently, there exists a variety of modes, with different frequencies, most of them laying inside the incoherent spectrum [74]. Also, the transverse feedback is always kept on during luminosity production, which prevents the observation of any coherent mode. For these reasons, no BB

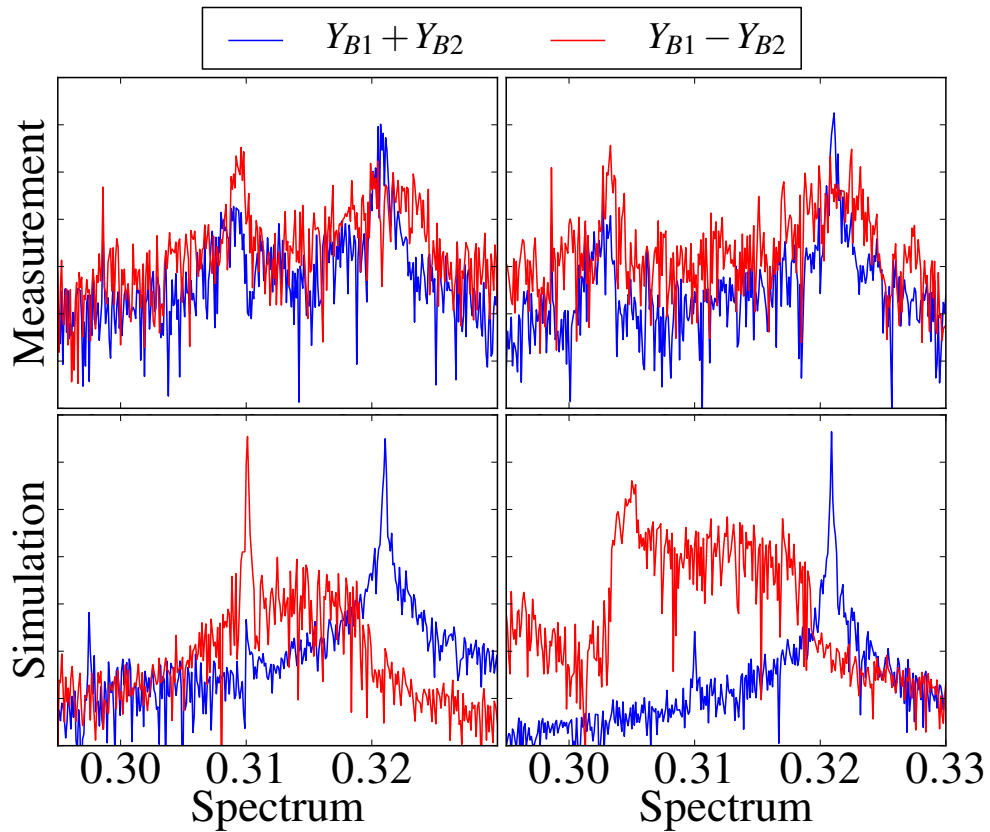


Figure 5.2 – The SVD of turn by turn data of both measurement and simulation gives two singular vectors corresponding to the addition (blue) and subtraction (red) of the data of both beams. The spectrum associated to the time singular vectors are plotted. The two column corresponds to the time defined in Fig. 5.1, i.e. for which the beams are colliding at one or two IPs. The upper plots show measurement from the BBQ and the lower plots results from self-consistent tracking with COMBI using measured intensities and emittances as input.

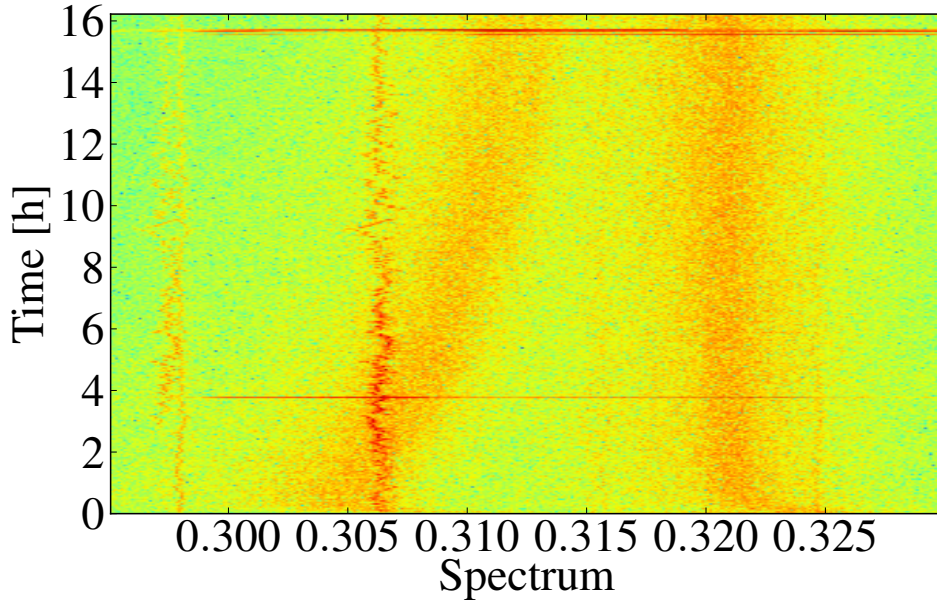


Figure 5.3 – Spectrogram in the vertical plane of beam 1, from measured BBQ data, during luminosity production. The blurred line at ~ 0.321 is the machine tune Q_v , the sharp lines at ~ 0.307 and ~ 0.298 are noise lines and the blurred line starting ~ 0.305 and moving towards the machine tune is consistent with $Q_v - \xi$, ξ being the BB parameter of the most common bunch, which decays during the fill with the beam brightness.

coherent modes have been observed during luminosity production. Nevertheless, as shown by Fig. 5.3, there are lines in the BBQ signal at frequencies consistent with both incoherent or coherent motion due to the BB interactions. However, without further diagnostics, it is not possible to distinguish between the two.

Looking again at the experiment dedicated to HO collisions of high brightness beams, towards the end of the experiment, we observe the signal of the coherent mode growing exponentially with time, a typical signature of a coherent instability (Fig. 5.4). This mode was previously demonstrated to be a π -mode (Sec. 5.1.1). The beams stabilize themselves naturally at the expense of large intensity losses and emittance growth. The frequency of the mode after the instability reflects the reduction of the BB parameter due to reduced beam brightness. The BB modes are not self-excited, there should be a driving force behind such an instability. This experiment was, however, not dedicated to the measurement of instabilities, consequently the attention was not focused on certain parameters which are critical for the beam stability, in particular the chromaticity. It is therefore difficult to make quantitative comparison with models. Also, the experiment was performed at injection energy, for which the impedance model is poorly known [19]. Yet, as demonstrated in Sec. 4.2.3, the stability diagram in such conditions is very large, such that any impedance driven mode should be stabilised. This suggests that the stability diagram, being derived from a dispersion integral

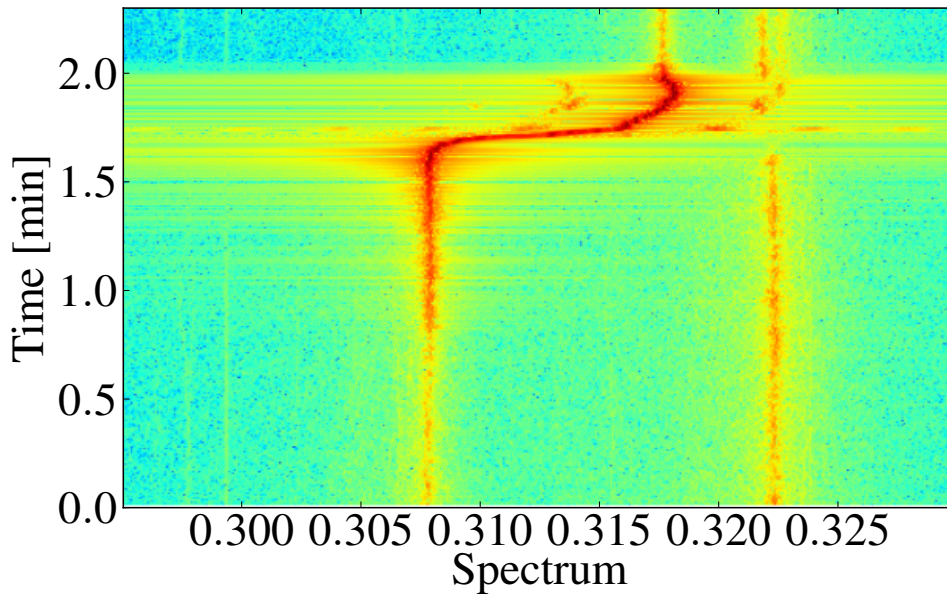


Figure 5.4 – Unstable π -mode observed during a dedicated experiment aiming at probing large HO BB parameter at injection energy with one high brightness bunch per beam colliding it the IPs 1 and 5.

that neglects the coherent contribution of BB, is not sufficient to explain such an instability.

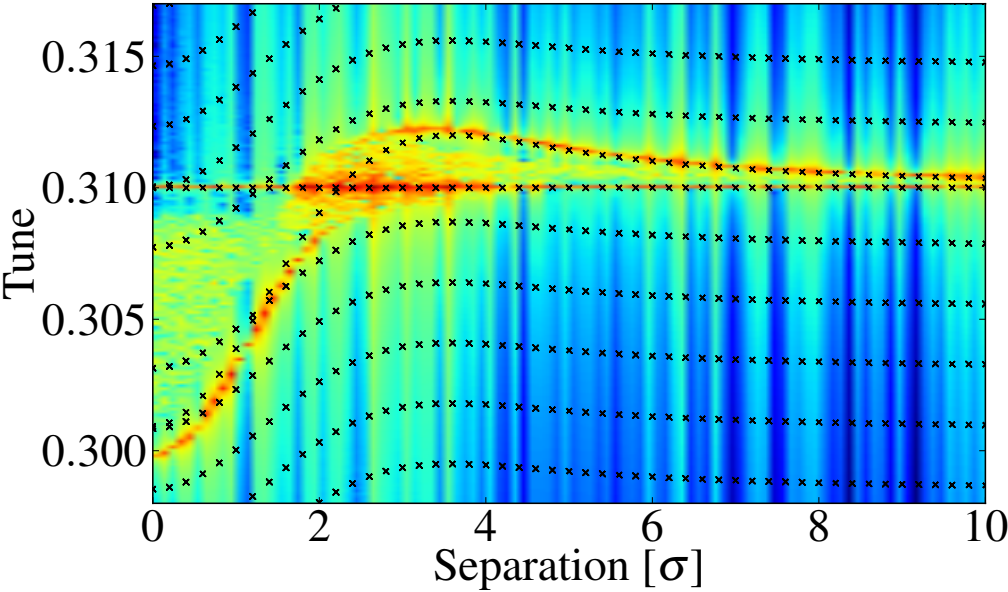
5.2 Coherent motion with impedance

5.2.1 Simulations

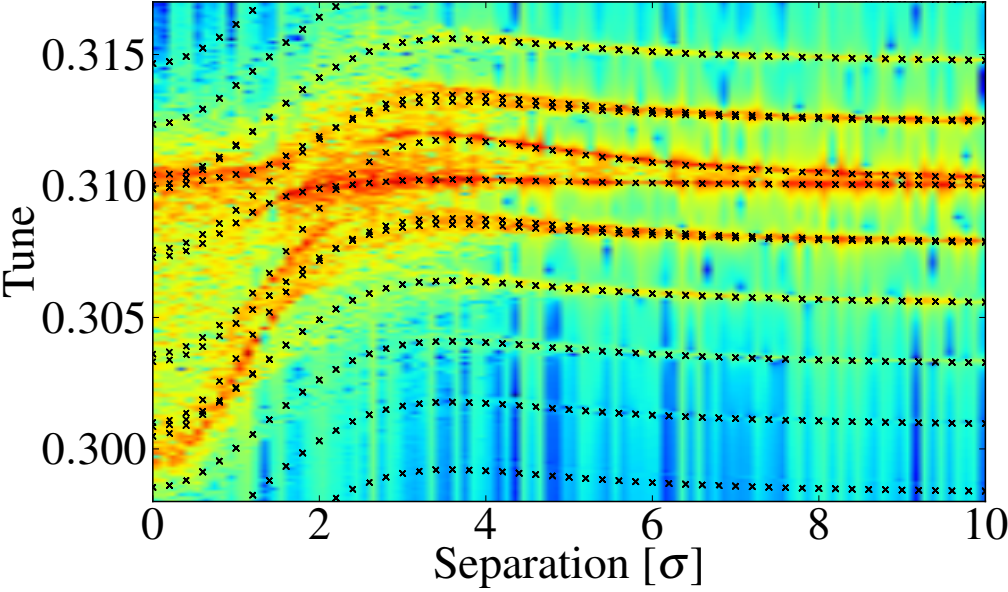
The following section relates work done in collaboration with S. White (Brookhaven National Laboratory). Some of the multi-particle tracking simulations are performed with the code BEAMBEAM3D [63], which uses the same physics model as COMBI, but is based on a different parallelisation paradigm. While COMBI is optimized for simulations with a large number of bunches, BEAMBEAM3D is optimized for fast computation of the full 6D BB kick and is therefore better suited to study synchro-betatron effects.

Benchmarking the codes

We will use the code BIMBIM (App. C), an implementation of the CMM, as well as COMBI and BEAMBEAM3D, two different implementations for multi-particle tracking. The field solvers used to compute the BB force of both multi-particle tracking codes have already been

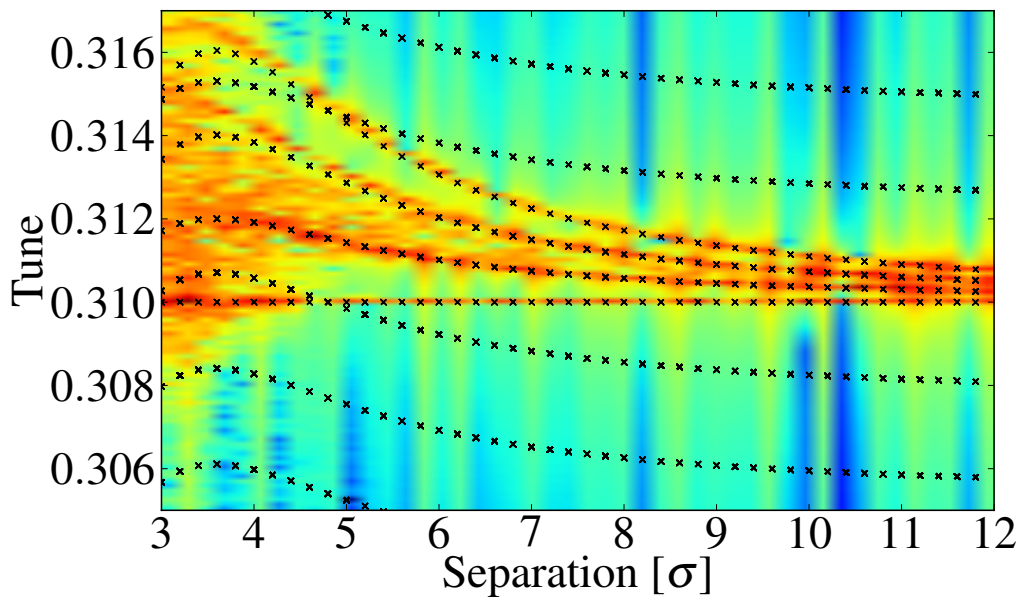


(a) Chromaticity of 0 unit

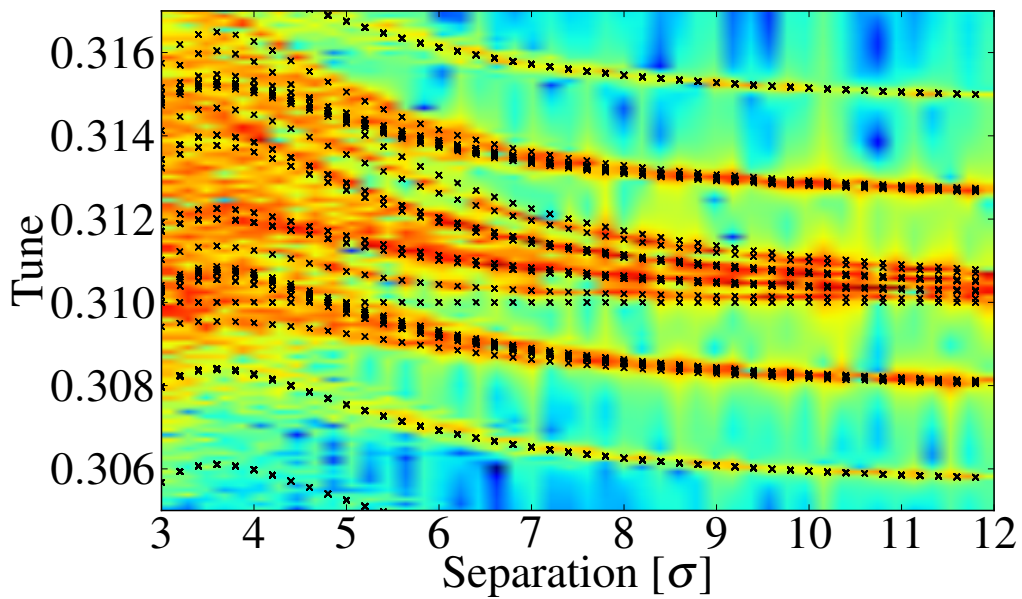


(b) Chromaticity of 10 units

Figure 5.5 – Evolution of the coherent frequencies for two bunches colliding at one single IP, as a function of the normalised separation between the beams at the IP for a chromaticity of zero (top) and 10 units (bottom). The plots show the comparison between simulations with COMBI (spectrogram) and BIMBIM (crosses).



(a) Chromaticity of 0 unit



(b) Chromaticity of 10 units

Figure 5.6 – Evolution of the coherent frequencies as a function of the normalised separation between the beams, obtained with COMBI (spectrogram) and BIMBIM (crosses). There are four bunches per beam, colliding at 4 IPs with identical separation with a chromaticity of zero unit (top) and 10 units (bottom).

benchmarked in [74] and [63]. The CMM is based on a linearised BB force and a transversally rigid bunch, BIMBIM could therefore be successfully benchmarked against exact analytical formulas. Yet, Figs. 5.5 and 5.6 emphasize the difference between the tracking simulations and the linearised model. We observe that, as expected, for separations larger than $\approx 6 \sigma$, the two models are in good agreement. For smaller separations, the Yokoya factor deviates from 1.

It is important to note that tracking simulations yield moments of the 6D distributions at a Poincaré section, whereas the spectrograms of Figs. 5.5 and 5.6 are based on the Fast Fourier Transform (FFT) of the transverse dipolar moment. Thus many modes without dipolar component are visible in the linearised model, but not in tracking simulation. In order to see higher-order head-tail modes, one may increase the chromaticity, in order to enhance their dipolar component (Figs. 5.5b and 5.6b). Certain modes are also not visible in tracking simulations, especially for small separations, as they are subject to Landau damping arising from the nonlinearity of the BB forces.

The impedance modules have recently been implemented in all these codes, we therefore make use of yet another multi-particle tracking code, HEADTAIL [75], which is well established for simulations of impedance driven instabilities. Figure 5.7 shows the comparison of growth rates obtained with HEADTAIL, COMBI and BIMBIM, we observe a very good agreement between the models. Let us note that, as impedance forces are linearised in the tracking simulations as well as in CMM, it is expected to obtain identical results. This is also confirmed by simulation of the TMCI, shown in Fig. 5.8.

In the multi-bunch regime, COMBI and HEADTAIL agree very well, as illustrated in Fig. 5.9, whereas a significant discrepancy exists with BIMBIM. This discrepancy is the result of the normal mode analysis in BIMBIM which does not describe properly a system that is actually non-normal. Indeed, the normal mode analysis gives an eigenspace which is not a complete basis for the one turn matrix. The kernel of this basis are non-normal modes, which are not described by the normal mode analysis. Thus, we study the behaviour of vectors in the kernel under powers of the one turn matrix and compare it to the behaviour of the eigenvectors. Let us consider the case of a train of 16 bunches, for which the normal mode analysis underestimates the growth rates by a factor 4, with respect to tracking simulations. In Figure 5.10a, we plot the amplitude of a mode described by the vector \underline{x} under powers of M , the one turn matrix defined by :

$$\|M^t \cdot \underline{x}\| \tag{5.1}$$

where t is the number of turns. We observe that the amplitude of the normal modes follows an exponential growth with a rate given by normal mode analysis. Yet, the non-normal modes develop much faster, with a behaviour different from an exponential. As shown by Fig. 5.10b, non-normal modes of the matrix given by BIMBIM exhibit a behaviour similar to tracking simulations with COMBI.

While the multi-bunch implementation of the different codes seems to agree very well, it

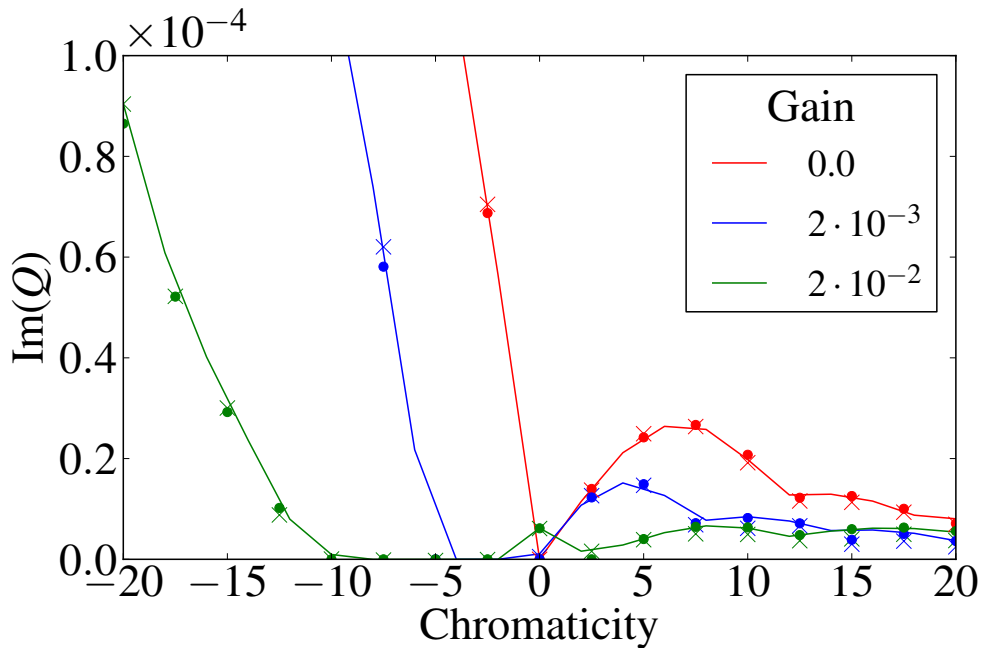


Figure 5.7 – Imaginary tune shift of the most unstable mode for a single bunch with typical 2012 LHC parameters as a function of the chromaticity, without transverse feedback (red) and for two different transverse feedback gains corresponding to a damping time of 1000 turns (blue) and 100 turns (green). The solid lines, crosses and dots represents results of BIMBIM, COMBI and HEADTAIL respectively.

appears that special care has to be taken when using normal mode analysis on such system. This topic is further discussed in Sec. 5.2.2.

Single bunch regime

Figure 5.11 shows the coherent frequencies as a function of the BB parameter considering a single bunch per beam colliding at a single IP and keeping constant the effect of the beam coupling impedance. As the π -mode approaches the head-tail mode $n_a = -1$ ($\xi \approx 0.003$), the coupling of the two modes leads to strong instabilities with similar rise times and characteristics to the impedance driven TMCI. This is observed both in the tracking and in the CMM with comparable rise times.

As shown in Fig. 5.11b, the CMM also indicates a coupling between the σ -mode and head-tail mode $n_a = +1$. This is not observed in the tracking simulations. However, the CMM does not include nonlinear effects and hence, Landau damping. It was shown in [13, 76] that in the presence of synchro-betatron coupling the coherent BB modes could be damped by the sidebands of the incoherent tune spread. The frequency of the sidebands is approximately given by $Q_\beta + m Q_s - \xi/2$, where $\xi/2$ is the coherent tune shift due to the BB force and m

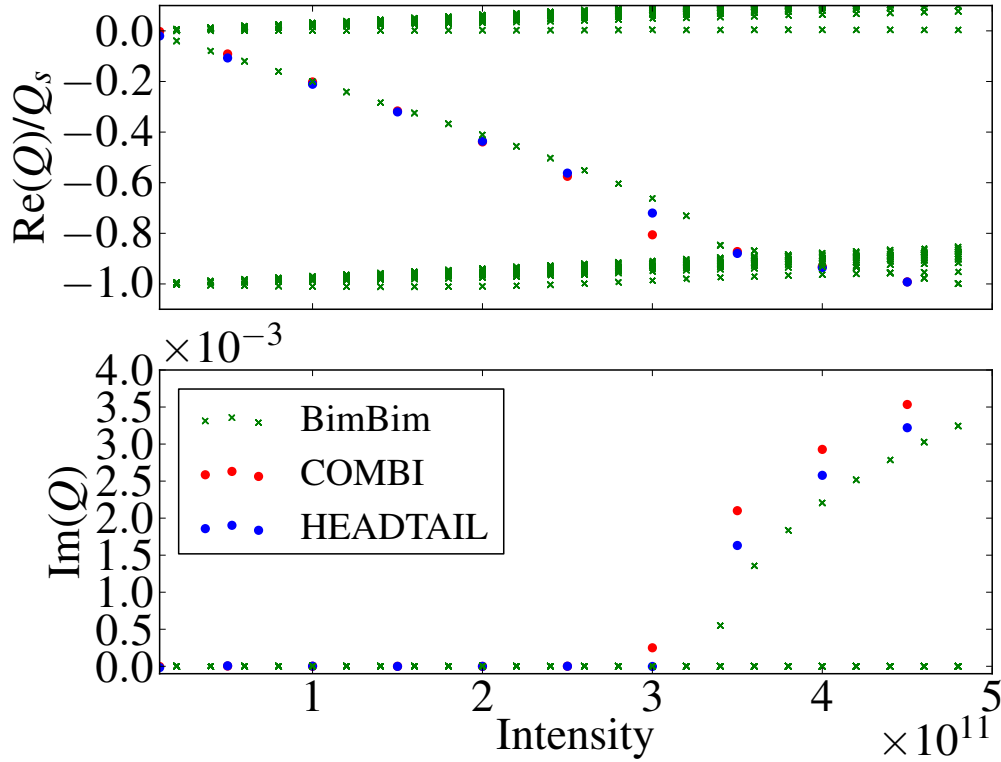


Figure 5.8 – Simulation of the TMCI threshold, i.e. zero chromaticity and no transverse feedback, with the different codes for identical machine and beam parameters. The real part of the coherent tunes normalised to the synchrotron tune, Q_s , (top) as well as the imaginary part (bottom) are in agreement and the instability threshold is found for an intensity slightly above $3 \cdot 10^{11}$ p per bunch in all codes.

is the order of the sideband. The incoherent tune spread extends from Q_β to $Q_\beta - \xi$ and its sidebands are centred around the frequencies $Q_\beta + m Q_s - \xi/2$, one would therefore think that when a coherent BB mode approaches a low order synchrotron sideband it would experience Landau damping. Nevertheless, the efficiency of the Landau damping depends on the particles frequency distribution around the frequency of the mode to be damped. The BB tune spread is not uniform and most of the particles oscillate at frequencies lower than its central value while very few particles are located above. The coupling between the σ -mode and head-tail mode $n_a = +1$ occurs with the mode $n_a = +1$ going down towards the σ -mode providing very efficient Landau damping, while it is the opposite for the coupling between the π -mode and head-tail mode $n_a = -1$ for which Landau damping will therefore be very ineffective. This provides a possible explanation for discrepancies observed between the tracking and CMM results and why the coupling between the π -mode and head-tail

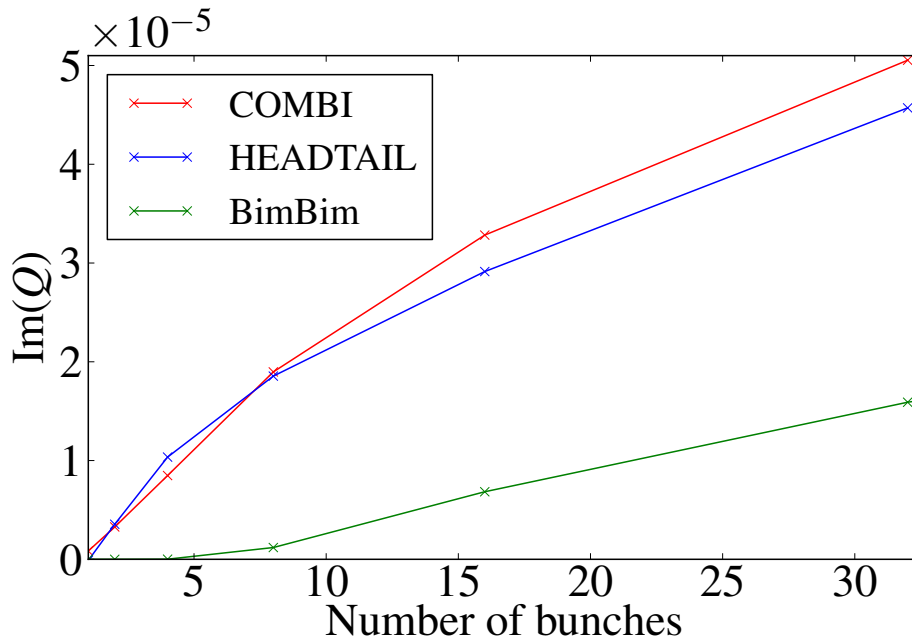


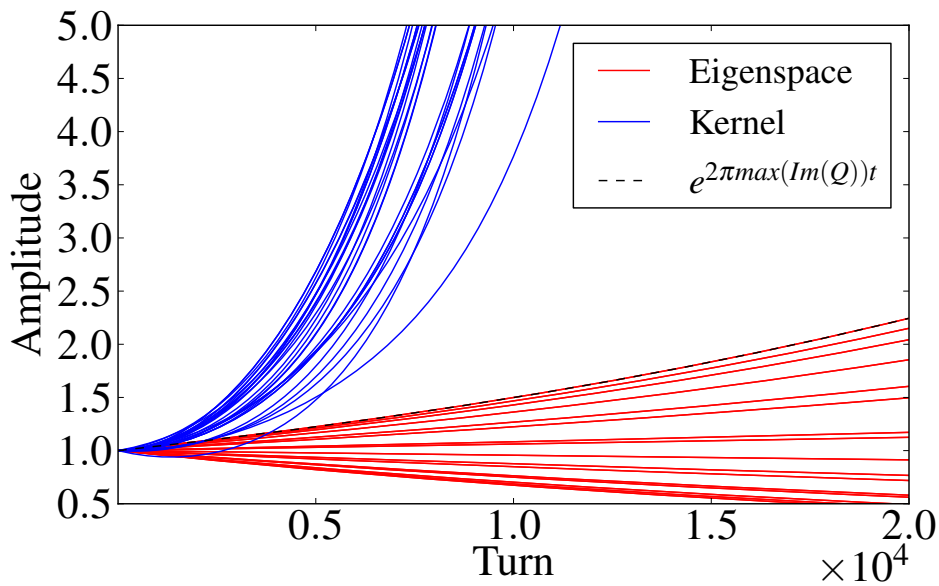
Figure 5.9 – Imaginary tune shift of the most unstable mode for a train of bunches of different size obtained with different codes. The machine and beam parameters are those of the LHC 2012 run with a chromaticity of zero unit and without transverse feedback.

mode $n_a = -1$ appears to be much stronger in the case of HO interactions.

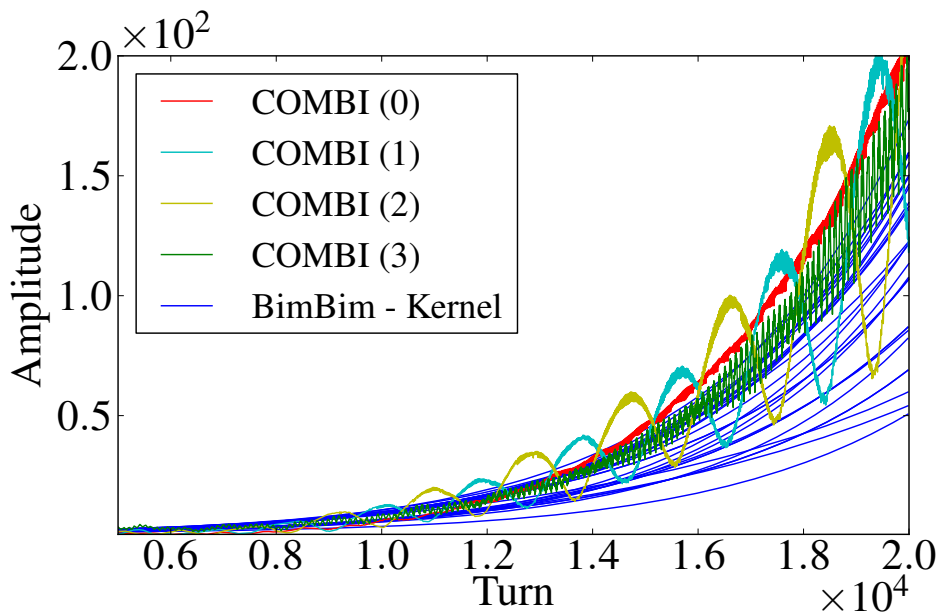
In the LHC, the HO tune shift is much larger than the synchrotron frequency, the mode coupling instability is therefore not a concern when colliding HO. Yet, while bringing the beams into collision, as well as while levelling the luminosity with a transverse offset at the IP, the tune shift due to BB strongly varies, possibly leading to similar effects. Indeed, Fig. 5.12 illustrates a scan of the separation including coherent BB effects and impedance at zero chromaticity and no transverse feedback. The mode coupling instability is observed when either the π -mode overlaps the head-tail mode $n_a = -1$ or the σ -mode overlaps the head-tail mode $n_a = +1$ at separations between 1.0 and 2.0σ . This is also the location at which the BB tune spread reaches a minimum (Sec. 4.2.2), explaining the absence of Landau damping, as opposed to the case of HO collision discussed above.

Multi-bunch regime

In the LHC, for 25 ns bunch spacing, individual bunches can experience up to 32 LR interactions per interaction regions, where the separation between the two beams is approximately 10σ . In some cases, the accumulated tune shifts from these interactions can become larger than the synchrotron frequency, potentially leading to mode coupling instabilities. In the following, each interaction regions is modelled as a series of LR interactions with constant



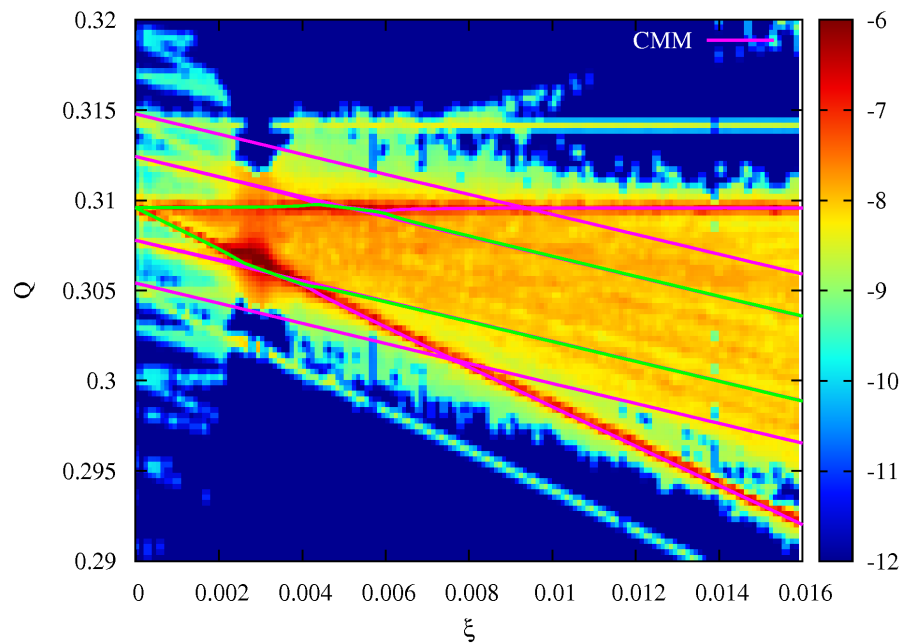
(a) Evolution of the norm of a set of vectors, forming a complete basis, under powers of the one turn matrix obtained with BIMBIM (Eq. 5.1). The plot shows the comparison between the vectors inside (red) and outside (blue) of the eigenspace of the one turn matrix



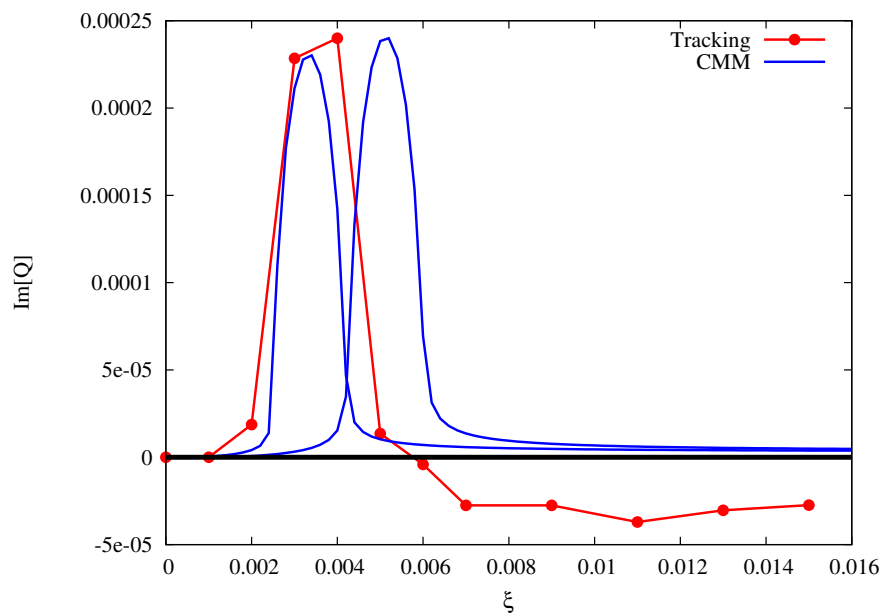
(b) Comparison between the time evolution of modes outside of the eigenspace of the one turn matrix obtained with BIMBIM with the time singular vectors corresponding to the four largest singular values obtained by SVD of tracking simulation data from COMBI.

Figure 5.10 – Comparison of the simulation of the time evolution of the most unstable modes obtained with BIMBIM and COMBI for a single beam composed of a train of 16 bunches with typical 2012 LHC parameters.

5.2. Coherent motion with impedance



(a) Comparison between the spectrogram from tracking simulations with BEAMBEAM3D and the real part of the coherent tunes derived with BIMBIM (solid green and pink lines).



(b) Comparison between the highest imaginary tune shift obtained with BEAMBEAM3D (red) and BIMBIM (blue).

Figure 5.11 – Coherent modes as a function of the BB parameter for two bunches colliding at a single IP with $\beta^*/\sigma_s \approx 90$ and a chromaticity of zero unit. The effect of the beam coupling impedance was set to be constant over the whole scan, based on the typical 2012 LHC machine and beam parameters.

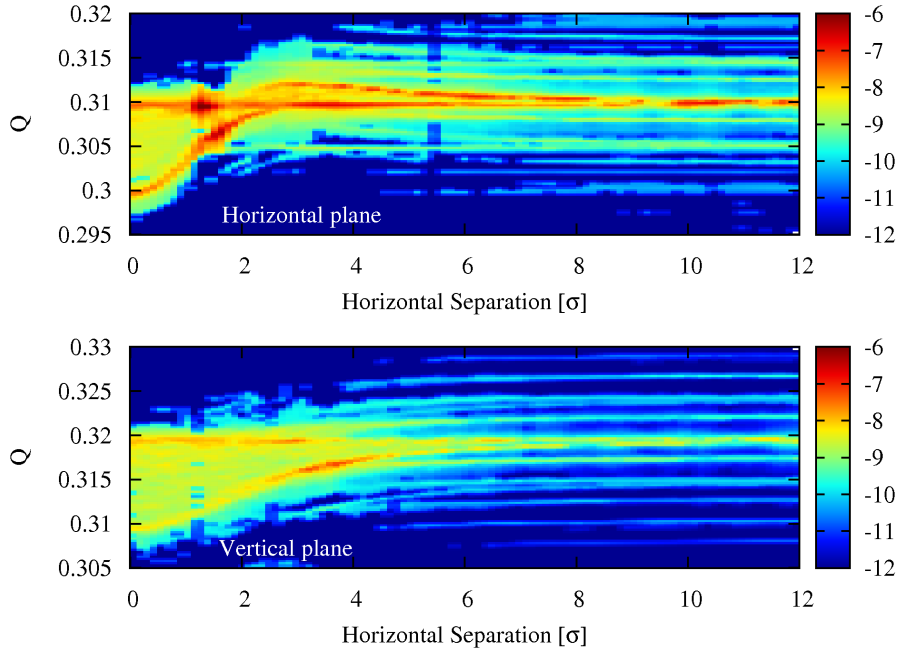


Figure 5.12 – Spectrogram in the horizontal (top) and vertical (bottom) planes for two bunches colliding at a single IP with $\beta^*/\sigma_s \approx 90$ and a chromaticity of zero unit, while varying the normalised separation between the beams in the horizontal plane at the IP. They were obtained with with BEAMBEAM3D using LHC 2012 machine and beam parameters as input.

separation located at a phase advances of $\pm\pi/2$ from the IP, which is a reasonable assumption according to Figs. 3.3c and 3.4. Once in collision, the beam dynamics is dominated by the HO interactions which were discussed in Sec. 5.2.1. We will therefore concentrate on the case with LR interactions only which corresponds to the situation of the LHC after the squeeze. In this configuration, the parallel separation at the IP is of the order of 40σ . This additional LR encounter is therefore neglected in the following analysis. At the locations of the LR encounters $\beta/\sigma_s \gg 1$ and the BB interaction can be reduced to the 4D case. As shown in Sec. 5.2.1 a direct comparison of the tune shifts obtained with the CMM is possible for separations of the order of 10σ which makes it a very valuable tool to study the case of LR interactions.

Figure 5.13 illustrates the impact of PACMAN effects for a simplified case. Two trains of 8 bunches are colliding at a single IP, the PACMAN effects are artificially enhanced by allowing collisions only on one side of the IP. Each bunch therefore experiences up to 7 LR interactions. Even for this simplified case a large number of mode coupling instabilities are observed involving various modes. As the separation is reduced, and hence the BB tune shift is increased, the probability for two modes to overlap become higher and in some cases multiple mode coupling instabilities can occur simultaneously.

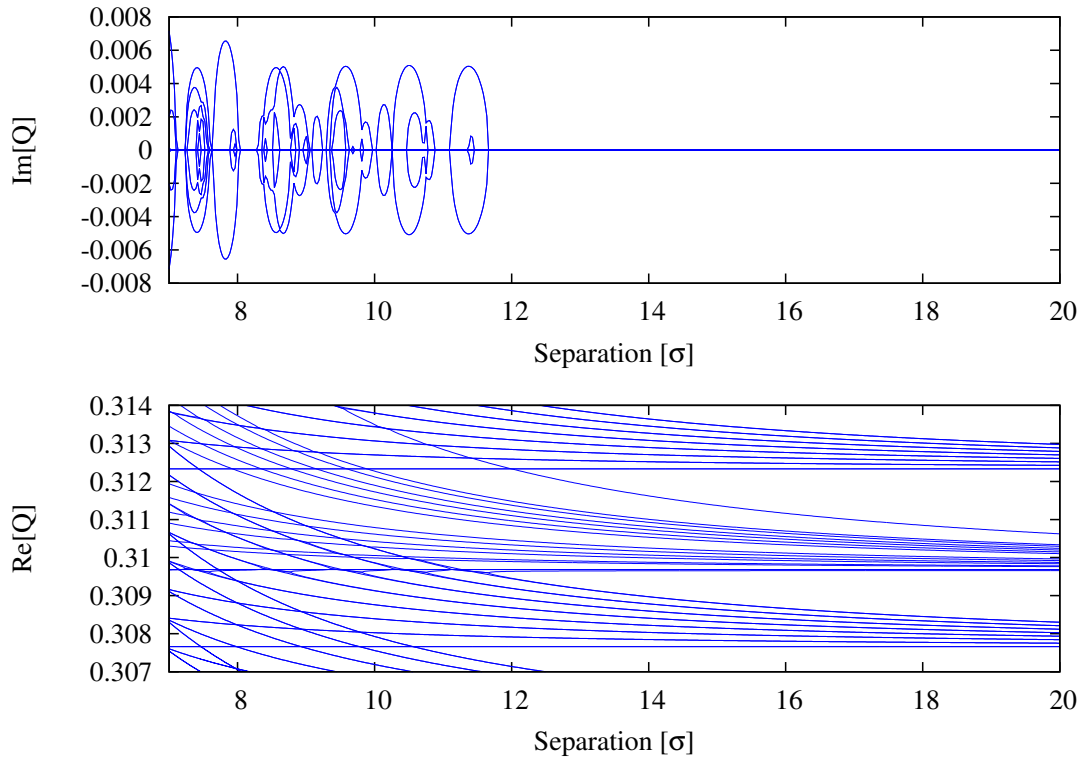


Figure 5.13 – Real (bottom) and imaginary (top) part of the coherent tunes of the modes obtained with the CMM for two trains of 8 bunches colliding in one interaction region with a chromaticity of 0 unit and no transverse feedback. The PACMAN effects are enhanced by allowing collisions only on one side of the IP.

Stabilisation techniques

Figure 5.14 shows the dependency of the imaginary part of the most unstable mode on the chromaticity and transverse feedback gain as a function of the BB parameter. For simplicity, we set the ratio β^*/σ_s to 100. Synchro-betatron coupling introduced by the BB interaction can therefore be neglected. The double peak structure characterizing the mode coupling instabilities shown in Fig. 5.11 is clearly observed. Operating at BB tune shifts where these instabilities occur is the most critical scenario for stability. It is seen that either high transverse feedback gain or high positive chromaticity can help mitigating these strong instabilities as the growth rate is significantly reduced (Fig. 5.14). The case without BB interactions is however not fully recovered and a combination of both may be more efficient. These results are confirmed by tracking simulation with BEAMBEAM3D [62].

Let us consider two beams composed of a single train of 16 bunches colliding in one interaction regions. These bunches experience from 8 to 16 LRs interactions depending on their position in the bunch train. The imaginary part of the tune of the most unstable mode for different settings of the octupoles and transverse feedback is shown in Fig. 5.15. For the con-

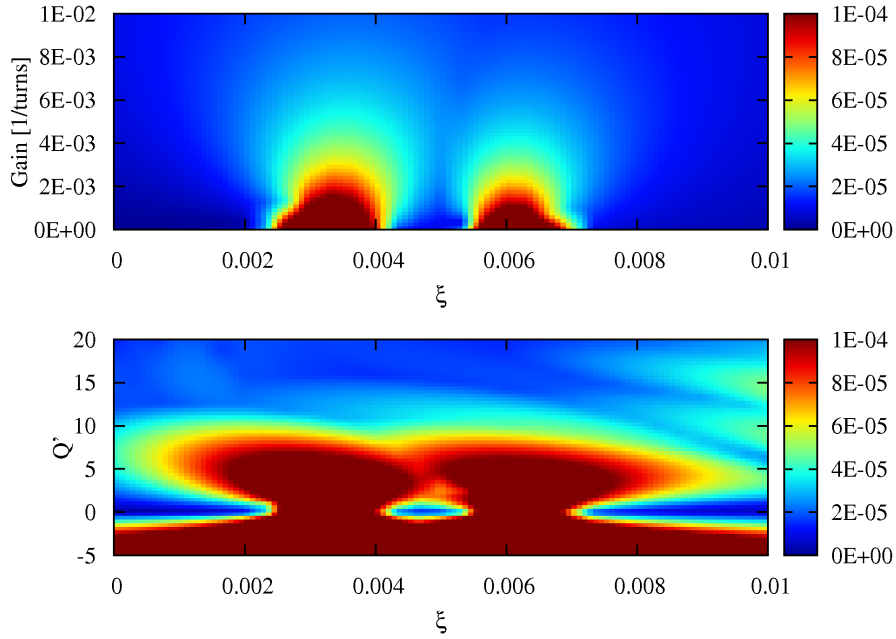
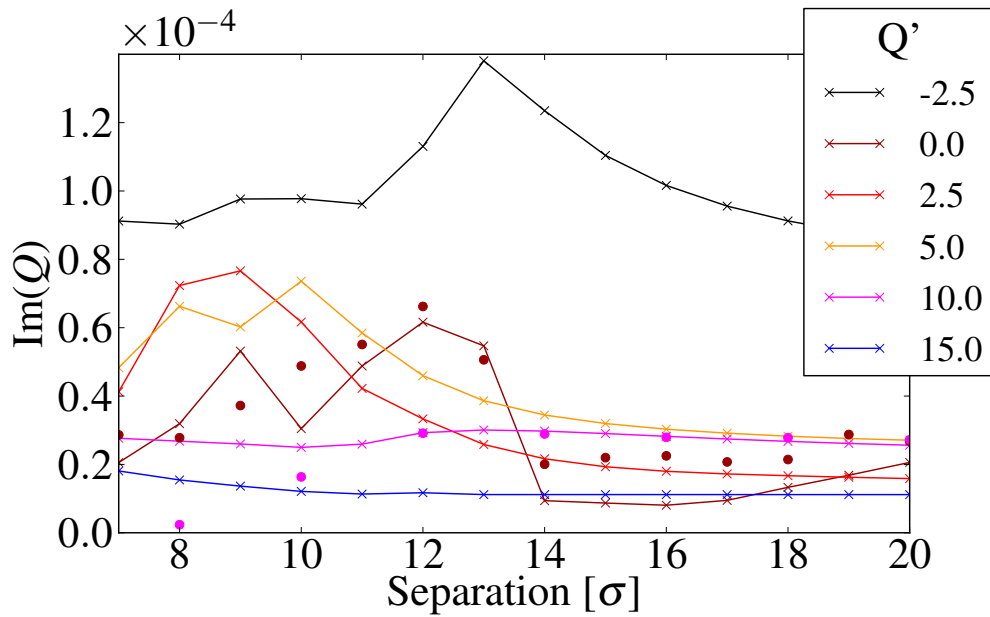


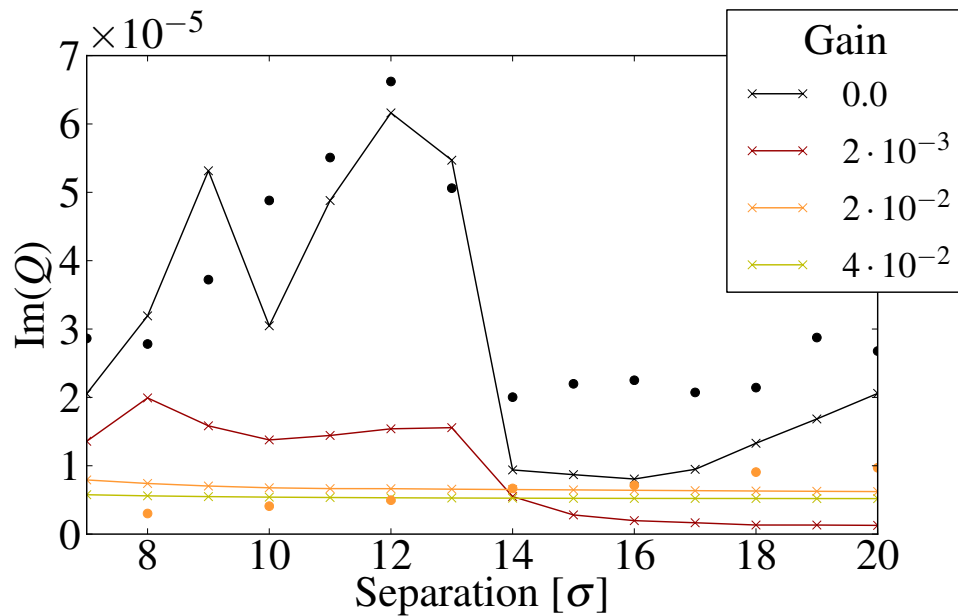
Figure 5.14 – Imaginary part of the most unstable mode (colours) for two bunches colliding at a single IP computed by the CMM as a function of the BB parameters for different transverse feedback gains (top) and chromaticities (bottom). The ratio β^*/σ_s is equal to 100, the other machine and beam parameters are those of the LHC in 2012.

figuration with a chromaticity of 0 unit and no transverse feedback, two peaks are observed for which the imaginary part of the tune goes up to high values. They correspond to distinct mode coupling instabilities. The peak at separations between 11 and 13 σ corresponds to the strongest instability and involves a BB mode with similar characteristics as the σ -mode, but in the multi-bunch regime, and the head-tail mode $n_a = -1$. Both in multi-particle tracking simulations and in the CMM, the mode coupling instabilities are suppressed by either a high transverse feedback gain (Fig. 5.15b) or a large chromaticity (Fig. 5.15a).

Figure 5.16 shows the imaginary part of the tune of the most unstable mode derived with the CMM as a function of both chromaticity and transverse feedback gain. We compare two configurations with either 20 or 13 σ separation between the beams at the location of the LR interactions. In the first configuration, the effect of LR is negligible, whereas in the second we observed strong coupling instabilities (Fig. 5.15). The effect of the coupling instabilities is noticeable in the difference in maximum imaginary tune shift between the two configurations, especially for chromaticities below 10 units and damper gain below 500 turns. The parts with higher transverse feedback gains or high chromaticity are similar in the two configurations, showing that the coupling instability is mitigated.



(a) Comparison between simulations with BIMBIM (lines) and COMBI without transverse feedback and a chromaticity of zero unit (black dots) and 10 units (pink dots).



(b) Comparison between simulations with BIMBIM (lines) and COMBI with a chromaticity of zero unit, without transverse feedback (black dots) and with a transverse feedback gain corresponding to a damping time of 100 turns (orange dots).

Figure 5.15 – Imaginary part of the coherent tune of the most unstable mode obtained with BIMBIM (lines) and tracking with COMBI (dots) for two trains of 16 bunches with LHC 2012 parameters colliding in one interaction region as a function of the normalised separation between the beams at the location of the LR encounters for different chromaticities (top) and transverse feedback gains (bottom).

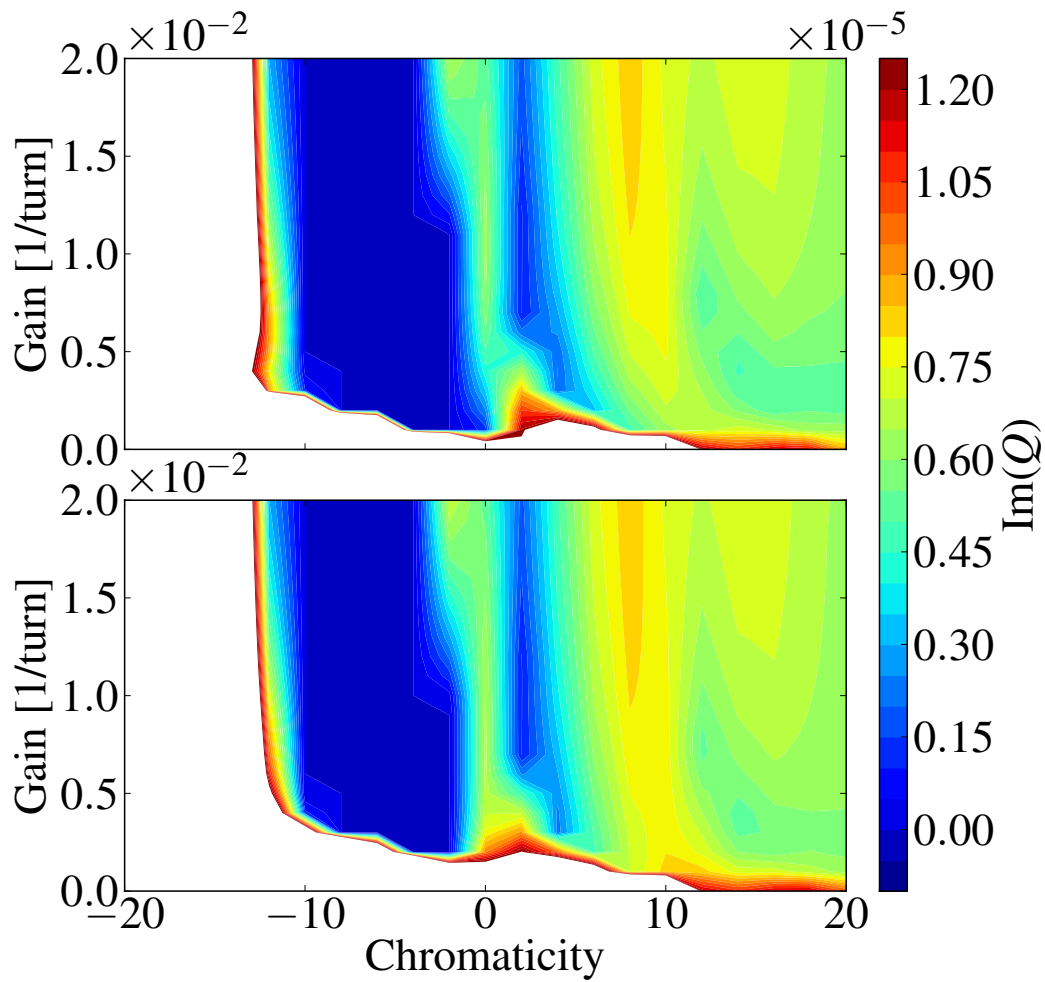


Figure 5.16 – Imaginary part of the coherent tune of the most unstable mode obtained with the CMM for two trains of 16 bunches colliding in one interaction region, for different chromaticities and transverse feedback gains, expressed as the corresponding damping time. The machine and beam parameters are those of the LHC in 2012, with separations at the location of LR encounters of 20σ (above) and 13σ (below).

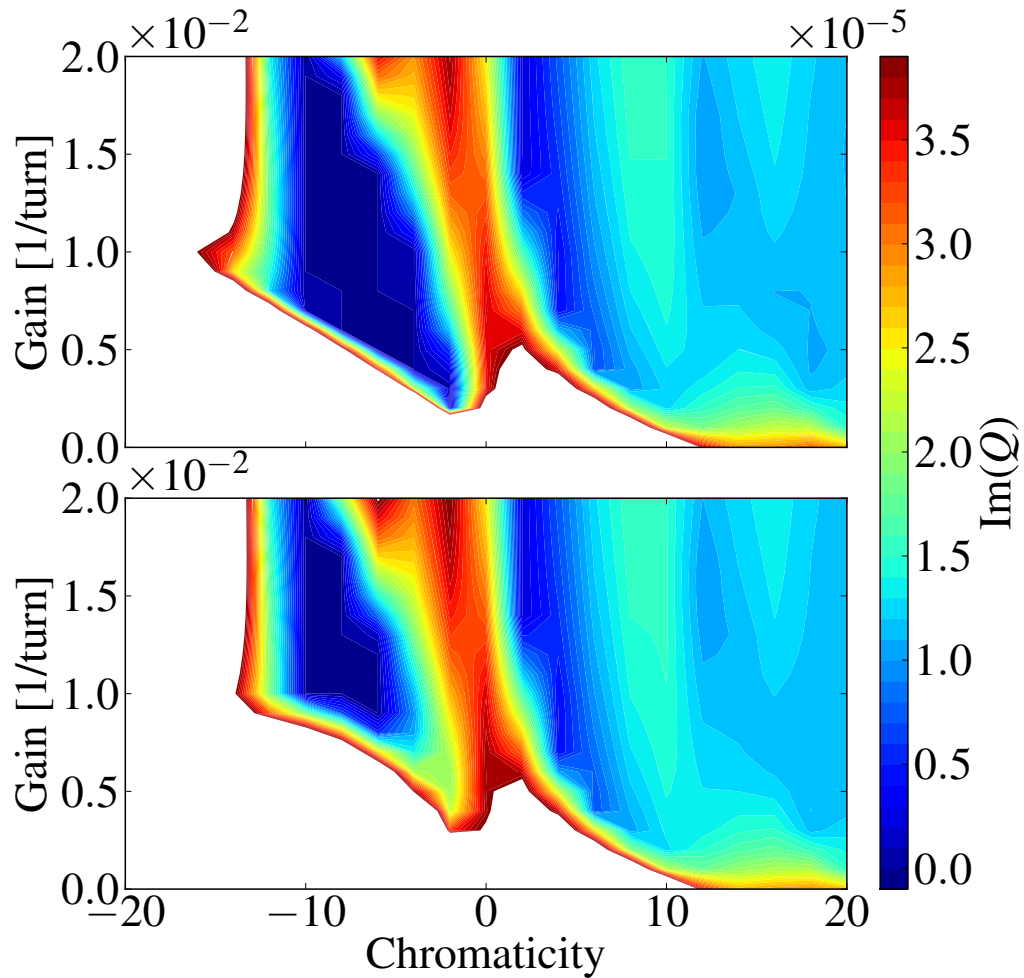


Figure 5.17 – Imaginary part of the coherent tune of the most unstable mode obtained with the CMM for two trains of 16 bunches colliding in one interaction region, for different chromaticities and transverse feedback gains, expressed as the corresponding damping time. The machine and beam parameters are those of the LHC in 2012, except for the effect of the beam coupling impedance which is doubled. The separations between the beams at the location of the LR encounters is 20σ (above) and 10σ (below).

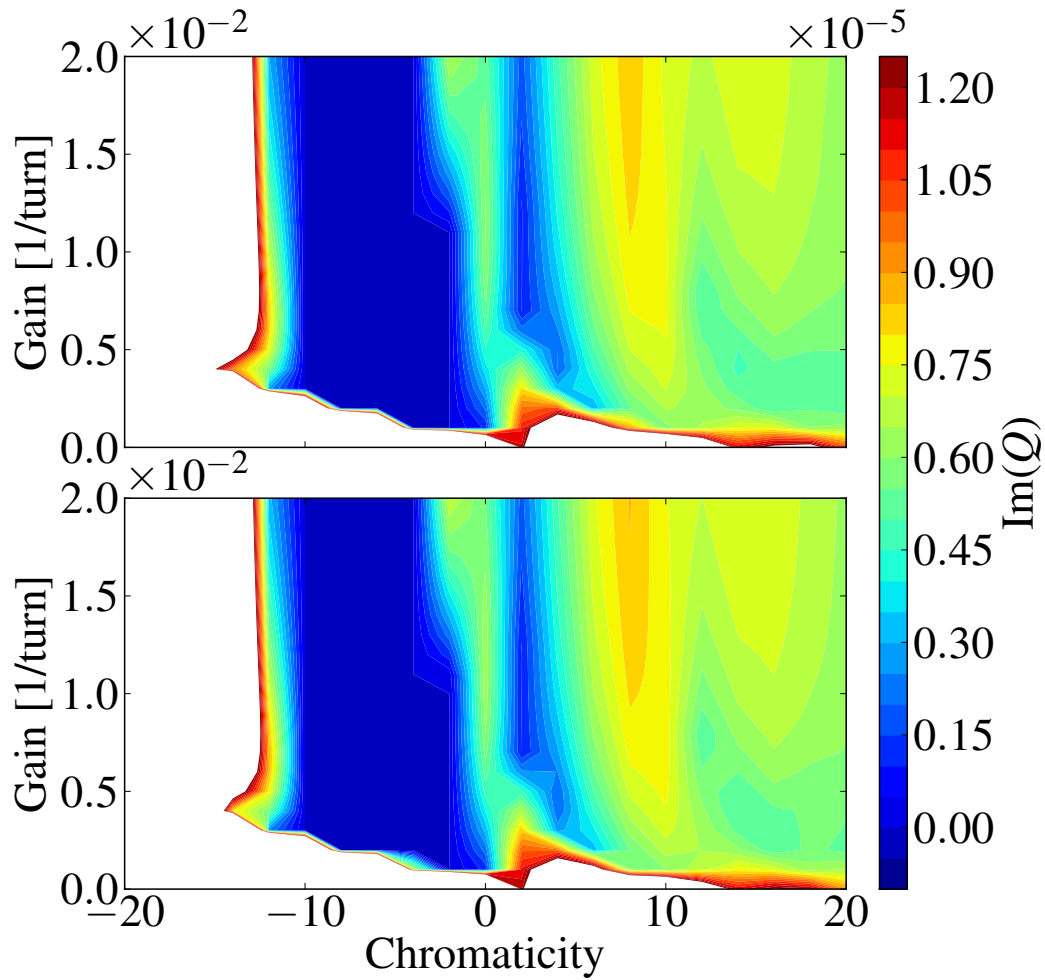


Figure 5.18 – Imaginary part of the tune of the most unstable mode obtained with the CMM for two trains of 16 bunches colliding in two interaction regions with alternating crossing angle planes, for different chromaticity and transverse feedback gain at separations of 20σ (above) and 10σ (below).

As a result of PACMAN effects, the BB tune spread is different for each bunch making very difficult to analytically evaluate the effect of Landau damping on the modes derived with the CMM. In addition, the presence of mode coupling instabilities drastically increases the difficulty. Tracking simulations are therefore well suited for this kind of study. The results of tracking simulations with different chromaticities and transverse feedback settings are compared to the results obtained with the CMM in Fig. 5.15. The maximum tune shift is deduced from tracking simulations by performing a singular value decomposition of all bunches centroid positions, turn by turn, and fitting an exponential to the time evolution singular vector corresponding to the largest singular value (Sec. 2.3). With a chromaticity of 0 unit, the coupled mode instability observed at 12σ is in agreement with the CMM. The second peak at 9σ separation is not visible, suggesting that it is Landau damped. More generally, discrepancies for all cases are observed at low separations for which the BB tune spread becomes relevant and therefore causes Landau damping of the modes.

Increasing the chromaticity to 10 significantly mitigates the mode coupling instability while a transverse feedback gain of 0.01 appears to fully suppress it. These observations are consistent with the single bunch results presented in Sec. 5.2.1 where it was shown that high chromaticity and transverse feedback gain can efficiently stabilize the mode coupling instabilities.

With a chromaticity of 0 unit and without transverse feedback, there is a significant discrepancy between the two models for separations larger than 14σ , which may be attributed to the non-normality of the system. The agreement is however good for high chromaticity or high transverse feedback gain. We shall discuss further this feature in Sec. 5.2.2.

The LHC beams are composed of up to 2808 bunches. These bunches are coupled through the machine impedance and the multiple BB interactions in the four interaction regions leading to a very complex system. Both the CMM and tracking simulations become very demanding in terms of computing resources with a large number of bunches and simulations of the full machine are, for now, out of reach. Nevertheless, the case of a single train of 16 bunches spaced by 50 ns colliding in a single interaction region provides a better understanding of the behaviour of the full machine under variations of critical parameters, such as the separation between the beams, the chromaticity and the transverse feedback gain. In order to extend these results to larger number of bunches, we consider a machine configuration with 16 possible BB interactions in a single interaction regions, therefore the maximum number of interactions per bunch is identical for all bunch trains of more than 16 bunches. Nevertheless, the PACMAN structure is slightly different for bunch trains of different lengths (Figs. 3.5 and 3.6) and the multi-bunch interaction through the beam coupling impedance is stronger for longer bunch trains. As shown in Fig. 5.20, while the largest imaginary tune shift is affected when changing the length of a bunch train from 16 to 64 bunches, the overall behaviour as a function of the separation between the beams is similar in all configurations. According to Fig 5.18, the presence of a second interaction region with alternating crossing angle, similarly to a real LHC configuration with IPs 1 and 5, doesn't change the behaviour.

The maximum imaginary tune shift are similar to the ones obtained with a single interaction region for large chromaticities or high transverse feedback gains (Fig. 5.16).

The nature of the beam coupling impedance has a strong impact on the stability of the beam, a complete study of the behaviour under different types of impedances is beyond the scope of this thesis. However, as experimental evidences suggests that the impedance model used for this study (Sec. 3.4) might be underestimated by a factor two [54], we consider the same configuration, with two trains of 16 bunches colliding in a single interaction region and doubling the effect of the beam coupling impedance with respect to the impedance model (Fig. 5.17). Similar conclusions as for the regular impedance model can be drawn for high positive chromaticities and transverse feedback gains. However, the negative chromaticity part is significantly more unstable. Moreover, the differences in maximum imaginary tune shift between the two configurations with either 20 or 13 σ separation in the negative chromaticity part shows that the coherent dynamic is strongly affected by the presence of LR interactions.

The simulations presented include one or two interaction regions, whereas the LHC counts four in total placed asymmetrically around the ring. Accounting for the full complexity of the problem would require the presence of the maximum number of bunches, which is out of reach. Simulations with the CMM have shown a similar behaviour with simplified, yet different configurations. While the absolute values of rise times and real tune shifts obtained vary, the characteristics of the coupled mode instability shown in Figs. 5.15 and 5.16 remained valid in the configurations tested.

Similarly to the single bunch case (Fig. 5.14), both high transverse feedback gain and high chromaticity appear to mitigate the coupling between low order modes. At high transverse feedback gain there are two regions for which the maximum imaginary tune shift is either negative or slightly positive, appearing as blue areas in Fig. 5.16. The chromaticity ranges between approximately one and five units as well as between -2.0 and -10.0 units. While appealing due to its robustness against chromaticity variations, the stability region with negative chromaticities, for which the imaginary tune shifts are exclusively below 0, was found to significantly shrink in configurations with stronger impedance (Fig. 5.17). Also, the CMM with a single bunch per beam and a single HO interaction shows that the maximum imaginary tune shift increases significantly with the BB parameter in the configuration with negative chromaticity, with respect to configurations with a chromaticity of 2 or 10 units Fig. 5.19. Such BB parameter are obtained with usual beam parameters during luminosity production, negative chromaticities may therefore not be optimal in this operational phase. Also, other studies of the coherent stability introducing the imperfections of the transverse feedback suggest that the coherent stability is very sensitive to the actual implementation of the feedback with negative chromaticities, whereas the configurations with positive chromaticities seems more robust (Sec. A.3.5, [77]). While these features suggest that a high transverse feedback gain and a slightly positive chromaticity maximise the coherent stability, the stability of the beams is very sensitive to chromaticity variations in this configuration.

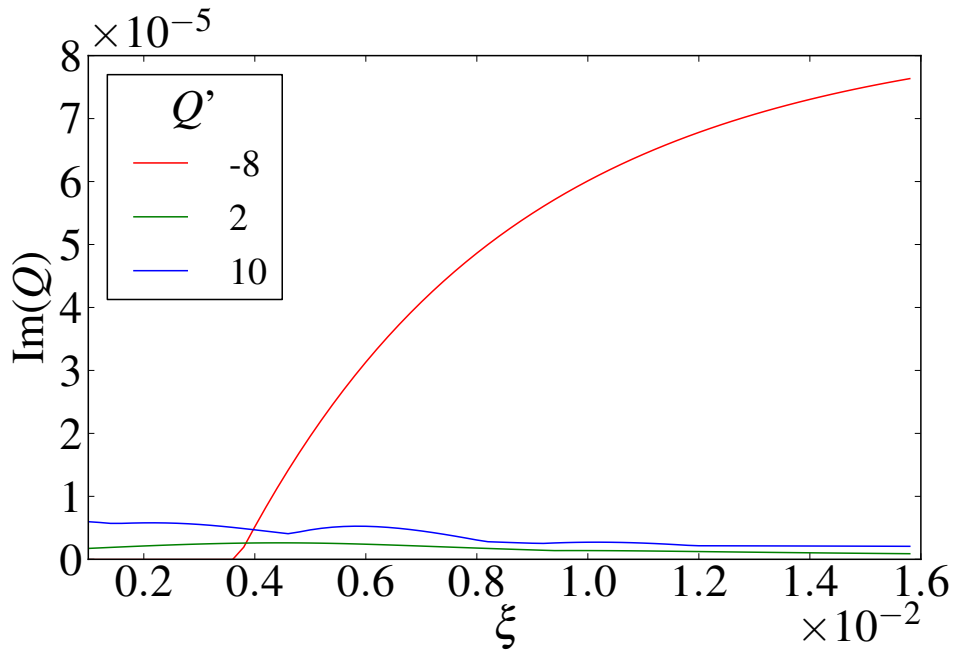


Figure 5.19 – Maximum imaginary tune shift obtained with the CMM in a configuration with a single bunch per beam colliding in a single IP and different chromaticities. The BB parameter is varied, while the effect of the beam coupling impedance is kept constant, based on LHC 2012 machine and beam parameters.

Experimental studies of the coherent stability for different chromaticities and transverse feedback gains are therefore required to define an optimal set of parameters. Such studies could not be performed due to the lack of time.

5.2.2 Non-normal behaviour

The non-normal aspects of the system have been invoked to explain discrepancies between the CMM and tracking simulations with low chromaticities and high transverse feedback gain (Fig. 5.15). The size of the matrices describing the two trains of 16 bunches with fine discretisation of the longitudinal distribution, i.e. several slices and rings, are significant. The computation of the pseudospectrum becomes very demanding in term of computing resources. In order to understand the non-normal feature of the system, let us study simplified configurations.

First, let us look at a single beam, composed of a series of bunches spaced by 50 ns. Similarly to the configuration in Fig. 5.17, we double the effect of the beam coupling impedance, such as to give pessimistic estimates. Figure 5.21 shows the pseudospectrum obtained with the CMM with 11 slices and a single ring for a single bunch and different transverse feedback gains. These parameters are not sufficient to give accurate estimates of the coherent tune

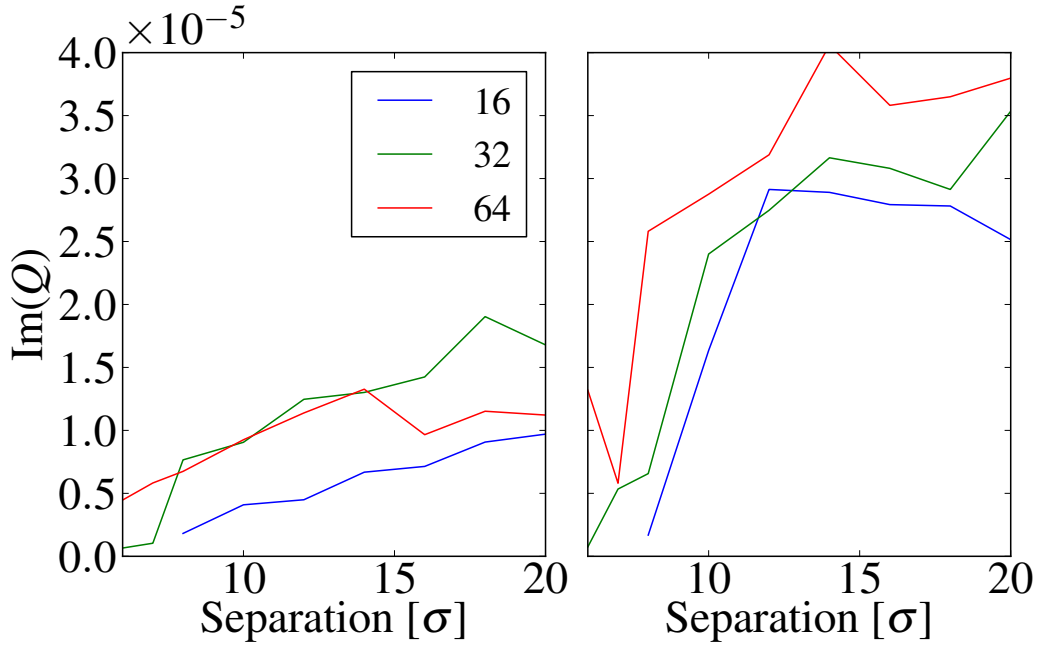


Figure 5.20 – Imaginary tune shift of the most unstable mode from tracking simulations with COMBI of two trains composed of 16, 32 and 64 bunches colliding in one interaction region as a function of the normalised separation between the beams at the location of the LR encounters. The two plots show a comparison between two configurations with typical 2012 LHC machine and beam parameters with a chromaticity of zero unit and transverse feedback gain corresponding to 100 turns damping time (left) and a chromaticity of 10 units and without transverse feedback (right).

shifts, yet allow for a good understanding of the underlying principles. The eigenvalues are clearly visible in the pseudospectrum, and we observe that the central mode (associated to head-tail mode $n_a = 0$), slightly shifted down from the unperturbed tune is strongly affected by the transverse feedback gain, while the two others (head-tail mode $n_a \pm 1$) are fairly insensitive. In this configuration, a transverse feedback gain corresponding to 250 turns is sufficient to bring all eigenvalues to the stable area. When increasing the number of bunches in the train, the eigenvalues remain unchanged, however the pseudospectrum is strongly affected, as can be observed in Fig. 5.22. The head-tail mode $n_a = 0$ strongly protrudes into the positive imaginary part. The effect on the Kreiss constant is clearly visible in Fig. 5.23. A slightly higher transverse feedback gain (200 turns) is required to fully stabilize the beam composed of trains with several bunches. These results are fully consistent with tracking simulations, as shown in Fig. 5.24. Indeed, a single bunch is stable in the configuration with a chromaticity of -8 units and a transverse feedback gain corresponding to 250 turns, as we see the amplitude of the mode with largest singular value decreasing with time. Considering a train of bunches, we observe a transient growth before a damping, which for large number of bunches can span several decades. The spacial singular vector shows a pattern typical

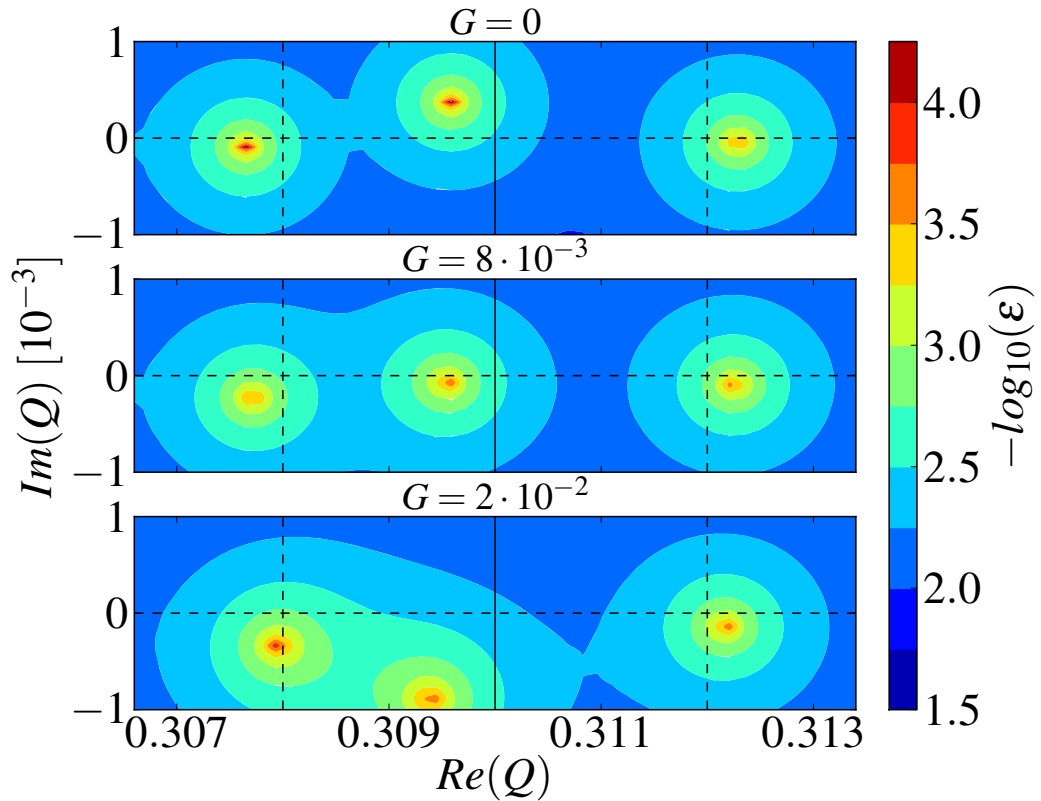


Figure 5.21 – Pseudospectrum of the one turn matrix obtained with BIMBIM corresponding to a single bunch with 2012 LHC machine and beam parameters and different transverse feedback gains. The effect of the impedance is enhanced by a factor two and the chromaticity is -8 units. Vertical lines mark the unperturbed tune (solid) and the first upper and lower synchrotron sidebands (dashed).

for a multi-bunch beam breakup instability, i.e. a perturbation growing along the bunch train. As predicted by the CMM, this behaviour disappears with a transverse feedback gain corresponding to 200 turns, i.e. a train of 64 bunches is fully stable, without transient growth (Fig. 5.25).

The prediction of the stability limit in terms of transverse feedback gains does not suffer significantly from the non-normality of the system, as the normal mode analysis predicted that 250 turns would be sufficient, whereas 200 turns are actually needed. However, the interpretation of tracking data, and possibly measurements, is deeply modified by the non-normality. Indeed, in realistic simulations, as well as in measurements, nonlinear effects and eventually the physical aperture will deteriorate the quality of the beam oscillating with large amplitude during the transient, thus preventing to observe the long term stability. Such observation will not be distinguishable from a regular instability, however the rise time

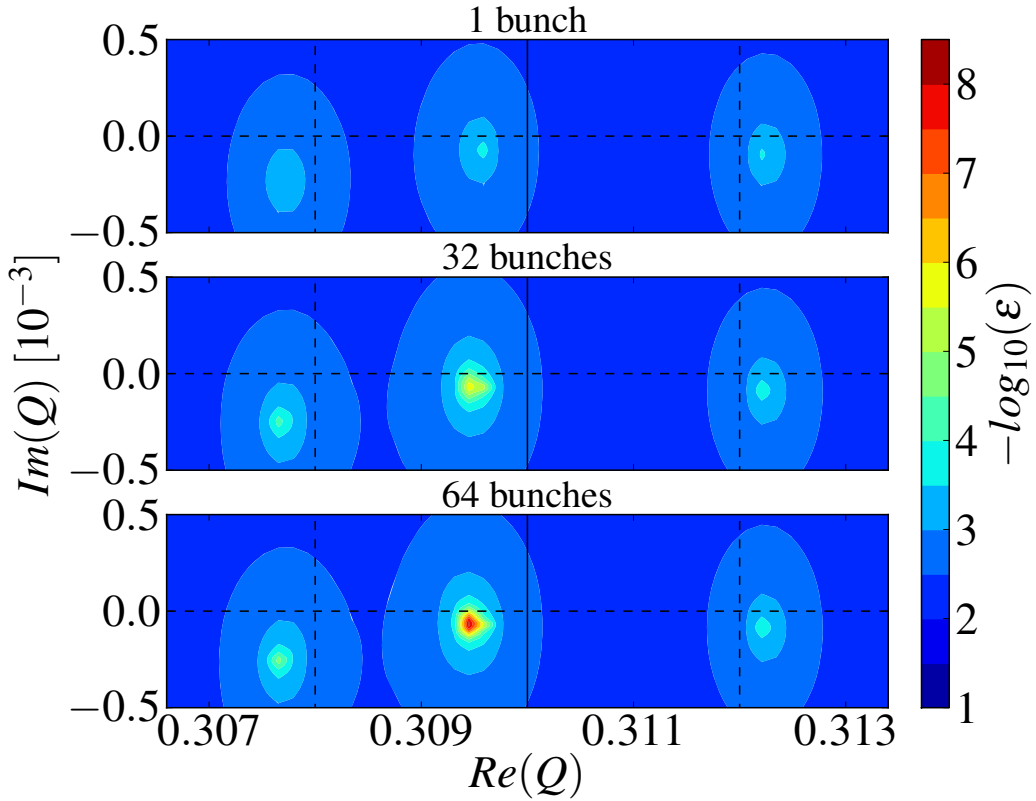


Figure 5.22 – Pseudospectrum of the one turn matrix obtained with BMBIM for single train composed of different numbers of bunches with 2012 LHC machine and beam parameters. The effect of the impedance is enhanced by a factor two, the chromaticity is -8 units and the transverse feedback gain corresponds to a damping time of 250 turns. Vertical lines mark the unperturbed tune (solid) and the first upper and lower synchrotron sidebands (dashed).

may be much larger than the one predicted by the normal mode analysis. The comparison of tracking data, measurements and predictions of the CMM have to be made including non-normal effects.

This effect explains the discrepancy observed between tracking simulations and the CMM with a train of 16 bunches per beam (Fig. 5.15). Indeed, for low transverse feedback gain and low chromaticity, the head-tail mode $n_a = 0$ is the most unstable. One therefore expects a strong impact from the non-normality of the system in the multi-bunch regime, which results in an increase of the strength of the instability visible in tracking simulations, but not in the normal mode analysis performed within the CMM.

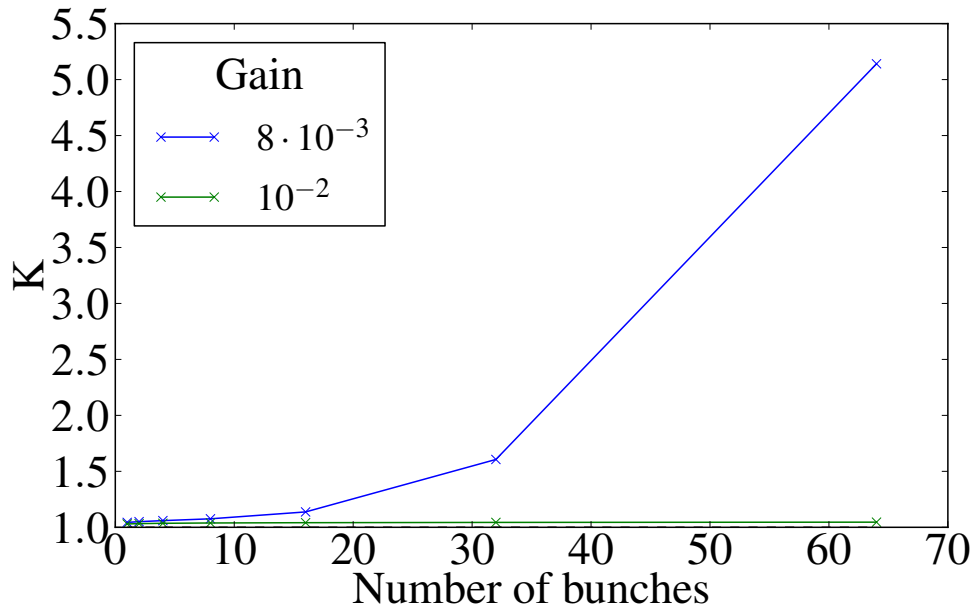
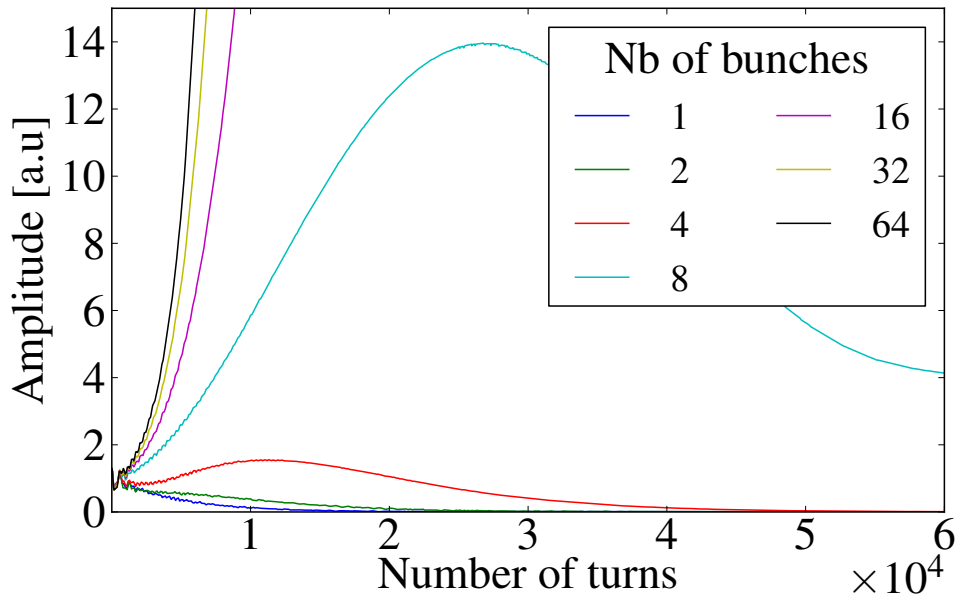


Figure 5.23 – Kreiss constant of the one turn matrix obtained with BIMBIM for single train composed of different numbers of bunches and different transverse feedback gains. The machine and beam parameters are those of the LHC in 2012, except for the effect of the impedance which is enhanced by a factor two and the chromaticity which is -8 units.

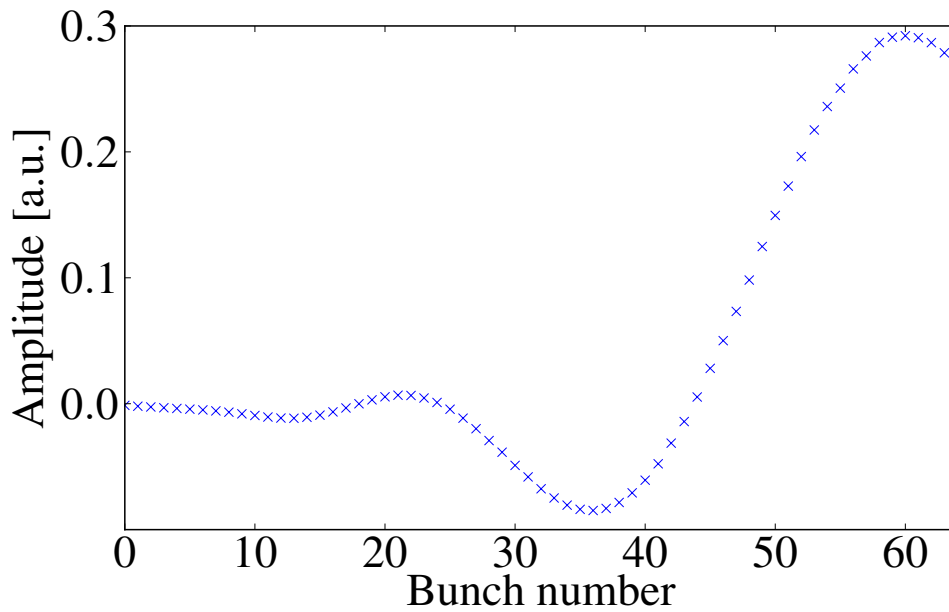
5.2.3 Observations

In dedicated experiment

A short experiment was dedicated to the measurement of coupling instability with beams colliding with a transverse offset, at the end of a special fill [78]. The experiment begun after the squeeze, with two bunches per beam colliding in IPs 1 and 5. First, the beams were re-separated by 6σ at both IPs and the chromaticities were measured. The measured machine and beam parameters are reported in Tab. 5.1a. Before $t = 0$, in Fig. 5.26, a series of spikes in the oscillation amplitude mark a few tests of the beams stability without transverse feedback, by switching it off and on again when an instability was observed. The octupole strength is increased after each tentative, it was found that a large strength (480 A) was not sufficient to stabilize the beams. At $t = 0$, the beams were brought into collision at IP5 with the transverse feedback on, with a gain corresponding to 50 turns damping time. Once the beams were colliding HO, the transverse feedback was no longer required to maintain the beams stability. The beams were then re-separated in steps, visible in Fig. 5.26. At each step, the stability without transverse feedback was tested, as previously. It was observed that the beams are stable without transverse feedback for separations below 0.7σ and from 1.8 to 6σ , whereas unstable from 0.7 to 1.8σ and at 6σ . Also, the instability at intermediate separations have



(a) Time singular vector corresponding to the largest singular value.



(b) Spatial singular vector corresponding to the largest singular value with a train of 64 bunches.

Figure 5.24 – Time and spacial singular vector from the SVD of tracking data with COMBI for a train composed of different numbers of bunches. 2012 LHC parameters were used as input, with a chromaticity of -8 units and a transverse feedback gain corresponding to a damping time of 250 turns.

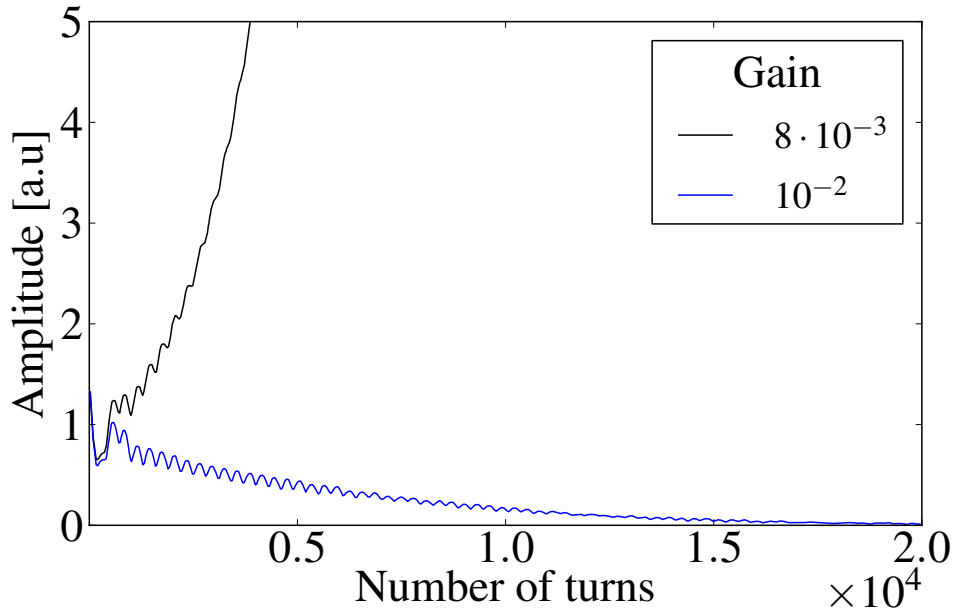


Figure 5.25 – Comparison of the behaviour of the amplitude of the time singular vector obtained with COMBI for the configuration with 64 bunches already shown in Fig. 5.24a (black) and for the same configuration with a slightly higher transverse feedback gain (blue).

different characteristics than for 6σ separation. The rise times are significantly different in the case of large and small separation (Tab. 5.1b) and most importantly, the frequency of the mode with separated beams is consistent with a head-tail mode with $n_a = -1$, whereas the frequencies of the modes with intermediate separations are consistent with the ones of coherent BB modes. Also, as shown by Fig. 5.27, at intermediate separations both beams are unstable, unlike for 6σ . It was however not possible to make a turn by turn correlation of the two beams due to lack of diagnostics.

It is important to stress that, as predicted, the transverse feedback was efficient to stabilise the beams. Indeed, during this experiment, no instabilities were observed while the transverse feedback was active.

Due to the lack of time, the scan in separation is extremely coarse, moreover, important parameters, such as chromaticities and emittances, are poorly known. In addition, the unknowns on the wake functions are fairly large. All these factors render a quantitative comparison with theoretical models difficult. In particular, one has to recall that the incoherent effect of BB varies strongly when changing the separation and, as discussed in Sec. 4.2.2, the resulting stability diagrams become very small for beams colliding with a transverse offset of the order of $1-2\sigma$. Thus, the observed instabilities could have started off as single beam, due to a loss of Landau damping of head-tail modes, and then be transmitted incoherently to the other beam via the BB force. In this case, one would expect that the nature of the unstable mode observed to be independent of the separation between the beams at the

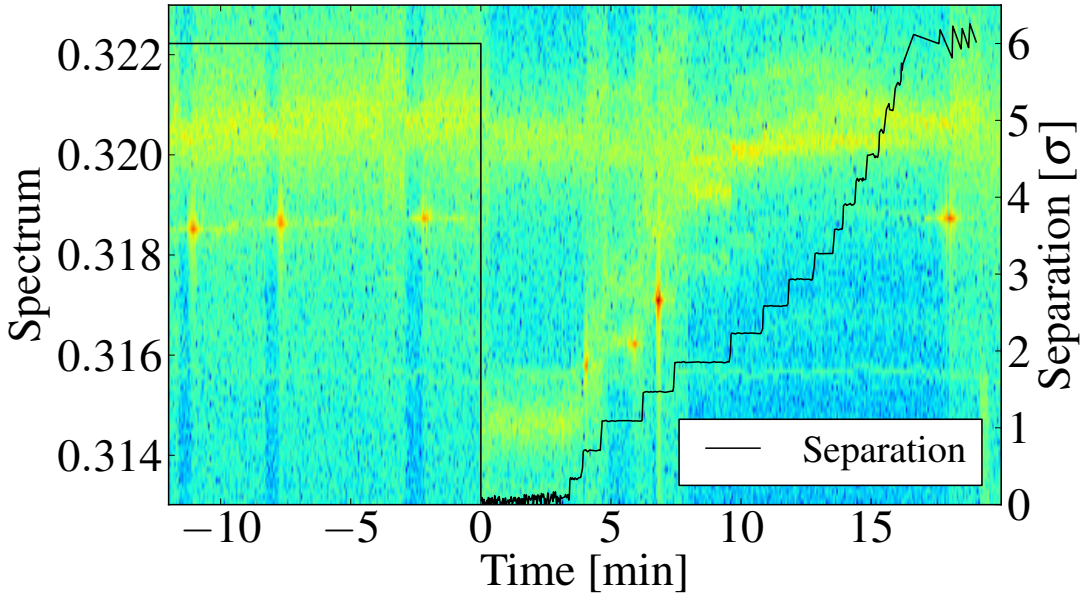


Figure 5.26 – Spectrogram measured by the BBQ in the vertical plane of Beam 1 during an experiment with two bunches per beam (Tab. 5.1a) colliding with a varying transverse offset in IP1. The normalised separation between the beams at the IP (black) is deduced from the measured luminosity reduction factor (Eq. 2.70).

Parameter	Bunch 1	Bunch 2
Intensity [10^{11} p]	1.1 ± 0.05	
Horizontal Emittance [μm]	2.15 ± 0.2	2.25 ± 0.2
Vertical Emittance [μm]	1.6 ± 0.2	1.9 ± 0.2
Horizontal tune	0.31 ± 10 ⁻³	
Vertical tune	0.3205 ± 5 · 10 ⁻⁴	
Horizontal chromaticity	8.0 ± 2.0	
Vertical chromaticity	4.0 ± 1.5	

(a) Machine and beam parameters

Full separation [σ]	Growth rate [1/s]	Coherent tune	BBQ signal
0.7 ± 0.04	2.7 ± 0.1	0.3158 ± 10 ⁻⁴	Vertical plane, both beams
1.1 ± 0.04	6.7 ± 0.2	0.3162 ± 10 ⁻⁴	Vertical plane, both beams
1.4 ± 0.04	1.8 ± 0.05	0.3171 ± 10 ⁻⁴	Vertical plane, both beams
6.0 ± 0.04	5.9 ± 0.2	0.3187 ± 10 ⁻⁴	Vertical plane, Beam 1

(b) Characteristics of the instabilities

Table 5.1 – Measured quantities during the experiment dedicated to the observation of mode coupling instabilities of colliding beams.

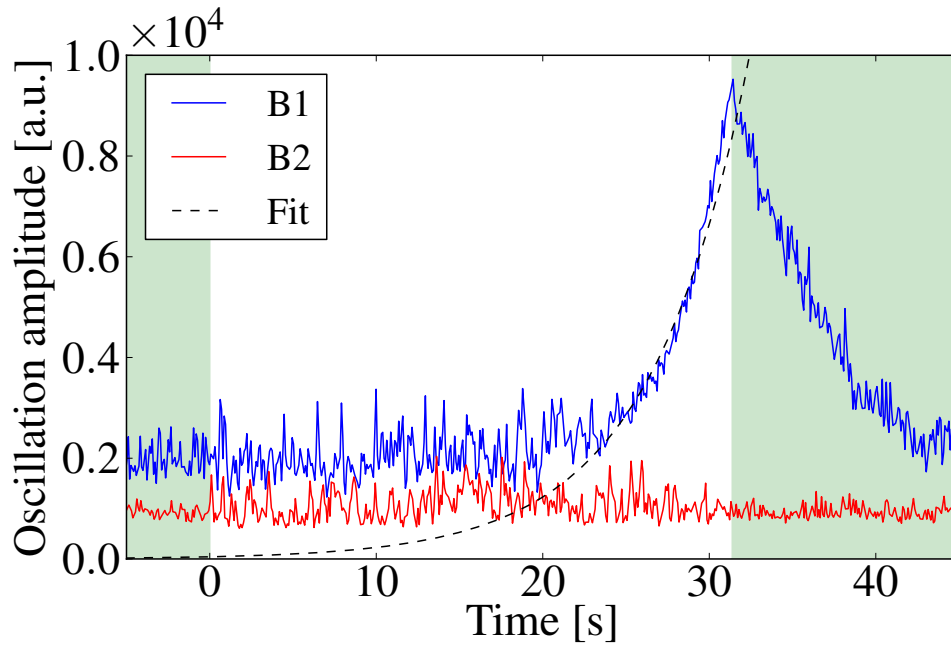
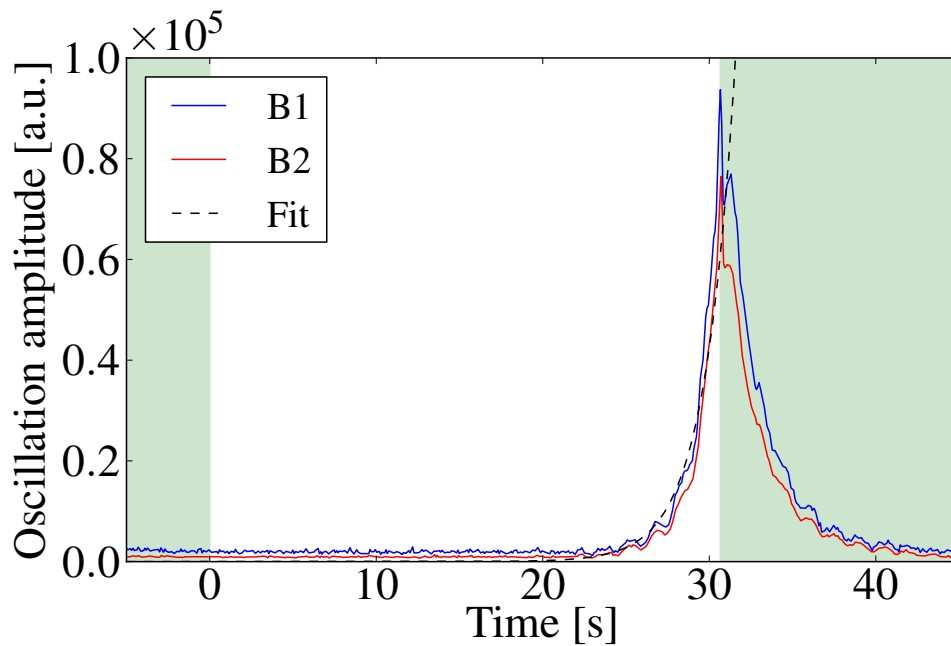
(a) 6σ separation.(b) 1.4σ separation.

Figure 5.27 – Beam oscillation amplitude measured with the BBQ in the vertical plane of both beams during an experiment with two bunches per beam (Tab. 5.1a) colliding with a normalised separation between the beams of 6σ (above) and 1.4σ (below) at IP1. The darkened area shows when the transverse feedback was active.

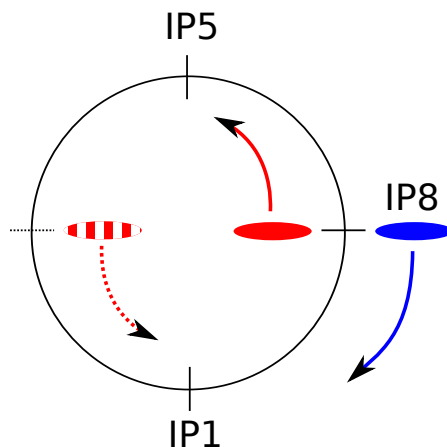


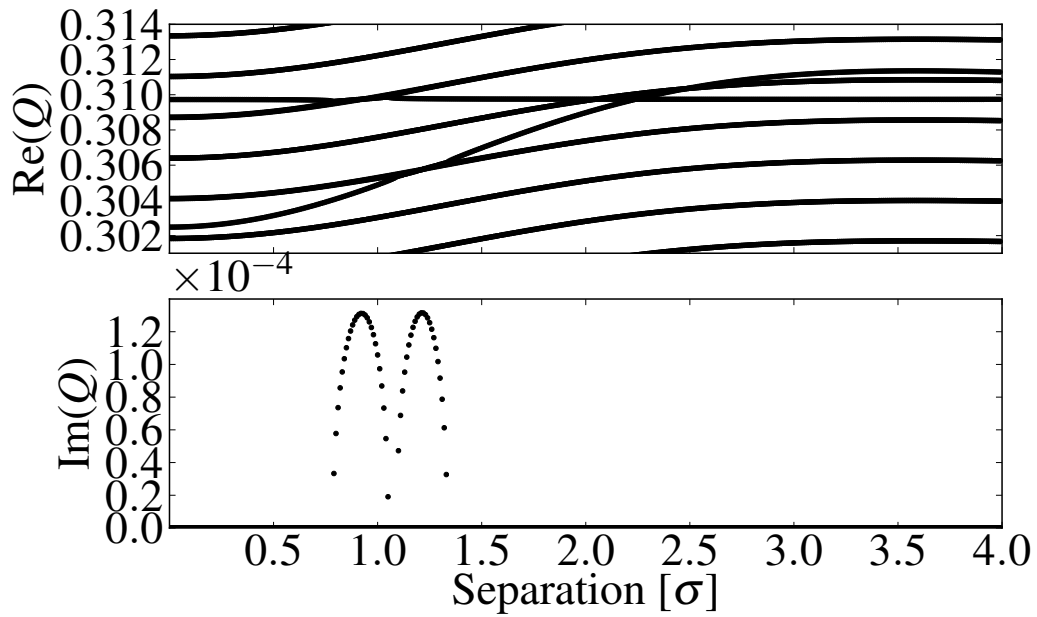
Figure 5.28 – Sketch of the simplified collision schedule used to model the bunches colliding HO at IP8 only. In the configuration with a single bunch per beam (solid), the two bunches collide with each other at IP8 only. In the asymmetric configuration (solid and stripped), the single bunch of Beam 1 (solid blue) collides with the second bunch of Beam 2 (stripped red) at the IPs 1 and 5, whereas the first bunch of Beam 2 (solid red) still collides only at IP8 with the single bunch of Beam 1.

IP. This is not observed as both the frequencies and rise times of the modes are different for different separations. Also, simulations with `BEAMBEAM3D` suggests that the instability could not be explained without considering coherent coupling between the beams [62]. For these reasons, the instabilities observed during this experiment are good candidates for the coupled mode instability predicted by the models.

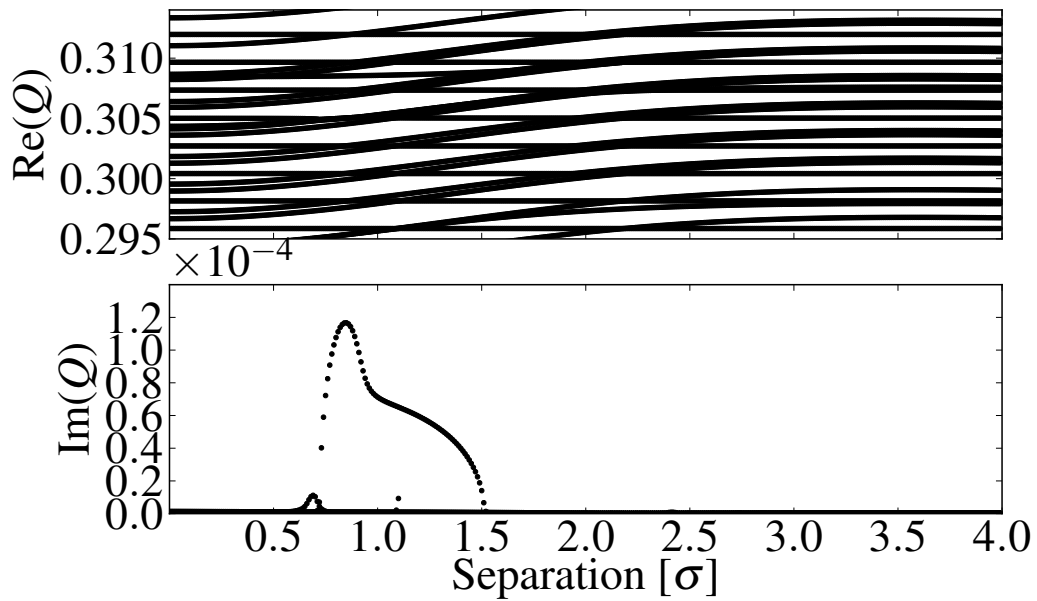
During luminosity production

During the 2012 proton run, the LHC filling schemes included bunches colliding HO only at IP8 (Tab. 3.2). As the luminosity was levelled with a transverse offset at IP8, these bunches are in conditions very similar to those in the dedicated experiment described in Sec. 5.2.3. When considering coherent modes, the collision scheme of all bunches involved in the mode are relevant. The colliding partner of the bunches colliding only at IP8 are colliding HO at the IPs 1 and 5. In order to assess a such configuration, let us consider a simplified case with a similar asymmetry between the beams sketched in Fig. 5.28. We have two configurations, in the first one we have a single bunch per beam (represented by solid ellipses) colliding only at IP8. In the second, including a second bunch in Beam 2 (represented by a striped ellipse). The additional bunch of Beam 2 collided HO at the IPs 1 and 5 with the single bunch of Beam 1, the BB interaction experienced by the first bunch of Beam 2 remains unchanged with respect to the former configuration. Let us note that the real phase advance between the IPs is taken into account and that the multi-bunch wake is neglected. Figure 5.29 shows the tune shifts of the mode computed with `BIMBIM`.

In both configurations, we observe the coupling instabilities with similar rise times at slightly



(a) Single bunch per beam



(b) Asymmetric filling scheme

Figure 5.29 – Spectrum, obtained with BIMBIM, of the simplified model of bunches colliding only at IP8 in the two configurations sketched in Fig. 5.28 for different normalised separations between the beams at IP8. The effect of the beam coupling impedance is based on the machine and beam parameters of the LHC in 2012.

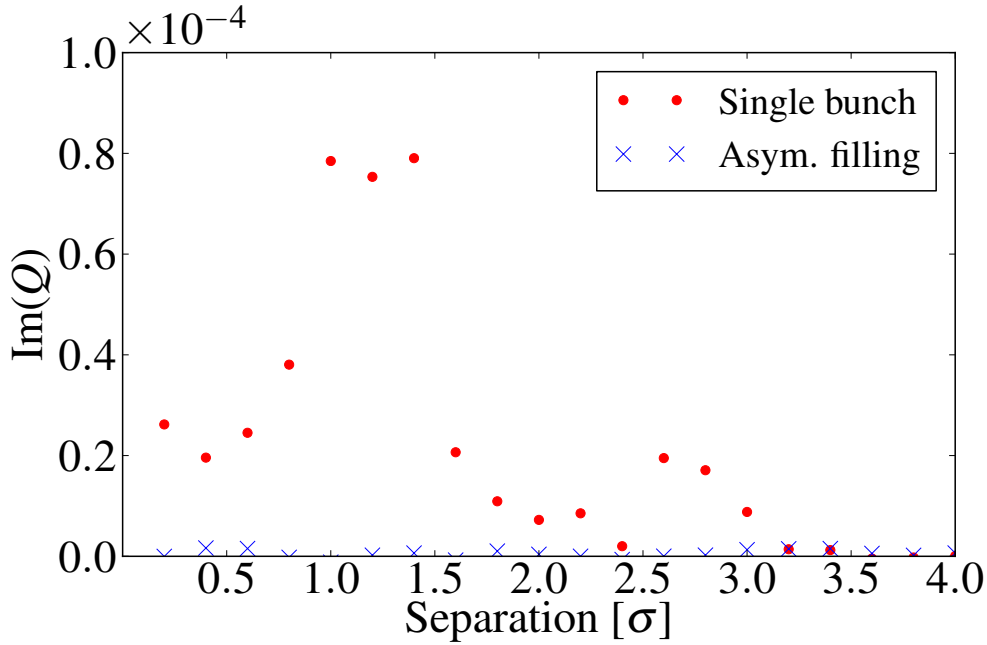


Figure 5.30 – Maximum imaginary tune shift simulated with COMBI in the two configurations sketched in Fig. 5.28 for different normalised separation between the beams at IP8. The effect of the beam coupling impedance is based on the machine and beam parameters of the LHC in 2012.

different separations. However, in the case of asymmetric filling scheme, the frequency of the unstable modes lie in the middle of the incoherent spectrum due to the HO collisions at the IPs 1 and 5. We can, therefore, expect Landau damping effect for these modes, as opposed to the single bunch configuration. This is confirmed by tracking simulations with COMBI. Indeed, Fig. 5.30 shows the maximum imaginary tune shift derived from an exponential fit of the amplitude of the time singular vector with the largest singular value obtained from the tracking data of the two configurations. In the configuration with asymmetric filling scheme, the beams are stable for all separations, whereas for the single bunch configuration, one observes the mode coupling instability between 1.0 and 1.5 σ . We note that the range of separations at which the instability occur is slightly different with respect to the linear model, due to the frequency shift in the self-consistent simulation (Sec. 2.2.2). Also, in the single bunch configuration, the existence of instabilities in the other plane, which is not considered in the linear model, results in an artificial growth in the plane under study. This explains the small, yet non-zero, imaginary tune shift for separations below 1.0 σ and between 2.5 and 3 σ .

It is important to realize that the collision schedule of the first bunch of Beam 2 is identical in the two configurations, in both it collides only at IP8. Yet, it is stable in one configuration and unstable in the other. We conclude that it is stabilized by the tune spread due to HO collisions experienced by its partner bunch.

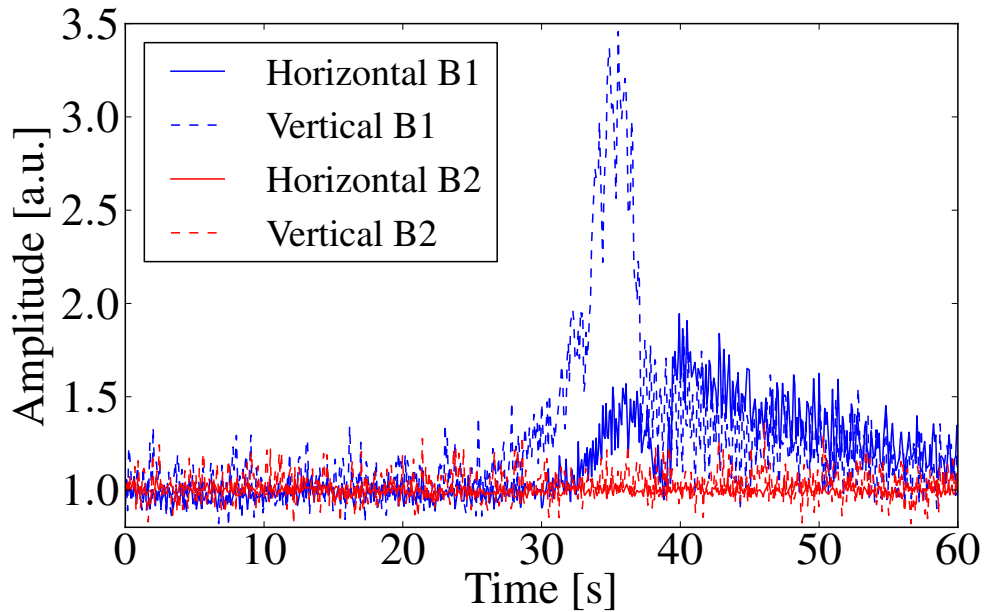


Figure 5.31 – Beam oscillation amplitude measured by the BBQ during an instability during luminosity production (Fill 2646). The beams were colliding HO in the IPs 1 and 5. Based on the relative difference in the measured luminosity at the IPs 1, 5 and 8, one finds the luminosity reduction factor and the corresponding normalised separation between the beams at IP8 (Eq. 2.70) of $1.5 \pm 0.4 \sigma$.

This model is rather simple with respect to the actual collision pattern during luminosity production. Due to the fact that IP8 is placed an octant left from IP1, rather than a quadrant in our simplified model, and to the presence of many other bunches in the machine, most of the bunches are actually colliding partners. While a full description of the coupled system would require large computing resources, this simplified model suggests that, as most bunches are colliding HO in the IPs 1 and 5, the frequencies of the coupled modes lie inside the incoherent spectrum and, as a consequence, they experience Landau damping.

Nevertheless, as already discussed in Sec. 4.2.4, there were observations of instabilities involving the bunches colliding at IP8 only. The oscillation amplitude measured by the BBQ system during one of these instabilities is shown in Fig. 5.31. The measurement of the bunch intensities before and after the instability reveals that only one bunch, colliding only in IP8, lost more than 50% of its intensity, whereas the others were unaffected. These features are common to a series of observations and were shown to be consistent with the lack of Landau damping for single bunch modes, caused by the incoherent contribution of the BB interaction with a small transverse offset (Secs. 4.2.2 and 4.2.4). The coupling of BB mode and impedance mode is critical in the same range of separations and thus appears as another possible explanation for the observation. Yet, the dipolar moments of all bunches are similar in the eigenmodes corresponding to the unstable frequencies for both configurations. The

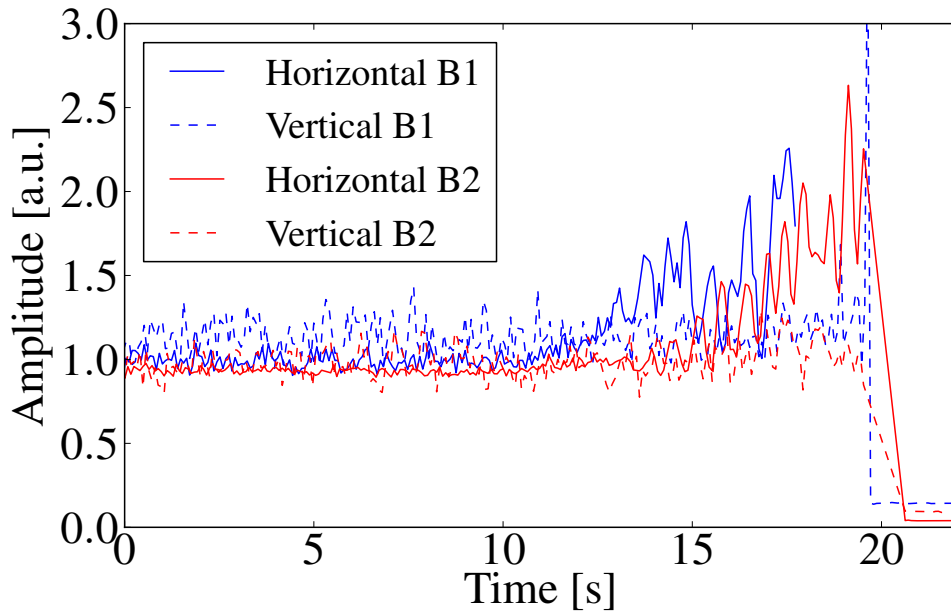


Figure 5.32 – Beam oscillation amplitude measured by the BBQ during an instability while bringing the beams at all IPs, according to the process described in Fig. 4.11 (Fill 2668). As the peak luminosity was not achieved due to the premature extraction of the beam, the separation between the beams at the IPs could not be evaluated based on the measured luminosity reduction factor.

absence of a coherent signal in the other beam visible in Fig. 5.31 is therefore not consistent a coupled mode instability.

When bringing the beams into collision

The situation when the beams are brought into collision is similar, yet different. Indeed, the IPs 1 and 5 are brought in collision together in a synchronous manner. In this configuration, the beams collide temporarily with a small transverse offset at the IPs 1 and 5 and there is no other HO collision to provide stability. Also, as discussed in Sec. 4.2.2, in the first part of the 2012 run, the process was slow enough to allow for instabilities with rise time in the order of several seconds to develop. There were several observations of such instabilities at the beginning of the proton run and we analyse one of them. Figure 5.32 shows the beam oscillation amplitude measured by the BBQ during an instability while bringing the beams into collision. This instability provoked large beam losses which have enforced an extraction of the beam, visible by the disappearance of the signal. Contrary to the case of bunches colliding at IP8 only, there is a coherent signal growing in the horizontal plane for both

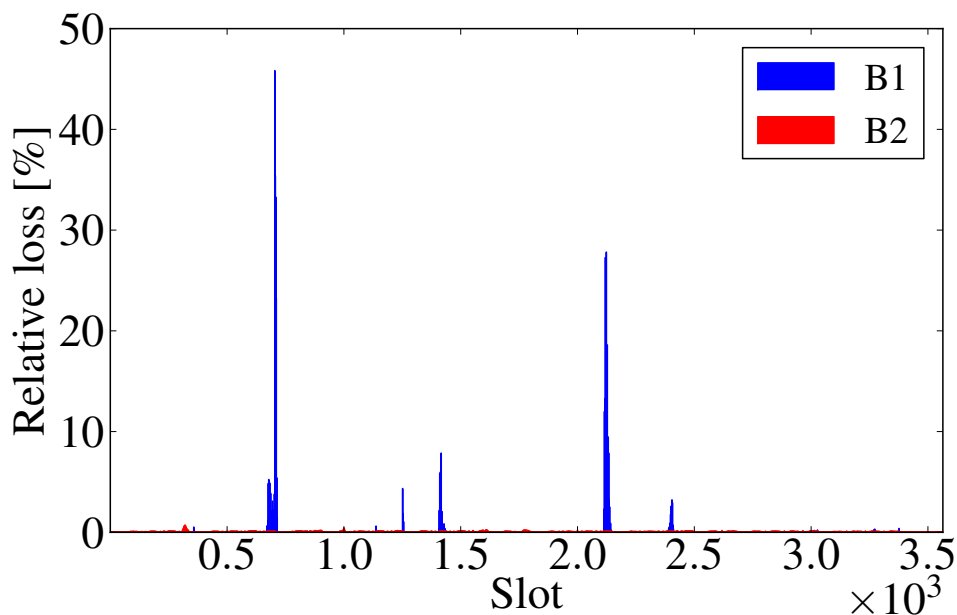


Figure 5.33 – Relative intensity loss measured by the FBCT during the last 20 seconds before the beams were extracted from the machine due to a coherent instability (Fig. 5.32).

beams. Figure 5.33 shows the comparison between the intensities of each bunch just before the extraction to 20 seconds before, that is before the coherent instability. We observe that only a few bunches of Beam 1 lost a significant part of their intensities, the losses of all the other bunches remained below the percent level. This asymmetry between the beams suggests that the instability was also not a coupled instability. The coherent signal observed in Beam 2 may come from an incoherent transmission of the signal of Beam 1 through the BB interactions.

5.3 Conclusion

Coherent BB modes have been observed in dedicated experiments. Their frequency is in good agreement with the ones obtained with multi-particle tracking simulations. Yet, in standard operation of the LHC, the presence of several bunches with a complex collision pattern, as well as the usage of a transverse feedback, brings the signal from such modes out of measurement reach.

Within the models developed, it was shown that the resonance of BB coherent modes with impedance driven head-tail modes can lead to strong coherent instabilities. In realistic configurations of the LHC, the transverse feedback was shown to be effective against these instabilities.

Results from a semi-analytical model based on normal mode analysis of the linearised

system are in agreement with self-consistent multi-particle tracking simulations. A short experiment dedicated to these effects showed results compatible with the predictions of the models. Nevertheless, lacking proper diagnostics the exact nature of the instability could not be determined.

Some observations of instabilities with beams separated with a small transverse offset at the IP during the 2012 run of the LHC are candidates for coupling instabilities predicted by the models. As for the dedicated experiment, the exact nature of these instabilities could not be determined due to the lack of diagnostics. A full understanding of the stability of the beams in such configurations, required to assess the feasibility of luminosity levelling using a separation between the beams at the IP, requires further experimental studies.

6 Applications for the operation of the LHC

This chapter depicts stability issues which have plagued the LHC 2012 proton run, for which a fully satisfactory explanation could not be found within the models described in previous chapters. As shown in Fig. 6.1, despite the improvements of the beam brightness provided by the injector chain, in particular thanks to the new Super Proton Synchrotron (SPS) optics Q20 [79], the brightness of the beams in collision remained constant over the year. This degradation of the beam brightness during the cycle is mainly due to transverse coherent

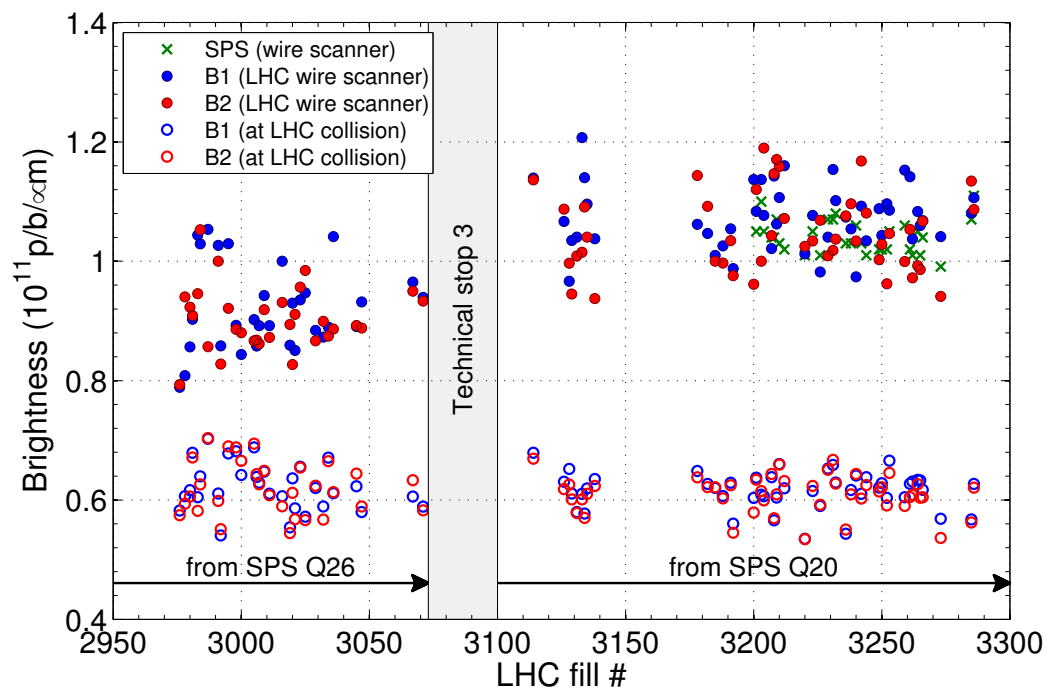


Figure 6.1 – Comparison of the beams brightness at injection and at the beginning of luminosity production, for different fills during the 2012 proton run. Courtesy H. Bartosik [79]

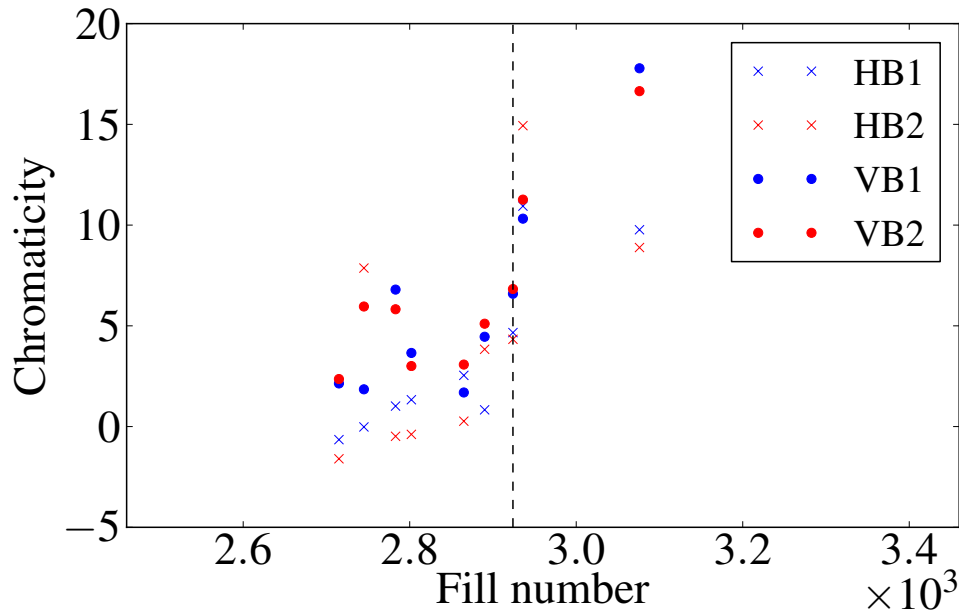


Figure 6.2 – Chromaticity measurements from the BBQ at the end of the squeeze for each fill for luminosity production of the LHC 2012 proton run. The vertical dashed line mark fill number 2924, when several operational parameters were changed, including the chromaticity.

instabilities occurring at the end of the squeeze. Despite the lack of a complete explanation for these instabilities, an operational solution is proposed and explored, such as to avoid them and provide large margin to further increase the beam brightness.

6.1 Instabilities at the end of the squeeze

6.1.1 First part of 2012

The starting values of the chromaticities in the LHC is 2 units in both planes and for both beams. These values were chosen based on single beam stability considerations [80], without consistent modelling of BB effects and of the transverse feedback. Figure 5.16 suggests that these considerations were justified, as the maximum imaginary tune shift is reasonably small in this area. The maximum imaginary tune shift is rather sensitive to the value of the chromaticity. Besides, as shown in Fig. 6.2, the chromaticity was measured rarely over the full LHC cycle, and the few measurements available suggest a lack of fill to fill reproducibility. In the first part of the year, the average chromaticity seems close to the 2 units, but with large deviation between -2 and seven units. During this period, there were several observations of instabilities at the end of the squeeze. Figure 6.3 shows the statistics of the fills that went to

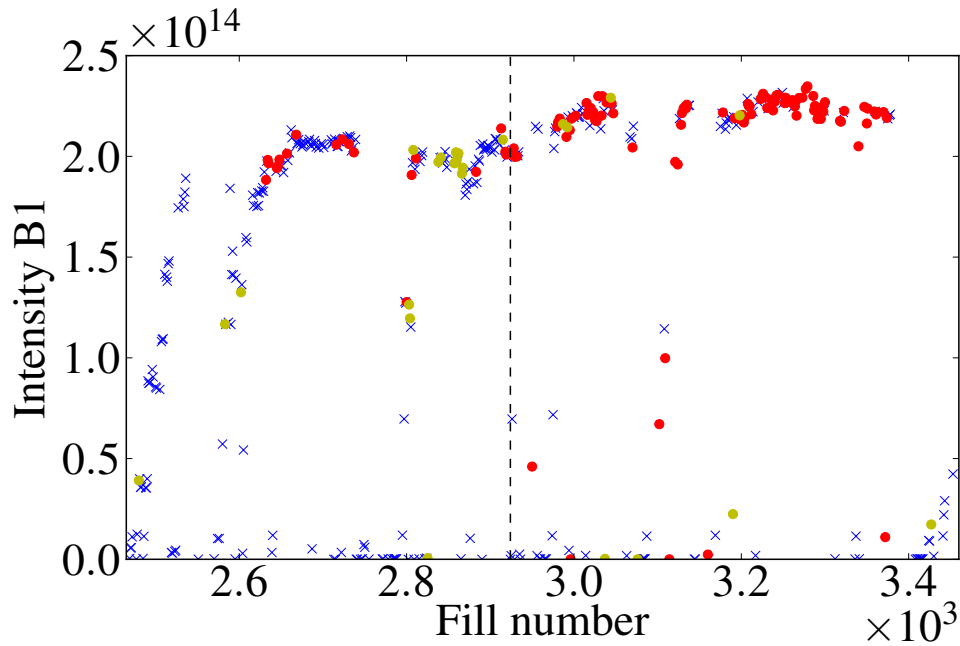


Figure 6.3 – Intensity at the end of the squeeze for all fills during the 2012 proton run. The intensity is marked with a blue cross for fills without observations of coherent instabilities, a red dot if an instability was observed at the end of the squeeze and a yellow dot if an instability was observed while bringing the beams into collision (Sec. 5.2.3). The vertical dashed line mark fill number 2924.

luminosity production without instabilities at the end of the squeeze and those which went to luminosity production with degraded beam brightness due to an instability at the end of the squeeze. While the beam parameters do not vary significantly during these fills, the stability of the beams strongly varies. The chromaticity measurements do not allow for a quantitative comparison with the models, yet the large chromaticity variations may explain the different behaviour from fill to fill, in term of coherent stability. During the second part of the year, i.e. with significantly higher chromaticity, the behaviour became very reproducible from fill to fill, again in accordance with Fig. 5.16. Indeed, the maximum imaginary tune shift is less sensitive to chromaticity variations in a configuration with large transverse feedback gain and large positive chromaticity.

As mentioned in Sec. 4.2.1, the negative polarity of the octupoles was chosen in the design phase due to single beam considerations, yet the incoherent effects of the LR interactions leads to a reduction of the stability diagram during the betatron squeeze. As the instabilities were observed at the end of the squeeze, this reduction appeared as a cause for the instability. It was therefore decided to change the polarity of the octupoles in order to avoid this effect [?], keeping in mind that in this configuration, the octupoles provide a more critical stability diagram before the squeeze, i.e. before the effects of the LR interactions becomes significant. As a result, instabilities were observed before the squeeze in the first cycles after the

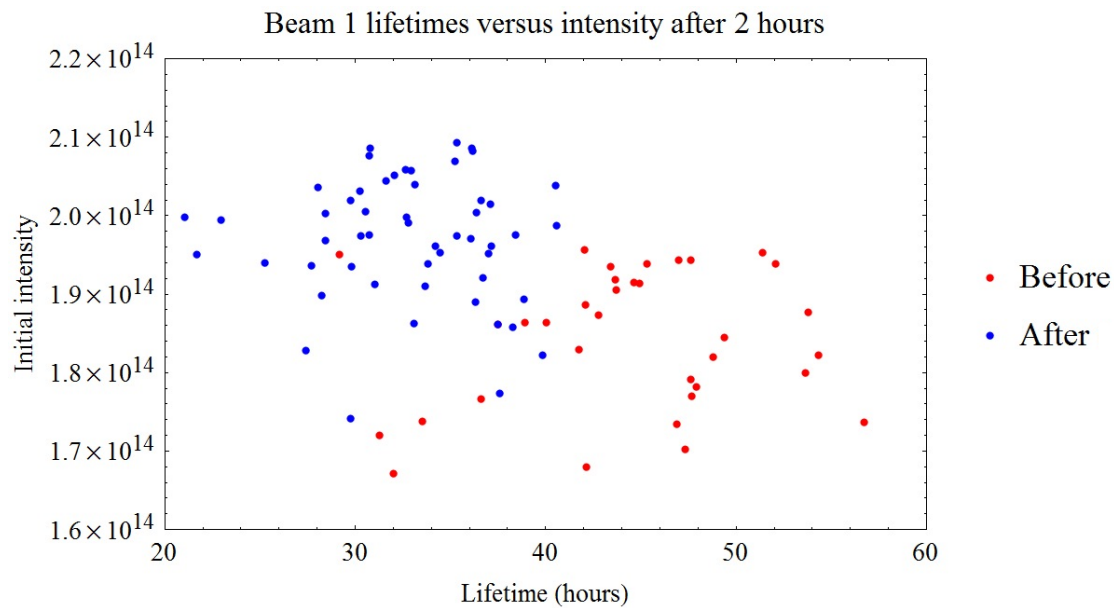


Figure 6.4 – Luminosity lifetime measurement before and after the change of configuration. Courtesy M. Lamont [81].

change of polarity of the octupoles, therefore the chromaticity was immediately increased by several units, which lead to a new type of instabilities, with a less severe impact on the beam parameters. The deterioration of the collider performance due to these instabilities were considered acceptable, therefore these new configuration, with positive polarity of the octupoles and high chromaticity, was used for the second part of the 2012 proton run.

6.1.2 Second part of 2012

While the new configuration allowed for a great performance of the LHC in 2012, there are two main aspects that suggest that this configuration is far from optimal. The first aspects is the limit in beam brightness, which was discussed previously. The second, is the luminosity lifetime. Indeed, the new configuration features strong lattice nonlinearities, high chromaticity and transverse feedback gain, the effects of which may potentially degrade the beam brightness through various processes. This is confirmed by the measured luminosity lifetime after 2 hours of luminosity production (Fig. 6.4). In other words, there is a strong interest in finding optimized parameters that improve both the peak luminosity and the beam lifetimes.

Referring again to Fig. 5.16, we observe that the new configuration does not suffer from the sensitivity to chromaticity variations, as opposed to the small positive chromaticity, in accordance with the observed reproducibility of the instabilities in this configuration, visible in the left part of Fig. 6.3. While this behaviour fits qualitatively well with the models,

comparing qualitatively the coherent tune shifts from the CMM to the stability diagram at the end of the squeeze (Fig. 4.6), we observe that all of the coherent tune shifts are well inside the stable area, even when doubling the effect of the beam coupling impedance. From Fig. ??, we see that the typical coherent tune shifts of the most unstable modes with high chromaticity and high damper gain have an imaginary part in the order of 10^{-5} , the corresponding real parts are in between $\pm 10^{-4}$. In this configuration, a current of around 100 A in the octupoles is sufficient to stabilize the beams. These results of the linear model are confirmed by short term multi-particle tracking. We deduce from this analysis that the cause for these instabilities lays outside of the models. Potential inaccuracies of the impedance model are under investigations [82], also distortions of the particle distribution and consequently of the stability diagram, as discussed in Sec. 4.3, is not excluded, yet experimental evidences are lacking.

The beams brightness in 2012 seemed limited to around $0.6 \cdot 10^{11}$ p/ μm per bunch, yet this represents twice the design value. While other configurations, in terms of chromaticity, transverse feedback gain and octupoles strength, may lead to a higher limit in term of beam brightness, it seems unlikely that larger factors may still be reached. However, observing the spectrogram of an instability at the end of the squeeze (Fig. 6.5), we notice that the instability vanished when the beams are brought into collision. This occurrence is not an exception, there were no observations of instabilities when the beams were colliding HO, consistent with the large stability diagram provided by the incoherent effect of the HO interactions (Sec. 4.2.3). This observation motivates studies of the possibility to use the stabilizing properties of the HO collisions earlier in the operational cycle, with a large potential improvement in term of brightness limitations.

6.2 Squeezing with colliding beams

Performing the squeeze with colliding beams has two main aims. First, it is a promising luminosity levelling technique, as it also offers advantages from the single particle dynamics point of view [83]. It is the main option considered for high luminosity upgrade of the LHC [84]. Secondly, it allows to avoid the critical phase of the current operational cycle, at the end of the squeeze, in terms of stability. When reducing β^* , the beam size in the final focusing magnets becomes large and they eventually become the limiting physical aperture, thus limiting the minimum β^* , consequently the maximum luminosity achievable. In order to protect these magnets, the collimators are set such that they define the aperture [53]. Consequently, the collimator gaps are closely related to the achievable β^* [85]. When pushing the performance, the gaps between the jaws of the collimators become small. This increases their contribution to the beam coupling impedance, having a significant impact on the beam stability [19]. The speed at which the collimators may be moved is limited, as the acceptable radiation dose due to particle losses when scraping the tails of the beam are limited. Therefore, in 2012, the movement of the primary and secondary collimators from their settings at injection

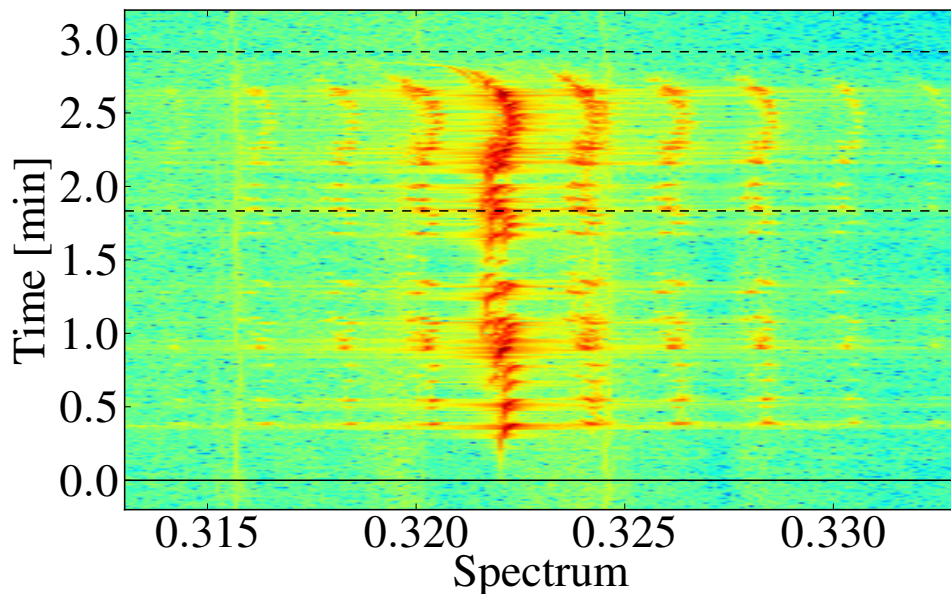


Figure 6.5 – Spectrogram measured by the BBQ in the vertical plane of beam 1 at the end of the squeeze, during fill 3253. The horizontal black lines mark the end of the squeeze (solid), as well as the start and end of the process that brings the beams into collision (dashed).

to the tighter settings required at the end of the squeeze was performed during the energy ramp. However, this results in an increased impedance from the end of ramp up to the end of the cycle, whereas the tighter settings are strictly required only at the end of the squeeze, when the minimum β^* is established. One could drastically reduce the beam brightness limitation due to impedance driven instabilities by moving the collimators to tight settings only once the beams are in collision, i.e. once the stability is ensured by the large detuning of HO collision. This, of course, implies that the beams are being brought into collision with a β^* larger than the minimum, i.e. before the end of the squeeze. The collimator movements, as well as the remaining part of the squeeze should then be performed while colliding HO.

Whereas very simple from the conceptual point of view, squeezing with colliding beams has many implications on the operation of the LHC. Also, those implications are different whether this procedure is considered for beam stability only or for luminosity levelling. A good control of the orbit at the IPs is required to maintain the beams in collision during the procedure. The current implementation of the LHC control system uses the concept of beam process to operate the squeeze [86]. The beam process contains functions to drive the power converters, collimators and RF systems for a fixed sequence of optics changes defined in advance. This implementation does not allow to have the flexibility required for luminosity levelling independently at all IPs. Different options to overcome the difficulties

of luminosity levelling with β^* will be discussed in Sec. 6.2.2.

6.2.1 Orbit stability at the IP

The key to reliably operate the betatron squeeze with colliding beams is the stability of the orbit at the IPs. As discussed in Sec. 4.2.2, the stability diagram from HO collision is drastically reduced when colliding with an offset in the order of $1 - 2 \sigma$. A series of experiment was performed in order to demonstrate that the squeeze can be executed with the required orbit stability at the IPs.

Results

In a first attempt, the machine was filled with two bunches per beam with intensities approximately $1.3 \cdot 10^{11}$ protons per bunch and normalised emittances around $1.6 \mu\text{m}$. The standard operational sequence was executed up to the $\beta^* = 3 \text{ m}$ step of the squeeze. The beams were then brought into collision at the IPs 1 and 5. The rest of the squeeze beam process has then been executed in steps down to $\beta^* = 0.6 \text{ m}$. The tune feedback was turn off during the procedure, while the orbit feedback was on during the execution of the squeeze steps. After each step, a luminosity optimization was performed and the resulting corrections incorporated. The specific luminosity measurement during this procedure is shown in Fig. 6.6. The degradation of the luminosity observed during the execution of each step is due to the drift of the orbit at the IPs. The expected luminosity is then recovered by an optimization of the collision point, as shown in Fig. 6.7 which compares the optimized luminosity for each step of the squeeze to the computed one. The separation between the beams at each IP can then be computed from the luminosity (Fig. 6.8), assuming a negligible variation of the emittances, which is consistent with the measurement. The variation of the separation during this first attempt would not be compatible with the usage of head-on collision during the squeeze to stabilize the beams, which requires the offset to remain below $\sim 1 \sigma$ in order to maintain a sufficiently large tune spread. This is confirmed by the observation of an instability before the last step of the squeeze. It is necessary to test the reproducibility of the corrections applied, in order to ensure smaller orbit variation at the IPs. Therefore, the same procedure was re-run three weeks later, once with a single bunch and then with a train of 36 bunches. During these tests, the maximum drift of the separation stayed below 1σ during the squeeze (Fig. 6.8), demonstrating the long term reproducibility of the corrections applied [87].

In order to get a deeper understanding of the operational options that would allow to reliably keep the beams in collision during the squeeze, it was tried, 3 months later, to go through a larger β^* range, from $\beta^* = 9 \text{ m}$ down to $\beta^* = 0.6 \text{ m}$, with colliding beams. It was hoped that the corrections applied in the last part of the squeeze during the first tests will still be

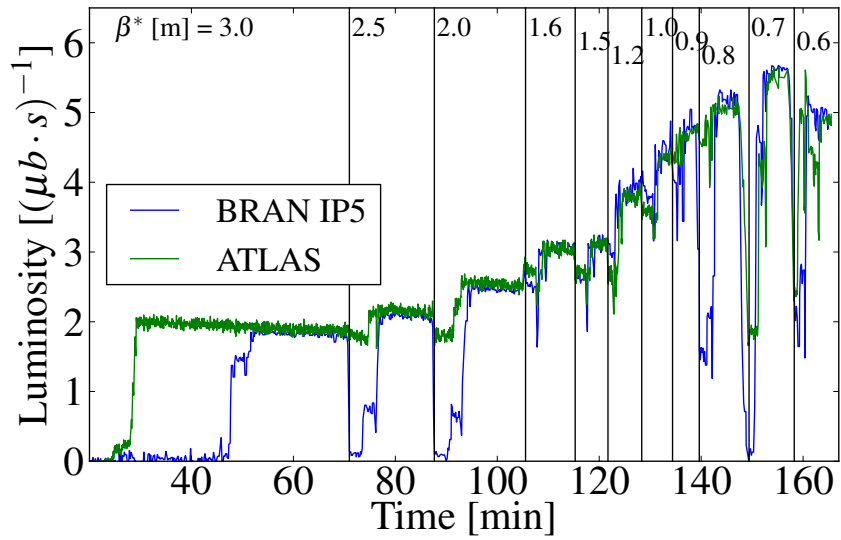


Figure 6.6 – Luminosity during first attempt of β^* levelling

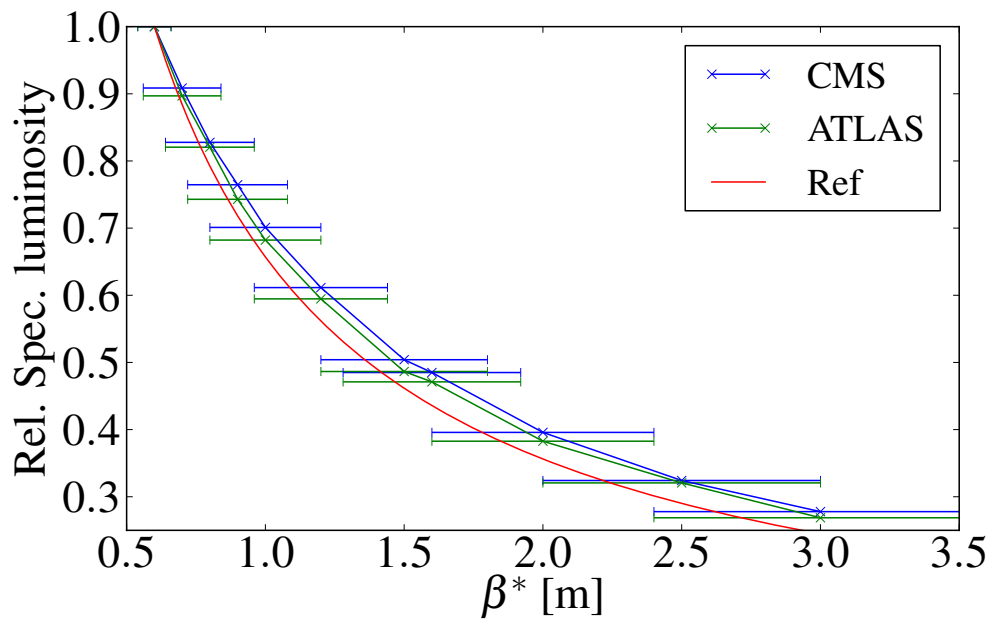


Figure 6.7 – Measured and expected (cf Eq. 2.68) specific luminosity reduction due to β^* .

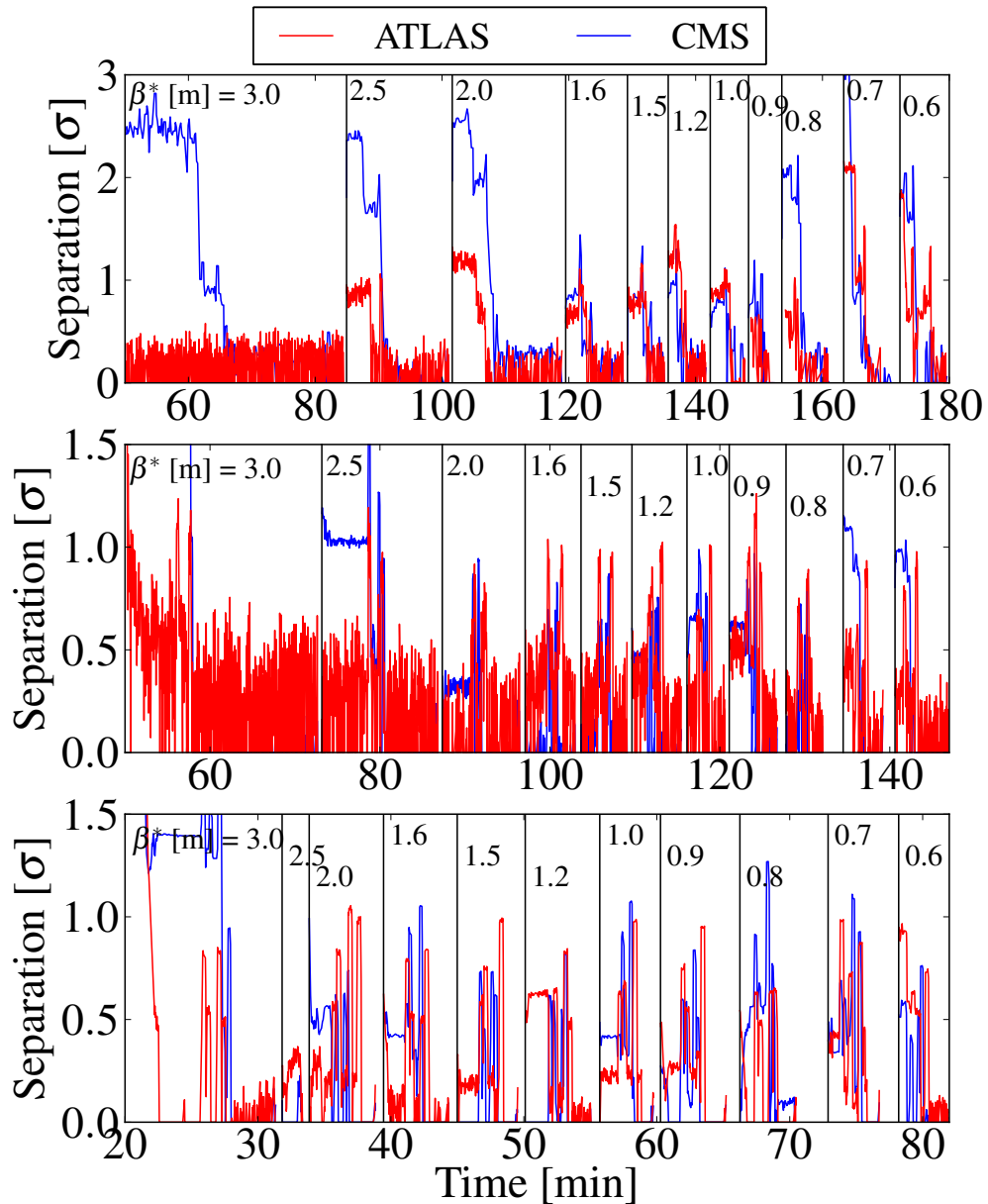


Figure 6.8 – Transverse separation at the IP deduced from the measured luminosity reduction factor during the first three executions of the squeeze with colliding beams, chronologically from top to bottom. The first two were executed with a single bunch per beam, the last with a train of 36 bunches spaced by 50 ns.

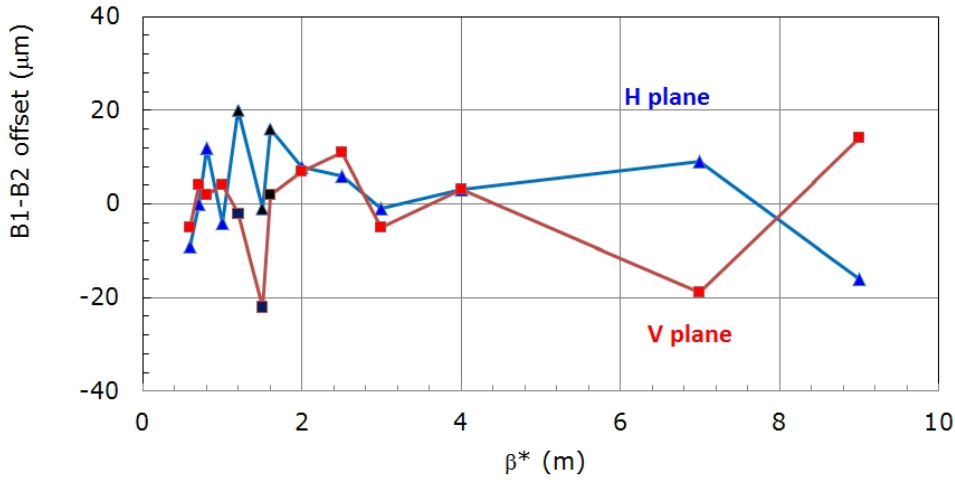


Figure 6.9 – Beam separation at the interaction point interpolated from adjacent BPMs.

	IP1	IP2
Horz.	0.3 ± 6.7	0.3 ± 5.7
Vert.	-0.5 ± 5.5	-0.1 ± 5.4

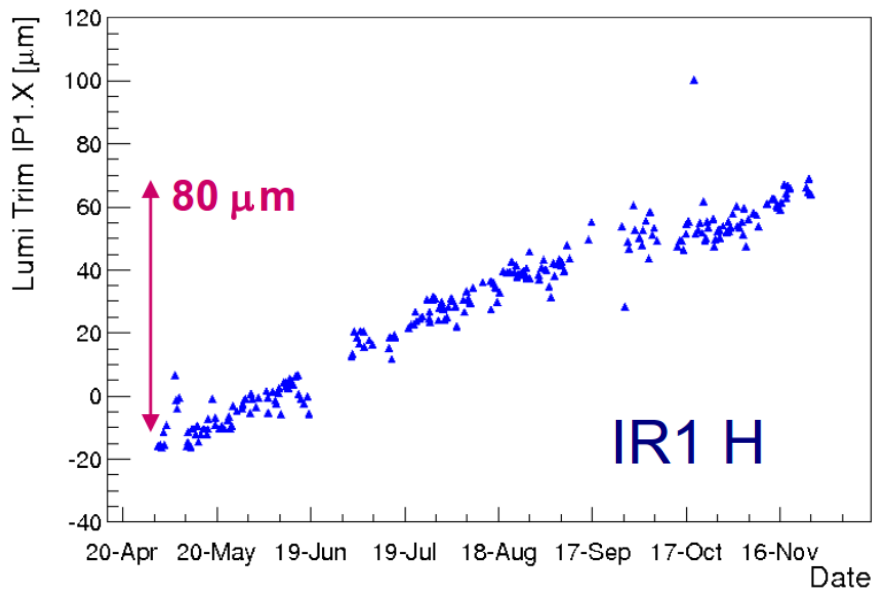
Table 6.1 – Average fill to fill difference of the orbit correction required to optimize the luminosity at the IPs 1 and 5 in μm .

valid. This was however not the case, as separations up to 2σ were observed during the procedure. This points out that a careful set-up of the orbit has to be performed, and possibly orbit corrections cleaning have to be performed from time to time, to account for the slow mechanical movement of the different element of the machine [88].

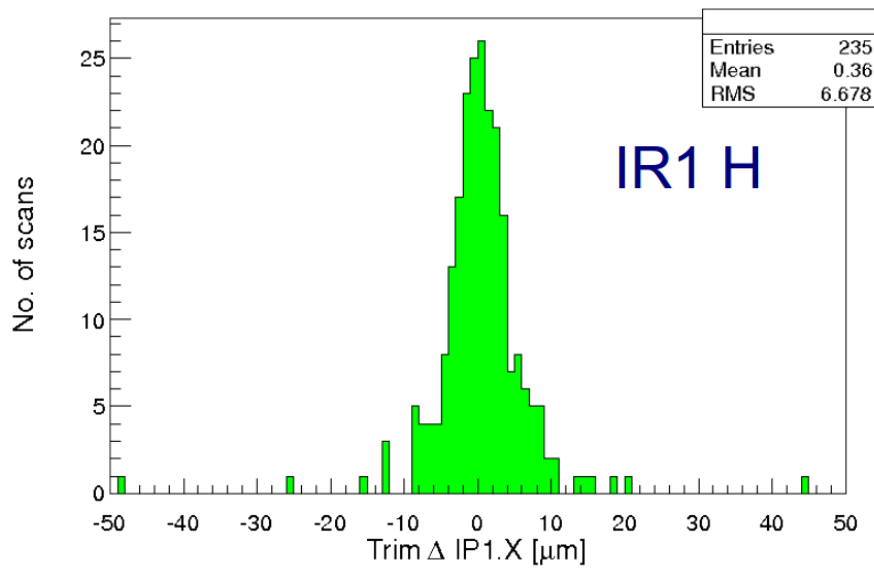
If the resolution permits, one could use the two Beam Position Monitors (BPMs) located on each side of the IPs to measure the beam separation and possibly feed this information to the orbit feedback. The measured beam separation during this last experiment is rather encouraging (Fig. 6.9).

Reproducibility in standard operation

Figure 6.10 shows the orbit corrections at the IPs that had to be applied to optimize the luminosity at the end of the squeeze during physics fills of the 2012 run. One observes a slow drift over the year, even though significant, this drift is not problematic. Indeed, the average fill to fill differences mainly remain within acceptable boundaries (Tab. 6.1). The distribution of these differences, in Fig. 6.10b, shows the existence of some outliers, during which the separation became larger than a few σ . This implies that, whereas most of the time a feed forward procedure would be sufficient, the orbit at the IPs may not behave well during a few



(a) Time dependence



(b) Distribution of fill to fill differences

Figure 6.10 – Correction of the orbit at the IP from luminosity optimisation during the 2012 run. Courtesy J. Wenninger.

fills. In order to define a robust operational procedure, these cases, even though of limited amount, should not be neglected and therefore the effect of the lack of reproducibility for certain fills should be minimized.

To that purpose, one could consider the options of using an automatized luminosity optimization after each squeeze step or at least for a subset of them. This multiple optimization of the luminosity constitutes a significant overhead compared to the current squeeze and may require some minor changes in the implementation of the settings management. One can however expect that practical experience will lead to a good balance between robustness and overhead. In particular, the possibility to use BPM data may be of great help to maintain the beams in collision, in the cases where the machine reproducibility is not sufficient.

6.2.2 Controls aspects

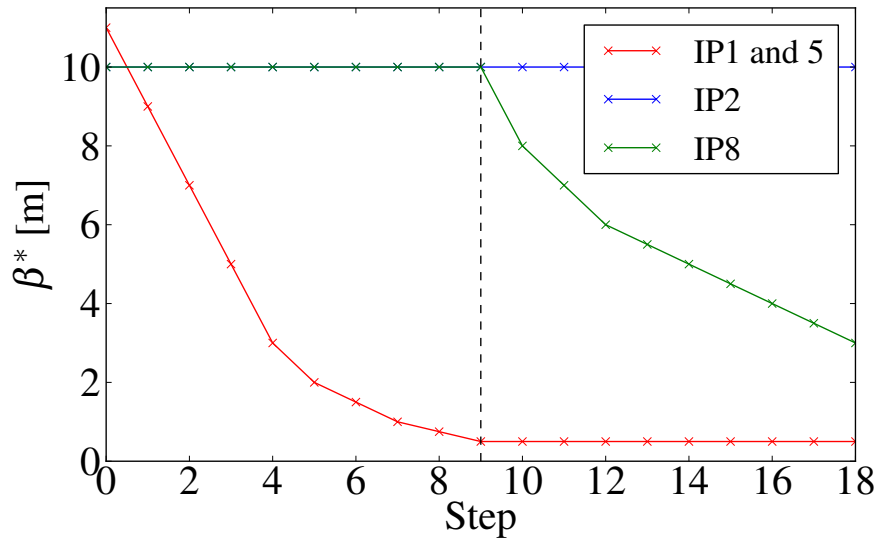
The implications on the controls when imposing collisions during the squeeze largely depend on the aim. Different scenarios have been sketched, they do not however represent the full set of possibilities.

Up to now, the squeeze has been operated in predefined series of step, from one optics to the next, each corresponding to defined values of β^* at the different IPs, varying towards the targeted values. The sequence of optics defines the squeeze beam process, which is executed during each fill. The beam process contains both global and local machine settings and corrections along the procedure [89], its full commissioning is not trivial. Therefore, the current control system does not allow to easily change the sequence of β^* configurations. We, therefore, distinguish two cases, whether the flexibility in the choice of β^* at each IP as a function of time is required or not.

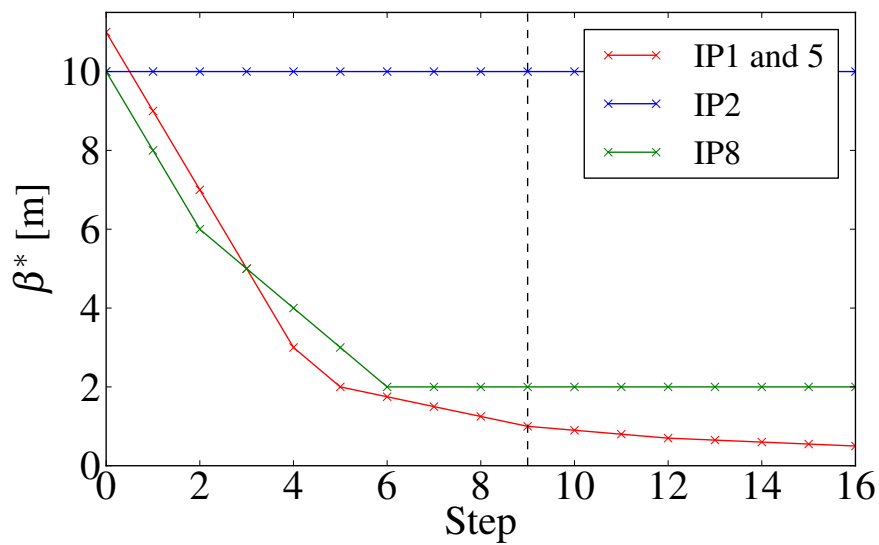
Low flexibility scenario

We are considering cases where a high flexibility in the choice of β^* at each IP is not required, e.g. if HO collision during the squeeze is required for stability reasons or in the case where the sequence of β^* could be defined in advance and run synchronously at the IPs. There are various scenarios in which this could be the case, two of them are pictured in Fig. 6.11.

In these cases, the present control system is appropriate, as one can define a beam process and play it in steps, as it has been done during the experiment presented above. Only minor changes have to be implemented such as to maximize the operational efficiency and robustness, as already discussed.



(a) β^* luminosity levelling only at IP8



(b) β^* luminosity levelling synchronously at the IPs 1 and 5

Figure 6.11 – Two examples of squeeze sequence for β^* luminosity levelling with low flexibility.

High flexibility scenario

In the case where each IP requires to change β^* at any time, independently from the other IPs, then the present control system is no longer appropriate. Indeed, the concept of beam process is no longer applicable, since the sequence will, a priori, be different at each run. Therefore, the global corrections defined for a specific sequence are no longer valid and a conceptual change of the control system is required.

6.2.3 Additional requirements for commissioning

As already mentioned, good orbit stability at the IP is a requirement to reliably operate the squeeze with colliding beams. Based on the excellent performance of the orbit feedback system, it is not considered to operate the squeeze without it. It is possible to improve the orbit stability as well as the effect of the orbit feedback by proper cleaning of the orbit corrections. Indeed, the feedback uses an SVD based method to compute the proper settings for each corrector based on the BPMs data, with specific algorithm to maximize robustness in case of noisy or faulty BPMs. These algorithms have side effects on the orbit reproducibility that can be minimized by proper correction of the orbit during the commissioning as well as regular re-correction during the year [88]. Also, optics corrections, as well as validations of the collimator settings are now focused on the fully squeezed machine. In case β^* luminosity levelling is used, the intermediate optics will require as much attention. A significant overhead with respect to the present commissioning time has to be expected.

6.3 Chromaticity control

As discussed in Chap. 5, the chromaticity has a strong impact on the beam stability. Especially for small positive chromaticity, the control of its value to the level of one unit is critical. This has strong consequences on the operation of the machine. The chromaticity measurement in the LHC is based on the measurement of tune modulations while modulating the beam momentum [90]. In typical conditions for luminosity production, a high transverse feedback gain is required for the coherent stability of the beam. This strongly reduces the signal measurable by the BBQ and consequently render the measurement of the tune difficult. Ways around these shortcomings are discussed in [91], based on a measurement of the tune of a subset of bunches for which the transverse feedback gain is lower. While not available during the 2012 run of the LHC, such a measurement is critical to properly control the chromaticity during operation with full intensity beams, for the following reasons. Long-range interactions have a strong impact on the chromaticity [92]. While their effect in the two high luminosity interaction regions is mitigated by the alternating crossing angles [36], the effect in the presence of uncorrected dispersion at the location of the LR interactions, as well as LR interactions in the two lower luminosity experiments may have an impact of few units on the chromaticity. Arising from LR interactions, the strength of these

effects varies with the beam parameters and is different for every PACMAN bunch. In the presence of collision with a small transverse offset, either while bringing the beams into collision or for luminosity levelling purposes, chromaticity variations in the order of few units are also expected [93]. Being driven by HO collisions, this effect will be different for different beam parameters and for every Super-PACMAN bunch. Also, the presence of strong octupole magnets may lead to variations of several units of chromaticity depending on orbit variations, due to feed down effect [94]. In 2012, the chromaticity was measured in dedicated fills with smaller intensity beams. While the effect of the octupole feed down is well measured, the effects linked to BB interactions are negligible in these conditions. Such a measurement is clearly not sufficient to maintain the chromaticity close to the values that maximise the coherent stability of the beam.

6.4 Conclusion

It was demonstrated that the models available cannot provide fully satisfactory explanations for some observations of instabilities during the 2012 run of the LHC, towards the end of the betatron squeeze. However, consistently with models, the beams were found to be coherently stable for all configurations where HO collisions are established. Consequently, establishing HO collision before the betatron squeeze appears as a good solution in order to push further the brightness limitation due to coherent instabilities. It was shown in dedicated experiments that the orbit stability required to maintain the collision during the procedure is within reach. The full procedure represents a significant operational complications that needs to be further assessed and tests are foreseen in 2015 [95].

7 Conclusion

Motivated by the observation of coherent instabilities during the 2012 physics run of the LHC, several aspects of the coherent stability of the beams have been studied taking into account the effects of the beam coupling impedance and the beam-beam interactions. Three models with different domains of applicability and computing requirements were developed or extended to explain the observed instabilities. Analysis of the data acquired during the operational cycles as well as dedicated experiments were performed to support the models.

The first model extends the stability diagram analysis by including the incoherent effect of beam-beam interactions in arbitrarily complex configurations. This was achieved by numerically integrating the dispersion integral using the amplitude detuning given by single particle tracking simulations as input. While this model neglects the coherent contributions of beam-beam interactions to the dynamics, it provides a good insight on the strength of the Landau damping in the presence of beam-beam interactions. Several observations of instabilities could be understood within this model. Some coherent instabilities at the end of the squeeze and while bringing the beams into collision could be explained by a destructive interplay between the long-range beam-beam interactions and the lattice nonlinearities, leading to a loss of Landau damping. Also, instabilities with beams separated with a small transverse offset for luminosity levelling purposes could be explained by a loss of Landau damping, caused by the modification of the amplitude detuning and consequently of the stability diagram due to the near HO interaction. The measurements of the separation between the beams at the IP when the instabilities occurred are compatible with the critical separations predicted by the model.

Several measurements of the beam stability were performed by probing the strength of the Landau damping required to stabilise the beam using the lattice octupoles. These measurements were found inconsistent with one another. The lack of proper measurement of the beam size, and most importantly of the full beam distribution, prevents quantitative comparison with the models.

A second model, the circulant matrix model, was revived and extended in order to study the coherent effects of the multiple beam-beam interactions and the beam coupling impedance. Nonlinear effects are neglected in this model, consequently it does not include the effect of Landau damping. This model shows the presence of strong coupling instabilities when the frequencies of the coherent beam-beam modes approach those of the impedance driven head-tail modes. This semi-analytical model was used to investigate the behaviour of the coherent modes of oscillation under variations of critical machine and beam parameters. The effect of the chromaticity, the transverse feedback, the bunch train structure of the beams as well as the type of beam-beam interactions were studied, giving quantitative predictions to be tested in dedicated experiments and also for realistic LHC operational configurations. It was shown that the perfect resistive transverse feedback works well against the coupled instabilities, in several LHC-like configurations of long-range and head-on beam-beam interactions. Machine configurations with high positive chromaticity also showed a reduced sensitivity to the coupling instability.

Extensive scans in chromaticity and transverse feedback gains showed that different combinations of these parameters may be suitable for the operation of the LHC. Experimental verifications are required to fully assess the potential of each configuration taking into account other constraints, e.g. the required chromaticity control, the effect on the beam lifetime, the unknowns on the impedance model and the imperfections of the transverse feedback.

A self-consistent analytical description of the coherent dynamics, including the effect of Landau damping, in the presence of multiple beam-beam interactions is currently lacking. The third model fills this gap by considering consistently both the coherent and incoherent effects of the beam-beam interactions, as well as the effect of the beam coupling impedance. This is achieved with multi-particle tracking simulations of the two beams, evaluating self-consistently the different forces on each particle. Such a model is very demanding in terms of computing resources. It is therefore not well suited for parameters scans but rather allows predictions of the simpler models to be tested, extends their domain of applicability and may allow other instability mechanisms to be explored. While most of the predictions of both the stability diagrams and the circulant matrix model were validated by the self-consistent model, the two following aspects required further investigations.

The stability diagram depends strongly on the exact beam distribution. As a result, one may expect a large impact on the beam stability from a distortion of the distribution due to various diffusion mechanisms. Using multi-particle tracking simulations, it was demonstrated that, in the presence of amplitude detuning, an external excitation from an active device or from the lattice leads to distortions of the beam distribution. The numerical integration of the dispersion integral, using the simulated distribution showed a significant deterioration of the stability diagram. This suggests that such an effect could be the cause for the discrepancies observed between measurements, performed in similar conditions, of the strength of the lattice nonlinearities that is required to stabilise the beams.

Careful comparison between the results provided by the circulant matrix model and tracking simulations on their common domain of applicability revealed the limitations of the normal mode analysis when studying the behaviour of bunch trains. The non-normal behaviour of such systems, similarly to multi-bunch beam breakup instabilities, dominates over the normal behaviour given by the normal mode analysis. Yet, the behaviour of the powers of the matrix given by the circulant matrix model shows that the two models are in good agreement. Investigations of the pseudo-spectrum of these matrices suggests that non-normal effects due to the presence of multiple bunches are well mitigated by the transverse feedback.

Despite their inherently large computing requirements, self-consistent tracking codes have proven very effective to describe complex mechanisms involving several different effects that were usually treated separately. In many cases, a purely analytical approach is far out of reach. Thus, a strong effort was put into optimising the code for state-of-the-art parallel computers. The use of ever more powerful computers will doubtlessly increase the reach of such an approach.

Finally, repeated observations of instabilities at the end of the squeeze, despite the large stability diagram available, may be attributed to the unknown distribution of the particles in the tails of the distribution which provide Landau damping. This has motivated the study of an innovative solution in order to push further the brightness limitations due to coherent instabilities. The possibility to perform the squeeze with colliding beams, so taking advantage of the strong Landau damping provided by head-on collisions, is being considered for the LHC and its upgrades. Experimental studies were carried out to demonstrate the feasibility of such a procedure. It was shown that the required orbit stability at the IP can be achieved. Some operational difficulties still need to be overcome; they will be addressed during the 2015 run of the LHC. The baseline for the HL-LHC includes this procedure.

A COMBI

COMBI is a multi-particle tracking code meant for self-consistent simulation of coherent multi-bunch BB interaction. It was initially developed by J. Jones and W. Herr [96, 97] and further extended with a first level of parallelisation with Message Passing Interface (MPI) by T. Pieloni [74]. Initially designed for accurate coherent spectrum simulation, the field of application of such simulations is much wider. COMBI, as well as other similar codes have been used to simulate the long term behaviour of the beam parameters, in particular the emittance [74, 98, 99]. Also, in Chap. 5.2.1, we showed the results of coherent stability simulations in the presence of BB interactions and beam coupling impedance. Nevertheless, the requirements in term of computing resources of such simulations are significant, efficient parallelisation techniques are therefore required. In the next sections, I will first demonstrate the performance of a hybrid parallelisation scheme and then describe the different modules available.

A.1 Implementation of the first level of parallelisation

Each beam is composed of a set of bunches counter rotating along their respective ring. These bunches are placed in the N_{slot} slots available for each beam. The rings are modelled by a sequence of **actions** (Sec. A.3) located at the $2 N_{\text{slot}}$ potential interaction points between the bunches of each beam. Each **action** implements the processing of the macro particles coordinates and momentum resulting from the the BB force or other magnetic elements at that location. While the effect of magnetic elements does not require communication with other bunches, the BB interaction requires the two colliding bunches to exchange informations. The execution of the code is pictured in Fig. A.1.

COMBI is parallelised at the bunch level using OPENMPI [100], an open implementation of a MPI library [101]. Each MPI process simulates the behaviour of a single bunch. These processes are referred to as **slave** processes, coordinated by a **master** process. The **master** is aware of the configuration of the machine, defined by the **action** sequence. The execution is done in steps, at which the **master** assigns **actions** to be executed by the **slaves** according to

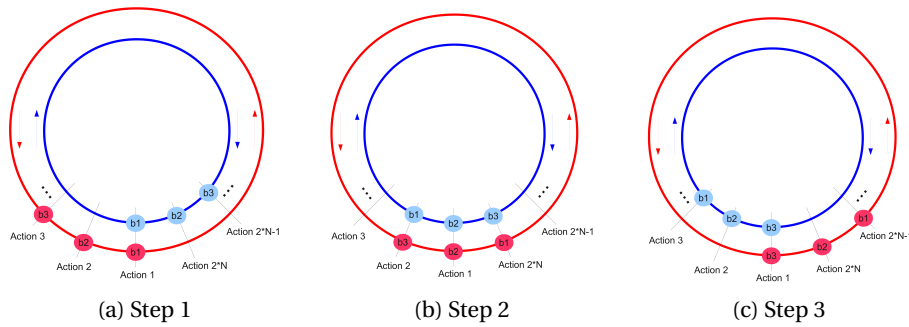


Figure A.1 – Three steps of the execution of the COMBI code with three bunches per beam. The blue disks represent bunches of the beam rotating clockwise and in red the bunches of the beam rotating counter-clockwise. The black lines linking the two beams shows the position of potential BB interactions. A BB interaction occurs only if the bunch finds a partner in the other beam.

their locations with respect to the **action** sequence. It then waits for all the **slaves** to finish their processing before moving each bunch one step along the **action** sequence and thus proceed to the next step, i.e. each bunch moves to the next potential interaction point. All messages are sent via MPI. This parallelisation allows to treat arbitrary configurations of **actions** and bunches, even with large number of bunches, without any modifications of the code. This flexibility is a requirement, nevertheless, there exists practical configurations for which this parallelisation is far from optimal.

A.1.1 Performance

The following performance tests were performed on a 12 core HP blade¹. Let us consider a practical case, a series of bunches colliding at a set of consecutive IPs, as described in Fig. A.1. Figure A.2 shows the performance of the parallelisation of COMBI in this configuration. The total number of **actions** to be performed per turn increases quadratically with the number of bunches per beam, whereas the number of **actions** per turn for each bunch increases linearly, which is clearly visible in the performance. The number of Central Processing Units (CPUs) required to achieve this scaling is equal to twice the number of bunches per beam plus one.

While already a remarkable gain, this parallelisation is often not sufficient when each **action** requires significant computing resources, for example when a high precision on the BB force, consequently a large number of macro particle, is required. Fig. A.3 shows the execution time as a function of the number of macro particles per bunch, for different number of bunches per beam.

An important drawback of this algorithm arises when considering real bunch configurations.

¹HP ProLiant BL460c G7 blade with 2 Intel(R) Xeon(R) CPU X5660 @ 2.80GHz with hyper-threading on.

A.1. Implementation of the first level of parallelisation

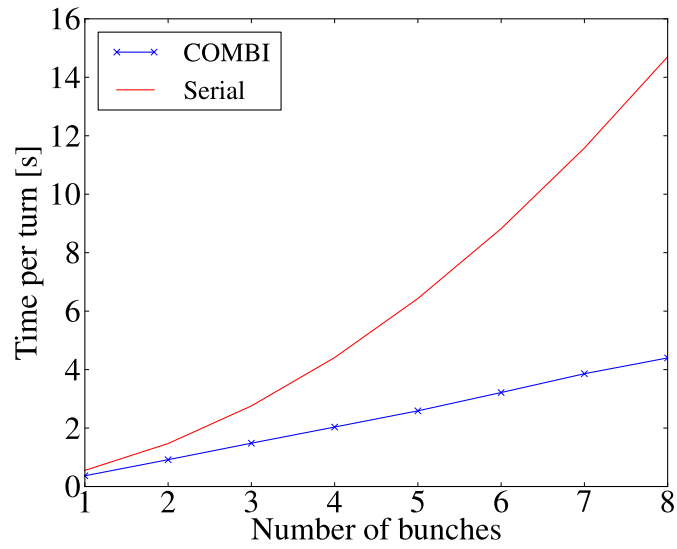


Figure A.2 – Comparison of the performance of the parallelised version of COMBI with an estimation of the equivalent serialized code.

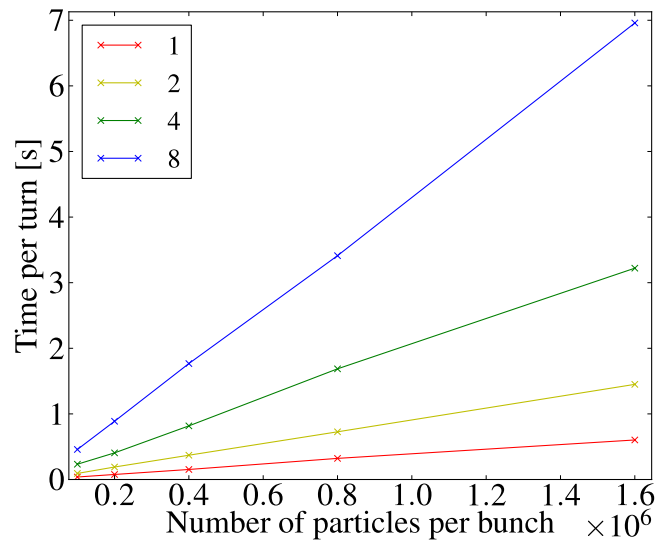


Figure A.3 – Execution time of COMBI as a function of the number of macro particle per bunch, for different number of bunches per beam.

The different bunches are usually not uniformly distributed along each ring. As pictured in Fig. A.1, most of the machine is actually empty. As a consequence, in this configuration, during step 1 (Fig. A.1a) and step 2 (Fig. A.1b), two bunches per beam do not have any **action** to perform, and therefore their respective CPUs are idling, waiting on the ones performing an **action**. In such configuration, a large amount of resources is wasted. Allowing **slaves** that have already finished their processing to move on to the next step instead of waiting on slower ones at each step is not an option, as, by nature, the **actions** to be taken in the next step depend on the result of previous ones.

Two approaches are considered to improve the execution speed of each **action** and avoid a waste of resources, by introducing a second level of parallelism.

A.2 A second level of parallelisation

The implementation of most **actions** is rather simple, but usually includes large independent loops over the macro particle representing the bunches, either to apply a modification of their position and momentum or to compute moments of the distribution. Such operation is not well parallelisable using MPI only, as the amount of memory to copy becomes significant, and therefore may become the bottleneck. Nevertheless, in many of nowadays machine a significant number of CPUs per node have access to shared memory, therefore a hybrid approach may lead to a significant speed-up. Two approaches will be considered, using either OpenMP or MPI with POSIX memory mapping.

A.2.1 Hybrid approach : COMBHY

Being written in FORTRAN and consisting of large independent loops, routines implementing the **actions** are parallelisable using OpenMP [102] without significant modifications of the code. Only the main thread will execute MPI calls and therefore the thread support level required is *MPI_THREAD_FUNNELED*.

While OpenMP provides an easy and effective way to speed-up the execution of each **action**, the waste of resources due to idling processes potentially remains an issue. Indeed, idling MPI processes are busy-waiting, the performance will, therefore, highly depend on the ability of the scheduler to use the CPUs running idling MPI process.

A.2.2 MPI and shared memory : COMBISH

In order to address the waste of resources, a pure MPI implementation sounds appropriate. However, most **actions** depend on all coordinates of each macro particles in the bunch, which then have to be copied. To overcome this issue, POSIX [103] memory mapping is used to share memory between processes, MPI is then only used to send instructions to the

different processes. As opposed to OpenMP, the sharing of the workload does not rely on the performance of the scheduler, however, the implementation requires major changes to the code and exposes the programmer to the topology of the machine.

The concept of **helper** process was implemented. The **master** being aware of the workload of the **slaves**, it can send the instruction to the idling ones to become **helper** for other working **slaves**, provided that the **master** is aware of which processes have access to shared memory. The **helper** then receives instructions from the **slave** that it has been assigned to, in order to share the processing to be applied on the macro particle coordinates stored in the shared memory.

A.2.3 Performance

The performances of both implementations are tested on a single node of Aries [104] in two configurations :

- **Low waste** N_b bunches colliding at 17 consecutive IPs.
- **High waste** N_b bunches colliding at a single IP.

In the low waste configuration, as there are many consecutive IPs, the number of BB interactions per bunch increases with the total number of bunches. The configuration during the significant proportion of the execution is like pictured in Fig. A.1b, therefore the processing of the **actions** is done in parallel. In other words, the first level of parallelisation is the most effective in this configuration.

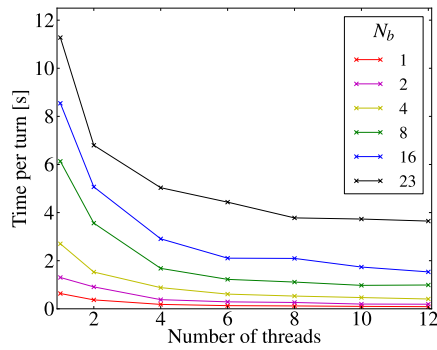
In the high waste configuration, there is a single IP, which implies that the number of BB interaction per bunch do not increase with the number of bunches. During the whole execution, the system is in a configuration similar to the one pictured in Fig. A.1a, i.e. most processes are waiting for a single **action** to be performed. The first level of parallelisation is highly ineffective in this configuration.

Most realistic configurations are neither like the low nor the high waste configuration, but rather in between. Therefore, the most attractive algorithm will be one performing well in both configurations.

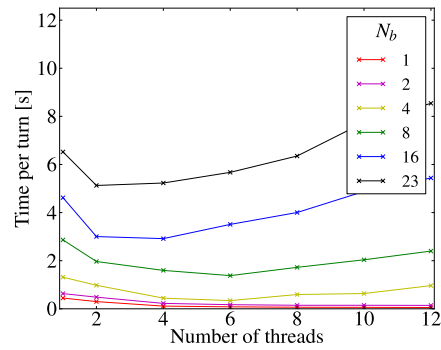
Figure A.4 compares the execution time of the hybrid version in the high waste configuration, compiled with either gcc² or Intel³. The Intel compiler allows a much better performance without parallelisation. It is interesting to note that, for both compilers, the performances with thread support enabled, yet using a single thread, are very similar to the version compiled without thread support. Nevertheless, the code compiled with Intel seems very sensitive

²Version 4.6.3

³Version 13.0.1

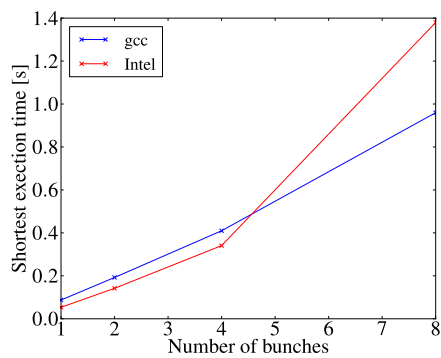


(a) gcc

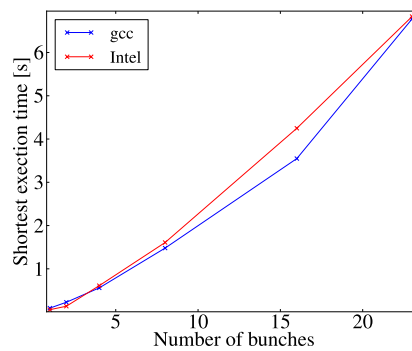


(b) Intel

Figure A.4 – Execution time of COMBHY as a function of the number of threads per process in the high waste configuration.



(a) High waste

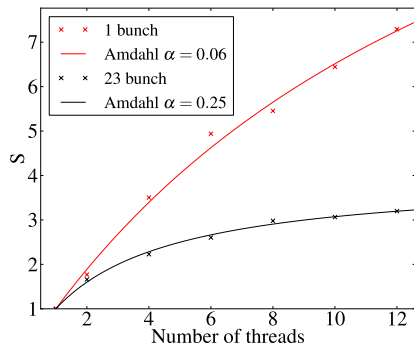


(b) Low waste

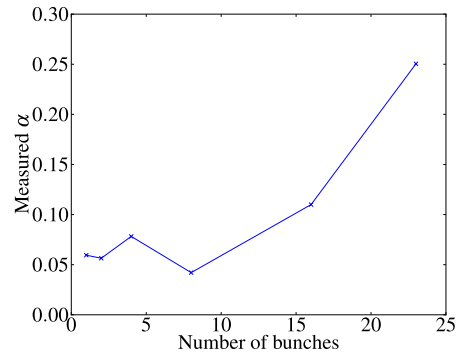
Figure A.5 – Best performance achieved by the hybrid version with both gcc and Intel compilers.

to oversubscription. Considering 4 bunches, i.e. 9 processes, the increase of the number of thread starts being unfavourable for more than 6 threads, which corresponds to a total of 54 threads running on 48 CPUs. However, in this high waste configuration, not more than 2 times 6 threads are busy at a time. This shows that, while performing well with a single thread, the hybrid code compiled with Intel is not capable of overcoming the waste of resources.

The code compiled with gcc performs much worse than the Intel compiled with a single thread. The parallelisation is however more effective, and does not lead to a deterioration of the performance while oversubscribing. As shown by Fig. A.5, the best performance achievable on a single node is very similar for both compilers, in both the low and high waste configurations.



(a) Amdahl's law fit



(b) Measured portion of non-parallelisable code

Figure A.6 – Least square fit of Amdahl's law on COMBHY's performance measurement in the high waste configuration.

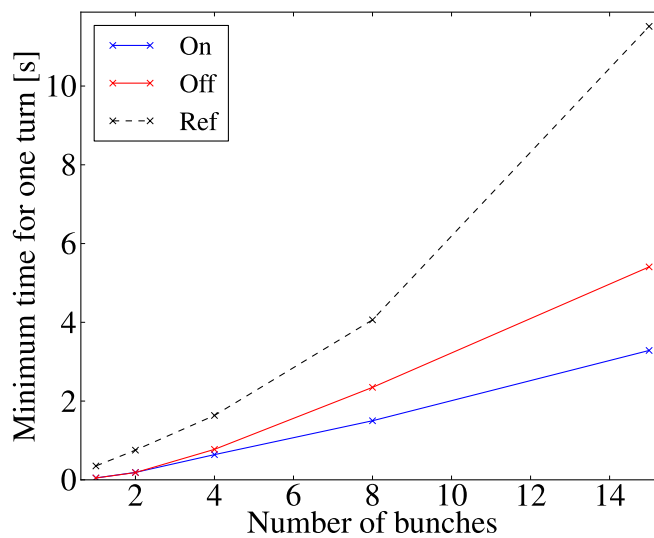
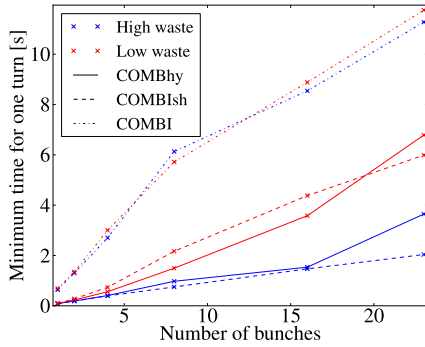
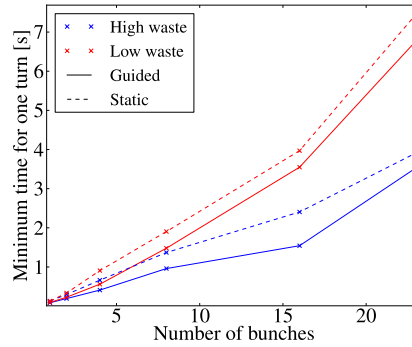


Figure A.7 – Performance with and without management of the processes priority at runtime. The performance with a single thread is given as a reference. (Tested on a 16 core HP ProLiant BL460c Gen8 blade with 2 Intel(R) Xeon(R) CPU E5-2690 @ 2.70GHz with hyper-threading on.)

In the high waste configuration, as only 2 MPI process are working at a time, one expects a good scaling with the number of threads, even for a large number of bunches. In order to empirically estimate the portion of code, α_{np} , that is not effectively parallelised, we fit the measured performance with Amdahl's law, relating the speed-up, S_u , to number of CPU



(a) COMBI / COMBHY (Guided) / COMBISH



(b) OpenMP with Static / Guided scheduling

Figure A.8 – Minimum execution time on a single Aries node.

available, N_{CPU} :

$$S_u(\alpha_{\text{np}}, N_{\text{CPU}}) = \frac{1}{\alpha_{\text{np}} + \frac{1-\alpha_{\text{np}}}{N_{\text{CPU}}}}. \quad (\text{A.1})$$

Figure A.6 shows that the portion of non-parallelisable code is around 6% when considering a single bunch, which is consistent with expectations. This portion of non-parallelisable code, should increase linearly with the number of bunches, which do not match the behaviour of the measured one (Fig. A.6b). The degradation of the scaling is due to the fact that, when considering a large number of bunches, the number of MPI processes becomes similar to the number of CPUs available on the node. In the case of 23 bunches, 47 of the 48 CPUs are running an MPI process. Therefore, the threads spawned by the 2 non-idling MPI processes have to be run on CPUs that are fully loaded by the constant polling of the idling MPI processes, which leads to a degradation of the performance.

This waste of resource could be mitigated by acting on the scheduler during the execution. Indeed, the **master**, being aware of the workload of each of the MPI processes, could in principle tell the **slave** processes to lower their priority in the operating system scheduler, leaving the room for working threads. It is however not wanted to lower the priority of non-idling processes which still rely on MPI communication during the processing, therefore the **yield_when_idle** option provided by OpenMPI is not satisfactory. Nevertheless, the proper system calls can be implemented using **setpriority** function from **sys/resource.h** (UNIX). As shown by Fig. A.7, the performance is increased by managing the priority of processes during the execution. Nevertheless, the necessary system calls require the capability to change processes priority during the execution which is not always given to users of shared computing facilities.

As shown by Fig. A.8a, the implementation of the second level of parallelisation using MPI and shared memory offers performances similar to the hybrid MPI/OpenMP version. Whereas in COMBHY, a waste of resources is still present because of the busy-waiting of idling MPI processes, this is not the case in COMBISH. The reason why COMBISH does not perform better is due to the work sharing algorithm, which is rather simple and does not take into account properly the topology of the machine. The work is split into equal sized loads that are distributed among **helper** processes. However, this often results in large amount of work given to CPUs potentially far away from the allocated memory. As a consequence, the execution is often limited by the least performing **helper**. Also, the **helpers** are not reassigned to a new **slave** once the processing is complete, but rather wait for the slowest slave to finish its processing. Ways around these drawbacks are implemented in OpenMP. First, by nature, the threads which have finished their processing will yield the resources available to other threads. Secondly, **Guided** scheduling has a slightly positive impact on the performance when compared to **Static** (Fig. A.8b), which is similar to the algorithm implemented in COMBISH. To be competitive, more advanced algorithm of work sharing should be implemented in COMBISH. The effort may, however, not be worth, as the COMBHY code already offers good performances.

A.2.4 Conclusion

Two concepts of a second level of parallelisation were implemented in COMBI, aiming at speeding up the processing of **actions** and avoid waste of resources. OpenMP was found very appropriate to speed up the execution of **actions**, allowing a linear speed-up of $\sim 95\%$ of the code. This implementation also allows a partial recovery of the resources otherwise wasted in the single level parallelism implemented. Nevertheless, the busy-waiting of idling MPI processes remains a large overhead, which can be slightly mitigated by changing the priorities of these processes at runtime and therefore help the operating system scheduler to favour the execution of working threads rather than idling MPI processes. The performance, however, highly depends on the implementation of the scheduler. The second implementation intended to circumvent the waste of resources using only MPI and taking advantage of POSIX memory mapping between processes with access to shared memory. However, this required major changes to the code structure, and only a rather simple algorithm for the sharing of the workload was implemented. Lacking many features available in OpenMP, this implementation did not provide better performances than the hybrid version in most configurations. Nevertheless, it is not excluded that more elaborate algorithm may lead to better performances.

A.3 Implementation of the actions

The machine is described by an **action** sequence, described in a text file. Each line describe an **action**, the first value giving the position of the **action** (Fig. A.1) , the second the Action Code (AC) and the following ones the arguments. Table A.1 summarizes the **actions** available at the time of the writing and their corresponding arguments. Here, we wish to describe in detail some of the **actions** that are relevant for our work.

A.3.1 Beam-beam

COMBI allows for two types of model for BB interactions. The first one (AC2) is based on the Hybrid Fast Multipole Method (HFMM) to compute the electromagnetic fields produced by the beams based on their macro particle distribution [96] and deduce the resulting kick on the other beam. This method is rather demanding in computing resources, and necessitates a significant data transfer between the CPUs executing the **actions**. It is possible to relax the computing requirements and memory exchange by computing the first and second order moments of the distribution, exchange this information only, and compute the kick assuming a Gaussian distribution according to Eq. 2.26 (AC10). This model, usually called the soft-Gaussian model is less CPU time consuming, yet it is not suitable for every type of studies. For example, the equilibrium distribution of the beam encountering strong BB interactions is slightly non Gaussian, which may have an impact on the dynamic. For example, it was shown that the soft-Gaussian model slightly underestimates the Yokoya factor, e.g. in [74]. However, the LR field weakly depends on the exact beam distribution and therefore is well described in the soft-Gaussian model. The HFMM is usually used to describe HO collisions only.

Both **actions** do not take into account the longitudinal aspects of the interactions. This is necessary to model synchro-betatron effects, which are mainly important in the presence of large crossing angle or a strong hourglass effect. An **action** taking into account these effects is currently under development.

In order to ease the modelling of the LHC, a phase advance of $\pi/2$ on each side of the IP has been introduced in AC2, which approximate the phase advance between the IP and the first LR interaction (Fig. 3.3c).

For every BB interaction, the **master** process checks for the presence of a bunch in each of the two beams at the location of the interaction. If only a single bunch is present, nothing is done, except for the extra phase advance when applicable. If two bunches are present, the **master** sends the **action** and the arguments including the process identification number of the **slave** process simulating the partner bunch. The two **slave** processes then exchange the information required for the computation of their respective fields.

A.3.2 Lattice transfer

The linear lattice transfer (AC3) implements the linear transfer in all planes according to Eq. 2.14 with $\alpha = \gamma = 0$. The longitudinal transfer assumes a linear RF bucket and is based on the parameters given as input.

Linear transverse detuning can be introduced with the nonlinear transfer map (AC13), which applies a linear transfer similar to AC3, but with a phase advance that depends on each particle's transverse actions :

$$\begin{cases} \Delta Q_x &= a_x J_x + a_y J_y \\ \Delta Q_y &= b_x J_x + b_y J_y. \end{cases} \quad (\text{A.2})$$

A.3.3 External noise

Different types of external noise may be introduced with AC7, the type is defined by the first argument. The first type introduces an identical dipolar kick to all particles in the bunch, with an amplitude varying each turn according to a random variable with uniform distribution within the limits given as second and third arguments. The second type introduces a sinusoidal excitation with finite correlation time. The frequency is given in unit of the revolution frequency, the phase is changed randomly in order to account for the finite correlation time. The kick is also constant over the bunch length, i.e. identical for all particles.

A.3.4 Beam coupling impedance

The modelling of beam coupling impedance, AC12, is inspired by the existing code HEAD-TAIL [75]. The beam is split longitudinally into equally spaced slices, within fixed boundaries set to ± 2 times the longitudinal rms bunch length. The average positions of each slice are computed and used to compute the effect of each slice on the trailing ones based on a wake file given as input. The wake file contains five column of values separated by spaces, the first one with increasing values of the longitudinal position expressed in ns, the next four contain the corresponding values of the horizontal dipolar, vertical dipolar, horizontal quadrupolar and vertical quadrupolar wake functions. The kick computed for each slice is then applied to all macro-particles inside.

Due to the synchrotron motion, the binning of particles in slices has to be re-done each turn.

Considering typical LHC wake functions (Fig. 3.9), the variation over the bunch length at the bunch-to-bunch distance is negligible. Therefore the average position of the bunch is sufficient to compute the wake on the trailing ones, and the kick computed from the wake table may be applied to all the particles in the different bunches, taking into account the proper longitudinal distances.

The bookkeeping for the multi-bunch effect of the wake is done by the **master** process. Each

time a **slave** perform the AC12, it sends the first order moments of its bunch distribution to the **master** process, which later sends these data to the next bunches performing the same **action**. As the wake may last longer than the revolution time, the **master** processes keeps the data for a fixed amount of turns, specified in the input. Thus, the **slave** processes receive a list of positions of the previous bunches, including their own positions and those of other bunches in the previous turns, and deduce the kick to be applied to all their macro-particles.

A.3.5 Transverse damper

The transverse feedback (AC14) is modelled by a modification of the position according to the measured average position $\langle \cdot \rangle$. The first type is a perfect resistive feedback :

$$\begin{cases} \Delta x &= G_x \cdot \langle x \rangle \\ \Delta y &= G_y \cdot \langle y \rangle \end{cases} \quad (\text{A.3})$$

with G_x and G_y the gain the respective plane. The second type is similar but acts only on bunches with a sufficiently large transverse position, simulating a finite resolution :

$$\begin{cases} \Delta x &= \begin{cases} G_x \cdot \langle x \rangle & , \text{if } |x| > T_x \\ 0 & , \text{otherwise} \end{cases} \\ \Delta y &= \begin{cases} G_y \cdot \langle y \rangle & , \text{if } |y| > T_y \\ 0 & , \text{otherwise} \end{cases} \end{cases} \quad (\text{A.4})$$

with T_x and T_y the threshold in the respective planes.

A third type of damper was introduced in order to include the effect of the modulation of the measured BPM signal around the main RF frequency, ω_{RF} . It is used to enhance the sensitivity of the transverse feedback in the LHC [105]. As a result, the measured position slightly differs from $\langle x \rangle$ in the presence of a head-tail motion. This implementation behaves like the perfect damper, rather using the following measured position :

$$\langle x \rangle_{meas} = \frac{I_\Delta I_\Sigma + Q_\Delta Q_\Sigma}{I_\Sigma^2 + Q_\Sigma^2} \quad (\text{A.5})$$

with:

$$I_{\Sigma} = \int_{\text{slot}} \cos(\omega_{RF} \frac{s}{c}) \lambda(s) ds \quad (\text{A.6})$$

$$I_{\Delta} = \int_{\text{slot}} \cos(\omega_{RF} \frac{s}{c}) x(s) \lambda(s) ds \quad (\text{A.7})$$

$$Q_{\Sigma} = \int_{\text{slot}} \sin(\omega_{RF} \frac{s}{c}) \lambda(s) ds \quad (\text{A.8})$$

$$Q_{\Delta} = \int_{\text{slot}} \sin(\omega_{RF} \frac{s}{c}) x(s) \lambda(s) ds \quad (\text{A.9})$$

where $\lambda(s)$ is the longitudinal beam profile and $x(s)$ the transverse displacement of the beam along the bunch.

Action	code	Arguments
Empty	0	
Head-on BB ($+2 \cdot \pi/2$ transfer)	2	Intensity scaling, H. full separation, V. full separation
Linear transfer	3	Q_H B1, Q_V B1, Q_s B1, Q_H B2, Q_V B2, Q_s B2, Q'_H B1, Q'_V B1, Q'_H B2, Q'_V B2
Noise source (Dip. white)	7	1, H. amplitude, V. amplitude
Noise source (sin)	7	2, H. amplitude, V. amplitude, H. frequency, V. frequency , H. correlation time [turn], V. correlation time [turn]
Noise source (Quad. white)	7	3, H. amplitude, V. amplitude
Sweeping sinusoidal excitation	8	H. amplitude, V. amplitude, Initial frequency, step in frequency
Long range BB	10	Separation plane (1 for H. and 2 for V.), Full separation
Collimator	11	H. lower boundary, H. upper boundary , V. lower boundary, V. upper boundary , L. lower boundary, L. upper boundary
Impedance	12	Number of slice, Intensity scaling B1, Wakefile number B1 , Intensity scaling B2, Wakefile number B2
Nonlinear transfer	13	H. detuning with J_x , H. detuning with J_y , V. detuning with J_x , V. detuning with J_y
Transverse feedback (perfect)	14	0, H. gain B1, V. gain B1, H. gain B1, V. gain B2
Transverse feedback (thresholded)	14	1, H. gain B1, V. gain B1, H. gain B1, V. gain B2, , H. threshold B1 [m], V. threshold B1 [m], H. threshold B2 [m], V. threshold B2 [m]
Transverse feedback (modulated)		2, H. gain B1, V. gain B1, H. gain B1, V. gain B2, modulation frequency

Table A.1 – Definition of the **actions** available in COMBI version 2.0. (H. stands for Horizontal, V. for Vertical and L. for Longitudinal.). The separations, amplitude and boundaries are given in beam σ in the respective plane. The frequencies are in tune units.

B PySSD

B.1 The module

PYSSD is a Python Solver for Stability Diagrams. It is based on a basic trapezoidal integration of the dispersion integral described by Eq. 2.60, that we report here for convenience, including the vanishing ϵ used for the numerical integration :

$$-\frac{1}{\Delta Q_x} = \int \frac{\frac{d\Psi(J_x, J_y)}{dJ_x} J_x dJ_x dJ_y}{q - Q_x(J_x, J_y) + i\epsilon}. \quad (\text{B.1})$$

The different classes of the module are pictured in Fig. B.1. An integrator is build based on instances of the abstract classes **Detuning** and **Distribution**, describing $Q_x(J_x, J_y)$ and

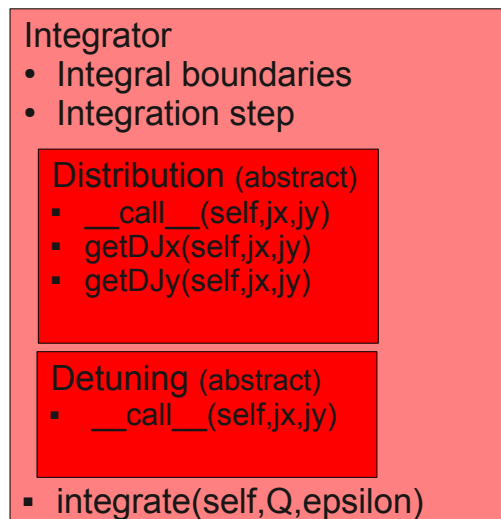


Figure B.1 – Description of the PYSSD module.

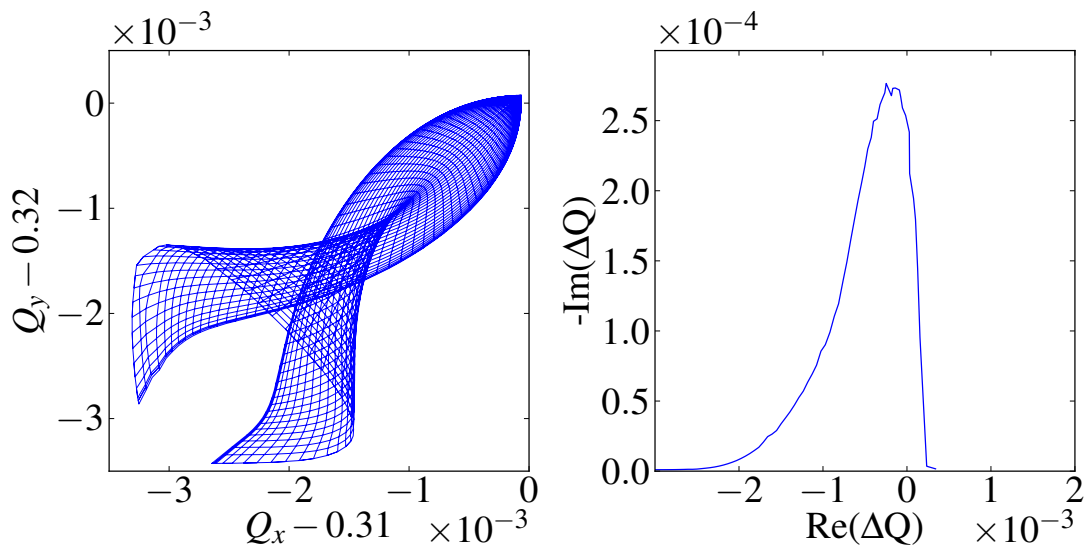


Figure B.2 – Footprint (right) and corresponding stability diagram (left) obtained with LHC 2012 parameters at the end of the squeeze, including LR interactions in interaction regions 1 and 5 with a full separation of 4σ at the IP and the octupoles powered with -500 A.

$\Psi(J_x, J_y)$ respectively. In order to build the stability diagram, one calls the **Integrator** instance for different values of $q \in \mathbb{R}$, using an appropriate $\epsilon \in \mathbb{R}^+$. Large values of ϵ lead to a significant error on the accuracy of the integral, while too small value increase the numerical noise. Also, a rapid analysis of the range of $Q_x(J_x, J_y)$ allows to determine the relevant values of q for which the imaginary part of the integral does not vanish. The integration range, as well as the discretisation step are attributes of the integrator.

B.2 Interface with MAD-X

The main advantage of this structure lies in the possibility to easily use distribution functions or amplitude detuning given by an analytical formula or by other sources, e.g. the output of another numerical code or a measurement. In Sec. 4.3, the output of the multi-particle tracking code COMBI is used as input. In Chap. 4, the detuning was obtained numerically from tracking simulation with MAD-X [106–108]. Particles with different actions are tracked for 1024 turns from which the tunes are evaluated using interpolated FFT [109]. This is implemented in the DYNAPTUNE module of MAD-X, which provides the horizontal and vertical tunes of the particles obtained from tracking as a function of their action. The interface to PYSSD is done via the **Footprint** class, which includes a parser for the DYNAPTUNE output, from which a **Detuning** instance can be build. The discrete footprint is interpolated using a weighted average over the nearest data points. In order to avoid strong discontinuities and numerical noise, the transverse phase space should be finely discretised. Figure B.2 shows two examples of footprints modelling $Q_x(J_x, J_y)$ on a radial mesh with radial step of 0.1 from

0 to 6σ and an angular step of $\pi/100$ from 0 to $\pi/2$.

B.3 Demo code

```
1 import numpy as np
2
3 from PySSD.Detuning import FootprintDetuning
4 from PySSD.Distribution import Gaussian
5 from PySSD.Integrator import FixedTrapezoidalIntegrator
6 from PySSD.Footprint import Footprint,parseDynapTune
7
8 # Define relevant values of Q based on the range of detuning
9 def findQs(detuning,stepSize=5E-5,maxJ=18.0,dJ=0.1,margin=1):
10     myMin = 1.0
11     myMax = 0.0
12     for jx in np.arange(0.0,maxJ,dJ):
13         for jy in np.arange(0.0,maxJ,dJ):
14             value = detuning(jx,jy)
15             if value < myMin :
16                 myMin = value
17             if value > myMax :
18                 myMax = value
19     return np.arange(myMin-margin*stepSize,myMax+margin*stepSize,stepSize)
20
21 if __name__ == '__main__':
22     # Built Distribution instance (Based on analytical formula)
23     distrib = Gaussian()
24
25     # Parse MAD-X output
26     strRep = parseDynapTune('dynaptune',101,51)
27     # dSigma : amplitude difference between two indices in the amplitude
28     # loop (in unit of sigma)
29     footprint = Footprint(strRep,dSigma=0.1)
30     # Remove faulty points of the footprint
31     footprint.repair()
32     # Build detuning instance based on footprint
33     detuning = FootprintDetuning(footprint)
34
35     # Integration range (0 to 6 sigma)
36     maxJ = 18.0
37     # Build Integrator instance
38     integrator = FixedTrapezoidalIntegrator(distrib,detuning,maxJ=maxJ)
39
40     for Q in findQs(detuning,stepSize=5E-5,maxJ=maxJ):
41         tuneShift = integrator.integrate(Q,epsilon=1E-6):
42         print tuneShift.real,tuneShift.imag;
```

C BimBim

BIMBIM is an implementation of the CMM in the Python language. It is meant to treat the full LHC complexity of IPs and filling schemes and, therefore, needs to be as flexible as possible. The module aims at building the coherent one turn matrix of the full system, including both beams, their interactions through the BB forces, the beam coupling impedance and the transverse feedback. As a consequence, multi-turn effects are neglected in this approach. Figure C.1 shows the different classes of the BIMBIM module, each being detailed in the following.

In order to optimise for memory usage, BIMBIM makes use of sparse matrices, using the module SCIPY.SPARSE.

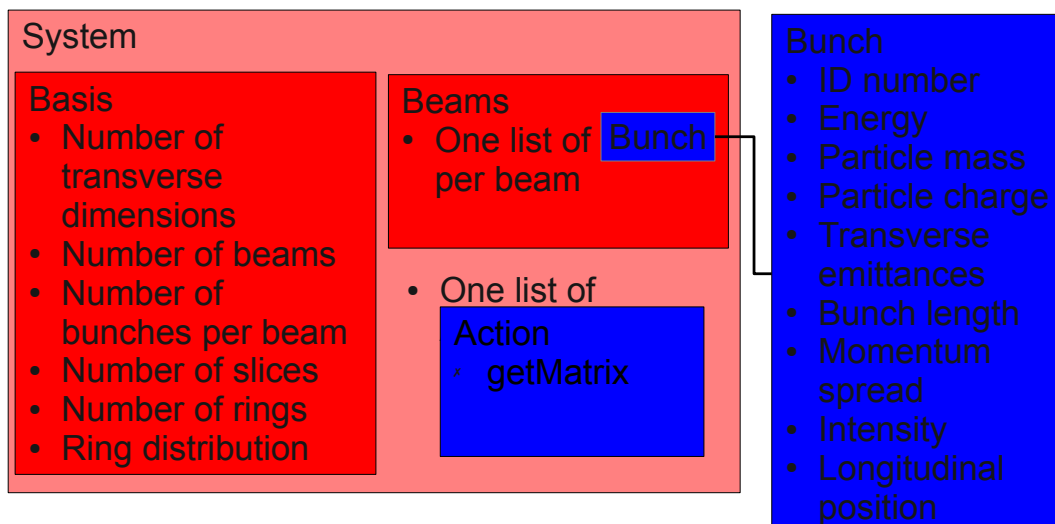


Figure C.1 – Classes

C.1 Beams

The **Beams** instance is the link to all **Bunch** instances and is responsible for bookkeeping the position of the bunches relatively to the **System**'s action sequence. All bunches are moved one step ahead by a call to the function `step(self)`.

The initialisation of the filling scheme is inspired from COMBI (Chap. A). The filling scheme of each beam is described by a string, made of a series of number going in pairs. The first of number of each pair gives the number of slots, whereas the second gives the state of these slots, i.e. 0 for empty and 1 for filled. For example, a beam composed of 72 consecutive bunches followed by 8 empty slots and 36 more consecutive bunches is written '72 1 8 0 36 1', for a total of 116 slots. This representation is very convenient to describe the train structure of the LHC beams (Sec. 3.2). The description of both beams must have the same number of slots. Yet, it is important to note that for single beam simulations, the description '116 0' which corresponds to 116 empty slots is valid. Also, the length of the action sequence must match the number of possible interaction points, which is twice the number of slots.

The constructor of the **Beams** class will construct a list of bunches according to the two strings representing the filling schemes of each beam. Each bunch will be initialised with the parameters provided as input. The attributes of each bunch are still accessible for changes after construction.

C.2 Basis

The **Basis** instance contains all information about the basis in which the one turn matrix is expressed and provides helper functions to be used by the **Action** instances to project their matrix in a common basis. The current implementation uses the following basis :

$$\text{Beam} \otimes \text{Bunch} \otimes \text{Ring} \otimes \text{Slice} \otimes \text{Transverse plane} \quad (\text{C.1})$$

where slices and rings refer to Sec. 2.2.3.

C.3 System

The **System** encapsulate all the different components in a consistent manner and is responsible for building the one turn matrix in the basis corresponding to its **Basis** instance, based on the **Beams** instance and the action sequence. For a **System** instance with action sequence of length N_a , the building of the matrix is done in N_a step. At each step, a matrix M_i is built, describing the interactions between all elements of the basis in this configurations, taking into account the position of the bunches with respect to the action sequence. The bunches of both beams are then moved one step ahead in the **Beams** instance in order to build the matrix M_{i+1} , similarly to the execution of COMBI (Fig. A.1). After N_a steps, the bunches are

back to their initial position, and the one turn matrix is given by :

$$M = M_1 \cdot M_2 \cdot \dots \cdot M_{N_a}. \quad (C.2)$$

C.4 Actions

The implementations of the abstract class **Actions** provide a function **getMatrix(self,basis)**, which computes a matrix of the interaction in the basis given as input.

C.4.1 Transport

The **Transport** action creates a linear synchro-betatron transfer matrix, built as follows. The betatron matrix for one element of the distribution is given by Eq. 2.14, with $\alpha = \alpha_0 = \gamma = \gamma_0 = 0$ and $\beta = \beta_0$. When considering the two transverse plane, we have :

$$B_0(\delta) = \begin{pmatrix} \cos(\phi_x(\delta)) & \beta_x \sin(\phi_x(\delta)) & 0 & 0 \\ -\frac{1}{\beta_x} \sin(\phi_x(\delta)) & \cos(\phi_x(\delta)) & 0 & 0 \\ 0 & 0 & \cos(\phi_y(\delta)) & \beta_y \sin(\phi_y(\delta)) \\ 0 & 0 & -\frac{1}{\beta_y} \sin(\phi_y(\delta)) & \cos(\phi_y(\delta)) \end{pmatrix}, \quad (C.3)$$

with $\phi_x(\delta)$ and $\phi_y(\delta)$ the phase advances in the two transverse planes, which depends on the energy deviation δ of the element considered

$$\begin{cases} \phi_x & = & \phi_{x,0} + Q'_x \delta \\ \phi_y & = & \phi_{y,0} + Q'_y \delta \end{cases}, \quad (C.4)$$

with $\phi_{x,0}$ and $\phi_{y,0}$ the unperturbed phase advances and Q'_x and Q'_y the chromaticities. The betatron matrix of a bunch is build by concatenation of the $B_0(\delta)$ in a diagonal matrix, taking into account the weight of the ring (Eq. 2.42).

The synchrotron motion is modelled by a circulant matrix, like Eq. 2.45, then the unperturbed synchro-betatron one turn matrix for a single bunch is given by :

$$M_0 = S_0 \otimes B_0. \quad (C.5)$$

The transfer of all bunches is identical, therefore the full matrix transfer matrix is given by a concatenation of identical M_0 matrices in a block diagonal matrix.

C.4.2 Beam beam

The coupling between two elements of the distribution by the BB force is given by Eq. 2.35, with two transverse planes, we have :

$$C_{BB,0} = \begin{pmatrix} 1 & 0 & 0 & 0 & 0 & 0 & 0 & 0 \\ -\frac{\partial \Delta x'_{\text{coh}}}{\partial x} & 1 & -\frac{\partial \Delta x'_{\text{coh}}}{\partial y} & 0 & \frac{\partial \Delta x'_{\text{coh}}}{\partial x} & 0 & \frac{\partial \Delta x'_{\text{coh}}}{\partial y} & 0 \\ 0 & 0 & 1 & 0 & 0 & 0 & 0 & 0 \\ -\frac{\partial \Delta y'_{\text{coh}}}{\partial x} & 0 & -\frac{\partial \Delta y'_{\text{coh}}}{\partial y} & 1 & \frac{\partial \Delta y'_{\text{coh}}}{\partial x} & 0 & \frac{\partial \Delta y'_{\text{coh}}}{\partial y} & 0 \\ 0 & 0 & 0 & 0 & 1 & 0 & 0 & 0 \\ \frac{\partial \Delta x'_{\text{coh}}}{\partial x} & 0 & \frac{\partial \Delta x'_{\text{coh}}}{\partial y} & 0 & -\frac{\partial \Delta x'_{\text{coh}}}{\partial x} & 1 & -\frac{\partial \Delta x'_{\text{coh}}}{\partial y} & 0 \\ 0 & 0 & 0 & 0 & 0 & 0 & 1 & 0 \\ \frac{\partial \Delta y'_{\text{coh}}}{\partial x} & 0 & \frac{\partial \Delta y'_{\text{coh}}}{\partial y} & 0 & -\frac{\partial \Delta y'_{\text{coh}}}{\partial x} & 0 & -\frac{\partial \Delta y'_{\text{coh}}}{\partial y} & 1 \end{pmatrix} \quad (\text{C.6})$$

where all derivatives are evaluated at the closed orbit, (x_0, y_0) and are given by the extension of Eq. 2.36 in 2 dimension :

$$\Delta x'_{\text{coh}}(x, y) \approx \Delta x'_{\text{coh}}(x_0, y_0) + \frac{\partial \Delta x'_{\text{coh}}}{\partial x}(x_0, y_0) \Delta x + \frac{\partial \Delta x'_{\text{coh}}}{\partial y}(x_0, y_0) \Delta y \quad (\text{C.7})$$

$$\Delta y'_{\text{coh}}(x, y) \approx \Delta y'_{\text{coh}}(x_0, y_0) + \frac{\partial \Delta y'_{\text{coh}}}{\partial x}(x_0, y_0) \Delta x + \frac{\partial \Delta y'_{\text{coh}}}{\partial y}(x_0, y_0) \Delta y \quad (\text{C.8})$$

with :

$$\frac{\partial \Delta x'_{\text{coh}}}{\partial x}(x, y) = -\frac{2N r_0}{\gamma_r} \left[\left(\frac{1}{r^2} - \frac{x^2}{r^4} \right) \left(1 - e^{-\frac{-r^2}{4\sigma^2}} \right) + \frac{x^2}{2r^2 \sigma^2} e^{-\frac{-r^2}{4\sigma^2}} \right]. \quad (\text{C.9})$$

$$\frac{\partial \Delta x'_{\text{coh}}}{\partial y}(x, y) = -\frac{2N r_0}{\gamma_r} x y \left[-\frac{2}{r^4} \left(1 - e^{-\frac{-r^2}{4\sigma^2}} \right) + \frac{1}{2r^2 \sigma^2} e^{-\frac{-r^2}{4\sigma^2}} \right] \quad (\text{C.10})$$

$$\frac{\partial \Delta y'_{\text{coh}}}{\partial x}(x, y) = -\frac{2N r_0}{\gamma_r} \left[\left(\frac{1}{r^2} - \frac{y^2}{r^4} \right) \left(1 - e^{-\frac{-r^2}{4\sigma^2}} \right) + \frac{y^2}{2r^2 \sigma^2} e^{-\frac{-r^2}{4\sigma^2}} \right] \quad (\text{C.11})$$

$$\frac{\partial \Delta y'_{\text{coh}}}{\partial y}(x, y) = \frac{\partial \Delta x'_{\text{coh}}}{\partial y}(x, y). \quad (\text{C.12})$$

To describe the interaction between two bunches, we have to take into account coupling between all the elements. Neglecting the variation of the optics parameters as a function of

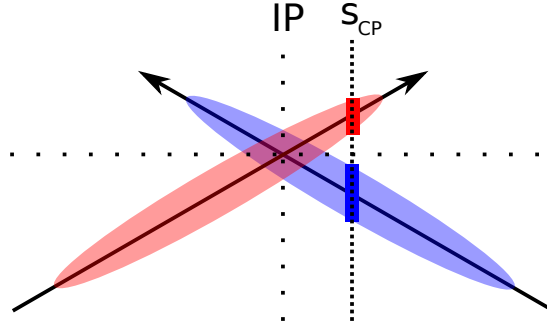


Figure C.2 – Illustration of the longitudinal displacement of the collision point, s_{CP} , with respect to the IP for two bunches colliding HO with a crossing angle.

the longitudinal position, we have :

$$(C_{BB,2b})_{ij} = \begin{cases} \begin{pmatrix} 1 & 0 & 0 & 0 \\ -\sum_k \frac{\partial \Delta x'_{coh}(i, k)}{\partial x} & 1 & -\sum_k \frac{\partial \Delta x'_{coh}(i, k)}{\partial y} & 0 \\ 0 & 0 & 1 & 0 \\ -\sum_k \frac{\partial \Delta y'_{coh}(i, k)}{\partial y} & 0 & -\sum_k \frac{\partial \Delta y'_{coh}(i, k)}{\partial x} & 1 \end{pmatrix}, & \text{if } i = j \\ \begin{pmatrix} 0 & 0 & 0 & 0 \\ \frac{\partial \Delta x'_{coh}(i, j)}{\partial x} & 0 & \frac{\partial \Delta x'_{coh}(i, j)}{\partial y} & 0 \\ 0 & 0 & 0 & 0 \\ \frac{\partial \Delta y'_{coh}(i, j)}{\partial x} & 0 & \frac{\partial \Delta y'_{coh}(i, j)}{\partial y} & 0 \end{pmatrix}, & \text{if } i \neq j \end{cases}, \quad (C.13)$$

where $\frac{\partial \Delta x'_{coh}}{\partial x}(i, j)$, $\frac{\partial \Delta x'_{coh}}{\partial y}(i, j)$, $\frac{\partial \Delta y'_{coh}}{\partial y}(i, j)$ and $\frac{\partial \Delta y'_{coh}}{\partial x}(i, j)$ are the linearised coherent kicks of the element j on the element i computed at the IP. $C_{BB,2b}$ can be rewritten in the full basis, as the other bunches are untouched by this operation, the diagonal is filled with 1, all other elements are zero. The **Action** named **FlatBeamBeam** implements such an interaction. It is used to describe LR interactions, or HO interaction without crossing angle and with negligible hourglass effect.

A full implementation of the BB interaction, taking into account energy variations [110], is not achievable within the CMM as the longitudinal phase space coordinates are fixed. Yet, following [18], we obtain a good approximation of the BB forces by computing the coherent kicks taking into account the orbit and optical properties of the beam at the location of the collision point between the elements, s_{CP} , rather than at IP, as illustrated in Fig. C.2. The interaction occurs away from the IP, one needs to take into account the drift of the elements between the IP and s_{CP} . using the drift matrix :

$$D(s_{\text{CP}}) = \begin{pmatrix} 1 & s_{\text{CP}} & 0 & 0 & 0 & 0 & 0 & 0 \\ 0 & 1 & 0 & 0 & 0 & 0 & 0 & 0 \\ 0 & 0 & 1 & s_{\text{CP}} & 0 & 0 & 0 & 0 \\ 0 & 0 & 0 & 1 & 0 & 0 & 0 & 0 \\ 0 & 0 & 0 & 0 & 1 & -s_{\text{CP}} & 0 & 0 \\ 0 & 0 & 0 & 0 & 0 & 1 & 0 & 0 \\ 0 & 0 & 0 & 0 & 0 & 0 & 1 & -s_{\text{CP}} \\ 0 & 0 & 0 & 0 & 0 & 0 & 0 & 1 \end{pmatrix}. \quad (\text{C.14})$$

The interaction between two elements thus given by :

$$C'_{\text{BB},0} = \begin{pmatrix} D(-s_{\text{CP}}) & 0 \\ 0 & D(-s_{\text{CP}}) \end{pmatrix} \cdot C_{\text{BB},0}(s_{\text{CP}}) \cdot \begin{pmatrix} D(s_{\text{CP}}) & 0 \\ 0 & D(s_{\text{CP}}) \end{pmatrix}. \quad (\text{C.15})$$

The matrix of interaction between two elements can be projected on the full beam basis by inserting the element in an identity matrix, as done previously. The matrix of the full HO interaction is then given by the product of the matrix obtained for the interaction of all the elements together, respecting causality.

C.4.3 Impedance

The impedance matrix for a single beam of N_b bunches can be written :

$$(C_w)_{i,j} = \begin{cases} C_{w,1b} & , \text{ if } i = j \\ C_{w,MB} & , \text{ if } i \neq j \end{cases}, \quad (\text{C.16})$$

where $C_{w,1b}$ is a square matrix of size $N_{\text{dof}} \cdot N_s \cdot N_I$ describing intra-bunch effects and $C_{w,MB}$ is matrix of the same size describing the coupling between two bunches. The diagonal terms of $C_{w,1b}$ corresponds to Eq. 2.47, take into account the the effect of the quadrupolar wake from other bunches. Considering two transverse degrees of freedom, we have :

$$(C_{w,1b})_{ij} = \begin{cases} \begin{pmatrix} 1 & 0 & 0 & 0 \\ c_x(i,j) & 1 & 0 & 0 \\ 0 & 0 & 1 & 0 \\ 0 & 0 & c_y(i,j) & 1 \end{pmatrix} & , \text{ if } i = j \\ \begin{pmatrix} 0 & 0 & 0 & 0 \\ W_{\text{dip},x}(s_i - s_j) & 0 & 0 & 0 \\ 0 & 0 & 0 & 0 \\ 0 & 0 & W_{\text{dip},y}(s_i - s_j) & 0 \end{pmatrix} & , \text{ if } i \neq j \end{cases}, \quad (\text{C.17})$$

with :

$$c_x(i, j) = \sum_k^{N_s \cdot N_t} W_{\text{quad},x}(s_i - s_k) + \sum_b^{N_b} W_{\text{quad},x}(s_0 - s_b) \quad (\text{C.18})$$

$$c_y(i, j) = \sum_k^{N_s \cdot N_t} W_{\text{quad},y}(s_i - s_k) + \sum_b^{N_b} W_{\text{quad},y}(s_0 - s_b). \quad (\text{C.19})$$

The matrix describing the effect of a bunch with longitudinal position s_i on another one at longitudinal position s_j is given by :

$$(C_{w,\text{couple}}(s_i - s_j))_{k,l} = \begin{pmatrix} 0 & 0 & 0 & 0 \\ W_{\text{dip},x}(s_i - s_j) & 0 & 0 & 0 \\ 0 & 0 & 0 & 0 \\ 0 & 0 & W_{\text{dip},y}(s_i - s_j) & 0 \end{pmatrix} \quad (\text{C.20})$$

The coupling between the different beams through the beam coupling impedance is neglected, therefore the coupling matrix for the two beams is simply given by :

$$C_w = \begin{pmatrix} C_w(\text{Beam 1}) & 0 \\ 0 & C_w(\text{Beam 2}) \end{pmatrix} \quad (\text{C.21})$$

C.4.4 Damper

The perfect bunch by bunch transverse feedback acts identically on all the elements of the distribution of each bunch, depending on its average position :

$$(C_{\text{FB}})_{i,j} = \begin{cases} \begin{pmatrix} 1 & 0 & 0 & 0 \\ 0 & 1 - k_{\text{FB},x} & 0 & 0 \\ 0 & 0 & 1 & 0 \\ 0 & 0 & 0 & 1 - k_{\text{FB},y} \end{pmatrix} & , \text{ if } i = j \\ \begin{pmatrix} 0 & 0 & 0 & 0 \\ 0 & -k_{\text{FB},x} & 0 & 0 \\ 0 & 0 & 0 & 0 \\ 0 & 0 & 0 & -k_{\text{FB},y} \end{pmatrix} & , \text{ if } i \neq j \end{cases} \quad (\text{C.22})$$

Appendix C. BimBim

with :

$$k_{\text{FB},x} = \frac{2 \cdot G_{\text{FB},x}}{N_s \cdot N_f} \quad (\text{C.23})$$

$$k_{\text{FB},y} = \frac{2 \cdot G_{\text{FB},y}}{N_s \cdot N_f} \quad (\text{C.24})$$

C.5 Demo code

```
1 import numpy as np
2
3 from BimBim.Matrix import *
4 from BimBim.Beams import Beams
5 from BimBim.Basis import Basis
6 from BimBim.System import System
7
8 from BimBim.Action.Damper import Damper
9 from BimBim.Action.Transport import Transport
10 from BimBim.Action.HeadOn import HeadOn
11 from BimBim.Action.FlatBeamBeam import FlatBeamBeam
12 from BimBim.Action.Impedance import Impedance
13
14 if __name__ == '__main__':
15     #define action sequence
16     actionSequence = [
17         HeadOn(...),
18         Transport(...),
19         Impedance(...),
20         Damper(...),
21         None, None, None, None]
22
23     #define the beams
24     fill1 = '2 1 2 0'
25     fill2 = '2 0 2 0'
26     beams = Beams(fill1, fill2, ...)
27
28     #define the basis
29     basis = Basis(beams.getNBunchB1(), beams.getNBunchB2(), ...)
30
31     #define the system
32     system = System(beams, actionSequence, basis)
33
34     #Build the one turn matrix
35     oneTurn = system.buildOneTurnMap()
36
37     #Analyze the one turn matrix, for example :
38     eigvals, eigvecs = np.linalg.eig(oneTurn)
```


D The online beam-beam footprint viewer

The understanding of bunch by bunch differences is crucial in a machine with several bunches as the LHC. Indeed, the collision pattern of the different bunches can be very different, the BB effects expected are therefore different for every bunch. While a precise evaluation of the effects requires a deeper analysis, the tune footprint allows to assess, at least qualitatively, many aspects in a rather simple way. It is then natural to bring this information to the control room, as this can allow to better understand measured bunch by bunch differences and guide the operator during, for example, an optimisation of the lifetime by variation of the lattice tunes.

D.1 Implementation

Each point of the footprint is the result of the tracking of one particle through the lattice, including the BB interactions. This kind of computation can be done within the `DYNAP` module of `MAD-X` [106]. In order to easily integrate the simulation to the control system of the LHC, which is implemented in Java, a new module of `JMAD` [111], a Java-Application Programming Interface (API) for `MAD-X`, was developed in order to give access to the tracking functionalities. This approach allows to profit from the tools developed in the frame of the `ONLINE MODEL` [112] for the acquisition of machine and beam parameters, via the `LOGGING` [113] and `LSA` [86] databases.

The application is mainly divided in two sub-packages, responsible for the tracking and the user interface. In particular, the Graphical User Interface (GUI) package collects the data from the user and the different databases to define tracking jobs. Each tracking job is then launched in a separate thread each running its own `MAD-X` instance. The result is sent back to the GUI for plotting, processing and saving. This procedure allows to parallelise the computation of several footprints simultaneously, such as to characterize simultaneously the large variety of different PACMAN bunches. In realistic configurations, the workload

becomes too heavy for a console in the control room, there the application is run on a dedicated remote server.

D.1.1 Automatic acquisition of machine and beam parameters

While in principle usable for simulations of footprint with parameters set by hand, the application does not offer much more than is already offered to the regular user via MAD-X scripting. The application rather aims at providing automatically footprints based on current machine and beam parameters. Respectively, the energy, the (bunch by bunch) intensity (FBCT), the current β^* s, the configuration of bunches, the octupole strength and the experiment's spectrometers strengths are loaded from the LOGGING database, the crossing angles and the full optics are loaded from the LSA database. The transverse emittances have to be set by hand, as no continuous and reliable measurements are currently available. The transverse separation at the IP requires a bit of complication. Indeed, it is not possible to measure it at any time of the LHC cycle based on the value of the separation knob stored in the LSA database, at least not to the precision required. The present version uses the luminosity measurement of each experiment to evaluate the separation, making assumptions on the cycle. In IP1, 2 and 5, where no levelling methods are used, the separation is set as full in case no luminosity is measured and 0 otherwise. In IP8, which is levelled with a transverse offset, the separation is computed based on the evaluation of the luminosity reduction factor R from the ratio of the measured luminosity in IP1 and IP8, taking into account the different number of bunches colliding in the two IPs as well as the different β^* s (cf. Eq. 2.70):

$$IP8_{sep} = \sqrt{-\ln(R)} \quad (D.1)$$

If set in *Online mode*, the application will reload these informations before each simulation of a footprint.

D.1.2 Bunch selection

Simulating the footprint for all bunches during a physics fill is not only out of reach from the computing power point of view, but it would also extremely difficult to interpret the result. It is therefore important to choose a subset of bunches that will be representative of the whole beam, a recommended bunch selection is then proposed automatically. The bunches are divided in HO families, i.e. bunches colliding HO in the same IPs. The set of bunches in each HO family is represented by the two extreme bunches experiencing respectively the least and the largest number of LR interactions. Within LHC configuration, there can be up to 7 HO family, therefore we need at most 14 footprints in order to obtain a relevant representation of the beam.

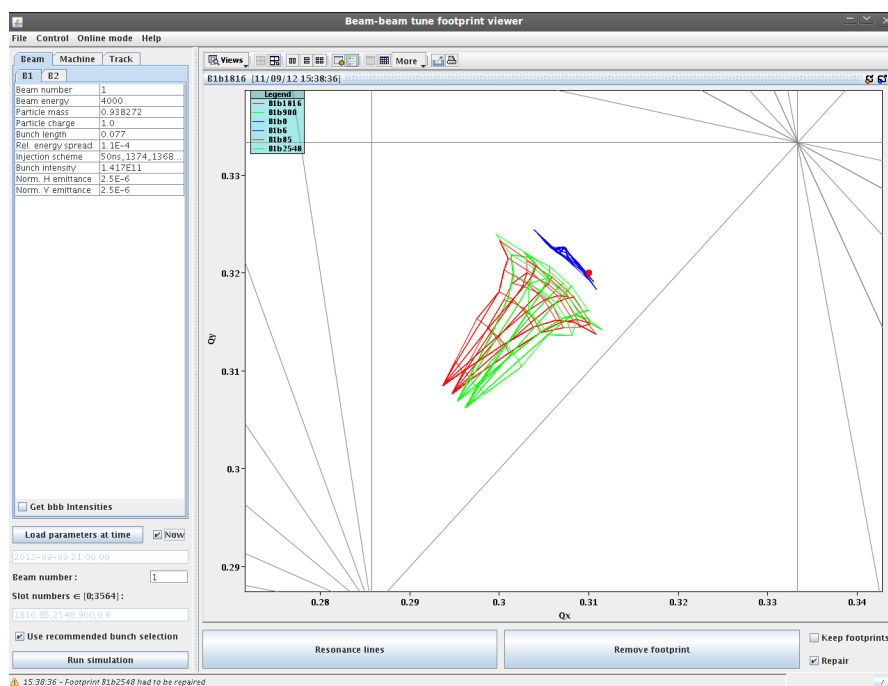


Figure D.1 – Example of the result of an automatic scan during a fill for physics.

D.1.3 Maintenance

The automatic acquisition of parameters heavily relies on the knowledge of the standard operational cycle. The according methods have to be updated to any change of the operational configuration (e.g. levelling strategies).

Being based on MAD-X module THINTRACK, the tracking requires thin lens optic. The thin lens optics must be generated based on the thick lens version used to generate the machine settings, checked and uploaded to the ONLINE MODEL. To avoid this workload one may want to use PTC tracking [114], which allow the use of thick lens. This upgrade could be done, at the expense of longer computing time and significant work on the implementation of the BB elements in the thick lens lattice.

D.2 Usage

D.2.1 Working point optimisation

The single particle dynamic is strongly affected by the presence of non-linearities, arising from BB interactions or from the lattice. A full understanding of the behaviour of the particles requires heavy analytical or numerical tools, such as Frequency Map Analysis (FMA) [115] and long term tracking simulations [34]. As illustrated by the FMA in Fig. D.2, the diffusion of particles is usually driven by resonance, having a strong impact on the beam lifetime. Far from allowing a quantitative evaluation of these effects, the footprints rather offer a

Appendix D. The online beam-beam footprint viewer

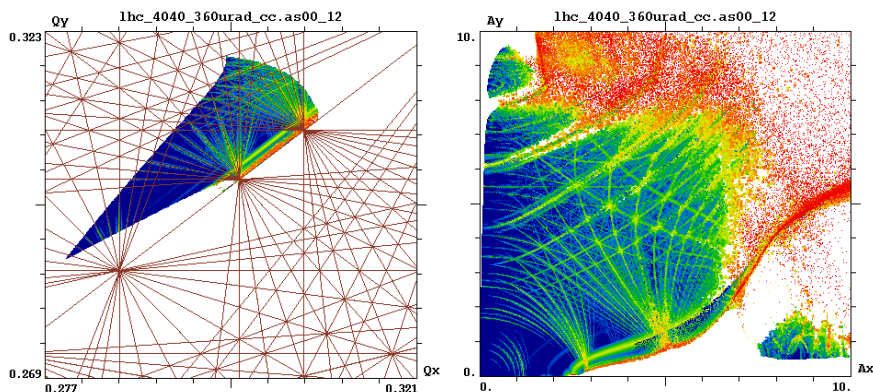


Figure D.2 – Two illustrations of a FMA for the HL-LHC project. On the left, the tunes of particles oscillating with different transverse amplitudes in the tune diagram, colour coded according to their diffusion rates obtained from single particle tracking simulations. Solid lines corresponding to different resonance conditions are shown for comparison. On the right, the same data in action space. Courtesy A. Valishev (FNAL, Batavia, USA).

possibility to make qualitative comparisons between the different bunches. Ultimately, one may use it in an empirical approach to look for better working points, i.e lattice tunes which would optimize the beam lifetime based on measured bunch by bunch differences. Indeed, being spread around in the tune diagram, the different bunches experiences different BB effects with different strength. The comparison of measured lifetimes against positions and extend in the tune diagram for the different bunch families may be used to guide the operator in a tune scan, aiming at maximizing the overall lifetime. As discussed in Sec. D.3.2, in the present LHC configuration, one might assume that the footprint, relatively to the unperturbed tune, is independent of the value of the unperturbed tune. Therefore, one can see the effect of a change of tune by shifting all the footprints. The overall lifetime therefore have a better chances to improve by choosing a shift that will move the footprints towards those who have the best lifetime.

As discussed in Sec. 4.2.3, the observation of coherent instabilities in 2012 enforced the usage of strong stabilizing techniques having themselves a strong impact on the beam lifetime. Consequently, there are machine parameters to be optimized with respect to beam lifetime, having a much stronger impact than the lattice tunes, in particular the octupole and transverse feedback gain and the chromaticities. Also, the lifetime of the LHC beams was not consider critical, as it is still longer than the usual fill duration (Fig. D.3). For these reasons, improvement of the beam lifetime by optimization of the working point was not a priority up to now in the LHC. However, such strategies may become relevant in a near future, when pushing the performance of the machine.

Figure D.3 – Luminosity lifetime at start and end of luminosity production (namely during stable beam (SB)) during the 2012 proton run of the LHC. Courtesy A.L. Macpherson [116].

D.2.2 Stability consideration

The LHC beams rely on Landau damping for the stability of impedance driven mode. Landau damping is a direct consequence of the tune spread created by the different non linearities. Even though the tune spread does not directly provide the stability diagram, it gives already a first insight in the evolution of the tune spread during operational processes, which could help explaining difference in the stability of different bunches. Going back to the example illustrated in Fig. D.1, it is clear that bunches that do not experience HO collision in IP1 and 5 (blue footprints) have a much smaller tune spread than other bunches. A different behaviour is expected in term of coherent stability for those bunches with respect to the others. It is however not planned to implement an online computation of the stability diagram, using PYSSD, due to the heavy computational requirement.

D.3 How to

D.3.1 Basics

The minimal user may want to follow the instructions of Fig. D.4. Once launched in online mode, the application will loop on the following procedure until the user stops it or an error is encountered. Eventually, the dump of one beam will stop the execution.

- Load current beam parameters

Appendix D. The online beam-beam footprint viewer

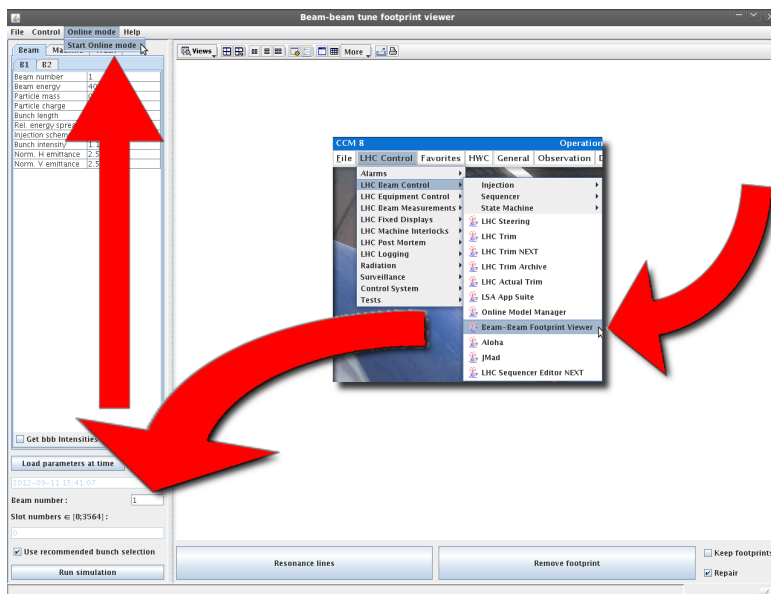


Figure D.4 – Start the application from the control room, select the beam and then start online mode.

- Start the computation of footprints for the (automatically) selected bunches
- Display footprints
- Wait until all jobs are finished

D.3.2 Advanced

A more advanced user may want to control the machine and beam parameters through the different control side panels (Fig. D.5). Also, the *track* panel allows to choose different parameter of the simulation. It is important to note that the computation time goes linearly with the number of particle to track. The current settings allow to easily spot the main feature of the footprints while keeping the computing time reasonably small.

Manipulation

The footprint describes the frequency spread of non-linear system, strictly speaking, every change of machine or beam parameter requires the footprint to be re-computed. However, one may use scaling laws to manipulate the footprint without having to recompute it, within a limited range and making a few assumptions. Firstly, neglecting the dynamic β as well as the effect of resonances, the footprint, relatively to the lattice tune, is independent of the value of the lattice tunes. Secondly, under the same assumptions, the footprint due to BB effects may be considered as linearly dependent on the intensity. This assumption is not valid for lattice non-linearities. The manipulation panel (Fig. D.5d) takes advantage of two

these laws to manipulate the footprints.

Display

The footprints are display in a tune diagram (Q_x vs. Q_y), colour-coded according to their HO family. For comparison, the working point is marked with a red dot. The *Resonance lines* button allow to choose which resonances are displayed on top.

When displaying a footprint, the already existing one of the same bunch will be overwritten. This can be avoided by checking *Keep footprints*.

The algorithm to find the tunes relies on the peak finding in the FFT of the tracking data. In the case of non-zero coupling, it is likely for the algorithm to mistake horizontal and vertical peaks for the particle oscillating at small amplitude in one plane and large in the other. If *Repair* is checked, such errors will be detected, and the corresponding point will not be displayed.

	B1	B2
Beam number	1	
Beam energy	4000.0	
Particle mass	0.938272	
Particle charge	1.0	
Bunch length	0.077	
Rel. energy spread	1.1E-4	
Injection scheme	Nominal 25ns sch...	
Bunch intensity	1.15E11	
Norm. H emittance	2.5E-6	
Norm. V emittance	2.5E-6	

Get bbb Intensities

(a) Beam parameters

Select optic :

- A060C060A300L300_THIN_2012
- A070C070A300L300_THIN_2012
- A080C080A300L300_THIN_2012
- A090C090A300L300_THIN_2012
- A100C100A300L300_THIN_2012
- A120C120A300L300_THIN_2012
- A150C150A300L300_THIN_2012
- A160C160A350L300_THIN_2012
- A200C200A400L325_THIN_2012
- A250C250A450L350_THIN_2012
- A300C300A500L375_THIN_2012
- A400C400A600L500_THIN_2012
- A700C700A750L600_THIN_2012
- A900C900A900L750_THIN_2012
- A1100C1000A1100L1000_THIN_2012

Machine :

Octupole [A] | 0.0

Collisions :

IP1 IP2 IP5 IP8

Selected collision configuration :

State [on/off]	on
Half HXing [μrad]	-130.0
Half YXing [μrad]	90.0
Half Hsep [mm]	0.0
Half Vsep [mm]	0.0
Spectr. Pol. (± 1)	1.0

(b) Machine parameters

Nb of sigma	6
dSigma	1.0
Nb of angle	6
Intensity scaling	1.0

(c) Tracking parameters

File Control Online mode Help

- Show simulation control
- Show manipulator control


Change tune 0.31 0.32

Scale intensity 1

WARNING: these manipulations are valid to a certain extend: know what you are doing

(d) Manipulation

Figure D.5 – Control side panels

- 
- [1] H. Goldstein, C. Poole, and J. Safko, *Classical Mechanics* (Addison Wesley, San Francisco, 1950).
- [2] A. Dragt, AIP conf. proc. **87**, 147 (1982).
- [3] E. Courant and H. Snyder, *Annals of Physics* **3**, 1 (1985).
- [4] W. Herr, in *CAS - CERN Accelerator School: Advanced Course on Accelerator Physics*, Trondheim, Norway, 18-29 August 2013, edited by W. Herr (CERN, Geneva, Switzerland).
- [5] R. Bailey, ed., *CAS - CERN Accelerator School: RF for Accelerators*, Ebeltoft, Denmark, 8-17 June 2010 (CERN, Geneva, Switzerland, 2011).
- [6] W. Herr, in *CAS - CERN Accelerator School: Intermediate Course on Accelerator Physics*, Zeuthen, Germany, 15-26 September 2003, edited by D. Brandt (CERN, Geneva, Switzerland, 2006) pp. 379–410.
- [7] V. Vaccaro, *Longitudinal instability of a coasting beam above transition, due to the action of lumped discontinuities*, ISR-RF/66-35 (CERN, Geneva, Switzerland, 1966).
- [8] A. W. Chao, *Physics of Collective Beams Instabilities in High Energy Accelerators*, edited by I. John Wiley & Sons (John Wiley and Sons, Inc, New York, 1993).
- [9] K. Schindl, in *CAS - CERN Accelerator School: Intermediate Course on Accelerator Physics*, Zeuthen, Germany, 15-26 September 2003, edited by D. Brandt (CERN, Geneva, Switzerland, 2006) pp. 305–320.
- [10] F. Sacherer, *Methods for computing bunched-beam instabilities*, CERN/SI-BR/72-5 (CERN, Geneva, Switzerland, 1972).
- [11] J. Laclare, in *CAS - CERN Accelerator School - Advanced Accelerator Physics*, Oxford, UK, 16-27 September 1985, edited by S. Turner (CERN, Geneva, Switzerland, 1987) pp. 264–326.
- [12] A. Burov, *Phys. Rev. ST Accel. Beams* **17**, 021007 (2014).

Bibliography

- [13] Y. Alexahin, Nucl. Instrum. Methods Phys. Res. A **480**, 253 (2002).
- [14] K. Hirata, Nucl. Instrum. Methods Phys. Res. A **269**, 7 (1988).
- [15] M. Schaumann and R. Alemany, in *Proceedings of the ICFA Mini-workshop on beam-beam effects in hadron colliders*, Geneva, Switzerland, 18-22 March 2013, edited by W. Herr and G. Papotti (CERN, Geneva, Switzerland, 2014) pp. 231–236.
- [16] K. Yokoya and H. Koiso, Part. Acc. **27**, 181 (1990).
- [17] V. Danilov and E. Perevedentsev, Nucl. Instrum. Methods Phys. Res. A **391**, 77 (1997).
- [18] E. A. Perevedentsev and A. A. Valishev, Phys. Rev. ST Accel. Beams **4**, 024403 (2001).
- [19] N. Mounet, *The LHC Transverse Coupled Bunch Instability*, Ph.D. thesis, EPFL (2012).
- [20] L. Landau, J. Phys. USSR **10**, 25 (1946).
- [21] L. N. Trefethen and M. Embree, *Spectra and pseudospectra: The behavior of nonnormal matrices and operators* (Princeton University Press, Princeton, 2005).
- [22] J. S. Berg and F. Ruggiero, *Landau damping with two-dimensional betatron tune spread*, SL-96-071-AP (CERN, Geneva, Switzerland, 1996).
- [23] E. Métral, *Coupled Landau damping of transverse coherent instabilities in particle accelerators*, Ph.D. thesis, Université Joseph Fourier, Grenoble (1999).
- [24] K. Satoh and T. Chin, Nucl. Instrum. Methods Phys. Res. A **207**, 309 (1983).
- [25] G. Golub and C. Van Loan, *Matrix Computation* (The John Hopkins University Press, Baltimore, 1996).
- [26] C.-X. Wang, V. Sajaev, and C.-Y. Yao, Phys. Rev. ST Accel. Beams **6**, 104001 (2003).
- [27] C. Moller, K.Danske Vidensk. Selsk. Mat.-Fys. Medd **23**, 1 (1945).
- [28] W. Herr and B. Muratori, in *CAS - CERN Accelerator School: Intermediate Course on Accelerator Physics*, Zeuthen, Germany, 15-26 September 2003, edited by D. Brandt (CERN, Geneva, Switzerland, 2006) pp. 361–378.
- [29] R. Jacobsson, in *Proceedings of the ICFA Mini-workshop on beam-beam effects in hadron colliders*, Geneva, Switzerland, 18-22 March 2013, edited by W. Herr and G. Papotti (CERN, Geneva, Switzerland, 2014) pp. 167–176.
- [30] O. Brüning, P. Collier, P. Lebrun, S. Myers, R. Ostojic, J. Poole, and P. Proudlock, eds., *LHC Design report*, Vol. 1 : The LHC Main ring (CERN, Geneva, Switzerland, 2004).
- [31] M. Benedikt, P. Collier, V. Mertens, J. Poole, and S. Karlheinz, eds., *LHC Design report*, Vol. 3 : The LHC Injector Chain (CERN, Geneva, Switzerland, 2004).

- [32] G. Rumolo, G. Iadarola, O. Dominguez, G. Arduini, H. Bartosik, S. Claudet, J. Esteban-Muller, F. Roncarolo, E. Shaposhnikova, and L. Tavian, in *Proceedings of the 2012 Chamonix workshop on LHC performance*, Chamonix, France, 6-10 February 2012, edited by C. Carli (CERN, Geneva, Switzerland, 2012) pp. 89–98.
- [33] R. Steerenberg, G. Aduini, K. Cornelis, H. Damerau, R. Garoby, S. Gilardoni, M. Giovannozzi, B. Goddard, S. Hancock, D. Manglunki, E. Métral, B. Mikulec, and J. Weninger, in *Proceedings of the 2012 Chamonix workshop on LHC performance*, Chamonix, France, 6-10 February 2012, edited by C. Carli (CERN, Geneva, Switzerland, 2012) pp. 145–149.
- [34] H. Grote, F. Schmidt, and L. Leunissen, *LHC dynamic aperture at collision*, LHC Project Note 197 (CERN, Geneva, Switzerland, 1999).
- [35] W. Herr, *Dynamic behaviour of nominal and PACMAN bunches for different LHC crossing schemes*, LHC Project Report 856 (CERN, Geneva, Switzerland, 2005).
- [36] W. Herr, *Features and implications of different LHC crossing schemes*, LHC Project Report 628 (CERN, Geneva, Switzerland, 2003).
- [37] O. Brüning, P. Collier, P. Lebrun, S. Myers, R. Ostojic, J. Poole, and P. Proudlock, eds., “LHC design report,” (CERN, Geneva, Switzerland, 2004) Chap. 5 - Collective effects.
- [38] <http://lpc.web.cern.ch/lpc/fillingschemes.htm>.
- [39] O. Brüning, W. Herr, and R. Ostojic, *A Beam Separation and Collision Scheme for IP2 and IP8 at the LHC for Optics Version 6.1*, LHC Project Report 367 (CERN, Geneva, Switzerland, 2000).
- [40] W. Herr, M. Meddahi, and Y. Papaphilippou, *How do we have to operate the LHCb spectrometer magnet?*, LHC Project Note 419 (CERN, Geneva, Switzerland, 2009).
- [41] B. Holzer, in *Proceedings of the 2012 Evian Workshop on LHC Beam Operation*, Evian-les-Bains, France, 17-20 December 2012, edited by B. Goddard and S. Dubourg (CERN, Geneva, Switzerland, 2012) pp. 33–40.
- [42] S. White, in *Proceedings of the second 2010 Evian workshop on LHC beam operation*, Evian-les-Bains, France, 7-9 December 2010, edited by B. Goddard and S. Dubourg (CERN, Geneva, Switzerland, 2010) pp. 205–210.
- [43] M. Krupa and L. Soby, in *Proceedings of the 20th International Conference "Mixed Design of Integrated Circuits and Systems"*, Gdynia, Poland, 20-22 June 2013, edited by A. Napieralski (IEEE, 2013) pp. 592–597.
- [44] F. Roncarolo, S. B. Pedersen, E. Bravin, A. Boccardi, J. Emery, A. Guerrero, T. Lefevre, A. Jeff, A. Rabiller, and M. Sapinski, in *Proceedings of the second 2010 Evian workshop on LHC beam operation*, Evian-les-Bains, France, 7-9 December 2010, edited by B. Goddard and S. Dubourg (CERN, Geneva, Switzerland, 2011) pp. 119–124.

Bibliography

- [45] M. Gasior and R. Jones, *The principle and first results of betatron tune measurement by direct diode detection*, LHC Project Report 853 (CERN, Geneva, Switzerland, 2005).
- [46] The CMS Collaboration, *Measurement of CMS luminosity*, CMS PAS EWK-10-004 (CERN, Geneva, Switzerland, 2010).
- [47] The ATLAS Collaboration, *Luminosity Determination in pp Collisions at $\sqrt{s} = 7$ TeV Using the ATLAS Detector at the LHC*, CERN-PH-EP-2010-069 (CERN, Geneva, Switzerland, 2010).
- [48] The LHCb Collaboration, *Absolute luminosity measurements with the LHCb detector at the LHC*, CERN-PH-EP-2011-157 (CERN, Geneva, Switzerland, 2011).
- [49] W. Höfle, G. Arduini, R. De Maria, G. Kotzian, D. Valuch, and V. Lebedev, in *Proceedings of the 2nd International Particle Accelerator Conference*, San Sebastián, Spain, 4-9 September 2011, edited by C. Petit-Jean-Genaz, A. Blanco, I. Etxebarria, F. Perez, A. Wolski, and V. Schaa (JACoW, Geneva, Switzerland, 2011) pp. 508–510.
- [50] E. Gorbachev, N. Lebedev, A. Makarov, N. Pilyar, R. Rabtsun, R. Smolkov, V. Zhabitsky, P. Baudrenghien, W. Höfle, F. Killing, I. Kojevnikov, G. Kotzian, R. Louwerse, E. Montesinos, V. Rossi, M. Schokker, E. Thepenier, and D. Valuch, in *Proceedings of RuPAC 2008*, Zvenigorod, Russia, 28 September - 3 October 2008, edited by M. Kuzin, E. Shirikova, and A. Philippov (JACoW, Geneva, Switzerland, 2008) pp. 97–100.
- [51] W. Höfle, in *Proceedings of the 4th International Particle Accelerator Conference*, Shanghai, China, 12-17 May 2013, edited by Z. Dai, C. Petit-Jean-Genaz, V. Schaa, and C. Zhang (JACoW, Geneva, Switzerland, 2013) pp. 3990–3994.
- [52] N. Mounet, Private communication (2012).
- [53] R. Assmann *et al.*, in *Proceedings of the 46th ICFA Advanced Beam Dynamics Workshop on High-Intensity and High-Brightness Hadron Beams*, Morschach, Switzerland, 27 September - 1 October 2010, edited by A. Adelman, J. Chrin, M. Marx, V. Schaa, and M. Seidel (JACoW, Geneva, Switzerland, 2011) pp. 21–33.
- [54] N. Mounet, X. Buffat, R. Bruce, W. Herr, E. Métral, G. Rumolo, and B. Salvant, in *Proceedings of the 2011 Evian workshop on LHC beam operation*, Evian-les-Bains, France, 12-14 December 2011, edited by B. Goddard and S. Dubourg (CERN, Geneva, Switzerland, 2012) pp. 143–156.
- [55] A. W. Chao, “Lecture notes on special topics in accelerator physics,” (SLAC-PUB-9574, 2002) Chap. 9 Lie Algebra Technique for nonlinear Dynamics.
- [56] W. Herr and L. Vos, *Tune distributions and effective tune spread from beam-beam interactions and the consequences for Landau damping in the LHC*, LHC project note 316 (CERN, Geneva, Switzerland, 2003).

-
- [57] E. Métral and A. Verdier, *Stability diagram for Landau damping with a beam collimated at an arbitrary number of sigmas*, CERN-AB-2004-019-ABP (CERN, Geneva, Switzerland, 2004).
- [58] G. Korn and T. Korn, *Mathematical Handbook for Scientists and Engineers* (Dover Publications, Inc, Mineola, 2000).
- [59] K. Atkinson, *An Introduction to Numerical Analysis* (John Wiley & Sons, Inc, New York, 1989).
- [60] J. Gareyte, J.-P. Koutchouk, and F. Ruggiero, *Landau damping, dynamic aperture and octupole in LHC*, LHC Project Report 91 (CERN, Geneva, Switzerland, 1997).
- [61] S. Fartoukh, “On the sign of the LHC octupole,” Presented at the LHC Machine Committee, CERN, July 2012.
- [62] S. White, X. Buffat, N. Mounet, and T. Pieloni, *Phys. Rev. ST Accel. Beams* **17**, 041002 (2014).
- [63] J. Qiang, M. A. Furman, R. D. Ryne, W. Fischer, and K. Ohmi, *Nucl.Instrum.Meth. A* **558**, 351 (2006).
- [64] S. Myers, *A Mechanism for Beam Loss during Vertical Steering*, ISR-RF/SM/ps (CERN, Geneva, Switzerland, 1979).
- [65] B. Sliverman, *Density Estimation for Statistics and Data Analysis* (Chapman & Hall, London, 1986).
- [66] R. Tomás, T. Bach, R. Calaga, A. Langner, Y. I. Levinsen, E. H. Maclean, T. H. B. Persson, P. K. Skowronski, M. Strzelczyk, G. Vanbavinckhove, and R. Miyamoto, *Phys. Rev. ST Accel. Beams* **15**, 091001 (2012).
- [67] G. Valentino, R. Assmann, R. Bruce, F. Burkart, V. Previtali, S. Redaelli, B. Salvachua, G. Stancari, and A. Valishev, *Phys. Rev. ST Accel. Beams* **16**, 021003 (2013).
- [68] A. Bazzani and L. Beccaceci, *Journal of Physics A: Mathematical and General* **31**, 5843 (1998).
- [69] R. Steinhagen, A. Boccardi, M. Gasior, O. Jones, and S. Jackson, in *Proceedings of the 2010 Beam Instrumentation Workshop*, Santa Fe, New Mexico, USA, 2-6 May 2010, edited by C. Dillingham and J. Chew (JACoW, Geneva, Switzerland, 2010) pp. 323–327.
- [70] R. Alemany, X. Buffat, R. Calaga, K. Cornelis, M. Fitterer, R. Giachino, W. Herr, A. Macpherson, R. Miyamoto, G. Papotti, T. Pieloni, F. Roncarolo, M. Schaumann, R. Suykerbuyk, G. Trad, and S. Paret, *Head-on beam-beam tune shifts with high brightness beams in the LHC*, CERN-ATS-Note-2011-029 MD (CERN, Geneva, Switzerland, 2011).

Bibliography

- [71] M. Albert, R. Alemany, R. Assmann, X. Buffat, R. Calaga, K. Cornelis, M. Fitterer, R. Giachino, W. Herr, R. Miyamoto, L. Norman, G. Papotti, T. Pieloni, L. Ponce, S. Redaelli, M. Schaumann, G. Trad, and D. Wollman, *Head-on beam-beam collisions with high intensities and long range beam-beam studies in the LHC*, CERN-ATS-Note-2011-058 MD (CERN, Geneva, Switzerland, 2011).
- [72] G. Trad, R. Alemany, X. Buffat, R. Calaga, K. Cornelis, G. Crockford, R. Giachino, W. Herr, G. Papotti, M. Pojer, and M. Schaumann, *Beam parameters observations during a high pile-up collisions fill*, CERN-ATS-Note-2011-105 MD (CERN, Geneva, Switzerland, 2011).
- [73] G. Trad, R. Alemany, X. Buffat, R. Calaga, K. Cornelis, W. Herr, D. Jacquet, G. Papotti, M. Schaumann, and W. Venturini Delsolaro, *Beam parameters observations during the second high pile-up collisions fill in 2011*, CERN-ATS-Note-2012-010 MD (CERN, Geneva, Switzerland, 2012).
- [74] T. Pieloni, *A Study of Beam-Beam Effects in Hadron Colliders with a Large Number of Bunches*, Ph.D. thesis, EPFL (2008).
- [75] G. Rumolo and F. Zimmermann, *Phys. Rev. ST Accel. Beams* **5**, 121002 (2002).
- [76] W. Herr and R. Paparella, *Landau damping of coherent beam-beam modes overlap with synchrotron side-bands*, LHC Project Report 304 (CERN, Geneva, Switzerland, 2002).
- [77] T. Pieloni, D. Banfi, J. Barranco, X. Buffat, N. Mounet, J. Qiang, C. Tambasco, S. White, E. Métral, and G. Arduini, in *Proceedings of the 2014 Evian workshop on LHC beam operation*, Evian-les-Bains, France, 2-4 June 2014, edited by B. Goddard and S. Dubourg (CERN, Geneva, Switzerland).
- [78] X. Buffat, W. Herr, T. Pieloni, and S. White, *Stability of Beams Colliding with a Transverse Offset*, CERN-ATS-Note-2013-016 MD (CERN, Geneva, Switzerland, 2013).
- [79] H. Bartosik, *Beam dynamics and optics studies for the LHC injectors upgrade*, Ph.D. thesis, Technische Universität Wien (2013).
- [80] E. Métral, in *Proceedings of Chamonix 2011 workshop on LHC performance*, Chamonix, France, 24-28 January 2011, edited by C. Carli (CERN, Geneva, Switzerland, 2011) pp. 252–260.
- [81] M. Lamont and O. Johnson, “Lifetimes in stable beam revisited,” Presented at the LHC Beam Operation Committee (2014).
- [82] N. Mounet, B. Salvant, R. Bruce, E. Métral, C. Zannini, O. Frasciello, M. Zobov, R. Wanzenberg, and O. Zagorodnova, “Transverse impedance in the HL-LHC era,” Presented at the 3rd joint HiLumi LHC - LARP annual meeting (2013).

- [83] X. Buffat, D. Banfi, G. Coombs, W. Herr, and T. Pieloni, in *Proceedings of 5th International Particle Accelerator Conference*, Dresden, Germany, 15-20 June 2014, edited by C. Petit-Jean-Genaz, G. Arduini, P. Michel, and V. Schaa (JACoW, Geneva, Switzerland, 2014) pp. 1061–1063.
- [84] R. De Maria, G. Arduini, D. Banfi, J. Barranco, H. Bartosik, R. Bruce, O. Brüning, R. Calaga, F. Cerutti, H. Damerou, L. Esposito, S. Fartoukh, M. Fitterer, R. Garoby, S. Gilardoni, M. Giovannozzi, B. Goddard, B. Gorini, M. Lamont, E. Métral, N. Mounet, T. Pieloni, S. Redaelli, L. Rossi, G. Rumolo, E. Todesco, R. Tomás, F. Zimmermann, and A. Valishev, “How to maximize the HL-LHC performance,” Review of LHC and injector upgrade plans workshop, Archamps, France, 29-31 October 2013, <http://indico.cern.ch/event/260492/session/4/contribution/17/material/paper/1.pdf>.
- [85] R. Bruce, R. Assmann, L. Lari, and S. Redaelli, in *Proceedings of the 2013 MPP Workshop*, Annecy, France, 11-13 March 2013, edited by M. Jonker (CERN, CERN, Geneva, 2014) pp. 99–107.
- [86] C. Roderick and R. Billen, *The LSA database to drive the accelerator settings*, CERN-ATS-2009-100 (CERN, Geneva, Switzerland, 2009).
- [87] X. Buffat, W. Herr, M. Lamont, T. Pieloni, S. Redaelli, and J. Wenninger, *Results of β^* luminosity leveling MD*, CERN-ATS-Note-2012-071 MD (CERN, Geneva, Switzerland, 2012).
- [88] X. Buffat, W. Herr, T. Pieloni, L. Ponce, S. Redaelli, and J. Wenninger, *MD on squeeze with colliding beams*, CERN-ATS-Note-2013-002 MD (CERN, Geneva, Switzerland, 2013).
- [89] M. Lamont, G. Müller, S. Redaelli, and M. Strzelczyk, in *Proceedings of the Evian 2010 workshop on LHC commissioning*, Evian-les-Bains, France, 19-20 January 2010, edited by B. Goddard and S. Dubourg (CERN, Geneva, 2010) pp. 79–86.
- [90] A. Boccardi, M. Gasior, R. Jones, and R. Steinhagen, *An overview of the LHC transverse diagnostics systems*, LHC Project Report 1166 (CERN, Geneva, Switzerland, 2009).
- [91] T. Lefevre, M. Andersen, G. Baud, M. Betz, C. Boccard, A. Boccardi, E. Calvo, J. Fullerton, M. Gasior, S. Jackson, L. Jensen, R. Jones, J. Olexa, J. Savioz, R. Steinhagen, M. Wendt, and J. Wenninger, in *Proceedings of the 2014 Evian workshop on LHC beam operation*, Evian-les-Bains, France, 2-4 June 2014, edited by B. Goddard and S. Dubourg (CERN, Geneva, Switzerland).
- [92] H. Grote, *Self-consistent orbits with beam-beam effect in the LHC*, LHC Project Report 404 (CERN, Geneva, Switzerland, 2000).
- [93] E. Métral, D. Banfi, J. Barranco, H. Bartosik, X. Buffat, O. Brüning, S. Fartoukh, W. Herr, W. Höfle, G. Iadarola, M. Kuhn, K. Li, N. Mounet, T. Pieloni, G. Rumolo, B. Salvachua,

Bibliography

- F. Zimmermann, A. Burov, and S. White, *Summary of the 2-day internal review of LHC performance limitations (linked to transverse collective effects) during run I*, CERN-ACC-NOTE-2014-0006 (CERN, Geneva, Switzerland, 2014).
- [94] G. Papotti, W. Herr, E. Maclean, E. Métral, N. Mounet, R. Tomás, and J. Wenninger, *Chromaticity dependence on octupole strength*, CERN-ATS-Note-2012-072 MD (CERN, Geneva, Switzerland, 2012).
- [95] A. Gorzawski, J. Wenninger, R. Bruce, R. Tomás, X. Buffat, and T. Pieloni, in *Proceedings of the 2014 Evian workshop on LHC beam operation*, Evian-les-Bains, France, 2-4 June 2014, edited by B. Goddard and S. Dubourg (CERN, Geneva, Switzerland).
- [96] W. Herr, M. P. Zorzano, and F. Jones, *Phys. Rev. ST Accel. Beams* **4**, 054402 (2001).
- [97] W. Herr, *Spectra of multiple bunches coupled by head-on and long-range interactions*, LHC Project Note 356 (CERN, Geneva, Switzerland, 2004).
- [98] K. Ohmi, in *Proceedings of the ICFA Mini-workshop on beam-beam effects in hadron colliders*, Geneva, Switzerland, 18-22 March 2013, edited by W. Herr and G. Papotti (CERN, Geneva, Switzerland, 2014) pp. 69–74.
- [99] S. Paret and J. Qiang, in *Proceedings of the ICFA Mini-workshop on beam-beam effects in hadron colliders*, Geneva, Switzerland, 18-22 March 2013, edited by W. Herr and G. Papotti (CERN, Geneva, Switzerland, 2014) pp. 237–242.
- [100] <http://www.open-mpi.org>.
- [101] The MPI Forum, *MPI: A Message-Passing Interface Standard Version 3.0* (University of Tennessee, Knoxville, 2012).
- [102] OpenMP Architecture Review Board, “OpenMP Application Program Interface,” <http://www.openmp.org> (2013).
- [103] The IEEE and The Open Group, “POSIX.1-2008,” <http://pubs.opengroup.org/onlinepubs/9699919799> (2013).
- [104] <http://aries.epfl.ch>.
- [105] G. Kotzian, W. Höfle, and D. Valuch, “Sensitivity of the ADT to intrabunch motion,” Presentation at the HSC section meeting, Jan. 2014 (2014).
- [106] <http://cern.ch/mad>.
- [107] W. Herr, *Particle Tracking with MAD-X including LHC beam-beam interactions*, LHC Project Note 344 (CERN, Geneva, Switzerland, 2004).
- [108] W. Herr, *Tune Shift and Spread Due to Short and Long Range Beam-Beam Interactions in the LHC*, LHC Note No. 119 (CERN, Geneva, Switzerland, 1990).

- [109] R. Bartolini and F. Schmidt, *A Computer Code for Frequency Analysis of Non-Linear Betatron Motion*, SL-Note-98-017-AP (CERN, Geneva, Switzerland, 1998).
- [110] K. Hirata, H. Moshhammer, and F. Ruggiero, *Part. Accel.* **40**, 205 (1993).
- [111] K. Fuchsberger, X. Buffat, Y. Levinsen, and G. Müller, in *Proceedings of 2nd International Particle Accelerator Conference*, San Sebastián, Spain, 4-9 September 2011, edited by C. Petit-Jean-Genaz, A. Blanco, I. Etxebarria, F. Perez, A. Wolski, and V. Schaa (JACoW, Geneva, Switzerland, 2011) pp. 2292–2294.
- [112] C. A. Pons, X. Buffat, M. Giovannozzi, G. Müller, S. Redaelli, K. Fuchsberger, M. Lamont, and F. Schmidt, in *Proceedings of 1st International Particle Accelerator Conference*, Kyoto, Japan, 23-28 May 2010, edited by A. Noda, C. Petit-Jean-Genaz, V. Schaa, T. Shirai, and A. Shirakawa (JACoW, Geneva, Switzerland, 2010) pp. 480–482.
- [113] R. Billen and C. Roderick, *The LHC Logging Service. Capturing, storing and using time-series data for the world's largest scientific instrument*, AB-Note-2006-046 (CO) (CERN, Geneva, Switzerland, 2006).
- [114] E. Forest, F. Schmidt, and E. McIntosh, *Introduction to the Polymorphic Tracking Code*, CERN-SL-2002-044 (AP) (CERN, Geneva, Switzerland, 2002).
- [115] J. Laskar and D. Robin, *Part. Acc.* **54**, 183 (1996).
- [116] A. Macpherson, in *Proceedings of the 2012 Evian workshop on LHC beam operation*, Evian-les-Bains, France, 17-20 December 2012, edited by B. Goddard and S. Dubourg (CERN, Geneva, Switzerland, 2013) pp. 1–6.

Xavier Buffat

Physicist

Accelerators and Beam Physics Group
CERN, BE Department
CH-1211 Geneva 23
☎ +4178/832.37.07
☎ +4122/767.93.35
✉ xavier.buffat@cern.ch

Personal Information

Born 24th Jan. 1988 in Saint-Aubain, Neuchâtel, Switzerland
Nationality Swiss
Language French (native), English (C1), German (B1)
Hobbies Sports, in particular Volleyball and mountain activities, such as snowboarding and hiking.
Address Impasse de la Grande Lignée 4
1044 Fey
Vaud - Switzerland

Education

2011-2014 **Ph.D. in Physics**, *École Polytechnique Fédérale de Lausanne / CERN.*
Transverse Beams Stability Studies at the Large Hadron Collider under the supervision of Prof. L. Rivkin and Dr. T. Pieloni
2009-2011 **Master of Science in Physics**, *École Polytechnique Fédérale de Lausanne, 5.33/6.*
Betatron squeeze optimisation at the Large Hadron Collider based on first year of operation data under the supervision of Prof. L. Rivkin and Dr. S. Redaelli
2006-2009 **Bachelor of Science in Physics**, *École Polytechnique Fédérale de Lausanne, 5.3/6.*

Experience

2010-2014 **Doctoral student**, *CERN, Geneva.*
Under the supervision of Dr. T. Pieloni, Accelerator and Beam Physics.

- Implemented advanced parallelization techniques in a multi-particle tracking code aiming at self-consistent beam-beam simulations.
- Studied numerically the emittance growth due to external sources of noise in the presence of beam-beam interactions.
- Took part in the design, execution and data analysis of several experimental studies on beam-beam effects in the LHC, as well as an experiment at RHIC dedicated to emittance growth due to external noise on colliding beams, in collaboration with Dr. W. Fischer and Dr. S. White (BNL).
- Studied and demonstrated the feasibility of luminosity leveling with β^* in the LHC, in collaboration with Dr. J. Wenninger and Dr. S. Redaelli (CERN).
- Developed a numerical integrator based on MAD-X to derive stability diagrams in arbitrarily complex beam-beam configurations, including lattice non-linearities.
- Studied the beams stability in the presence of multiple beam-beam interactions and beam coupling impedance in the multi-bunch regime, through a semi-analytical model and multi-particle tracking, in collaboration with S. White (BNL).

- 2010–2011 **Technical student**, *CERN*, Geneva.
 Under the supervision of Dr. S. Redaelli, LHC operation group.
- Characterization and optimization of the betatron squeeze through systematic fill by fill analysis of measured beam parameters and losses.
 - Reduction of the duration of the squeeze, and consequently the turn-around time, by implementing on-line simulation of linear beam parameters with MAD-X.
- 2007–2012 **Teaching assistant**, *École Polytechnique Fédérale de Lausanne*.
- *Informatique (C++)*, J.C. Chappellier
 - *Physique générale*, Prof. A. Pasquarello
 - *Physique générale*, Prof. E. Kapon
 - *Travaux pratique de physique*, Prof. F. László
 - *Introduction to Particle Accelerators*, Prof. L. Rivkin

Visits, conferences

- 2013 **ICFA Mini-Workshop on Beam-Beam effects in Hadron Colliders**, Geneva, Switzerland.
 Part of the local organizing committee.
- 2012 **Two weeks visit at Brookhaven National Laboratory**, Upton, USA.
 Experimental study on emittance effects in the presence of external noise.

Lectures attended

- 2013 **Parallel computing and pThreads**, *École Polytechnique Fédérale de Lausanne*, V. Rezzonico.
- 2012 **Magnetic Confinement**, *École Polytechnique Fédérale de Lausanne*, Dr. W.A Cooper, Dr. J.M. Moret, Dr. D. Testa, Prof. M.Q. Tran, Dr. O. Sauter, Prof. P. Ricci, Prof. A. Fasoli.
- 2011 **CERN Accelerator School**, Intermediate level, Chios, Greece.

Computer skills

Language	Experienced with C/C++, Fortran, Java, Python, Matlab, Bash and L ^A T _E X.
Parallel computing	Experienced with MPI, openMP and pThreads. Basic knowledge of CUDA.

References

Dr. Stefano Redaelli, *CERN*, BE - ABP - HSS.

+4122/767.41.09

stefano.redaelli@cern.ch

Dr. Tatiana Pieloni, *CERN*, BE - ABP - HSC.

+4122/767.36.08

tatiana.pieloni@cern.ch

Prof. Leonid Rivkin, *EPFL*, Particle accelerator physics laboratory.

+4121/693.04.76

leonid.rivkin@epfl.ch

Oral presentations

- 2013 **Stability diagrams of colliding beams**, *ICFA Mini-Workshop on Beam-Beam Effects in Hadron Colliders*, CERN.
- 2013 **Operational considerations on the stability of colliding beams**, *ICFA Mini-Workshop on Beam-Beam Effects in Hadron Colliders*, CERN.
- 2013 **Coherent beam-beam modes in the LHC**, *ICFA Mini-Workshop on Beam-Beam Effects in Hadron Colliders*, CERN.
- 2012 **Squeezing with colliding beams**, *LHC Beam Operation Workshop*, Evian.
- 2012 **LHC Beam-Beam studies**, *Accelerator Physics Seminar*, BNL.

Publications

Journal

- S. White, X. Buffat, N. Mounet, and T. Pieloni, "Transverse mode coupling instability of colliding beams," *Phys. Rev. ST Accel. Beams* **17**, 041002 (2014).
- X. Buffat, W. Herr, N. Mounet, T. Pieloni, and S. White, "Stability diagrams of colliding beams in the Large hadron Collider," Submitted for publication in *Phys. Rev. ST Accel. Beams* in June 2014

Conference

- X. Buffat, D. Banfi, G. Coombs, W. Herr, and T. Pieloni, "Beam-beam effects in different luminosity levelling scenarios for the LHC," in *Proceedings of 5th International Particle Accelerator Conference*, Dresden, Germany, 15-20 June 2014, edited by C. Petit-Jean-Genaz, G. Arduini, P. Michel, and V. Schaa (JACoW, Geneva, Switzerland, 2014) pp. 1061–1063.
- X. Buffat, W. Herr, M. Lamont, T. Pieloni, S. Redaelli, and J. Wenninger, "Colliding during the squeeze and β^* levelling in the LHC," in *Proceedings of the 4th International Particle Accelerator Conference*, Shanghai, China, 12-17 May 2013, edited by Z. Dai, C. Petit-Jean-Genaz, V. Schaa, and C. Zhang (JACoW, Geneva, Switzerland, 2013) pp. 1415–1417.
- X. Buffat, W. Herr, E. Métral, N. Mounet, and T. Pieloni, "Head-on and long-range beam-beam interactions in the LHC: Effective tune spread and beam stability due to Landau damping," in *Proceedings of the 4th International Particle Accelerator Conference*, Shanghai, China, 12-17 May 2013, edited by Z. Dai, C. Petit-Jean-Genaz, V. Schaa, and C. Zhang (JACoW, Geneva, Switzerland, 2013) pp. 1421–1423.
- W. Herr, G. Arduini, R. Giachino, E. Métral, T. Pieloni, X. Buffat, and N. Mounet, "Observation of instabilities in the LHC due to missing head-on beam-beam collision," in *Proceedings of the 4th International Particle Accelerator Conference*, Shanghai, China, 12-17 May 2013, edited by Z. Dai, C. Petit-Jean-Genaz, V. Schaa, and C. Zhang (JACoW, Geneva, Switzerland, 2013) pp. 1412–1414.
- T. Pieloni, G. Arduini, R. Giachino, W. Herr, M. Lamont, E. Métral, N. Mounet, G. Papotti, B. Salvant, J. Wenninger, X. Buffat, and S. White, "Observation of two-beam instabilities

- during the 2012 LHC physics run,” in *Proceedings of the 4th International Particle Accelerator Conference*, Shanghai, China, 12-17 May 2013, edited by Z. Dai, C. Petit-Jean-Genaz, V. Schaa, and C. Zhang (JACoW, Geneva, Switzerland, 2013) pp. 1418–1420.
- S. Redaelli, X. Buffat, M. Lamont, G. Müller, M. S. Camillocci, R. Tomàs, and J. Wenninger, “Operation of the betatron squeeze at the LHC,” in *Proceedings of the 4th International Particle Accelerator Conference*, Shanghai, China, 12-17 May 2013, edited by Z. Dai, C. Petit-Jean-Genaz, V. Schaa, and C. Zhang (JACoW, Geneva, Switzerland, 2013) pp. 1430–1432.
- S. Paret, J. Qiang, R. Alemany, X. Buffat, R. Calaga, K. Cornelis, M. Fitterer, R. Giachino, W. Herr, A. Macpherson, G. Papotti, T. Pieloni, S. Redaelli, F. Roncarolo, M. Schaumann, R. Suykerbuyk, G. Trad, and R. Miyamoto, “Tune studies with beam-beam effects in the LHC,” in *Proceedings of the 4th International Particle Accelerator Conference*, Shanghai, China, 12-17 May 2013, edited by Z. Dai, C. Petit-Jean-Genaz, V. Schaa, and C. Zhang (JACoW, Geneva, Switzerland, 2013) pp. 1703–1705.
- R. Giachino, W. Herr, E. Métral, G. Papotti, T. Pieloni, G. Trad, X. Buffat, and D. Kaltchev, “Performance limitations in the LHC due to parasitic beam-beam encounters - parameter dependence, scaling and pacman effects,” in *Proceedings of the 4th International Particle Accelerator Conference*, Shanghai, China, 12-17 May 2013, edited by Z. Dai, C. Petit-Jean-Genaz, V. Schaa, and C. Zhang (JACoW, Geneva, Switzerland, 2013) pp. 2672–2674.
- G. Papotti, G. Arduini, R. Giachino, W. Herr, E. Métral, T. Pieloni, S. White, X. Buffat, and N. Mounet, “Effect of collision pattern in the LHC on the beam stability: Requirements from the experiments and operational considerations,” in *Proceedings of the 4th International Particle Accelerator Conference*, Shanghai, China, 12-17 May 2013, edited by Z. Dai, C. Petit-Jean-Genaz, V. Schaa, and C. Zhang (JACoW, Geneva, Switzerland, 2013) pp. 1409–1407.
- T. Pieloni, X. Buffat, W. Herr, R. Giachino, E. Métral, and G. Papotti, “Colliding high brightness beams in the LHC,” in *Proceedings of the 52nd ICFA Advanced Beam Dynamics Workshop on High-Intensity and High-Brightness Hadron Beams*, Beijing, China, 17-21 September 2012, edited by N. Zhao, J. Chrin, D. Ji, C. Petit-Jean-Genaz, V. Schaa, and H. Yan (JACoW, Geneva, Switzerland, 2012) pp. 180–182.
- B. Salvant, O. Aberle, G. Arduini, R. Assmann, V. Baglin, M. Barnes, P. Baudrenghien, A. Bertarelli, C. Bracco, R. Bruce, X. Buffat, F. Carra, G. Cattenoz, F. Caspers, S. Claudet, H. Day, J. E. Mueller, M. Garlasché, L. Gentini, B. Goddard, A. Grudiev, B. Henrist, W. Herr, S. Jakobsen, R. Jones, G. Lanza, L. Lari, T. Mastoridis, E. Métral, N. Mounet, A. Nosych, J. L. Nougaret, S. Persichelli, T. Pieloni, A. M. Piguiet, S. Redaelli, F. Roncarolo, G. Rumolo, B. Salvachua, M. Sapinski, E. Shaposhnikova, L. Tavian, M. Timmins, J. Uythoven, A. Vidal, R. Wasef, D. Wollman, A. Burov, and S. White, “LHC impedance model: Experience with high intensity operation in the LHC,” in *Proceedings of the 52nd ICFA Advanced Beam Dynamics Workshop on High-Intensity and High-Brightness Hadron Beams*, Beijing, China, 17-21 September 2012, edited by N. Zhao, J. Chrin, D. Ji, C. Petit-Jean-Genaz, V. Schaa, and H. Yan (JACoW, Geneva, Switzerland, 2012) pp. 349–353.
- M. Pereira, X. Buffat, K. Fuchsberger, M. Lamont, G. Müller, S. Redaelli, R. Steinhagen, and J. Wenninger, “Feed forward in the LHC,” in *Proceedings of the 13th International Conference on*

Accelerator and Large Experimental Physics Control Systems, Grenoble, France, 10-14 October 2011, edited by M. Robichon (JACoW, Geneva, Switzerland, 2011) pp. 1302–1305.

- G. Müller, X. Buffat, K. Fuchsberger, M. Giovannozzi, S. Redaelli, and F. Schmidt, “Toolchain for online modeling of the LHC,” in *Proceedings of the 13th International Conference on Accelerator and Large Experimental Physics Control Systems*, Grenoble, France, 10-14 October 2011, edited by M. Robichon (JACoW, Geneva, Switzerland, 2011) pp. 277–280.
- X. Buffat, M. Lamont, S. Redaelli, and J. Wenninger, “Beam based optimization of the squeeze at the LHC,” in *Proceedings of 2nd International Particle Accelerator Conference*, San Sebastián, Spain, 4-9 September 2011, edited by C. Petit-Jean-Genaz, A. Blanco, I. Etxebarria, F. Perez, A. Wolski, and V. Schaa (JACoW, Geneva, Switzerland, 2011) pp. 1867–1869.
- X. Buffat, W. Herr, G. Papotti, T. Pieloni, R. Calaga, and S. White, “Observation of coherent beam-beam effects in the LHC,” in *Proceedings of 2nd International Particle Accelerator Conference*, San Sebastián, Spain, 4-9 September 2011, edited by C. Petit-Jean-Genaz, A. Blanco, I. Etxebarria, F. Perez, A. Wolski, and V. Schaa (JACoW, Geneva, Switzerland, 2011) pp. 1870–1872.
- X. Buffat, G. Müller, S. Redaelli, and M. Strzelczyk, “Simulation of linear beam parameters to minimize the duration of the squeeze at the LHC,” in *Proceedings of 2nd International Particle Accelerator Conference*, San Sebastián, Spain, 4-9 September 2011, edited by C. Petit-Jean-Genaz, A. Blanco, I. Etxebarria, F. Perez, A. Wolski, and V. Schaa (JACoW, Geneva, Switzerland, 2011) pp. 1873–1875.
- K. Fuchsberger, X. Buffat, Y. Levinsen, and G. Müller, “Status of JMAD, the Java-API for MAD-X,” in *Proceedings of 2nd International Particle Accelerator Conference*, San Sebastián, Spain, 4-9 September 2011, edited by C. Petit-Jean-Genaz, A. Blanco, I. Etxebarria, F. Perez, A. Wolski, and V. Schaa (JACoW, Geneva, Switzerland, 2011) pp. 2292–2294.
- S. Redaelli, M. Lamont, G. Müller, R. Steinhagen, J. Wenninger, and X. Buffat, “Commissioning of ramp and squeeze at the LHC,” in *Proceedings of the 46th ICFA Advanced Beam Dynamics Workshop on High-Intensity and High-Brightness Hadron Beams*, Morschach, Switzerland, 4-9 September 2011, edited by A. Adelman, J. Chrin, M. Marx, V. Schaa, and M. Seidel (JACoW, Geneva, Switzerland, 2010) pp. 202–206.
- C. A. Pons, X. Buffat, M. Giovannozzi, G. Müller, S. Redaelli, K. Fuchsberger, M. Lamont, and F. Schmidt, “The online model for the Large Hadron Collider,” in *Proceedings of 1st International Particle Accelerator Conference*, Kyoto, Japan, 23-28 May 2010, edited by A. Noda, C. Petit-Jean-Genaz, V. Schaa, T. Shirai, and A. Shirakawa (JACoW, Geneva, Switzerland, 2010) pp. 480–482

Workshop

- X. Buffat, W. Herr, and T. Pieloni, “Operational consideration on the stability of colliding beams,” in *Proceedings of the ICFA Mini-workshop on beam-beam effects in hadron colliders*, Geneva, Switzerland, 18-22 March 2013, edited by W. Herr and G. Papotti (CERN, Geneva, Switzerland, 2014) pp. 193–197.

- X. Buffat, W. Herr, N. Mounet, and T. Pieloni, "Stability diagram of colliding beams," in *Proceedings of the ICFA Mini-workshop on beam-beam effects in hadron colliders*, Geneva, Switzerland, 18-22 March 2013, edited by W. Herr and G. Papotti (CERN, Geneva, Switzerland, 2014) pp. 57–62.
- X. Buffat, R. Calaga, R. Giachino, W. Herr, G. Papotti, N. Mounet, T. Pieloni, and S. White, "Coherent beam-beam mode in the LHC," in *Proceedings of the ICFA Mini-workshop on beam-beam effects in hadron colliders*, Geneva, Switzerland, 18-22 March 2013, edited by W. Herr and G. Papotti (CERN, Geneva, Switzerland, 2014) pp. 227–230.
- S. White and X. Buffat, "Beam-beam and impedance," in *Proceedings of the ICFA Mini-workshop on beam-beam effects in hadron colliders*, Geneva, Switzerland, 18-22 March 2013, edited by W. Herr and G. Papotti (CERN, Geneva, Switzerland, 2014) pp. 217–226.
- G. Papotti, X. Buffat, W. Herr, R. Giachino, and T. Pieloni, "Observations of beam-beam effects at the LHC," in *Proceedings of the ICFA Mini-workshop on beam-beam effects in hadron colliders*, Geneva, Switzerland, 18-22 March 2013, edited by W. Herr and G. Papotti (CERN, Geneva, Switzerland, 2014) pp. 1–6.
- W. Herr, X. Buffat, R. Calaga, R. Giachino, G. Papotti, T. Pieloni, and D. Kaltchev, "Long-range beam-beam effects in the LHC," in *Proceedings of the ICFA Mini-workshop on beam-beam effects in hadron colliders*, Geneva, Switzerland, 18-22 March 2013, edited by W. Herr and G. Papotti (CERN, Geneva, Switzerland, 2014) pp. 87–92.
- X. Buffat, W. Herr, M. Lamont, S. Redaelli, and J. Wenninger, "Squeezing with colliding beams," in *Proceedings of the 2012 Evian workshop on LHC beam operation*, Evian-les-Bains, France, 18-22 March 2013, edited by B. Goddard and S. Dubourg (CERN, Geneva, Switzerland, 2012) pp. 27–32.
- E. Métral, G. Arduini, R. Assmann, O. Brunning, X. Buffat, A. Burov, W. Herr, W. Hofle, M. Lamont, N. Mounet, T. Pieloni, G. Rumolo, B. Salvant, F. Schmidt, E. Shaposhnikova, D. Valuch, J. Wenninger, S. White, and F. Zimmermann, "Review of the instabilities observed during the 2012 run and actions taken," in *Proceedings of the 2012 Evian workshop on LHC beam operation*, Evian-les-Bains, France, 17-20 December 2012, edited by B. Goddard and S. Dubourg (CERN, Geneva, Switzerland, 2013) pp. 87–94.
- N. Mounet, E. Métral, G. Arduini, T. Pieloni, S. White, X. Buffat, R. Calaga, J. Esteban-Müller, R. Bruce, S. Redaelli, B. Salvachua, and G. Rumolo, "Beam stability with separated beam at 6.5 TeV," in *Proceedings of the 2012 Evian workshop on LHC beam operation*, Evian-les-Bains, France, 17-20 December 2012, edited by B. Goddard and S. Dubourg (CERN, Geneva, Switzerland, 2013) pp. 95–100.
- T. Pieloni, G. Arduini, R. Bruce, W. Herr, E. Métral, N. Mounet, X. Buffat, and S. White, "Beam stability of colliding beams at 6.5 TeV," in *Proceedings of the 2012 Evian workshop on LHC beam operation*, Evian-les-Bains, France, 17-20 December 2012, edited by B. Goddard and S. Dubourg (CERN, Geneva, Switzerland, 2013) pp. 101–108.
- W. Herr, R. Alemany, X. Buffat, R. Calaga, R. Giachino, G. Papotti, T. Pieloni, G. Trad, and M. Schaumann, "Observations of beam-beam effects in MDs in 2011," in *Proceedings of the 2012 Chamonix workshop on LHC performance*, Chamonix, France, 6-10 February 2012, edited by C. Carli (CERN, Geneva, Switzerland, 2012) pp. 99–104.

- S. Redaelli, R. Assmann, R. Bruce, X. Buffat, M. Giovannozzi, M. Lamont, R. Miyamoto, G. Müller, R. Thomàs, G. Vanbavinckhove, and J. Wenninger, "Aperture and optics - measurements and conclusions," in *Proceedings of the 2011 Evian workshop on LHC beam operation*, Evian-les-Bains, France, 12-14 December 2011, edited by B. Goddard and S. Dubourg (CERN, Geneva, Switzerland, 2012) pp. 77–84.
- N. Mounet, R. Bruce, X. Buffat, W. Herr, E. Métral, G. Rumolo, and B. Salvant, "Impedance effects on beam stability," in *Proceedings of the 2011 Evian workshop on LHC beam operation*, Evian-les-Bains, France, 12-14 December 2011, edited by B. Goddard and S. Dubourg (CERN, Geneva, Switzerland, 2012) pp. 143–156

CERN internal notes

- E. Métral, D. Banfi, J. Barranco, H. Bartosik, X. Buffat, O. Brüning, S. Fartoukh, W. Herr, W. Höfle, G. Iadarola, M. Kuhn, K. Li, N. Mounet, T. Pieloni, G. Rumolo, B. Salvachua, F. Zimmermann, A. Burov, and S. White, *Summary of the 2-day internal review of LHC performance limitations (linked to transverse collective effects) during run I*, CERN-ACC-NOTE-2014-0006 (CERN, Geneva, Switzerland, 2014).
- R. Thomàs, J. Barranco, X. Buffat, E. Maclean, and S. White, *Collecting amplitude detuning measurements from 2012*, CERN-ACC-NOTE-2014-0027 (CERN, Geneva, Switzerland, 2014).
- J. Abelleira, X. Buffat, C. Bhat, K. Cornelis, R. D. Maria, S. Fartoukh, R. Giachino, B. Holzer, M. Lamont, and T. Mastoridis, *Large Piwinski angle*, CERN-ATS-Note-2012-091 MD (CERN, Geneva, Switzerland, 2012).
- N. Mounet, Y. L. Borgne, X. Buffat, A. Burov, G. Hemelsoet, E. Métral, G. Papotti, T. Pieloni, M. Pojer, and B. Salvant, *Single-beam measurements of LHC instability threshold in terms of octupole current*, CERN-ATS-Note-2012-073 MD (CERN, Geneva, Switzerland, 2012).
- X. Buffat, W. Herr, M. Lamont, T. Pieloni, S. Redaelli, and J. Wenninger, *Results of β^* luminosity leveling MD*, CERN-ATS-Note-2012-071 MD (CERN, Geneva, Switzerland, 2012).
- R. Assmann, R. Bruce, X. Buffat, R. Calaga, R. Giachino, W. Herr, E. Métral, G. Papotti, T. Pieloni, and G. Roy, *Results of long-range beam-beam studies - scaling with beam separation and intensity*, CERN-ATS-Note-2012-070 MD (CERN, Geneva, Switzerland, 2012).
- G. Arduini, H. Bartosik, N. Biancacci, X. Buffat, O. Dominguez, G. Iadarola, E. Métral, G. Rumolo, B. Salvant, and C. Zannini, *25 ns studies in the LHC - MD held on 14/10/2011*, CERN-ATS-Note-2012-042 MD (CERN, Geneva, Switzerland, 2012).
- R. Alemany, R. Assmann, X. Buffat, R. Calaga, M. Fitterer, R. Giachino, G. Hemelsoet, W. Herr, G. Papotti, and T. Pieloni, *Observed Orbit Effects during Long Range Beam-Beam Studies*, CERN-ATS-Note-2012-021 MD (CERN, Geneva, Switzerland, 2012).
- G. Trad, R. Alemany, X. Buffat, R. Calaga, K. Cornelis, W. Herr, D. Jacquet, G. Papotti, M. Schaubmann, and W. V. Delsolaro, *Beam parameters observations during the second high pile-up collisions fill in 2011*, CERN-ATS-Note-2012-010 MD (CERN, Geneva, Switzerland, 2012).

- R. Alemany, R. Assmann, X. Buffat, R. Calaga, M. Fitterer, R. Giachino, G. Hemelsoet, W. Herr, G. Papotti, and T. Pieloni, *Results of long range beam-beam studies and observations during operation in the LHC*, CERN-ATS-Note-2011-120 MD (CERN, Geneva, Switzerland, 2011).
- M. Albert, R. Alemany, R. Assmann, X. Buffat, R. Calaga, K. Cornelis, M. Fitterer, R. Giachino, W. Herr, and R. Miyamoto, *Head-on beam-beam collisions with high intensities and long range beam-beam studies in the LHC*, CERN-ATS-Note-2011-058 MD (CERN, Geneva, Switzerland, 2011).
- R. Alemany, X. Buffat, R. Calaga, K. Cornelis, M. Fitterer, R. Giachino, W. Herr, A. Macpherson, R. Miyamoto, and G. Papotti, *Head-on beam-beam tune shifts with high brightness beams in the LHC*, CERN-ATS-Note-2011-029 MD (CERN, Geneva, Switzerland, 2011).
- H. Burkhardt, X. Buffat, R. Calaga, S. Cavalier, M. Fitterer, Y. Levinsen, A. Macpherson, R. Miyamoto, G. Müller, and S. Redaelli, *Un-squeeze to 90 m*, CERN-ATS-Note-2011-032 MD (CERN, Geneva, Switzerland, 2011)